



Rasmus Cornelius

Fast Spherical Near-Field Antenna Measurement Methods

Fast Spherical Near-Field Antenna Measurement Methods

Rasmus Cornelius



Spherical near-field antenna measurement is an established method for characterizing the electrical properties of antennas. Compared to far-field measurements, however, a mathematical transformation of the near-field data is necessary to determine the desired far-field characteristics. In order to obtain accurate and complete transformation results, it is necessary to acquire near-field data on a closed surface (e.g. a sphere) around the test antenna. This significantly increases the measurement time compared to far-field measurements. This is particularly relevant in view of the increase of mobile communication devices and the associated measurement burden.

After introducing the theory and the transformation algorithms, several possibilities for accelerating the near-field measurements are investigated and evaluated. A simple approach is the reduction of measurement points by truncation of the measurement surface. This method aims to determine only certain, selected areas of the far field correctly. Due to the lack of information however, approximation errors always occur.

The main contribution of this thesis to the state-of-the-art is the investigation of non or minimally redundant sampling grids and the development of the associated transformation methods. It is shown that the number of measurement points can always be minimized by a suitable selection of the transformation origin. Furthermore, it is comprehensively analyzed which scanning grids enable time-efficient and accurate measurements. Using the proposed methods, a measurement time reduction between 5% and 50% has been achieved for the investigated examples. The determined uncertainties show that this does not reduce the measurement accuracy significantly.

In summary, different acceleration methods can be used and combined. Truncation can considerably reduce the measurement time in certain cases, but has the disadvantage that the antenna properties can only be approximated and not completely determined. In comparison, non-redundant sampling grids reduce the measurement time without significantly reducing the measurement accuracy. In general, the spherical mode spectrum can be determined with the developed methods from measured data on any closed measurement surface. The methods presented can therefore also be used to develop novel measuring systems that are adapted to the corresponding measuring task, since a spherical measuring geometry is generally not required.

ISBN 978-3-86359-769-6



Fast Spherical Near-Field Antenna Measurement Methods

Von der Fakultät für Elektrotechnik und Informationstechnik der
Rheinisch-Westfälischen Technischen Hochschule Aachen zur Erlangung
des akademischen Grades eines Doktors der Ingenieurwissenschaften
genehmigte Dissertation

vorgelegt von

Diplom-Ingenieur
Rasmus Cornelius

aus Köln

Berichter: Universitätsprofessor Dr.-Ing. Dirk Heberling
 Universitätsprofessor Dr. rer. nat. Michael Vorländer

Tag der mündlichen Prüfung: 10.07.2019

Diese Dissertation ist auf den Internetseiten der Universitätsbibliothek online
verfügbar.

Bibliografische Information der Deutschen Nationalbibliothek

Die Deutsche Nationalbibliothek verzeichnet diese Publikation in der Deutschen Nationalbibliografie; detaillierte bibliografische Daten sind im Internet über <https://portal.dnb.de> abrufbar.

Rasmus Cornelius:

Fast Spherical Near-Field Antenna Measurement Methods

1. Auflage, 2019

Gedruckt auf holz- und säurefreiem Papier, 100% chlorfrei gebleicht.

Apprimus Verlag, Aachen, 2019

Wissenschaftsverlag des Instituts für Industriekommunikation und Fachmedien
an der RWTH Aachen

Steinbachstr. 25, 52074 Aachen

Internet: www.apprimus-verlag.de, E-Mail: info@apprimus-verlag.de

Printed in Germany

ISBN 978-3-86359-769-6

D 82 (Diss. RWTH Aachen University, 2019)

Kurzfassung

Die sphärische Nahfeldmessmethode ist ein etabliertes Messverfahren zur Charakterisierung der Abstrahleigenschaften von Antennen. Es ermöglicht die präzise Ermittlung der Abstrahlcharakteristik in allen Raumrichtungen. Im Vergleich zu Fernfeldmessungen ist jedoch eine mathematische Transformation der Nahfelddaten nötig, um die Fernfeldcharakteristik zu ermitteln. Um genaue und vollständige Transformationsergebnisse zu erzielen, ist es notwendig, Nahfelddaten auf einer geschlossenen Oberfläche (z.B. Kugeloberfläche) um die Testantenne zu messen. Dies erhöht im Vergleich zu Fernfeldmessungen die Messdauer deutlich, was im Hinblick auf die Zunahme von mobilen Kommunikationsgeräten und dem damit einhergehenden Messaufwand besonders relevant ist. Eine Beschleunigung des Messverfahrens würde es ermöglichen, mehr Antennen in derselben Messkammer zu vermessen und so die Kosten für eine Messung zu reduzieren. Des Weiteren wäre es bei gleichem Zeitaufwand möglich, mehr Konfigurationen oder Frequenzen der Testantenne zu vermessen.

In dieser Arbeit werden verschiedene Verfahren zur Beschleunigung des Messverfahrens untersucht und bewertet. Zunächst wird hierzu die Theorie der sphärischen Modenzerlegung als Transformationsmethode erläutert. Diese Methode hat gegenüber anderen Transformationsmethoden (z.B. basierend auf der Berechnung von äquivalenten elektrischen und magnetischen Strömen) den Vorteil, dass sie ein einfaches und mathematisch abgeschlossenes System bildet. Um aus den Messdaten die sphärischen Moden zu ermitteln, existiert eine Vielzahl verschiedener Algorithmen. In dieser Arbeit werden diese erläutert und ihre Eigenschaften diskutiert. Es wird gezeigt, dass die Transformationszeit für die meisten Antennen kein relevanter Faktor ist. Zudem lässt sich die mathematische Transformation der Messdaten auf separaten Computern durchführen, so dass in der Messkammer bereits eine weitere Messung durchgeführt werden kann. Üblicherweise ist die Messkammer die begrenzte Ressource. Deswegen ist es häufig von Vorteil, die Komplexität der Transformationsprozesse zu erhöhen, um Messkammerzeit zu sparen. Darüber hinaus bieten neue Transformationsverfahren verbesserte Möglichkeiten in Hinsicht auf Messsondenkorrektur und Messflexibilität.

Nach der Ausarbeitung der Grundlagen und der Transformationsalgorithmen werden verschiedene Möglichkeiten zur Beschleunigung der Nahfeldmessungen betrachtet. Zunächst wird die Möglichkeit erörtert, durch verbesserte Messsysteme die Messdauer zu reduzieren. Hierzu zählt neben Messachsen mit höherer Geschwindigkeit auch die Verwendung von mehreren Messkanälen. Eine weitere Möglichkeit der Messzeitreduzierung kann durch Verringerung der Messpunkte erreicht werden. Ein einfacher Ansatz ist die Reduzierung der Messfläche (engl. Truncation). Hierbei wird der Ansatz verfolgt, nur gewisse, ausgewählte Bereiche des Fernfeldes korrekt zu ermitteln. Aufgrund der fehlenden Informationen treten zwar immer Approximationsfehler auf, die jedoch in vielen Messszenarien die Messgenauigkeit nur geringfügig verringert.

Der Hauptbeitrag der Arbeit zum wissenschaftlichen Erkenntnisstand ist die Untersuchung von nicht oder minimal redundanten Abtastgittern und die Entwicklung der zugehörigen Transformationsmethoden inklusive Messsondenkorrektur. Es wird gezeigt, dass die Anzahl der benötigten Messpunkte durch eine geeignete Wahl des Transformationsursprungs minimiert werden kann. Des Weiteren wird umfassend analysiert, welche Abtastgitter zeiteffiziente und genaue Messungen ermöglichen. Hierzu werden zwei typische Messsysteme (Roll-Over-Azimuth und Robot-Arm-System) betrachtet und gezeigt, dass das jeweilige Messsystem einen maßgeblichen Einfluss auf die Messdauer abhängig von den verschiedenen Abtastgittern hat. Des Weiteren wird hervorgehoben, dass die Beschleunigungen vom Betriebsmodus des Messsystems abhängen. Im step mode (es wird an jedem Messpunkt angehalten) ist die Reduktion der Messdauer fast gleich der Reduktion der Messpunkte. Somit lässt sich die Messdauer im Vergleich zu äquidistanter Abtastung durch Verwendung nicht redundanter Abtastgitter fast halbieren. Wird das Messsystem allerdings im continuous mode (kontinuierliche Achsenbewegung) betrieben, hängt die Messdauer maßgeblich von der Pfadlänge durch alle Messpunkte ab. Da diese stets über die ganze Kugel verteilt sein müssen, reduziert sich die Pfadlänge und somit die Messdauer nicht so stark wie die Anzahl der Messpunkte. Trotzdem lassen sich Messungen durch die Verwendung nicht redundanter Abtastgitter beschleunigen. Realistisch sind hier Werte zwischen 5% und 20%. Die ermittelten Messunsicherheiten zeigen, dass nicht redundante Abtastgitter die Messgenauigkeiten in der Regel nicht signifikant erhöhen. Natürlich kann zusätzliche Redundanz, je nach Anforderung an die Messgenauigkeit, zur Filterung von Störeinflüssen hinzugefügt werden. Eine weitere Reduzierung der Messpunkte führt zu unterbestimmten Gleichungssystemen, deren Lösung im Allgemeinen uneindeutig ist. Allerdings ist es durch Methoden des Compressed Sensing trotzdem möglich das Modenspektrum unter gewissen Umständen korrekt zu bestimmen. Diese Methoden sind nicht Gegenstand dieser Arbeit. Zusammenfassend kann gesagt werden, dass verschiedene Beschleunigungsmethoden eingesetzt und kombiniert werden können. Verbesserte Hardware erfordert im Allgemeinen einen Umbau des Messsystems und ist vornehmlich für neue Messanlagen relevant. Truncation kann im Einzelfall die Messzeit erheblich reduzieren, hat aber den Nachteil, dass die Antenneneigenschaften nur näherungsweise und nicht vollständig bestimmt werden können. Im Vergleich dazu reduzieren nicht redundante Abtastgitter die Messzeit ohne die Messgenauigkeit nennenswert zu verringern. Dies ist besonders für existierende Messanlagen interessant, da keine Änderungen an der bestehenden Hardware notwendig sind. Des Weiteren ist eine weitere Beschleunigung durch die Verwendung mehrerer Messkanäle oder Truncation uneingeschränkt möglich. Generell kann mit den entwickelten Verfahren aus Messdaten auf jeder beliebigen geschlossenen Hüllfläche das sphärische Modenspektrum ermittelt werden. Die vorgestellten Methoden können daher ebenfalls dazu verwendet werden neuartige Messsysteme zu entwickeln, die an die entsprechende Messaufgabe angepasst sind, da eine sphärische Messgeometrie im Allgemeinen nicht erforderlich ist.

Summary

Spherical near-field antenna measurement is an established method for characterizing the electrical properties of antennas. It allows the precise determination of the radiation characteristic in all spatial directions. Compared to far-field measurements, however, a mathematical transformation of the near-field data is necessary to determine the far-field characteristics. In order to obtain accurate and complete transformation results, it is necessary to acquire near-field data on a closed surface (e.g. a sphere) around the test antenna. This significantly increases the measurement time compared to far-field measurements, which is particularly relevant in view of the increase of mobile communication devices and the associated measurement burden. An acceleration of the measurement would make it possible to measure more antennas in the same measurement chamber and, thus, to reduce the cost of an antenna measurement. Furthermore, it would be possible to measure more configurations or frequencies of the test antenna within the same time.

In this thesis, different methods for accelerating spherical near-field antenna measurements are investigated and evaluated. First, the theory of spherical wave expansion as a transformation method is explained. This method has the advantage over other transformation methods (e.g. based on the calculation of equivalent electric and magnetic currents) that it forms a simple and mathematically complete system. In order to determine the spherical modes from the measured data, a variety of different algorithms exist. In this work, these are explained and their properties are discussed. It is shown that the transformation time is not a relevant factor for most antennas. In addition, the transformation can be carried out on a dedicated computer, so that another measurement can already be performed. Usually the measuring chamber is the limiting resource. Therefore, it is often beneficial to increase the complexity of the transformation to reduce measurement chamber utilization. In addition, new transformation techniques offer improved possibilities in terms of probe correction and measurement flexibility.

After introducing the theory and the transformation algorithms, several possibilities for accelerating the near-field measurements are investigated. First, the possibility of reducing the measuring time by means of improved measuring systems will be discussed. Besides faster measuring axes, this also includes the use of several measuring channels. Another possibility is the reduction of measurement points. A simple approach is the truncation of the measurement surface which aims to determine only certain, selected areas of the far field correctly. Due to the lack of information however, approximation errors always occur, which, however, only marginally reduce the measurement accuracy in many measurement scenarios.

The main contribution of this thesis to the state-of-the-art is the investigation of non or minimally redundant sampling grids and the development of the associated transformation methods including probe correction. It is shown that the number of measurement points can always be minimized by a suitable selection of the transformation origin. Furthermore, it is comprehensively analyzed which scanning grids enable time-efficient and accurate measurements. For this purpose, two typical mea-

surement systems (roll-over-azimuth and robotic arm system) are considered. It is shown that the respective measuring system has a significant influence on the measurement duration depending on the different sampling grids. Furthermore, it is emphasized that the acceleration depends on the operating mode of the measuring system. In step mode (axes are stopped at each measuring point), the reduction of the measurement duration is almost equal to the reduction of the measurement points. Thus, the measurement time can be almost halved compared to equidistant sampling by using non-redundant sampling grids. However, if the measurement system operates in continuous mode (continuous axis motion), the measuring time depends mainly on the path length through all measurement points. Since these must always be distributed over the entire sphere, the path length and, thus, the measurement duration is not reduced as much as the number of measurement points. Nevertheless, measurements can be accelerated by using non-redundant sampling grids. Realistic values are between 5% and 20%.

The determined uncertainties show that non-redundant sampling grids do not significantly reduce the measurement accuracy. Of course, additional redundancy can be added to filter errors depending on the accuracy requirements. A further reduction of the measurement points leads to a underdetermined system of equations whose solution is generally not unique. However, using Compressed Sensing methods, it is still possible to correctly determine the spherical mode spectrum under certain circumstances. However, using Compressed Sensing methods, it is still possible to correctly determine the mode spectrum under certain circumstances. These methods are not covered by this thesis. In summary, different acceleration methods can be used and combined. Improved hardware generally requires a modification of the measurement system and is primarily relevant for the design of new measurement chamber. Truncation can considerably reduce the measurement time in certain cases, but has the disadvantage that the antenna properties can only be approximated and not completely determined. In comparison, non-redundant sampling grids reduce the measurement time without significantly reducing the measurement accuracy. This is particularly interesting for existing measuring systems, since no changes to the existing hardware are necessary. Furthermore, additional acceleration through the use of multiple measurement channels or truncation is possible without restriction. In general, the spherical mode spectrum can be determined with the developed methods from measured data on any closed measurement surface. The methods presented can therefore also be used to develop novel measuring systems that are adapted to the corresponding measuring task, since a spherical measuring geometry is generally not required.

Contents

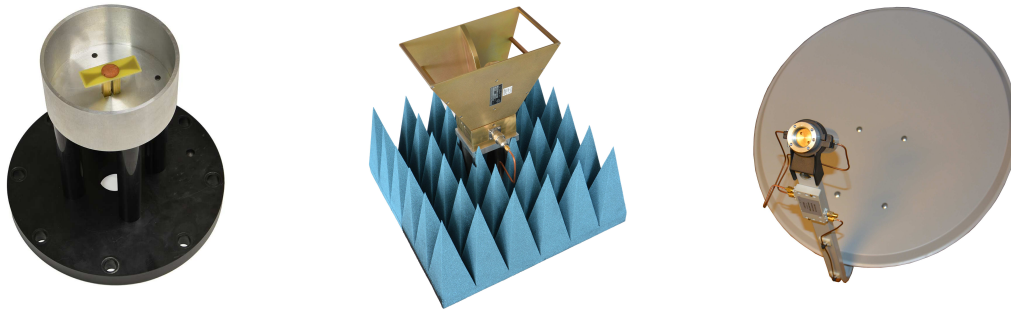
1	Introduction	1
2	Spherical wave expansion	5
2.1	Theory	5
2.1.1	Antenna scattering matrix	6
2.1.2	Spherical transmission formula	9
2.2	Transformation algorithms	13
2.2.1	Algorithms based on solving a linear equation system	14
2.2.1.1	Direct methods	14
2.2.1.2	Iterative methods	15
2.2.2	Wacker algorithm	16
2.2.3	Probe correction	17
2.2.4	Transformation times	19
2.3	Summary	19
3	Probe array system	23
	Pointwise probe correction	24
4	Truncation	29
4.1	Direct extrapolation	32
4.2	Alternating orthogonal projections	35
4.3	Other techniques	40
4.3.1	Slepian functions	41
4.3.2	Equivalent current representation	42
4.4	Summary	42
5	Non or minimal redundant sampling	45
5.1	Point distribution	45
5.1.1	Equiangular	46
5.1.2	Thinned equiangular	47
5.1.3	Spirals	47
5.1.4	Maximum determinant	53
5.1.5	Others	54
5.1.6	Comparison	55
5.2	Measurements	66
5.3	Summary	72
6	Translation and rotation of the transformation origin	75
6.1	Spherical transmission formula for an arbitrary transformation origin	76
6.2	Sampling point projection	79
6.3	Measurements	81
6.4	Summary	94

7	Measurement uncertainties	95
7.1	Uncertainty budget calculation	97
7.1.1	Term 1 & 4: Probe related uncertainties	97
7.1.2	Term 7: Antenna under test (AUT) alignment error	100
7.1.3	Term 8: Data point spacing	101
7.1.4	Term 10: Position error	102
7.1.5	Term 12: Multiple reflections	107
7.1.6	Term 13: Receiver amplitude nonlinearity	111
7.1.7	Term 14: System amplitude and phase errors	112
7.1.8	Term 15: Receiver dynamic range	114
7.1.9	Term 16: Room scattering	114
7.1.10	Term 17: Leakage and crosstalk	126
7.1.11	Term 18: Miscellaneous random errors	126
7.2	NF pattern averaging	126
7.3	Summary	129
8	Sub-Nyquist sampling	131
9	Conclusion	137
A	IHF measurement chamber	141
A.1	SNF range	141
A.2	SH800 near-field probe	142
B	BTS measurements	143
B.1	BTS specifications	143
B.2	BTS measurement uncertainties	143
C	QH2000 measurements	147
C.1	QH2000 specifications	147
C.2	QH2000 measurement uncertainties	147
D	Test zone simulation	163
E	List of abbreviations	165
	Bibliography	167
	List of publications	181
	Curriculum vitae	183

Introduction

Mobile data communication has a similar impact on the world as other disruptive technologies such as the steam engine, the electrification, the railroad or the internet. The new technology has an increasing influence on the economy and the daily life. The global mobile data traffic raises around 50% per year [1,2] and new applications such as the Internet Of Things (IOT), smart cities and car2X communication will increase the demand in the future. It is expected that 20% of the IP based traffic will be caused by mobile communication systems in 2021 [2]. Providing the required capacities is already challenging today and causes limited user data rates in metropolitan areas during peak hours [1]. Currently, a lot of research is conducted in the area of the fifth generation (5G) cellular networks and address the upcoming challenges of modern wireless communication [3, 4]. In conclusion, more and more data will be transferred wirelessly and smart antennas covering multiple frequency bands (including mmWaves) with Multiple Input Multiple Output (MIMO) and beam-forming capabilities will be required in order to provide a high quality of service. Furthermore, small cells will increase the total number of base station antennas which in addition should be embedded in the surrounding in order to conceal the antenna [5]. Overall, the demand for testing antennas and the complexity (e.g. number of frequencies and antenna configurations) of the measurements will increase. Simulations might reduce the amount of testing but finally only measurements can provide confidence. Depending on the application, antenna failures might create high reparation costs [6]. For this reason, antenna measurements are a significant part of an antenna's development and production. Fast antenna measurements would allow to measure more antennas in the same time and, thus, decrease the costs. Alternatively, more antenna configurations (e.g. antenna ports, frequencies) could be measured within the same total measurement time.

The appropriate antenna measurement range configuration depends mainly on the application [7]. The history of microwave antenna measurements started with far-field ranges [8,9]. Near-field techniques (including compact ranges) started to become popular in the 1980s and detailed discussions can be found for example in [10–13]. In general, near-field measurements are performed in the radiated near-field region of the antenna under test (AUT) on a plane, cylinder or sphere. For these three geometries, the Helmholtz differential equation can be solved by separation of variables and the measurement setup can be easily realized by rotation and linear translation stages. Usually, the acquired near-field data is analytically transformed to a modal expansion in the corresponding coordinate system from which the far-field radiation properties of the AUT are derived. Due to the required transformation, near-field techniques are also called *indirect* antenna measurements. Over the last decades near-field antenna measurements have become a well-established measuring



(a) Dipole antenna (size $< \lambda$ @ 2 GHz). (b) Double ridge horn antenna (size $\approx 6\lambda$ @ 6 GHz). (c) Dish antenna (size $\approx 20\lambda$ @ 10 GHz).

Figure 1.1: Test antenna examples with maximum physical dimension stated in λ .

technique and have led to a IEEE standard (more precisely a recommended practice) on near-field antenna measurements in 2012 [10]. Among the near-field techniques, spherical near-field antenna measurements provide certain advantages and might be seen as the most accurate antenna measurement technique [14, 15]. Most important, the technique acquires the near field on a closed surface around the AUT, meaning that the complete radiation of the AUT is measured and the far-field radiation pattern in every direction can be determined. For this reason, the technique is generally applicable for all types of antennas (some examples are shown in Fig. 1.1). Furthermore, spherical near-field systems are cost efficient [16–19] which makes them an optimal choice for many measurement applications. However, near-field measurements are in general time consuming because the electromagnetic field has to be measured on the complete surface in the near field before it can be transformed to the far field. Therefore, acceleration of the measurement is highly desirable in order to increase the practicability of this accurate measurement method.

An obvious way to accelerate the measurement is to use improved measurement equipment such as faster scan axes or to use multiple measurement channels. Probe array measurement systems [20], as a special case, are commercially available and frequently used. Though the acquisition times are reduced, improved measurement equipment does not increase the efficiency of the measurement because the number of measurements is unchanged. Typically, the measurement is oversampled because equiangular sampling point distributions are used and, hence, the efficiency can be increased by reducing the number of samples which has already been studied in [21]. A straightforward approach is to reduce the scan area (*truncation*) and, consequently, to measure the spherical surface partially, but this leads to approximation errors in the estimated far-field radiation pattern [21]. Therefore, many approaches to reduce the approximation error have been introduced in the literature and are discussed in Chapter 4. Another possibility is to use non redundant sampling point distributions which has been theoretically addressed by Bucci et. al. in [22]. Based on these results, a spiral scanning scheme has been developed [23] which, however, requires oversampling in order to control the band-limitation error [23]. Though the number of points compared to equiangular sampling is reduced, the practical spiral scanning scheme is also redundant in relation to the number of unknown AUT

coefficients. Furthermore, explicit acquisition time reductions are not stated and, furthermore, [24] showed that the realization of fast spiral scans is difficult. Another aspect that has to be considered in measurement practice, is the location of the AUT. In cases where the AUT is not centered in the measurement coordinate system, large phase variations occur. For this reason, more samples are generally needed. However, a procedure which takes the AUT offset into account and, by this, reduces the number of required samples has been presented in [25]. However, the procedure neglects the effect of the measurement probe which is not always justified. Overall, a variety of approaches exists but a comprehensive comparison has not been performed and explicit measurement time reductions are rarely stated. In addition, the effect on the measurement accuracy, which is an important aspect of every measurement, has up until now not been investigated. The aim of this thesis is to close these gaps.

At first, a detailed investigation of measurement limitations due to the spherical wave expansion theory and the used transformation algorithms is performed in Chapter 2. It will be pointed out that the spherical wave expansion theory is very general and that many requirements which limit the acquisition speed are related to the used transformation algorithm and not the theory itself. The acceleration of the measurement by using multiple probe antennas is discussed in Chapter 3 with special emphasis on probe correction. Though using multiple measurement channels reduces the acquisition time, the efficiency of the sampling point distribution is unchanged because the number of samples is the same but measured in parallel. The reduction by truncation is discussed in Chapter 4 where the introduced approximation error and several error mitigation methods are evaluated. The main contribution of this thesis to the state of the art is described in Chapter 5 and Chapter 6 where the degrees of freedom provided by modern transformation algorithms are exploited in order to increase the acquisition speed and reduce the total measurement time. It will be shown that different sampling schemes on the sphere can be used to reduce the number of required measurement samples to a minimum regardless of the AUT position. In addition, it will be pointed out that it is possible to sample the near field on every closed surface around the AUT allowing new sampling geometries. In conclusion, a fast acquisition procedure must jointly optimize the overall length of the measurement path and the speed along that path. This means a change in the paradigm of spherical near-field scanning that presupposes that it is of utmost importance to measure on a perfect spherical surface. The theoretical investigations are tested in measurement practice and detailed uncertainty evaluations are presented in Chapter 7. Chapter 8 introduces the topic of sub-Nyquist sampling for spherical near-field antenna measurements which is currently a very active research field and has the potential to further reduce the number of required measurement samples under certain conditions. A more general outlook and the conclusions are given in the final Chapter 9 where the plethora of possibilities provided by the view on spherical near-field antenna measurements introduced in this thesis will be outlined. Citations of the author's publications are printed in bold (e.g. [12]). A complete list containing all publications can be found at the end of this thesis.

Spherical wave expansion

Spherical wave expansion is a standard technique for spherical near-field antenna measurements [10]. Spherical waves (also called vector spherical harmonics or spherical modes) are solutions of the Maxwell equation in a linear, isotropic and homogeneous medium. They form an orthogonal basis on the sphere and are therefore often used for the representation of antenna radiation patterns. The aim of this chapter is to introduce the concepts and methods of the spherical wave expansion for near-field antenna measurements necessary for the understanding of this thesis. This chapter explains the spherical wave expansion theory for near-field antenna measurements based on the antenna scattering matrix theory. Furthermore, different algorithms to derive the spherical mode spectrum of an AUT from near-field measurements will be reviewed. Since an antenna measurement includes at least two antennas, the unknown AUT and the known probe antenna (sensor), the discussion in this chapter is restricted to methods which include the probe effect. The knowledge about the theory and the algorithms is important for the understanding of the succeeding chapters on fast acquisition because some measurement restrictions are imposed by the theory and others by the used transformation algorithm. It will be pointed out that most restrictions and limitations are actually due to the used transformation algorithm in order to make the transformation procedure efficient and fast. However, modern computer and transformation algorithms allow general spherical wave expansion techniques so that the restrictions due to the implementation can be overcome.

2.1 Theory

Spherical waves were introduced in 1935 by W. W. Hansen [26] as a theoretical solution of the vector wave equation. Montgomery and Dicke [27] proposed in 1948 a scattering matrix approach for antennas similar to classical circuit theory. This is a very useful formalism and is still used today to describe scattering, radiation and coupling properties of antennas. However, the first derivation of the probe-corrected spherical transmission formula by Jensen [28] uses the Lorentz reciprocity instead of scattering matrices. Wacker [29,30] was the first who used the scattering matrix approach to describe the transmission formula which was further developed by Larsen in his dissertation [31]. A comprehensive exposition of the subject can be found in the authoritative book from J. E. Hansen [21]. A review including recent advantages was published by Breinbjerg in 2016 [15]. In this section, the basic theory required for the understanding of this thesis is reviewed. Some aspects will only be mentioned briefly and discussed later in more detail. In contrast to most literature, a different way to derive the transmission formula will be used in this section in

order to emphasize the generality of the equation. This is an important property used throughout this thesis to derive fast measurement schemes.

2.1.1 Antenna scattering matrix

Every antenna can be regarded as a transducer between a guided wave (e.g. in a coaxial cable) and free space. Similar to circuit theory it is possible to derive an antenna scattering matrix

$$\underline{\mathbf{S}} = \begin{bmatrix} \underline{\mathbf{\Gamma}} & \underline{\mathbf{R}} \\ \underline{\mathbf{T}} & \underline{\hat{\mathbf{S}}} \end{bmatrix} \in \mathbb{C}^{\infty \times \infty} \quad (2.1)$$

where $\underline{\mathbf{\Gamma}}$ represents the complex reflection coefficients at the local port(s) of the antenna, $\underline{\mathbf{R}}$ and $\underline{\mathbf{T}}$ are the complex receive and transmit coefficients and $\underline{\hat{\mathbf{S}}}$ represents the reflection at the radiation port(s). In general, the matrix is of infinite size, but, as will be discussed later, the size can be truncated according to the band-limitation of practical antennas. In the following, only one local port will be assumed so that $\underline{\mathbf{\Gamma}} = \underline{s}_{11}$. However, the derivations can be applied to antennas with multiple local ports in a similar way. The radiation port is connected to a so called modal transmission line. Typically, the modes represent solutions of the Maxwell equation. Most common are plane, cylindrical or spherical waves. In this thesis, a spherical wave representation of the antennas transmit and receive characteristics will be used. The relationship between incoming and outgoing waves can be represented by

$$\begin{bmatrix} \underline{w} \\ \underline{\mathbf{b}} \end{bmatrix} = \begin{bmatrix} \underline{s}_{11} & \underline{\mathbf{R}} \\ \underline{\mathbf{T}} & \underline{\hat{\mathbf{S}}} \end{bmatrix} \begin{bmatrix} \underline{v} \\ \underline{\mathbf{a}} \end{bmatrix} \quad (2.2)$$

where \underline{w} and \underline{v} are the complex amplitudes of the incoming and outgoing signal at the local port. The complex vectors $\underline{\mathbf{a}}$ and $\underline{\mathbf{b}}$ represent the complex amplitudes of the incoming and outgoing spherical waves. The situation is illustrated in Fig. 2.1 and Fig. 2.2. The radius r_0 (also called maximum radial extend (MRE)) describes the size of the smallest sphere, measured from the coordinate origin, which includes the AUT.

The properties of the scattering matrix depend on the definition and normalization of the spherical modes used in (2.2). The notation presented in Hansen [21] is used throughout this thesis and shortly summarized in the following paragraphs. The electromagnetic vector fields of the spherical modes can be derived from the power normalized scalar generating function that fulfills the Maxwell equation ($-i\omega t$ time dependency):

$$F_{mn}^{(c)}(r, \theta, \phi) = \frac{1}{\sqrt{2\pi}} \frac{1}{\sqrt{n(n+1)}} \left(-\frac{m}{|m|} \right)^m \underline{z}_n^{(c)}(kr) \overline{P}_n^{|m|}(\cos \theta) e^{im\phi} \quad (2.3)$$

The evaluation point is specified in spherical coordinates (r, θ, ϕ) . The index pair (m, n) , where $|m| \leq n$, specifies the order and degree of the spherical wave, respectively. The radial function $\underline{z}_n^{(c)}(kr)$ describes the radial dependency of the spherical

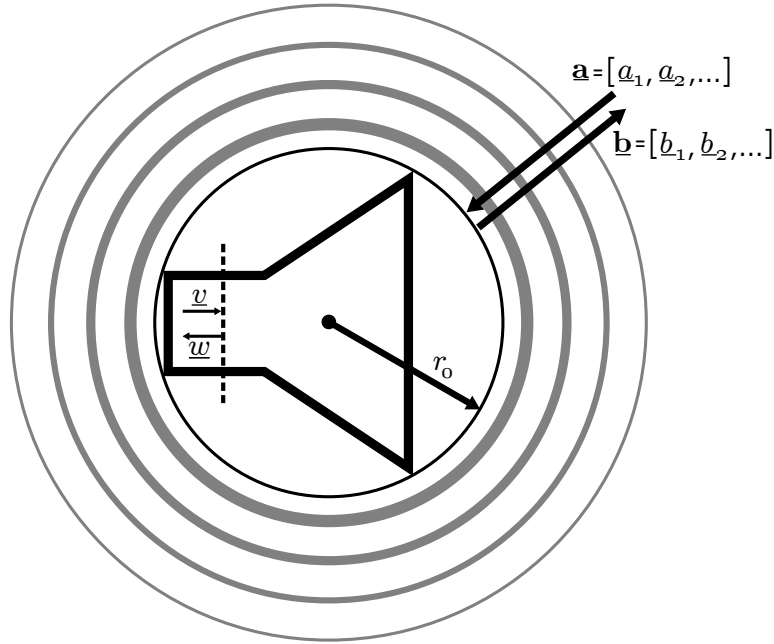


Figure 2.1: Visualization of the antenna scattering matrix.

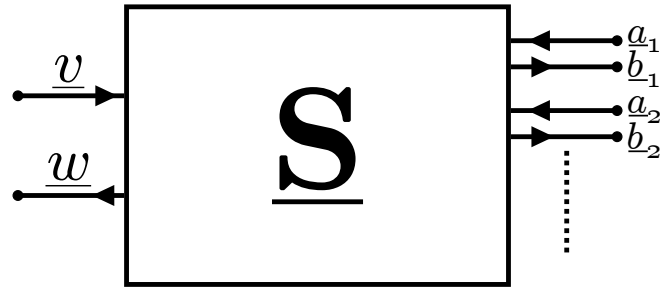


Figure 2.2: Block diagram of the antenna scattering matrix.

wave for a specific wavenumber $k = \frac{2\pi}{\lambda}$, where λ is the wavelength. The upper index (c) specifies one of the four radial functions

$$z_n^{(1)}(kr) = j_n(kr) \quad , \text{ spherical Bessel function} \quad (2.4a)$$

$$z_n^{(2)}(kr) = n_n(kr) \quad , \text{ spherical Neumann function} \quad (2.4b)$$

$$z_n^{(3)}(kr) = \underline{h}_n^{(1)}(kr) = j_n(kr) + in_n(kr) \quad , \text{ spherical Hankel function of the first kind} \quad (2.4c)$$

$$z_n^{(4)}(kr) = \underline{h}_n^{(2)}(kr) = j_n(kr) - in_n(kr) \quad , \text{ spherical Hankel function of the 2nd kind} \quad (2.4d)$$

where $c = 1$ and $c = 2$ are standing waves, while $c = 3$ and $c = 4$ are outward and inward traveling waves, respectively. The term $\bar{P}_n^{|m|}(\cos \theta)$ in (2.3) is the normalized associated Legendre function. From (2.3) by insertion into the Maxwell equations,

the vector spherical wave functions can be derived by

$$\begin{aligned}\vec{E}_{1mn}^{(c)}(r, \theta, \phi) &= \nabla F_{mn}^{(c)}(r, \theta, \phi) \times \vec{r} \\ &= \frac{1}{\sqrt{2\pi}} \frac{1}{\sqrt{n(n+1)}} \left(-\frac{m}{|m|}\right)^m \left\{ \underline{z}_n^{(c)}(kr) \frac{im\bar{P}_n^{|m|}(\cos\theta)}{\sin\theta} e^{im\phi} \vec{e}_\theta \right. \\ &\quad \left. - \underline{z}_n^{(c)}(kr) \frac{im\bar{P}_n^{|m|}(\cos\theta)}{\sin\theta} e^{im\phi} \vec{e}_\phi \right\}\end{aligned}\quad (2.5)$$

and

$$\begin{aligned}\vec{E}_{2mn}^{(c)}(r, \theta, \phi) &= k^{-1} \nabla \times \vec{F}_{1mn}^{(c)}(r, \theta, \phi) \\ &= \frac{1}{\sqrt{2\pi}} \frac{1}{\sqrt{n(n+1)}} \left(-\frac{m}{|m|}\right)^m \left\{ \frac{n(n+1)}{kr} \underline{z}_n^{(c)}(kr) \bar{P}_n^{|m|}(\cos\theta) e^{im\phi} \vec{e}_r \right. \\ &\quad + \frac{1}{kr} \frac{d}{d(kr)} \{kr \underline{z}_n^{(c)}(kr)\} \frac{d\bar{P}_n^{|m|}(\cos\theta)}{d\theta} e^{im\phi} \vec{e}_\theta \\ &\quad \left. + \frac{1}{kr} \frac{d}{d(kr)} \{kr \underline{z}_n^{(c)}(kr)\} \frac{im\bar{P}_n^{|m|}(\cos\theta)}{\sin\theta} e^{im\phi} \vec{e}_\phi \right\}.\end{aligned}\quad (2.6)$$

In order to differentiate between the solutions \vec{F}_{1mn} and \vec{F}_{2mn} the index s is used. The magnetic field of the TM wave is described by modes with index $s = 1$ and the corresponding electric field with $s = 2$. For TE waves this is interchanged. The electric field in a source-free region outside the sphere with radius r_0 can be written as weighted sum

$$\vec{E}(r, \theta, \phi) = k\sqrt{Z} \sum_{csmn} \underline{Q}_{smn}^{(c)} \vec{F}_{smn}^{(c)}(r, \theta, \phi) \quad (2.7)$$

where $Z = \sqrt{\mu/\varepsilon}$ is the wave impedance and $\underline{Q}_{smn}^{(c)}$ are the complex weights also called spherical mode coefficients (SMC).

It is useful to introduce a single index notation with

$$j = 2\{n(n+1) + m - 1\} + s \quad (2.8)$$

so that the triple summation over s , m and n reduces to a single summation over j . The index (c) is not included because the antenna analysis is typically restricted to one type of waves (e.g. outward traveling waves).

Now that the spherical modes are defined it is possible to link the SMC $\underline{Q}_j^{(c)}$ to the antenna scattering matrix. According to (2.2) we can state that $\underline{\mathbf{b}} = \underline{Q}_j^{(3)}$ and $\underline{\mathbf{a}} = \underline{Q}_j^{(4)}$. Due to the chosen normalization, the power of a spherical wave with unity amplitude is 0.5 W. Furthermore, it can be shown [21] that the simple relations

$$\underline{R}_{smn} = (-1)^m \underline{T}_{s,-m,n} \quad (2.9)$$

$$\underline{T}_{smn} = (-1)^m \underline{R}_{s,-m,n} \quad (2.10)$$

hold for reciprocal antennas. Please note that these equations depend on the normalization in 2.3 as pointed out in [32].

So far, the antenna scattering matrix has infinite size. However, the fields generated by antennas or scatterers of finite size can be represented by a truncated series [33]. The effective bandwidth W_0 depends on the wavenumber k and the radius r_0 of the sphere (see Fig. 2.1) and can be calculated by

$$W_0 = kr_0 \quad . \quad (2.11)$$

In [33] it is shown that a sampling based on the bandwidth $w = \chi W_0$, $\chi > 1$ is sufficient for an accurate field representation. The factor $\chi = \chi_1 \chi_2$ is used to control the error due to truncation (χ_1) and aliasing (χ_2) in the spectrum [34]. In spherical near-field antenna measurements the band-limit

$$N = kr_0 + n_1 \quad (2.12)$$

is typically used [10]. According to Hansen [21], $n_1 = 10$ is sufficient for most practical cases. A more comprehensive analysis [35] proposed to use

$$n_1 = 0.0045 \sqrt[3]{kr_0(P_{r_0} - P_{tr})} \quad (2.13)$$

where P_{tr} is the maximum allowed, excluded power fraction (in dB) and P_{r_0} is the relative power (in dB) of the source at $r = r_0$. In the case of small antennas ($r_0 < \lambda$), the required number of modes might be even smaller. Furthermore, it is possible to truncate the azimuthal index m at some $|m| = M = kr_c + n_1$ according to the radius r_c of the smallest cylinder parallel to the z-axis which surrounds the antenna. In conclusion, the size of the antenna scattering matrix can be truncated for a certain value $j \leq J = 2N(N + 2)$. In addition, if $M < N$ the size can be further reduced. The description of an antenna by its scattering matrix has many advantages. The spherical modes form an orthogonal basis and are mathematically exact solutions of the vector wave equation. In addition, they are valid in the complete volume around the antenna which eliminates the problem of spatial truncation observed in planar and cylindrical mode expansion techniques. In addition, the far-field pattern ($r \rightarrow \infty$) can be easily derived by asymptotic formulas of the wave functions. Furthermore, the scattering matrix description allows simple calculation of antenna parameter like directivity, gain and others from the mode spectrum. For a more comprehensive discussion including the corresponding formulas, the interested reader is referred to [21]. Finally, the scattering matrix approach is well-suited to describe the transmission between two antennas as will be shown in the next section.

2.1.2 Spherical transmission formula

In this section the spherical transmission formula will be derived. This formula describes, in the most simple case, the transmission between two antenna systems which are described by their scattering matrix. In contrast to other literature, the derivation is slightly different because it reflects the measurement perspective where the goal is to determine the radiation characteristics of the unknown AUT by the means of measurements. By this the generality of the formula is emphasized.

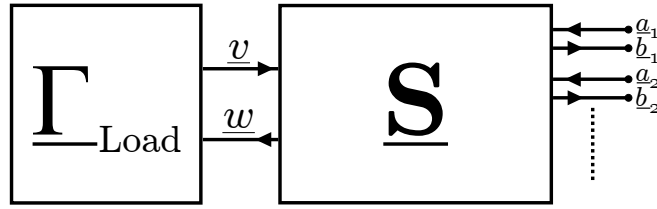


Figure 2.3: Load attached to an antenna.

According to the previous section, the signal \underline{w} received by a load attached to an antenna (see Fig. 2.3) can be represented by

$$\underline{w} = \frac{1}{1 - \underline{\Gamma}_{\text{Load}}\underline{\Gamma}} \mathbf{R} \mathbf{a} \quad (2.14)$$

where $\underline{\Gamma}_{\text{Load}}$ and $\underline{\Gamma}$ are the reflection coefficients of the load and AUT, respectively. The general goal of an antenna measurement is to determine the unknown receiving coefficients \mathbf{R} which represent the three dimensional radiation pattern of the AUT. The reflection coefficients $\underline{\Gamma}_{\text{Load}}$ and $\underline{\Gamma}$ affect the total received power and are thus only important for gain or efficiency measurements. They can be easily measured with a vector network analyzer directly connected to the antenna local port. For an accurate reflection coefficient measurement, it is of course necessary to eliminate any incoming spherical wave at the radiation ports because they would superimpose with the reflected signal at the local port. Therefore, this measurement should be performed in a shielded, anechoic measurement chamber. The measurement of the radiation ports is more complex because many measurements are required. For a determined linear equation system,

$$L = J = 2N(M + 2) \leq 2N(N + 2) \propto (kr_0)^2 \quad (2.15)$$

linear independent measurement samples

$$\underline{w}^{(l)} = \frac{1}{1 - \underline{\Gamma}_{\text{Load}}\underline{\Gamma}} \mathbf{R} \mathbf{a}^{(l)} \quad (2.16)$$

with $l = [1, 2, \dots, L]$ need to be acquired. Typically, oversampling is applied in order to reduce the effect of measurement noise and other error sources. Beside the acquisition of L samples, it is also necessary to know the incoming spherical modes $\mathbf{a}^{(l)}$. A straightforward approach would be to generate an incoming mode spectrum $\mathbf{a}^{(l)}$ which contains only a single mode

$$\underline{a}_{jp} = \begin{cases} \underline{a}_j, & \text{if } j = p, \\ 0, & \text{if } j \neq p, \end{cases} \quad (2.17)$$

and to vary over all possible AUT modes. This would allow to determine the coefficients \underline{R}_j directly from a single measurement. Unfortunately, this measurement approach requires a measurement setup with the possibility to generate only a single spherical mode. This is extremely difficult because it requires a controllable spherical source distribution surrounding the AUT. It might be approximated by a spherical

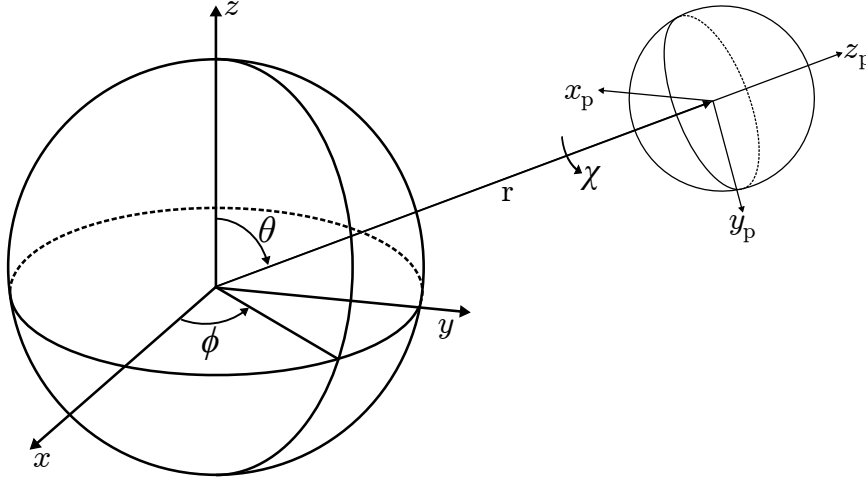


Figure 2.4: AUT coordinate system (x, y, z) and probe coordinate system (x_p, y_p, z_p) .

probe antenna array but many practical problems like probe mutual coupling, reflections and feeding network arise. Due to this reason, this approach is not used in antenna measurement practice. Instead of requiring a single mode, it is possible to generate linear independent measurements by changing the relative orientation of AUT and probe. Fig. 2.4 shows the typical measurement coordinate systems of AUT and probe. The relative orientation of two coordinate systems can be expressed by the Euler angles (α, β, γ) . For antenna measurements, it is more convenient to describe the rotation in spherical coordinates (θ, ϕ, χ) . Please note that the minimum spheres of AUT and probe are not allowed to intersect. The rotation of a spherical wave spectrum is well defined [21] (Appendix A2) and thus (2.16), using summations instead of matrix multiplications, can be rewritten as

$$\underline{w}^{(l)}(\theta, \phi, \chi) = \frac{1}{1 - \underline{\Gamma}_{\text{Load}}\underline{\Gamma}} \sum_{\substack{smn \\ \mu}} \underline{R}_{smn} (e^{-im\phi} a_{m\mu}^n(-\theta) e^{-i\mu\chi}) \underline{a}_{s\mu n}^{(l)}. \quad (2.18)$$

The index $\sigma\mu\nu$ instead of smn are used if it is necessary to distinguish between the probe and AUT coefficients. The rotations are defined as rotations of the AUT coordinate system in order to use the same convention as Hansen [21]. The probe system is fixed in space and, for this reason, negative rotations signs are needed in the equation. Thus, by changing the relative orientation of AUT and probe, it is not necessary to modify $\underline{\mathbf{a}}^{(l)}$ in order to generate linear independent measurements. However, it is still necessary to know $\underline{\mathbf{a}}^{(l)}$. The incoming mode spectrum can be derived if the source (probe) and the propagation path are known. For example, an x-polarized plane wave in the direction of the positive z-axis can be expressed analytically by [21] (Appendix A1.6)

$$\underline{a}_{s\mu n} = \begin{cases} \frac{\sqrt{\eta}}{k} \underline{E}_0 \sqrt{4\pi} i^{n+1} \frac{1}{2} \sqrt{2n+1}, & \text{for } a_{11n}, a_{1,-1,n} \text{ and } a_{21n}, \\ -\frac{\sqrt{\eta}}{k} \underline{E}_0 \sqrt{4\pi} i^{n+1} \frac{1}{2} \sqrt{2n+1}, & \text{for } a_{2,-1,n}, \\ 0, & \text{otherwise} \end{cases} \quad (2.19)$$

and contains only modes with index $\mu = \pm 1$. Here, $\eta = \sqrt{\varepsilon/\mu}$ is the wave admittance and \underline{E}_0 the amplitude of the plane wave. Interestingly, the amplitude of the spherical wave $\underline{a}_{s\mu n}$ raises with $\sqrt{2n+1}$ and the spectrum is not band-limited. The plane wave can be interpreted as dirac impulse in the far field ($r = \infty$) which creates an infinitely broad mode spectrum. In a far-field antenna measurement range the plane wave condition is the ideal measurement condition. In this case, the measured signal \underline{w} is proportional to the far-field pattern of the AUT and no near-field to far-field transformation is required. In typical near-field antenna measurement ranges, the source is not located at $r = \infty$ so that the radiation of the source cannot be regarded as plane wave inside the test volume of the AUT. For a finite distance r , the incoming mode spectrum must be calculated from the known probe spherical mode spectrum $\underline{T}_{\sigma\mu\nu}$ by [21] (Appendix A3.1)

$$\underline{a}_{s\mu n} = \frac{\underline{v}}{2} \sum_{\sigma\nu} \underline{C}_{s\mu n}^{\sigma\nu(3)}(-kr) \underline{T}_{\sigma\mu\nu} \quad . \quad (2.20)$$

The translation coefficients $\underline{C}_{s\mu n}^{\sigma\nu(3)}(-kr)$ describe a translation of $-r$ along the positive z-axis; from probe to AUT. Equation (2.20) connects the outward traveling waves of the probe $\underline{\mathbf{b}} = \underline{v} \underline{\mathbf{T}}$ at a certain distance r with the incoming waves $\underline{\mathbf{a}}$ at the AUT. By $\underline{\mathbf{b}} = \underline{v} \underline{\mathbf{T}}$ it is implicitly assumed that no multiple reflection between AUT and probe exist. This is a valid assumption for most measurement scenarios where the AUT and probe are separated by some λ . However, it is possible to include multiple reflections as well by the scattering matrix approach [21]. Furthermore, it is assumed that no sources except for the probe exist and that the propagation path is perfectly free space, hence no room scattering exist. These assumptions are usually valid if the measurements are performed in a shielded, anechoic measurement chamber. Nevertheless, they will only be approximately met in real measurement scenarios due to, for example, limited absorber performance or scattering from mounting structures. Therefore, they contribute to the measurement uncertainties. Equation (2.20) is an analytical description of the test zone field around the AUT if the source radiation characteristics is known from simulation or measurement. Instead of an analytical derivation it is also possible to measure the test zone field explicitly [36]. The incoming waves $\underline{\mathbf{a}}$ including all room reflections can be calculated from the test zone measurement. This approach is very powerful because it does not require assumptions about the propagation path, the probe radiation pattern or the alignment. Though, accurate test zone field measurements are difficult to perform. First approaches used an arm mounted on the roll-over-azimuth positioner [36–38] with an outward looking probe. This is very convenient because no extra axis is needed, but it ignores the fact that the scattering from the positioner itself is not static during the test zone measurement. In general, for every axis position a different test zone field measurement is required. Furthermore, the measurements (amplitude and phase) have to be performed for every frequency and might not be time invariant (e.g. after changing the setup). Up until now, the method was mainly used for general room qualification and hence moderate accuracy was sufficient. No comprehensive uncertainty analysis has been performed but it can be expected that the requirements for high precision near-field antenna measurements will be challenging. Results for a non-anechoic environment have shown improvements but are still not

comparable to state-of-the art near-field measurements [15,39–41]. Also the long additional measurement time for the test zone field measurements is a severe drawback of the method. Beside practical challenges, another important aspect is the higher complexity of the transformation with a measured test zone field which was a limiting factor in the development of the method [42]. Nowadays, commercially available computing speed and accessible memory have increased dramatically enabling the possibility to solve complex electromagnetic problems in an acceptable time so that this method has become applicable. Mainly for practical and accuracy reasons, the analytical derivation (2.20) of the test zone field is still used in practice. If an adequate accuracy of test zone field measurements can be reached, it might be an option for high precision measurements or measurements in non-anechoic environments. Using the analytical derivation, assuming a perfect matched load ($\Gamma_{\text{Load}} = 0$) and combining (2.20) and (2.18) results in the Jensen-Wacker transmission formula for a receiving AUT [21] (page 68)

$$\underline{w}^{(l)}(r, \theta, \phi, \chi) = \frac{v}{2} \sum_{\substack{smn \\ \sigma\mu\nu}} \underline{R}_{smn} e^{-im\phi} d_{m\mu}^n(-\theta) e^{-i\mu\chi} \underline{C}_{s\mu\nu}^{\sigma\nu}(-kr) \underline{T}_{\sigma\mu\nu}^{(l)} \quad . \quad (2.21)$$

Without loss of generality it has been assumed that the AUT was receiving. The formula for a reciprocal AUT and probe in transmit/receive mode is

$$\underline{w}^{(l)}(r, \theta, \phi, \chi) = \frac{v}{2} \sum_{\substack{smn \\ \sigma\mu\nu}} \underline{T}_{smn} e^{im\phi} d_{\mu m}^n(\theta) e^{i\mu\chi} \underline{C}_{\sigma\mu\nu}^{sn}(kr) \underline{R}_{\sigma\mu\nu}^{(l)} \quad . \quad (2.22)$$

The spherical transmission formulas (2.21) and (2.22) describe the transmission between two antennas, represented by spherical mode spectra, in free space depending on their relative position and orientation (r, θ, ϕ, χ) . Although this final formula is very significant, it is important to understand that it is based on the general calculation of the complex amplitude at the radiation ports of the transmission matrix for every measurement point. The general perspective is useful for an intuitive understanding of the spherical wave expansion procedures for multiprobe systems and irregular sampling on arbitrary surfaces.

2.2 Transformation algorithms

In the previous section, the general spherical wave transmission formula was derived. It was pointed out that a certain number of measurement samples is needed to determine the unknown AUT spherical mode coefficients. In this section, different algorithms which provide probe correction are investigated. The discussion in this section will start with the most intuitive approach — solving a linear equation system based on (2.22). Although this approach is straightforward, it is computational demanding, especially at the time of the development of the spherical near-field antenna measurement technique. Historically, it was therefore of utmost importance to find a fast and efficient transformation algorithm in order to bring spherical near-field scanning into practice. A extremely important step was achieved by Wacker [29, 30] who fully exploited the orthogonality properties of the transmission formula by Fourier transformations. With this technique it was possible to solve

the spherical near-field transmission formula including probe correction introduced by Jensen [28]. This Wacker algorithm has been the standard for many years and most transformation software still use this approach. However, the Wacker algorithm imposes some restrictions on the measurement data as will be discussed later in this section. Commercially available computing speed and accessible memory have increased dramatically over the last years and, thus, alternative transformation algorithms have become reasonably fast. Computational efficiency of the transformation algorithm gets less important and the research focus shifts towards algorithms which provide more flexibility in the measurement design as for example higher-order probe correction and irregular sampling.

2.2.1 Algorithms based on solving a linear equation system

2.2.1.1 Direct methods

The most general approach to determine the AUT spherical mode coefficients is to set up a linear equation system based on the transmission formula (2.22) or even more general on (2.16). This procedure offers maximum flexibility in the measurement design, e.g. measurement point distribution and geometry. Rewriting the problem in vector matrix notation yields

$$\underline{\mathbf{w}} = \underline{\Phi} \underline{\mathbf{q}} \quad (2.23)$$

where the vector $\underline{\mathbf{w}} \in \mathbb{C}^L$ contains $L \geq J$ measurements and $\underline{\mathbf{q}} \in \mathbb{C}^J$ is the vector of the spherical mode coefficients \underline{T}_{smn} or \underline{R}_{smn} . The row entries $\underline{\Phi}_{smn}$ of the measurement matrix $\underline{\Phi} \in \mathbb{C}^{L \times J}$ for the l -th measurement point represent the incoming \underline{a}_{smn} or outgoing \underline{b}_{smn} spherical waves at the radiation ports of the AUT. A deterministic equation system $L = J$ might be theoretically solved by inverting the measurement matrix $\underline{\Phi}$. The mode coefficients $\underline{\mathbf{q}}$ can consequently be determined by

$$\underline{\mathbf{q}} = (\underline{\Phi})^{-1} \underline{\mathbf{w}} \quad . \quad (2.24)$$

However, (2.24) might suffer from numerical instabilities if the measurement matrix $\underline{\Phi}$ is ill-conditioned. Up until now, no deterministic design method for the case of spherical near-field measurements is known (although distributions can be found by numerical optimization, see Chapter 5) and, thus, oversampling is used to guarantee a good condition of the matrix. In these cases, the solution of the equation system is not unique. The Moore–Penrose pseudoinverse provides a solution in the least squares sense (radiated power) and is defined as

$$\underline{\Phi}^+ = \underline{\Phi}^H (\underline{\Phi} \underline{\Phi}^H)^{-1} \quad (2.25)$$

where $\underline{\Phi}^H = (\underline{\Phi}^*)^T$ is the Hermitian transpose (also called conjugate transpose) of $\underline{\Phi}$. The vector $\underline{\mathbf{q}}$ in a least squares sense can be calculated by

$$\underline{\mathbf{q}} = \underline{\Phi}^+ \underline{\mathbf{w}} = \underline{\Phi}^H (\underline{\Phi} \underline{\Phi}^H)^{-1} \underline{\mathbf{w}} \quad . \quad (2.26)$$

In practice, explicit matrix inversions as used in (2.24) and (2.26) are avoided for numerical reasons. Instead, other, more stable and efficient methods such as the

QR decomposition might be used to solve the problem in a least squares sense. The direct method allows the most general definition of the measurement matrix and has been already proposed in the first publications about spherical near-field antenna measurements [31, 43]. However, the computational complexity is of order $\mathcal{O}(J^3) = \mathcal{O}((kr_0)^6)$ and, for this reason, it is rarely used.

In order to increase the transformation speed and to handle electrical large problems, it is necessary to use different methods. Already during the development of the theory, it was found that the terms $e^{im\phi}$ and $e^{i\mu x}$ in the transmission formula (2.22) can be interpreted directly as Fourier series. Jensen and Holm provide good overviews in their publications [31, 43]. Instead of solving one big matrix, the problem is reformulated to solve multiple smaller matrices so that the numerical complexity is reduced to $\mathcal{O}((kr_0)^4)$ and is known as FFT / matrix method. This idea was used many years later by Laitinen [44] in order to include full probe correction in the transformation without increasing the number of measurements.

2.2.1.2 Iterative methods

In the previous section, direct methods were investigated that have numerical complexities of $\mathcal{O}((kr_0)^4)$ to $\mathcal{O}((kr_0)^6)$. The computational costs are mainly determined by the size of the largest equation system that has to be solved because the complexity scales in general with $\mathcal{O}(n^3)$, where n represent the number of unknowns. However, if the matrix is large and sparse, i.e. contains mostly zeros, efficient algorithms with $\mathcal{O}(n)$ exist which exploit these properties [45]. Unfortunately, the measurement matrix $\underline{\Phi}$ itself is not sparse and cannot be used directly. But $\underline{\Phi}$ is usually almost an orthogonal basis because it is a sampled version of the rotation functions which are orthogonal on the sphere. This means that for a good measurement point distribution and a typical probe antenna

$$\underline{\Phi}^H \underline{\Phi} \approx \mathbf{I} \quad (2.27)$$

where \mathbf{I} is the identity matrix. Therefore, instead of solving (2.23) the following problem is solved

$$\underline{\Phi}^H \underline{\mathbf{w}} = \underline{\Phi}^H \underline{\Phi} \underline{\mathbf{q}} \quad . \quad (2.28)$$

Equation (2.28) can be solved with different algorithms like conjugate gradient (CG) or GMRES [45]. These algorithms will always converge and differ mainly in their convergence speed. Typically, only a few iterations compared to the number of equations are required to achieve an accuracy in the range of the random measurement noise. Practically, they provide the same accuracy but require less numerical operations. With these methods, the overall complexity of the transformation is usually not anymore determined by the costs of the matrix inversion but by the numerical cost to setup the measurement matrix $\underline{\Phi}$. Ludwig proposed already in 1972 [46] to use Fourier transforms in $e^{im\phi}$ and $e^{i\mu x}$ and to solve the linear equations systems with an iterative procedure. The algorithm has a complexity of $\mathcal{O}((kr_0)^3)$ which is equal to the complexity of the Wacker algorithm. Although the order of both algorithms is equal, the Wacker algorithm is faster and provides the same flexibility. Probably that is the reason why the Wacker algorithm has become the de-facto standard for the spherical wave expansion. Further reasearch on spherical wave expansion was

motivated by compensating for non-ideal positioning of the probe during the measurement. In 2002 Wittmann [47, 48] proposed an algorithm with $\mathcal{O}((kr_0)^3)$ which is based on an unequally spaced fast Fourier transform [49] in θ , ϕ and interpolation in r . The linear equation system is solved with the conjugate gradient method. Beside unequally spaced near-field measurements, full probe correction without multiple polarization measurements has attracted researchers. Hansen introduced in 2011 [50] an algorithm with $\mathcal{O}((kr_0)^3)$. Similar to Wittmann, he used fast Fourier transforms in conjunction with the conjugate gradient method to keep the complexity low but included full probe correction capabilities. He also proposed a direct method based on Neumann series which requires that (2.27) is approximately fulfilled. As stated above, the numerical costs depend heavily on the initialization of the measurement matrix Φ . In 2008, Schmidt et. al. [51] proposed to replace the full spherical wave translation operator by a plane wave translation operator. By this, the complexity was reduced from $\mathcal{O}((kr_0)^6)$ to $\mathcal{O}((kr_0)^4)$. Furthermore, the complexity could be reduced to $\mathcal{O}((kr_0)^2 \log(kr_0))$ by employing a multilevel expansion procedure [52]. Although these algorithms are very efficient and suitable for large electromagnetic problems, they do not anymore directly provide a spherical wave spectrum.

In conclusion, iterative techniques allow an efficient spherical wave expansion even for large problems. However, attention has to be paid to the implementation of the procedure in order to avoid high complexities during the filling of the measurement matrix. It is important to note, that the filling of the measurement matrix is independent of the measured near-field values and can thus be calculated in parallel to the acquisition or even during the mounting or alignment of the AUT. In addition, the matrix can be stored on hard disk and used for all measurements with the same configuration.

2.2.2 Wacker algorithm

Algorithms based on solving a linear equation system as discussed in the previous section are getting more common in measurement practice because they offer higher flexibility in the measurement setup and the numerical complexity can be handled. During the development of the spherical near-field measurement technique, computers were very expensive and provided only very limited CPU speed and memory. Therefore, it was of practical importance to have efficient transformation algorithms. Although Ludwig presented an iterative procedure in 1972 [46] the more important step was the efficient algorithm presented by Wacker in 1974-1975 [29, 30]. Wacker introduced a procedure which decoupled the transmission formula by Fourier transforms into sets of two equations and two unknowns. Especially important was the calculation of the rotation coefficients $d_{\mu m}^n(\theta)$ by means of Fourier transforms. The work of Wacker was reviewed and clarified by the excellent work of Larsen [31]. Furthermore, some numerical improvements were achieved and implemented in the Spherical Near-Field Transformation program with probe-Correction (SNIFTC) at the Technical University Denmark. A comprehensive description of the method can be found in [21]. The Wacker algorithm has a complexity of $\mathcal{O}((kr_0)^3)$ and is the de-facto standard transformation procedure. Due to the usage of Fourier transformations the algorithm requires equiangular measurement data in ϕ , θ and χ on a sphere with radius r .

2.2.3 Probe correction

Probe correction is an important concept in spherical near-field measurements and describes the compensation of the effect of the probe antenna on the measured values. The most important aspect is the radiation characteristic of the probe which performs a sort of spatial filtering of the electromagnetic field at the measurement position. Since the probe usually points towards the center of the sphere, the angular region of the probe pattern that *sees* the AUT is relatively small and does not change between different measurement positions (see Fig. 2.5). Therefore, probe correction is less important for spherical scanning compared to planar or cylindrical scanning, especially if the AUT-probe distance is large. Nevertheless, for accurate transformation results probe correction is mandatory and can usually not be neglected. A special class of probes is the so called first-order or $\mu \pm 1$ probe. These probes have a spherical mode spectrum $\underline{R}_{\sigma\mu\nu}$ which only contains modes with index $\mu = \pm 1$ [10, 21, 30]. These probes guarantee that only waves, according to (2.20), with index $\mu = \pm 1$ exist. However, the translation coefficients $\underline{C}_{s\mu\nu}^{\sigma\nu(3)}(-kr)$ perform a kind of low-pass filtering in μ and, thus, attenuates higher μ -modes with increasing kr . In the far field ($kr \rightarrow \infty$), every probe can be regarded as first-order probe because the wave in the test zone is a plane wave which fulfill this property (see (2.19)). A spectrum which only contains modes with index $\mu = \pm 1$ also implies that the far-field pattern of the probe can be expressed by

$$\begin{aligned} \vec{E}(\theta, \phi) = & \{ \underline{E}_\theta(\theta, 0)\vec{e}_\theta + \underline{E}_\phi(\theta, 0)\vec{e}_\phi \} \cos(\phi) \\ & + \{ \underline{E}_\theta(\theta, \pi/2)\vec{e}_\theta + \underline{E}_\phi(\theta, \pi/2)\vec{e}_\phi \} \sin(\phi) \end{aligned} \quad (2.29)$$

where $\underline{E}_{\theta,\phi}(\theta, [0, \pi/2])$ represent the \vec{e}_θ , respectively \vec{e}_ϕ , polarized far-field pattern for an angle ϕ of 0 or $\pi/2$. From (2.29) it can be seen that the complete probe far-field pattern is determined by two far-field cuts with co- and cross-polar component. It is not necessary that the probe is perfectly polarized and the cross-polarization can be a function of the angle θ . In addition, the radiation pattern in both cuts can be different. The benefit is, that the probe signal at every measurement point contains only two modes

$$\underline{w}(r, \theta, \phi, \chi) = \underline{w}_1(r, \theta, \phi)e^{i\chi} + \underline{w}_{-1}(r, \theta, \phi)e^{-i\chi} \quad (2.30)$$

and that the relation

$$\underline{w}(r, \theta, \phi, \chi) = -\underline{w}(r, \theta, \phi, \chi + \pi) \quad (2.31)$$

holds. This means that two polarization measurements (e.g. $\chi = 0^\circ$ and $\chi = 90^\circ$) are sufficient to determine the probe signal for all angles χ . In general, $2\mu + 1$ measurements are required for an arbitrary probe. Another important aspect of first-order probes is, that the measurement process can be regarded as an ideal dipole probes measuring an effective field [53]. Therefore, the measured near field can be expanded in spherical modes assuming an ideal dipole and probe correction is applied afterwards. Furthermore, this property allows exact interpolation of near-field data as will be discussed in later chapters. Probes which do not fulfill the $\mu = \pm 1$ requirement are called higher-order probe (HOP). Although perfect first-order probes do not exist in practice, circular horn antennas or open-ended waveguides approximately fulfill this property. However, they cover only a limited frequency range and, thus, different probes and measurements are needed for different frequencies. Broadband

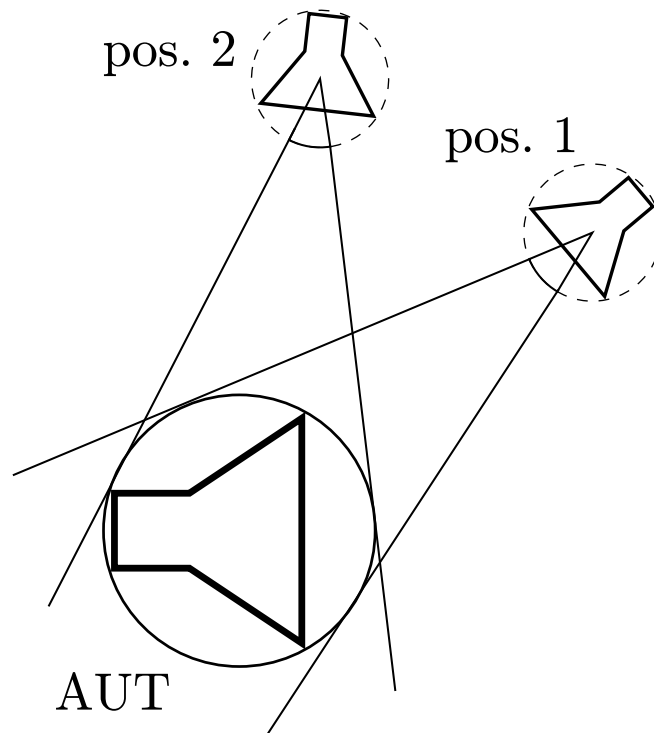


Figure 2.5: Visualization of the geometrical probe pattern angle for two measurement positions.

probes can be used for a wider frequency range but usually have strong higher order modes [54–56] which requires a HOP correction. The error by neglecting higher-order modes in the transformation can be neglected in many measurement scenarios if the measurement distance kr is large [57, 58]. This is a consequence of the mentioned properties of the translation coefficients $C_{s\mu n}^{\sigma\nu(3)}(-kr)$. Thus, the translated probe spectrum might be a better candidate to evaluate the effect of higher-order modes [59, 60]. It is important to note, that the Wacker algorithm can be used for HOP correction but requires more measurements in χ which makes it unattractive in practice. Algorithms presented previously can be used to overcome this drawback and were the main motivation for their development [44, 50]. The applicability is intuitive because the number of unknowns in the equation system, e.g. the spherical modes of the AUT, does not depend on the used probe. In fact, it is not even necessary to measure two polarizations at every measurement point as will be discussed later. However, this is often done because it prevents ill-conditioning of the measurement matrix. In conclusion, first-order probes are a special class of probes which might simplify the transformation and reduce the transformation time. Modern transformation algorithms typically provide full probe correction of arbitrary probes and do not require additional measurement. From a transformation algorithm point of view, arbitrary probe correction is no problem nowadays.

2.2.4 Transformation times

In the previous sections it was pointed out that the asymptotic transformation time depends on the used algorithm. Although the \mathcal{O} -notation is useful for a general comparison of algorithms, it provides only little information about the expected transformation time for a realistic measurement scenario. In this section, the transformation times for different simulated spherical near-field data are compared. The transformation routines are implemented with Matlab 2016 (64-bit) and use the inbuilt functions for the QR decomposition and conjugate gradient method. The equiangular near-field data is generated by a random mode spectrum including a HOP ($\mu = \nu = 30$). At first, the transformation times on a desktop computer (3.1 GHz, 4 cores, 16 GB RAM) for different AUT sizes are compared in Fig. 2.6. As expected, the Wacker algorithm is the fastest. The difference to the FFT / matrix method is mainly caused by the higher complexity of probe response calculation including all modes of the HOP which was not necessary for the Wacker algorithm. The transformation time for solving the equation system by QR decomposition raises quickly with the AUT size. However, reducing the floating-point precision to single precision (32 Bit) or using an iterative technique increase the speed and introduce only negligible errors. It is important to note that the stated times refer to one frequency and antenna port. Consequently, the transformation time of a complete set of antenna measurement data can take longer depending on the number of configurations including different frequencies. The results for a more sophisticated commercially available computer system (2.2 GHz, 24 cores, 256 GB RAM) are displayed in Fig. 2.7. As discussed before, the calculation time consists of mainly two parts: Initializing and solving the linear equation system. Fig. 2.8 shows the partial calculation times for $N = 89$ ($r_0 \approx 12\lambda$) and it can be observed that the total calculation time for the CG method is dominated by the initialization time of the measurement matrix. The initialization time is slightly longer compared to QR decomposition because of the additional matrix multiplication (2.28). The transformation time in contrast has been drastically reduced compared to the QR decomposition. Furthermore, the measurement matrix can be precalculated and saved, e.g. during the near-field acquisition. However, the initialization time depends on the measurement design parameter such as the number of probe modes and the measurement point distribution. For irregular distributed measurement points as used in later chapters, the required times may increase up to several minutes. Nevertheless, optimization of the software routines could reduce the complexity but is not the focus of this thesis. In conclusion, transformation times for AUTs of moderate size ($r_0 \leq 20\lambda$) might nowadays be regarded as acceptably fast.

2.3 Summary

In this chapter, the spherical wave expansion of a radiated electromagnetic field was discussed. It was shown that the concept of an antenna scattering matrix is advantageous because it allows a simple theoretical description of the electromagnetic radiation problem. The spherical transmission formula 2.22 is the key element for describing the coupling of two antennas in the near or far field. The theory of spherical wave expansion is well-defined and has been used for many years in spherical

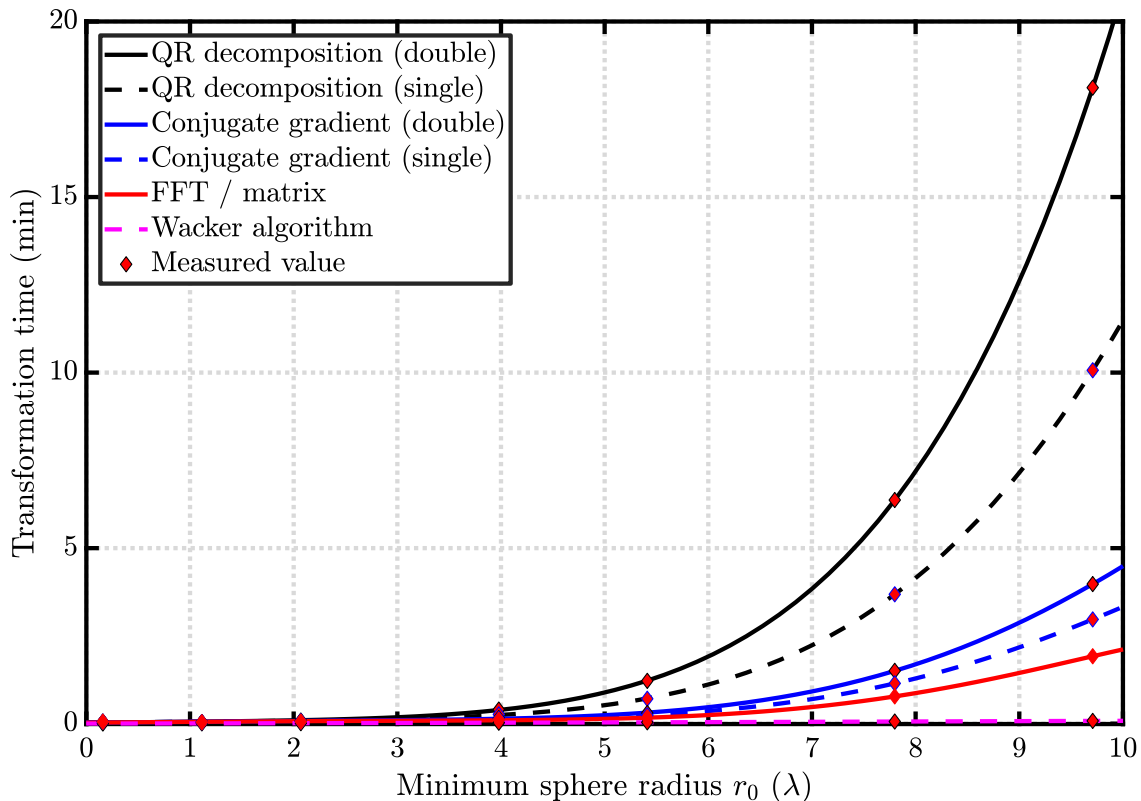


Figure 2.6: Transformation times on a desktop computer.

near-field antenna measurements. Furthermore, a variety of different transformation algorithms exist which provide different features. The commonly used and very efficient Wacker algorithm requires equiangular measurement data in ϕ , θ and χ on a sphere with radius r . More general transformation procedures based on solving a linear equation system provide full probe correction and can be applied to measurement data with irregular sampling grids and arbitrary surfaces. Except for very large antennas ($r_0 > 20\lambda$), computational complexity is less important due to available computing speed and accessible memory. For this reason, it has become possible to accurately represent even complex measurement scenarios like spiral scanning over a perfect conducting ground plane. However, up until now the degrees of freedom provided by the scattering matrix approach have by far not been exploited in practice. In general, it is possible to determine the spherical mode coefficients of the AUT from a certain number of linear independent measurements. The key challenges are to design measurement scenarios that provide linear independent measurement samples while providing other benefits, e.g. simple mechanical scanning geometries, and the incorporation of information about the measurement scenario like chamber reflections or AUT position.

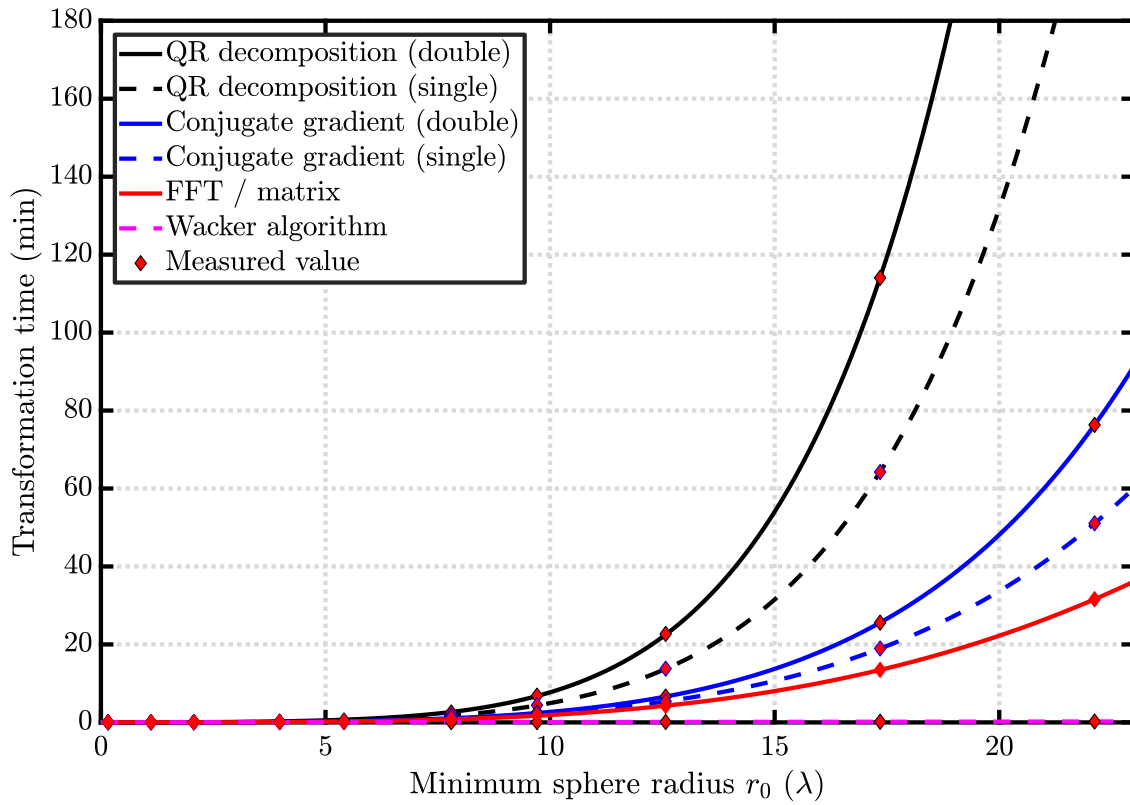
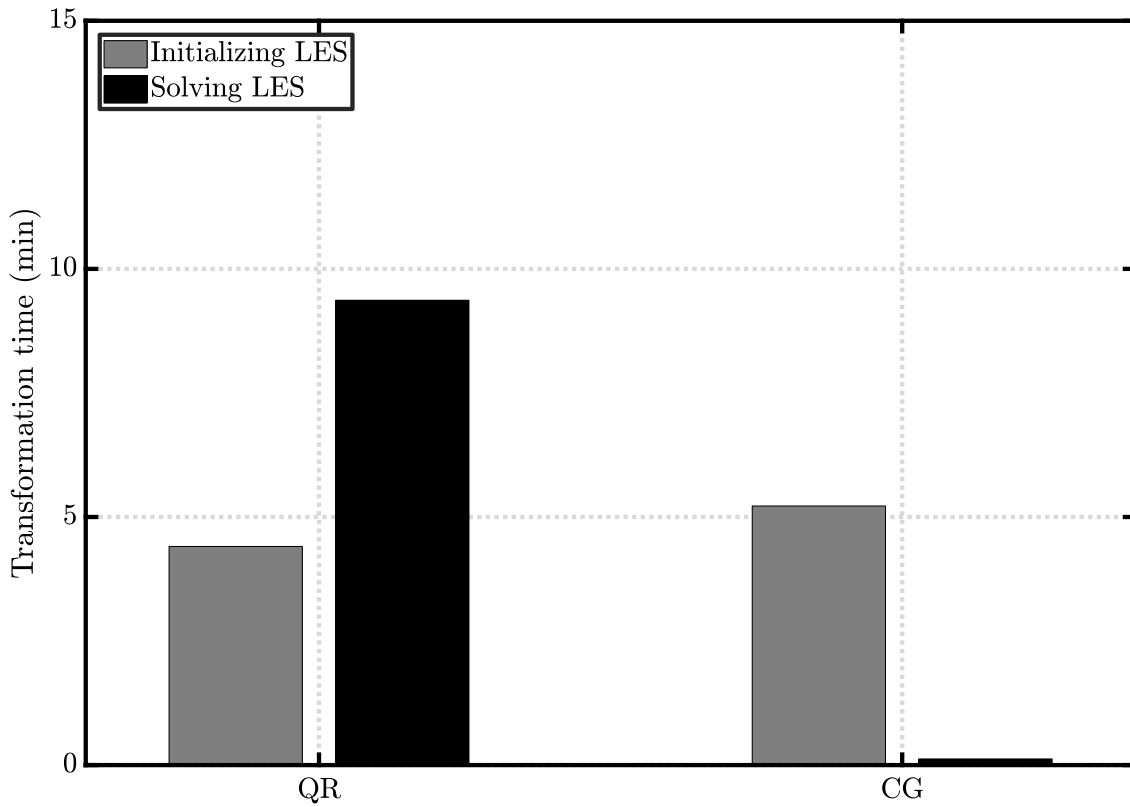


Figure 2.7: Transformation times on a more sophisticated computer.

Figure 2.8: Transformation times on a more sophisticated computer (single precision) for $N = 89$ ($r_0 \approx 12\lambda$).

Probe array system

After reviewing the theory of the spherical wave expansion in the previous chapter, the focus will now be on minimizing the measurement acquisition time. At first, fast near-field acquisition by means of a probe array measurement system will be discussed. Instead of moving the probe, multiple probes are used and the probe channels are switched electronically. By this straightforward approach, the measurement time is reduced by a factor according to the number of probes if the switching time is negligible as opposed to moving a positioner. In fact, a single dual-polarized probe is a special case of a probe array and was used in the early days of spherical near-field scanning [21, 61]. However, for a huge number of channels, the classical array approach with microwave multiplexer is expensive. Therefore, this approach is only acceptable for two or a limited number of channels [21, 62]. In order to avoid the costs of the microwave multiplexer, a modulated scattering technique can be used [63–65]. Instead of measuring the signal received by the probe, the signal scattered by the probe is measured. Furthermore, the probe is connected to a non-linear element (e.g. diode) and the scattered signal is modulated with a low-frequency (typically below 1 MHz) signal. The modulation signal is used to electronically switch the probes and allow fast measurements. A good survey on the modulated scattering technique can be found in [20]. Satimo, founded by Prof. Jean-Charles Bolomey in 1986 as a spin-off from the French engineering school *École Supérieure d'Électricité*, used this technique to develop an antenna measurement system for the telecommunication market. The first Stargate (SG64) was installed in 1998 and contained 64 dual-polarized measurement probes [66]. Other array concepts have been introduced in the following years [67, 68]. This measurement technique is accepted by the measurement community and has been included in the IEEE near-field antenna measurement standard [10]. Although probe arrays provide fast measurement capabilities by replacing a mechanical axis by an electronically scanned axis, they introduce new contributions to the uncertainty budget such as mutual coupling [69]. As discussed in section 2.2.3, probe correction is generally an important aspect in spherical near-field scanning. In the case of probe array systems, the probe correction is more complex compared to a single probe measurement system because, in general, the probes in an array do not have the same radiation pattern, including polarization, and the signal paths do not have the same attenuation and electrical length. Therefore, additional calibration measurements are required.

Typically, a known linearly polarized reference antenna with high polarization purity is used for that purpose [10, 21]. The reference antenna is aligned with each probe element and rotated in order to change the incoming polarization. The calibration data is then derived and used to correct the measured amplitudes of the AUT measurement. It is important to note, that this calibration procedure includes both

the effect of the probe (e.g. gain) and the effect of the signal path (e.g. losses). In any case, a good reference antenna is required and the measurement might be affected by room scattering. A prerequisite for the effectiveness of this calibration method is that the probe patterns are similar. This assumption is also implicitly used in the Wacker algorithm and is one of the reasons to use similar probes with equal radiation pattern in a probe array measurement system. However, this assumption is never exactly fulfilled in practice and limits the degrees of freedom in the probe array design. In the next section, a transformation algorithm with pointwise probe correction based on solving a linear equation system, discussed in section 2.2, will be introduced.

Pointwise probe correction

In this section, a probe correction procedure will be introduced which allows an individual correction of each probe radiation pattern. This idea has been published in [70] but is repeated here for completeness and extended by some examples. From the derivation of the spherical transmission formula (2.22)

$$\underline{w}^{(l)}(r, \theta, \phi, \chi) = \frac{v}{2} \sum_{\substack{smn \\ \sigma\mu\nu}} \underline{T}_{smn} e^{im\phi} d_{\mu m}^m(\theta) e^{i\mu\chi} \underline{C}_{\sigma\mu\nu}^{sn}(kr) \underline{R}_{\sigma\mu\nu}^{(l)}$$

it can be concluded that we can assign a different probe mode spectrum $\underline{R}_{\sigma\mu\nu}^{(l)}$ for every l -th measurement point $\underline{w}^{(l)}(r, \theta, \phi, \chi)$. Commonly, the probe response constants $\underline{P}_{s\mu n}^{(l)}(kr)$, defined by

$$\underline{P}_{s\mu n}^{(l)}(kr) = \frac{1}{2} \sum_{\sigma\nu} \underline{C}_{\sigma\mu\nu}^{sn}(kr) \underline{R}_{\sigma\mu\nu}^{(l)} \quad , \quad (3.1)$$

are used to represent the translated spherical mode spectrum of the probe in the AUT coordinate system. The translation coefficients $\underline{C}_{\sigma\mu\nu}^{sn}(kr)$ are independent of the probe and they only need to be calculated once if r is constant during the measurement. Therefore, the time to initialize the measurement matrix is not significantly increased if different probes are used for each point l . Furthermore, the probe spectrum $\underline{R}_{\sigma\mu\nu}^{(l)}$ does directly include the gain and the polarization of the antenna. Therefore, the signal path can be calibrated with an insertion loss measurement by connecting the AUT port directly with the probe port. In order to avoid saturation of the receiver an additional, known attenuation in the order of the expected path loss should be inserted. By this, inaccuracies due to effects of the measurement chamber such as room reflections are avoided. However, additional time might be required for the probe calibration procedure. Furthermore, mismatch errors in the receive path are not included here but are usually small and can be neglected. Nevertheless, they could be included in the model if necessary. In conclusion, the proposed procedure is mathematically exact and offers individual probe correction at every measurement point. Though this procedure has been discussed in the context of probe array systems, the applications are not limited to this case. In general, (3.1) allows to include every change of the probe pattern during the measurement for example due to varying orientation or measurement distance.

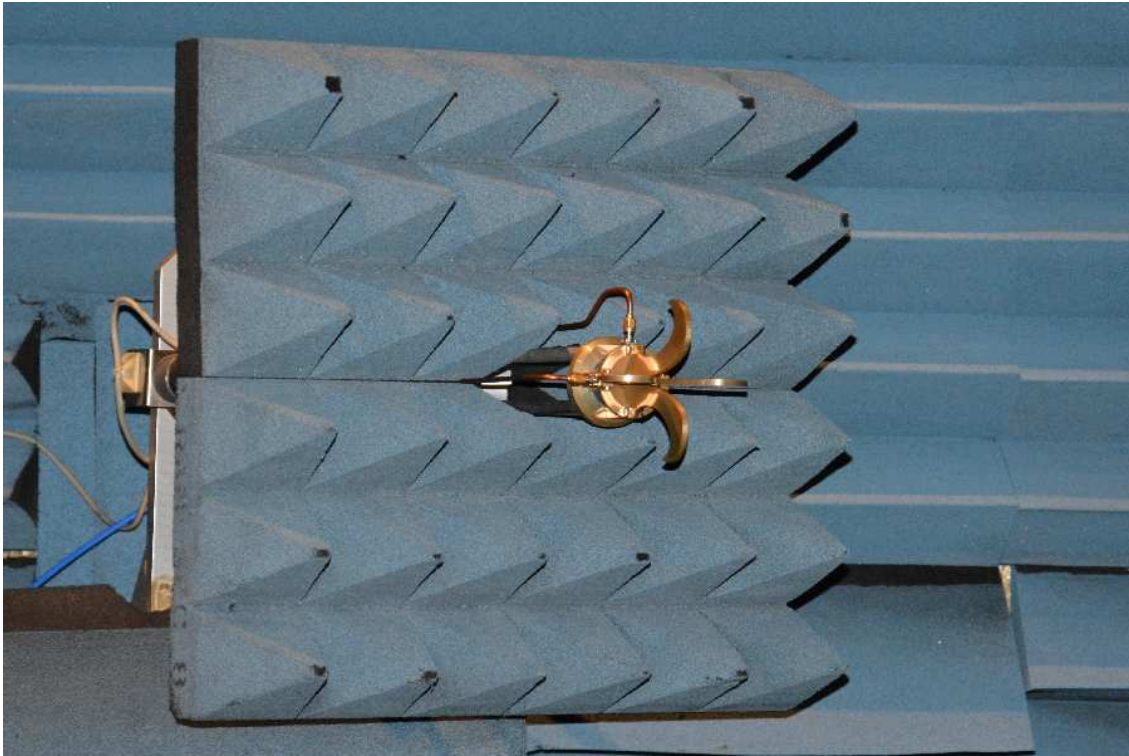


Figure 3.1: QH2000 in spherical near-field probe position.

The proposed procedure has been tested in the spherical near-field chamber of the Institute of High Frequency Technology (IHF). An open boundary wideband quad ridge horn QH2000 (Fig. 3.1) is used as probe antenna. The antenna is designed to have similar radiation patterns for both ports. The E-plane far-field pattern of both ports are compared in Fig. 3.2 where the difference is expressed as Equivalent Error Signal (EES)

$$\text{EES} = 20 \log_{10} \left| |E_{1,\text{norm}}| - |E_{2,\text{norm}}| \right|. \quad (3.2)$$

Due to the small differences, the introduced far-field error is expected to be small but, nevertheless, avoidable by the proposed procedure.

Measurement results presented in [70] have shown small pattern differences which might be small compared to other error sources. Furthermore, the probe correction effect depends always on the specific setup. The error will increase for larger differences between the port radiation patterns. Furthermore, it correlates with the influence of the probe on the measurement depending mainly on the probe pattern, the AUT size and the measurement distance [21, 60, 71]. For these reasons, the following investigation is based on simulations in order to extend the results presented in [70]. Similar to [70], the base transceiver station (BTS) antenna, represented by its measured SMC, is used as AUT.

It has been chosen to vary the distance between AUT and probe between 0.1 and 0.5 times of the far-field measurement distance ($r_{\text{FF}} = 2D^2/\lambda$). The near-field to far-field transformation is performed with the classical dual-polarized probe correction scheme [21], assuming the same radiation pattern for port 1 and port 2, and compared to the reference field in order to evaluate the error. Please note, that

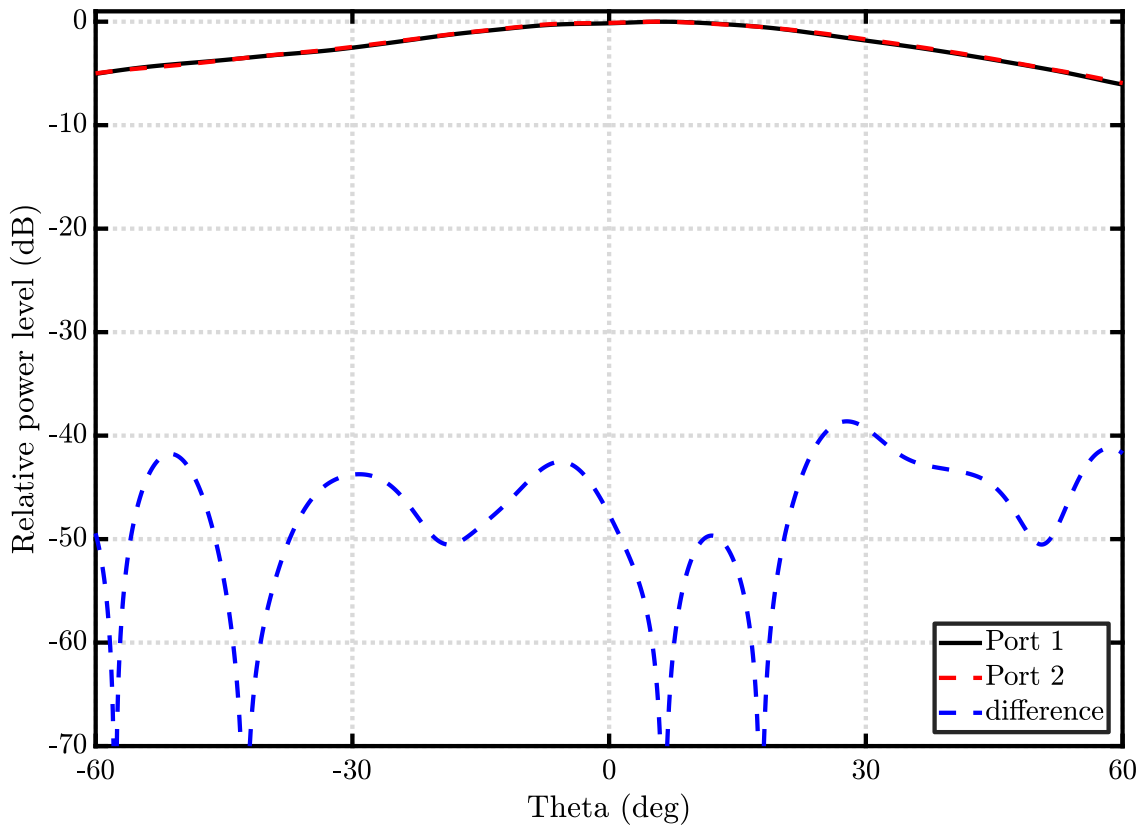


Figure 3.2: QH2000 E-Plane pattern (port 1 and port 2) at 2.4 GHz.

using a pointwise probe correction scheme is analytically exact and, thus, no error exist in this case. The linear equation system is solved in the least squares sense by QR decomposition including higher order probe correction ($\mu = 15$). The co-polar reference far-field radiation pattern and the errors for both distances are shown in Fig. 3.3. As expected, the error level for ignoring the pattern differences between the ports decreases with distance and is generally low (mostly below -60 dB). Next, the pattern differences between the two ports are increased by using the probe port 2 radiation pattern of a different frequency (i.e. 2.11 GHz instead of 2.4 GHz). This artificial probe is called probe B in the following. The resulting error levels are shown in Fig. 3.4 and the increased pattern differences for probe B significantly increase the error. This emphasizes that for a well-designed probe with almost equal radiation pattern for both ports the error might be acceptable but can be significant in other cases. Since the effect depends on the specific setup, the error has to be calculated and evaluated for every case separately.

In conclusion, the example shows that, even for a well-designed dual-polarized probe, the assumption of identical probe port pattern leads to errors in the calculated far field. Therefore, probe design has been crucial for probe array systems. The introduced pointwise probe correction procedure overcomes this limitation and offers individual probe correction for every probe of a probe array measurement system. In addition, the procedure can generally be used in measurement scenarios where the probe pattern changes during the acquisition.

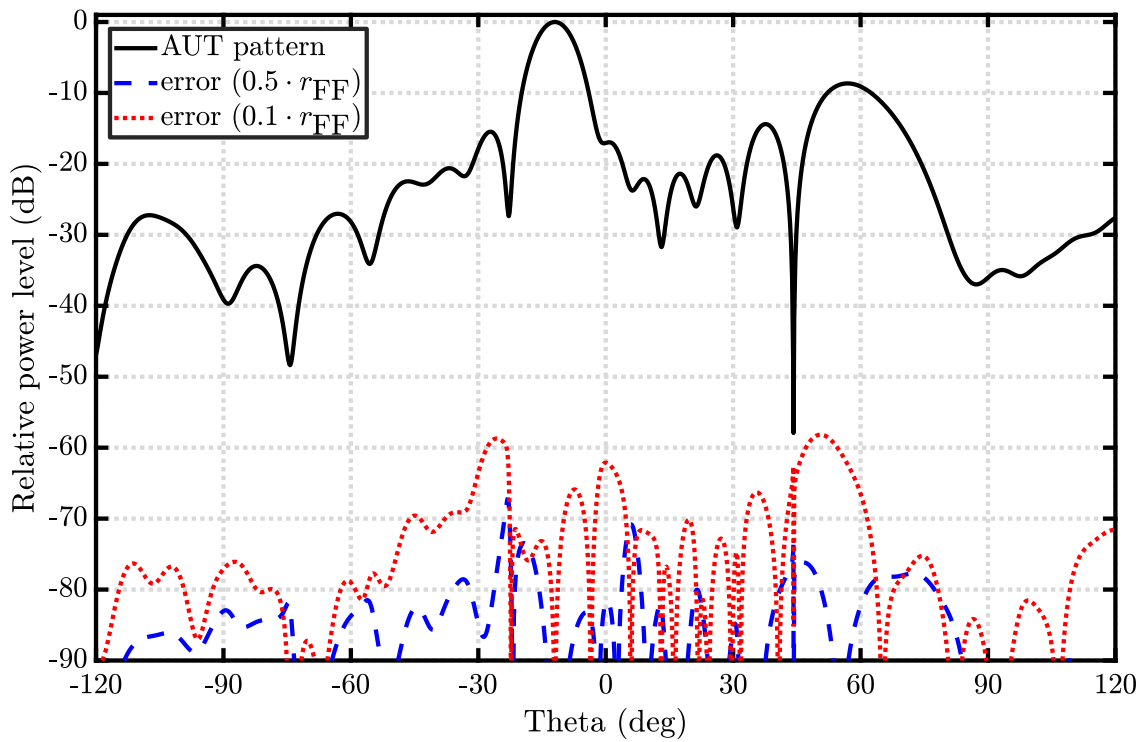


Figure 3.3: Error in the vertical co-polar BTS far-field radiation pattern cut (2.4 GHz) for two different measurement distances.

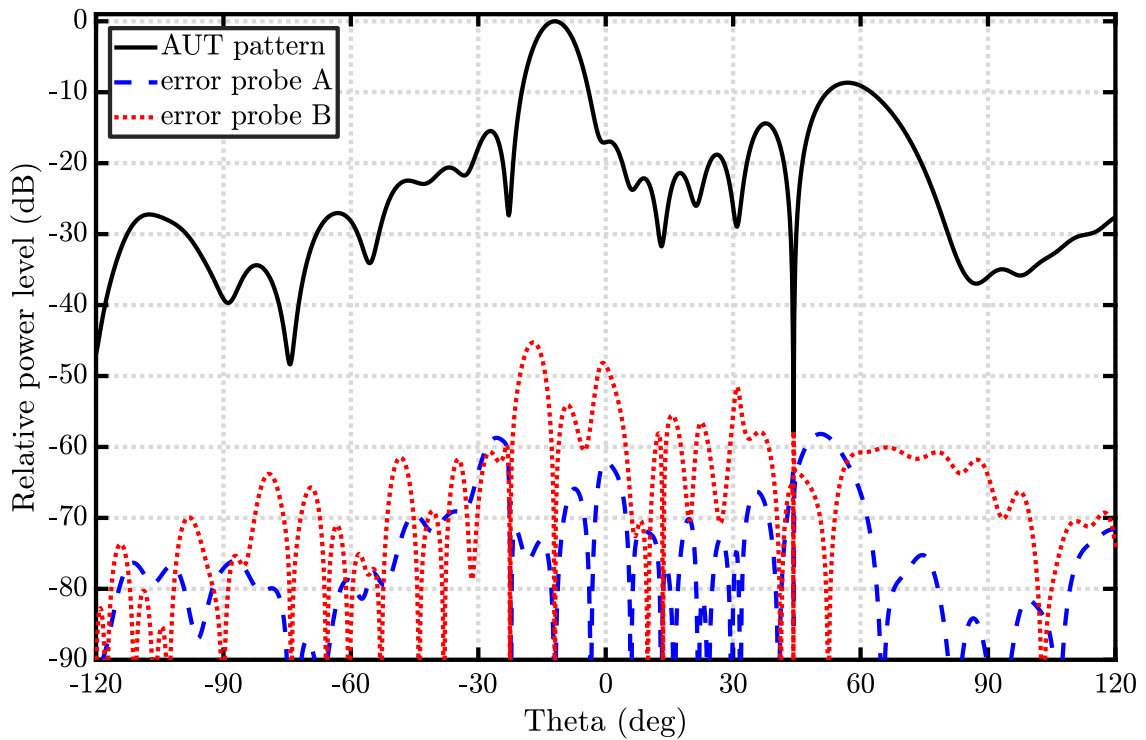


Figure 3.4: Error in the vertical co-polar BTS far-field radiation pattern cut (2.4 GHz, $r_{\text{meas}} = 0.1 \cdot r_{\text{FF}}$) for two different probes.

Truncation

In antenna near-field measurements, truncation means that only a part of the mathematically required surface for the exact transformation is measured. Theoretically, spherical near-field antenna measurements are performed on a closed surface and, thus, the measurement is generally not truncated. In contrast, planar or cylindrical near-field measurements are inherently truncated due to the finite size of the scan surface. For this reason, most of the research on truncation is focused on these two geometries. However, spherical near-field measurements might be truncated in practice due to:

1. Full spherical coverage is not possible due to mounting / positioning equipment or
2. time constraints and small region of interest.

According to the topic of this thesis, the following discussion is focused on intentional truncation due to time constraints. In general, spherical modes are orthogonal on the full sphere but not on a truncated area. Hence, this property cannot be used in the spherical wave expansion. Furthermore, the spherical mode spectrum is no longer band-limited because only the trivial always-zero signal is limited in both domains [72]. This fact is well-known and has been investigated in the field of signal theory as will be touched upon later. In summary, inaccuracies due to truncation comparable to planar or cylindrical near-field measurements can be expected for spherical scanning. Furthermore, the effect depends on the AUT and the measurement scenario. Although no universal theory exists, guidelines can be derived for certain applications.

Research on truncation was already conducted in the early days of spherical near-field antenna measurements and presented at the IEEE International Symposium on Antennas and Propagation in 1977 [73, 74]. It was found that the spherical measurement can be truncated for narrow-beam antennas without losing accuracy in the main beam direction. The truncated data was assumed to be zero which is approximately correct in the case of narrow-beam (i.e. high directive) antennas. If the radiation is concentrated only in one hemisphere, it is also possible to reduce the transformation time significantly [75]. A detailed discussion of truncation and zero extrapolation in spherical near-field measurements can be found in [21]. The main result, analogous to previous results, is that the far field can be accurately determined from near-field measurements only in a region smaller than the measured region.

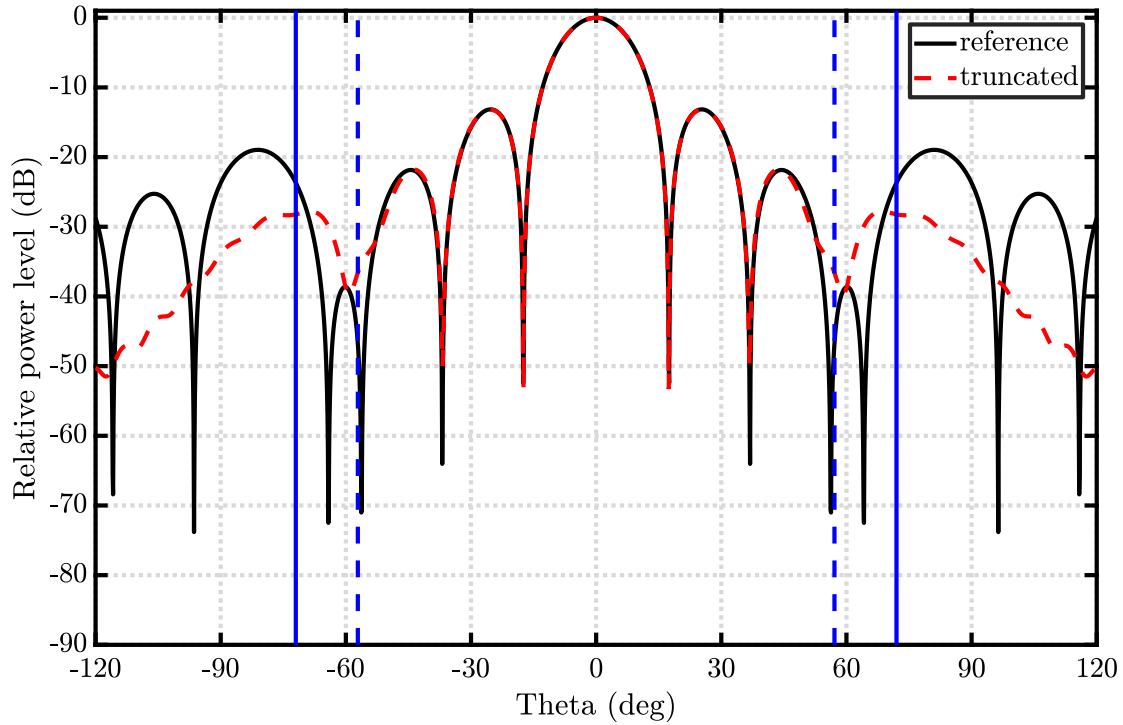


Figure 4.1: Co-polar H-plane far-field pattern cut of the dipole array calculated from full and truncated $\theta_{\text{meas,max}} = 72^\circ$ (vertical solid blue lines) near-field data.

The rule for truncation depends on geometrical considerations and can be expressed by

$$\theta_{\text{valid}} = \theta_{\text{meas,max}} - \arcsin(r_0/r) \quad (4.1)$$

where r_0 and r are the minimum sphere and the measurement radius, respectively. Interestingly, the formula does not involve the amplitude. Though, the formula is stated for a polar truncation it is equally valid for equatorial truncation [21]. It is important to note that θ_{valid} indicates the region where the error might be acceptable small. Due to the truncation, the transformation is not exact and, thus, also the field for $\theta \leq \theta_{\text{valid}}$ is only approximated. As an example, a simulated dipole array ($4 \times 4 \times 4$, see [21] p. 234) which consists of 64 y-directed Hertzian dipoles is used in the following. The element spacings are $5\lambda/6$, $15\lambda/16$ and $3\lambda/8$ in x , y and z , respectively. The phase of the excitation changes with $-11\pi/12$ along z . Fig. 4.1 shows the far-field results where the near-field measurement of the dipole array has been truncated at $\theta_{\text{meas,max}} = 72^\circ$ (vertical solid blue lines). The measurement distance is 8λ so that $\theta_{\text{valid}} \approx 57^\circ$ (vertical dashed blue lines). It can be seen that the main beam and the first side-lobes are accurately determined by the truncated measurement. As expected, the deviation gets larger close to the truncation angle. The effect of the truncation can also be seen in the spherical mode spectrum in Fig. 4.2. The spectrum calculated from the truncated near-field measurement is not anymore band-limited. In addition, modes with low degree n are also distorted and indicate that the complete far-field pattern is erroneous.

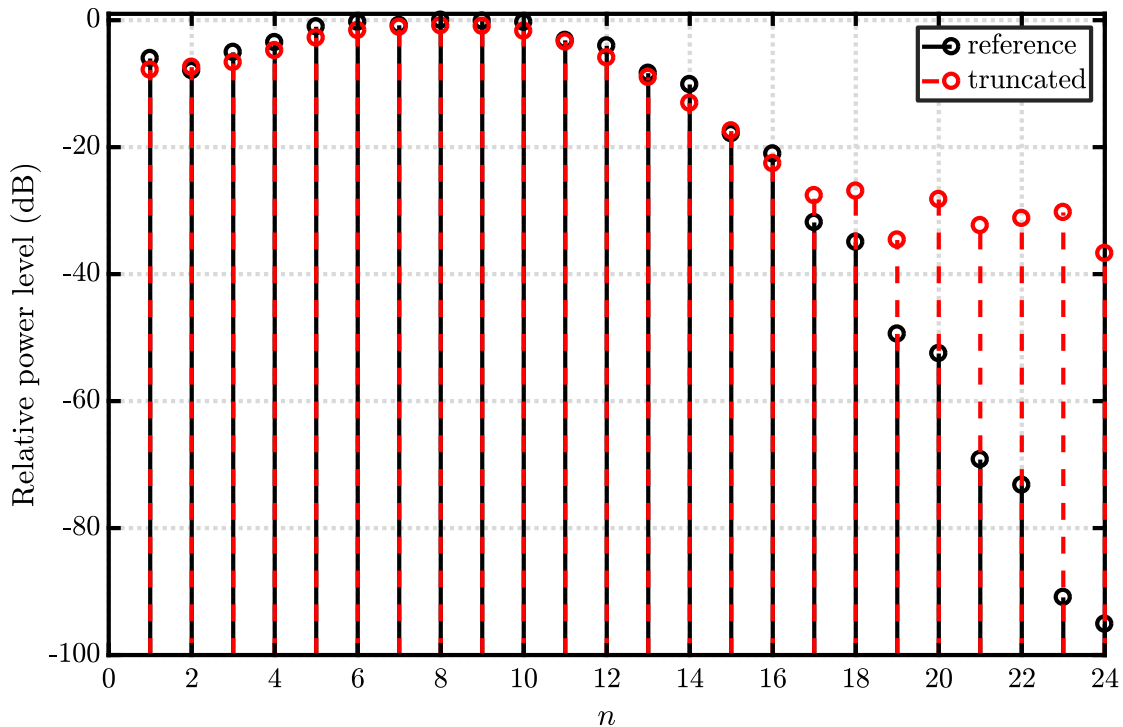


Figure 4.2: SMC of dipole array calculated from full and truncated $\theta_{\text{meas,max}} = 72^\circ$ near-field data.

For polar cap truncation, it was pointed out in [21], that the equiangular sampling step $\Delta\phi$ can be increased to

$$\Delta\phi = \frac{\pi}{M_{\text{max}}} = \frac{\pi}{N \sin(\theta_{\text{meas,max}})} \quad (4.2)$$

due to the cut-off properties of the Legendre functions. This thinned sampling scheme has been exploited many years later for measurements of electrically large antennas [76].

In summary, truncation with zero extrapolation is a simple and convenient technique to accelerate the near-field acquisition. However, information is lost and the accuracy is reduced. Over the last decades, different methods were developed for truncation error reduction and are reviewed in the following sections. Most of the methods were designed for planar and cylindrical measurements and later transferred to spherical near-field measurements. Direct extrapolation (Section 4.1) aims to extrapolate the field outside the measured region, for example, by filter functions or periodic extrapolation. The main goal of these techniques is to extend the valid region and to reduce the error inside that region. The method of alternating orthogonal projections discussed in Section 4.2 is another method for band-limited signal extrapolation known from signal theory. Here, the band-limited properties are exploited in order to derive an iterative, successive approximation method. This method converges only in the noiseless case and noisy data requires an additional stop criteria. Furthermore, the convergence speed might be slow so that a huge number of iterations is required. These two methods can directly be applied to the spherical wave expansion method presented in chapter 2 and have been investigated

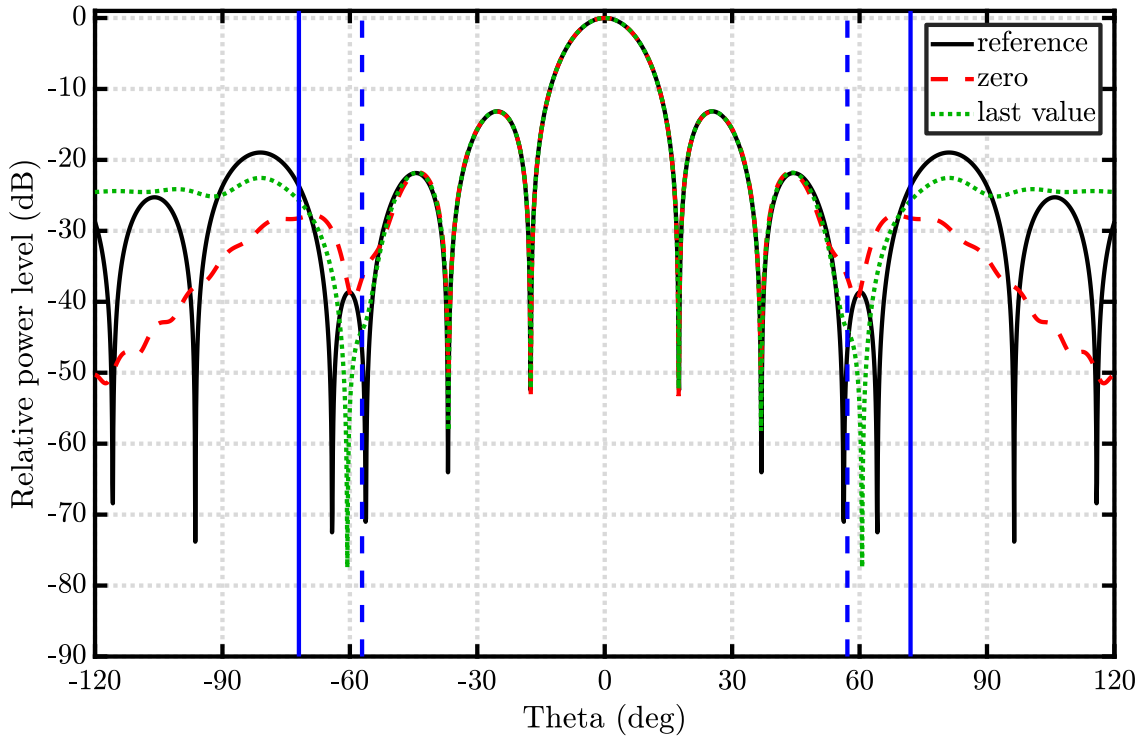


Figure 4.3: Co-polar H-plane far-field pattern cut of the dipole array calculated from full and truncated $\theta_{\text{meas,max}} = 72^\circ$ (vertical solid blue lines) near-field data (zero and last value extrapolation).

in more detail. Further techniques can be used if a different transformation approach (e.g. source reconstruction) is used and are discussed in Section 4.3 for comparison. The variety of different methods indicates that truncation error reduction depends on the measurement scenario and that no method is superior in every case as will be discussed in the following.

4.1 Direct extrapolation

As previously discussed, the far field can be accurately calculated from spatially truncated data in an area smaller than the area where the data was acquired. The error due to truncation is not uniformly distributed and is larger close to the border (see Fig. 4.1). Some methods have therefore been developed in order to enlarge the so-called *valid region* up to the size of the measured area. The primary goal is to reduce the truncation error in the measured area and not to estimate the field in other directions. An extrapolation with zeros can be regarded as filtering the data with a rectangular window. For this reason, high oscillating ripples are expected due to the abrupt change in the signal amplitude. Therefore, it is beneficial to truncate the pattern in a valley instead of a peak [77]. The abrupt change can also be avoided by extrapolating the signal constantly with the last measured value [78]. This approach is compared with zero extrapolation in Fig. 4.3 for the simulated dipole array. The truncation error close to the borders of the valid region is reduced if last value extrapolation is used. However, the improvement is small. Instead of a

rectangular window (zero extrapolation), a smooth continuation of the signal can be achieved by filtering [79]. The main purpose described in the paper is to improve the accuracy of the gain measurement in a planar near-field range. Although the error in the main beam direction is reduced, the size of the valid region is reduced as well. Therefore, this technique might be adequate for improving the estimation in the main beam but is not sufficient to enlarge the valid region. Other approaches use a priori information about the antenna and the surrounding. For example, if the antenna is placed over a large conducting ground plane (e.g. the earth surface) the electromagnetic problem has an electrical symmetry along z . This allows the application of the image theory and the extrapolation of the lower hemispherical data based on the measured data in the upper hemisphere [80]. If the ground plane is infinitely large and a perfect electrical conductor, the approach is exact. However, in practice the assumptions are only fulfilled approximately and, hence, a residual error exists. Furthermore, the ground plane has to be located exactly in the xy -plane ($z = 0$) which is not always possible in measurement practice. In this case, however, it is possible to use a slightly modified spherical wave expansion algorithm which takes the offset (usually only in z) into account. In [81] the boundary condition of the half space problem is translated while in [82] the transformation origin is translated. The latter approach has the benefit that the number of measurement points is minimal while the transformation routine is slightly more complex compared to the first approach. A simple example of a dipole over an infinitely large and perfect electrically conducting ground is shown in Fig. 4.4a. Fig. 4.4b shows the corresponding far-field pattern cuts for zero and image extrapolation. The result for image extrapolation is identical to the reference pattern because the symmetry plane is exactly in the xy -plane. If instead the ground plane is not in the xy -plane ($z = 0$) as shown in Fig. 4.5a the classical image extrapolation is not correct (Fig. 4.5b). Taking the translated origin into account [82] an exact transformation is again possible. This modification of the transformation algorithm allows always to exploit the symmetry relation due to the ground plane and can be regarded as generalization of the classical image extrapolation.

Other field repetition (e.g. along ϕ [21]) can also be regarded as an application of boundary conditions. In summary, existing boundary conditions can be used to extrapolate the field mathematically. However, since the boundary condition is enforced by the extrapolation, the far field is equally forced to fulfill this condition. Therefore, the far field does not provide information about the validity of the boundary condition assumption. Furthermore, only in some measurement scenarios boundary conditions can be assumed and, hence, they are rarely applicable.

The prediction of an arbitrary signal outside the measured region is in general not possible. Therefore, we have to require that the signal is band-limited. The extrapolation problem is still ill-posed but can be solved. However, due to measurement noise, only a limited number of samples can be extrapolated [83, 84]. This can be, for example, performed by a singular value decomposition [85]. If the near field is sampled at Nyquist rate, the additional samples do not enlarge the region significantly. For this reason, it is beneficial to use a non-redundant field representation based on its spatial bandwidth [22, 33]. In this case, the sampling step size is much larger than Nyquist and, hence, the extrapolated area is larger and the truncation error smaller [86, 87]. In some cases, the maximum scan area might be too lim-

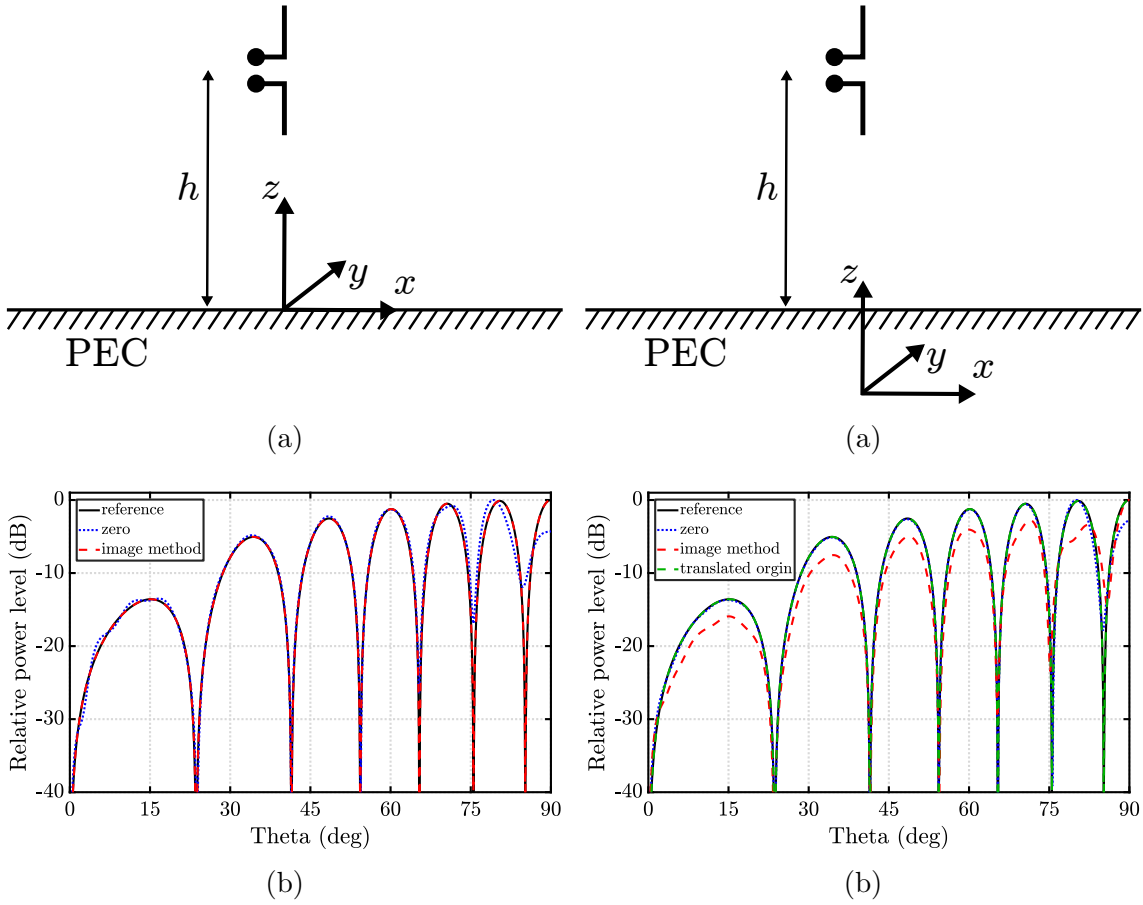


Figure 4.4: Coordinate system (a) and co-polar far-field pattern cut comparison (b) for i) zero extrapolation and ii) image extrapolation without coordinate system offset.

Figure 4.5: Coordinate system (a) and co-polar far-field pattern cut comparison (b) for i) zero extrapolation, ii) image extrapolation and iii) translated origin method with coordinate system offset.

ited and the aforementioned approach not be sufficient to achieve accurate results. Bucci et al. proposed in [88] to vary the distance between probe and AUT during the measurement. In cylindrical near-field measurements, for example, this means to measure additional points on the top and the bottom of the cylinder. By this, the measurement surface gets almost closed around the AUT and the truncation error is further reduced. In the mentioned methods, the measured signal is extrapolated on lines, taking all samples on that line into account. This might be seen as a global extrapolation. However, it is also possible to extrapolate the signal based on a few samples close to the border in a similar manner [89]. Though, it is necessary to acquire additional data close to the border in order to generate the required information for the extrapolation. Nevertheless, in [89] it was shown that an extrapolation for plane-polar scanning based on a local optimal sampling scheme performs better than an extrapolation based on cardinal series. The same method was used in [90] in order to extrapolate spherical near-field measurement data at the pole. Although additional data on rings close to the border is required, the method is suited to extrapolate measurement data in a region where the acquisition might be

inaccurate due to positioning equipment. Hence, a measurement time reduction is not achieved.

An important aspect concerning inter- and extrapolation is probe correction. It is important to note, that inter- and extrapolation of the electric near field is different from interpolating the measurement signal received by the probe. The probe, similar to the AUT, has a band-limited spectrum and, thus, the measurement signal is also band-limited. However, for an arbitrary probe for example, it is not possible to determine the measured values for different polarization rotation values χ from only two measurements (e.g. $\chi = 0^\circ$ and $\chi = 90^\circ$). This fact was already discussed in Section 2.2.3 in the context of probe correction. Similarly, direct inter- and extrapolation methods are usually restricted to measurements with a first-order probe. Multiple measurements in χ would be necessary for HOP. Furthermore, the methods are only applicable for measurements with a single probe, i.e. the probe is the same for every measurement point.

In conclusion, direct extrapolation methods can be used to reduce the truncation error. Exploiting boundary conditions such as a perfect conducting ground plane are well-suited but exist only in some special scenarios. The truncation error would be completely eliminated in an ideal scenario. If boundary conditions do not exist, other methods are capable to extrapolate some samples outside the measured region. But due to the ill-posed extrapolation problem, these methods are sensitive to measurement noise and can therefore not recover all truncated samples. In addition, they are usually limited to single first-order probe correction.

4.2 Alternating orthogonal projections

The method of alternating orthogonal projections is popular for band-limited signal extrapolation. The benefit of alternating orthogonal projections is that the numerical complexity is low because the algorithm uses the fast Fourier transform. The method is often called Papoulis-Gerchberg algorithm after the first publications from Papoulis [91] and Gerchberg [92]. A more general description of alternating orthogonal projections and discrete signal extrapolation can be found in [83, 93]. In principle, the method is an iterative signal extrapolation algorithm and illustrated in Fig. 4.6. In a first step ①, the spectrum is estimated based on the oversampled truncated (i.e. finite) signal. Next, spectral components which exceed the band-limit of the signal are set to zero, because they are non-physical ②. The filtered spectrum is then used to calculate an estimated non-truncated signal ③. The known part of the signal (red) is replaced while the extrapolated part is maintained ④. This four-step procedure is iteratively repeated and converges towards the true solution in the noise-free and strictly band-limited case. In the presence of noise the procedure has to be aborted after a certain number of iterations [91]. In general, the problem is ill-posed and, thus, in practical applications only a limited part can be extrapolated [84]. Nevertheless, the algorithm has gained popularity and has been used in the area of antenna measurements. At first it was applied to surface diagnosis of a large reflector antenna [94]. Later, it has been used for truncation error reduction in planar near-field measurements [95]. The algorithm exploits the fact that the electric and magnetic field in the aperture of an AUT are space-limited. Instead of

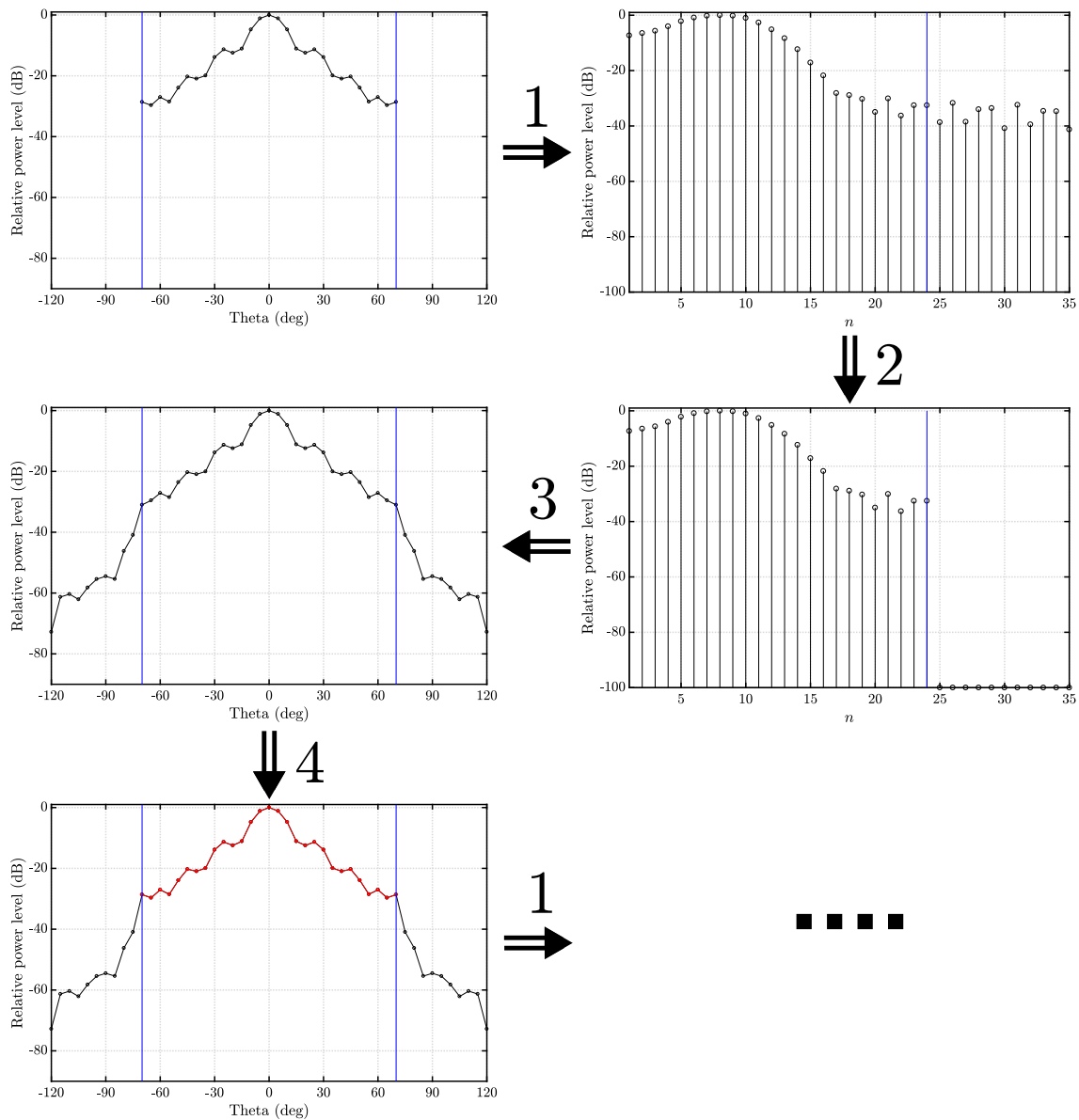


Figure 4.6: Iterative 4-step near-field extrapolation algorithm.

extrapolating the measured planar near-field data, the plane wave spectrum is extrapolated beyond its valid region. It is stated in [95] that the convergence is faster compared to an extrapolation of the near-field because more a priori information (e.g. size of the AUT) are used. The algorithm significantly reduces the truncation error for simulated and measured data. Although the iterative algorithm has to be stopped after a certain number of iterations due to measurement noise [95, 96], already few iterations improve the accuracy of the calculated far field. This approach has been transferred to spherical near-field antenna measurements by exploiting the band-limit properties of the spherical wave expansion [97]. In [78] it was shown that this approach increases the accuracy in the valid region even for complex antennas. Again, few iterations (≤ 100) already decrease the truncation effect in the valid region significantly. Fig. 4.7 shows the resulting far-field pattern of the simulated dipole array for 50 and 1000 iterations. The near-field is oversampled by a factor

of 2 and the truncation angle has been set to $\theta = 70^\circ$ for a convenient comparison with other oversampling ratios. The improvements compared to zero extrapolation are clearly visible in Fig. 4.8 where the relative error is shown. Although the error in the main beam region decreases, the error close to the truncation angle stays high. The convergence towards the correct full sphere pattern is extremely slow. Larger oversampling increases the convergence speed and is shown in Fig. 4.9 where the relative error in the mode spectrum

$$\epsilon = \frac{P_\epsilon}{P_{\text{ref}}} = \frac{\frac{1}{2} \sum_{smn} |Q_{smn}^{\text{ref}} - Q_{smn}^{\text{trunc}}|^2}{\frac{1}{2} \sum_{smn} |Q_{smn}^{\text{ref}}|^2} \quad (4.3)$$

is displayed. The calculation time of each iteration is typically fast and takes much less than a second (2 ms in the example). Interestingly, if one compares the calculated far fields for both near-field oversampling factors and 5000 iterations (see Fig. 4.10), it can be observed that the lower oversampling factor shows a lower error in the main beam, while the larger oversampling factor has a lower error outside the main beam. Hence, depending on the region of interest, the oversampling factor should be taken into account. A small oversampling factor is sufficient to improve the main beam region while higher oversampling factors are required to decrease the overall error. However, oversampling is limited to spherical modes with degree $N \approx kr_{\text{meas}}$ because modes with higher degree are highly attenuated since they cannot be excited inside the measurement sphere. Another reason for the slow convergence is that the AUT band-limitation is the only used a priori knowledge. In contrast to the planar near-field algorithm, other properties of the AUT are not exploited in the spherical case. However, in [98] it was shown that both approaches can be combined. The data is still acquired on a spherical grid in front of the AUT but the iterative steps are applied in the plane wave spectrum and the planar aperture field. This procedure requires an additional transformation step from spherical near-field data to the plane wave spectrum. Therefore, it is necessary to calculate the spherical wave spectrum of the AUT first and transform it to a plane wave spectrum in a following step. This can be accomplished by a direct transformation of the spectrum [99] or by the explicit calculation of the far field [98]. Due to the plane wave expansion, the field calculations are restricted to one hemisphere. A comprehensive description of the method and different applications can be found in [100] and the corresponding dissertation [101]. In summary, the method extends the approach presented in [95] from planar to spherical measurement geometries and it can be expected that a similar approach can be used for arbitrary measurement geometries.

In conclusion, the method of alternating orthogonal projections has shown that the truncation error can be reduced in simulations and measurements, especially for aperture antennas. Furthermore, the approach includes probe correction and is computationally efficient. However, the extrapolation problem is ill-posed and therefore the iterative algorithm is not stable. Hence, the truncation error inside the valid region can be significantly reduced but only partially in the truncated region. In addition, oversampling is required which reduces the time savings by the truncation.

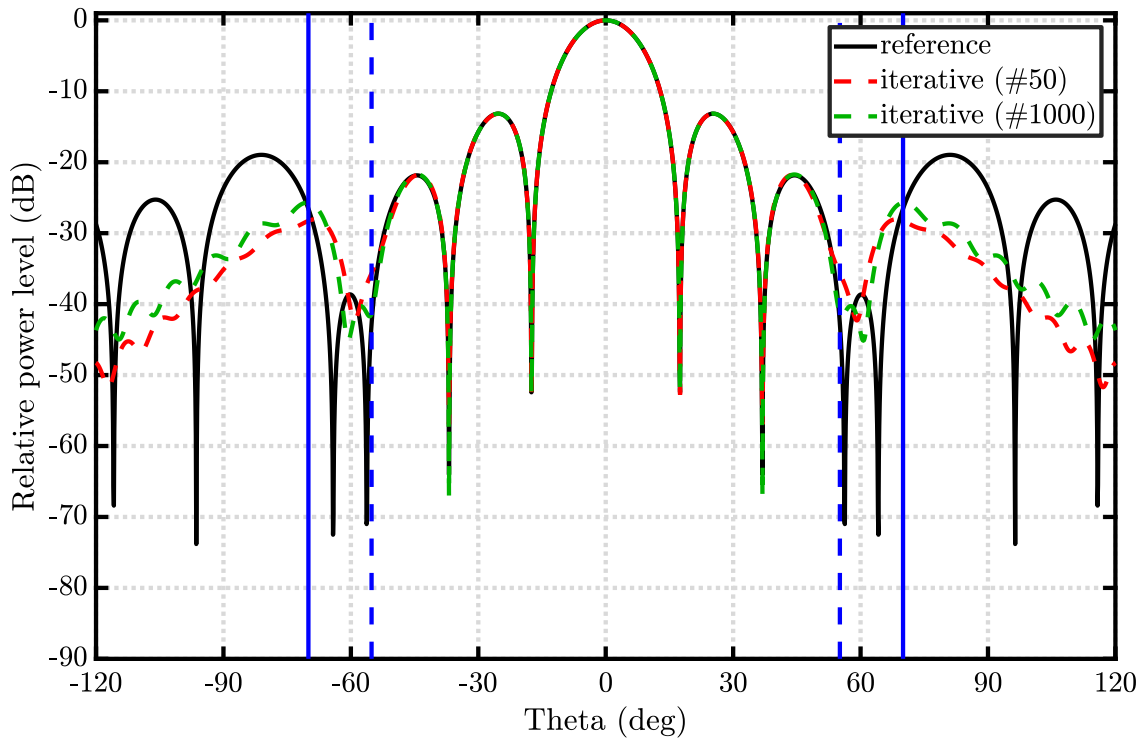


Figure 4.7: Co-polar H-plane far-field pattern cut of the dipole array calculated from full and truncated $\theta_{\text{meas,max}} = 70^\circ$ (vertical solid blue lines) near-field data (zero and iterative extrapolation with 50 and 1000 iterations).

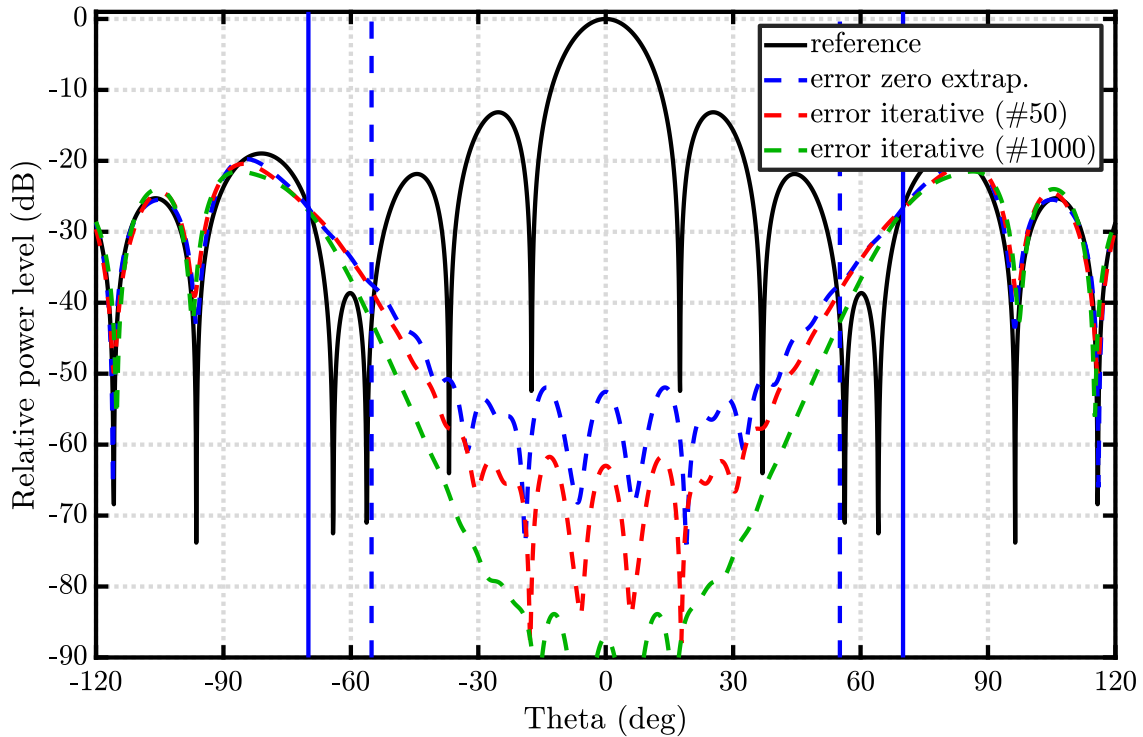


Figure 4.8: Co-polar H-plane far-field pattern cut and error of the dipole array calculated from full and truncated $\theta_{\text{meas,max}} = 70^\circ$ (vertical solid blue lines) near-field data (zero and iterative extrapolation with 50 and 1000 iterations).

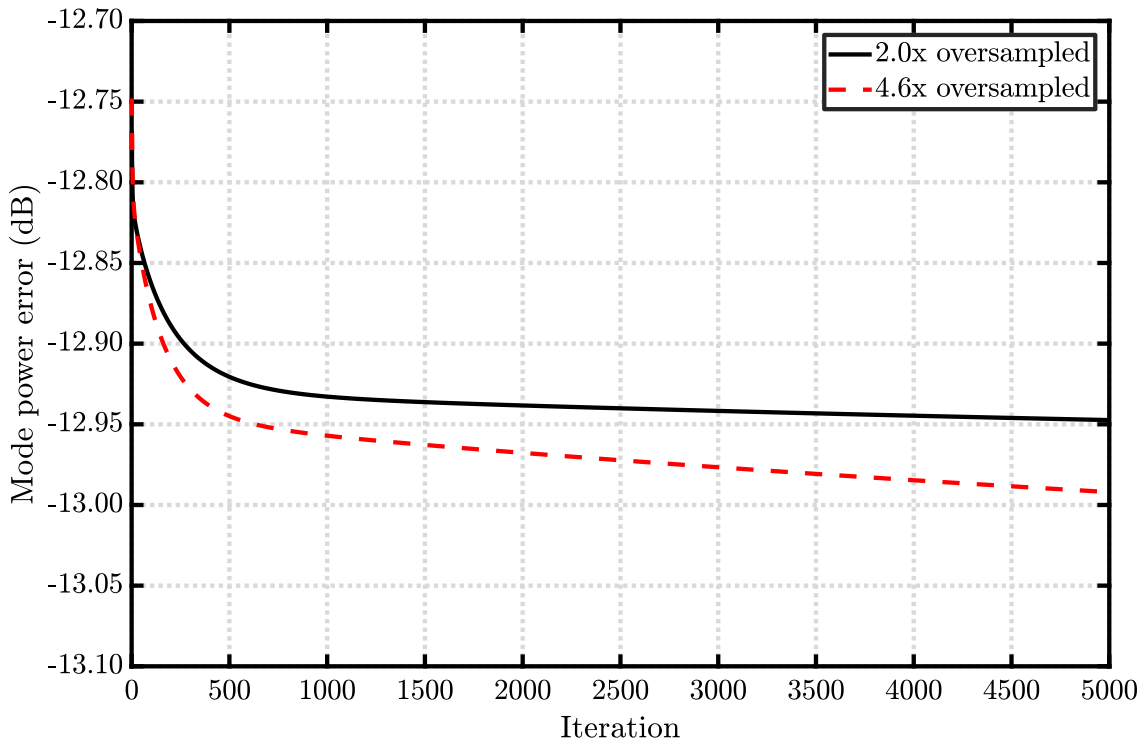


Figure 4.9: Relative mode power error of the iterative extrapolation method for two different oversampling ratios.

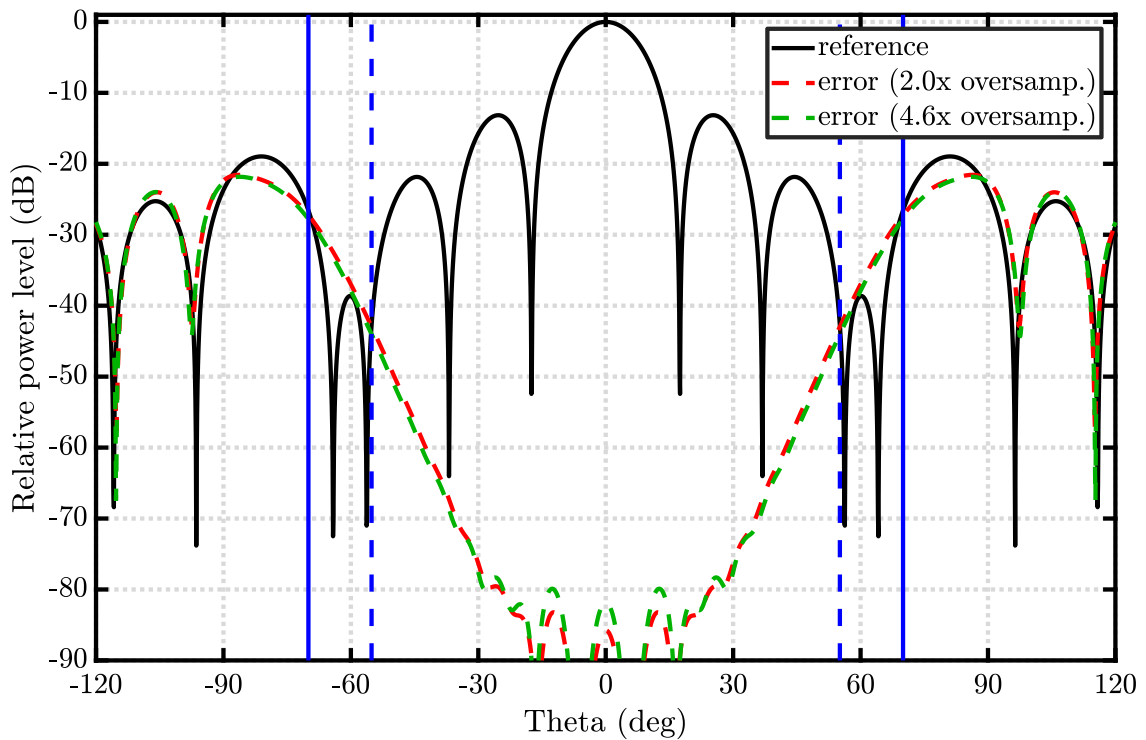


Figure 4.10: Co-polar H-plane far-field pattern cut of the dipole array calculated from full and truncated $\theta_{\text{meas,max}} = 70^\circ$ (vertical solid blue lines) near-field data and iterative extrapolation for two different oversampling ratios.

4.3 Other techniques

The two presented approaches are directly applicable to the spherical wave expansion procedure. However, other techniques based on different transformation methods have been developed and are reviewed in the following for comparison.

A famous technique for band-limited signal extrapolation is the usage of Slepian basis functions (Section 4.3.1). As mentioned before, the spherical waves are not orthogonal on a truncated spherical surface. So called *slepian functions* are functions that are orthogonal on the full sphere as well as on the truncated area (Section 4.3.1). This double orthogonality can be used to solve the truncation problem but requires almost the same number of measurements as a full sphere measurement. Thus, no increased measurement speed is expected. Slepian basis functions, similar to the method of alternating orthogonal projections, can solve the extrapolation problem but are similarly affected by noise. A different technique to mitigate the truncation error is based on source reconstruction by equivalent currents and is discussed in Section 4.3.2. In contrast to modal expansions as used in this thesis, source reconstruction algorithms represent an AUT by equivalent sources (e.g. electric and magnetic currents). These sources are determined from the measurement data by solving the inverse problem. This technique has inherently a good truncation error reduction because if the equivalent currents of the AUT are known, the far field can be calculated without truncation error. However, how good the equivalent currents can be determined from partial measurements has, up until now, not been comprehensively answered. Beside these two well-established approaches, further attempts have been made to solve the truncation problem.

A straightforward approach only suitable for inherently truncated measurement geometries such as planar near-field scanning is the data acquisition on multiple scan surfaces [102]. Wittmann et al. proposed a constrained least-squares technique for small antennas and oversampled hemispherical near-field data [103]. Due to the large oversampling the truncation error can be reduced but the measurement time remains unchanged. In addition, the general applicability of the method for different truncation angles and reduced sampling has to be investigated further. As discussed in this chapter, truncation error reduction requires some sort of additional knowledge about the signal or the AUT. Typically, it is required that the signal be band-limited and oversampling has to be used. Information about the AUT is often limited to the physical dimensions. However, nowadays antennas are typically simulated during the design of the AUT. Thus, information about the expected radiation characteristic is available from simulation. Up until now, they are rarely used for improving the near-field to far-field transformation. In [104] the information from a variety of simulations with different parameters are used to create a set of basis functions. By this, the amount of required measurement data can be reduced. However, simulated data could be used also for direct extrapolation or alternating orthogonal projections. Of course, attention has to be paid that the introduced simulated data does not overrule the measurement data. Nevertheless, the huge amount of a priori knowledge provided by simulation might be useful to improve existing truncation error reduction techniques.

A complete different class of transformation approaches which do not suffer from truncation can be used if the measurements are performed in the Fresnel-zone where

the $1/R^3$ radiation terms can be neglected [105]. These transformation procedures are not strictly valid in the near field and will not be discussed in detail. However, they motivated the research about single-cut near-field to far-field transformations [106] where it is shown that, under the assumption of a separable AUT pattern function, it is possible to accurately estimate the far field from a single near-field cut.

4.3.1 Slepian functions

The problem of signal extrapolation has attracted many researchers over more than 50 years and in many different disciplines. For example, D. Slepian, H. O. Pollack and H. Landau discussed and analyzed properties of prolate spheroidal wave functions in a series of publication in the Bell System Technical Journal [107–111]. A more general discussion of the results can be found in a later paper of D. Slepian [72]. These band-limited functions are orthogonal over $(-\infty, \infty)$ as well as over a defined finite interval. They concentrate the function simultaneously in time and frequency although no non-trivial signal can be perfectly limited in time and frequency. Hence, these functions allow an accurate approximation of the spectrum from limited but highly oversampled observations. The concentration problem on the line was later called *Slepian problem* and the used class of prolate spheroidal wave functions is often called *Slepian functions*. The method was later extended to a bounded spherical domain by Albertella et al. [112]. The complexity of calculating the Slepian basis is generally high because the basis has to be calculated numerically. However, in certain scenarios (e.g. polar cap truncation) analytical formulas can be used for scalar and vector spherical harmonics [113–115]. By this, exact and efficient computation of the Slepian basis is possible. Slepian functions are used in diverse applications and have also been applied to the truncation problem in near-field antenna measurements by Kim [116–118]. In [117] the formulation for scalar waves [116] was extended to vector waves. In [118], measurement data instead of simulated data was used. Though the data represents a measured standard gain horn, it was generated by a spherical wave expansion. This means that the data was strictly band-limited and noise-free. For this reason, the effects of noise and aliasing were not investigated. It can be expected that due to low eigenvalues in the basis the procedure is similarly noise sensitive as the method for scalar spherical waves [116]. These low eigenvalues point out that an extrapolation of the signal on the complete sphere is not possible in practice [84]. In conclusion, a comprehensive analysis and demonstration of the applicability to practical near-field antenna measurements has not yet been performed. In addition, similar to direct extrapolation in the previous section, the approach works only for a single first-order probe measurement. Nevertheless, Slepian functions show potential to mitigate the truncation error in antenna measurements. However, oversampling is required and, in fact, the number of points is not reduced but only limited to a certain region. In theory, the complete spectrum can be determined from a spatial limited, noise-free observation. The approach is, hence, useful for measurement scenarios where the data cannot be acquired on the complete sphere and does not inherently reduce the measurement time. If the electrical acquisition at every measurement point is much faster than the continuous mechanical movement, i.e. the receiver is idle over a certain time, oversampling can be performed at no additional costs. This

oversampling in conjunction with a Slepian basis could then be used to truncate the scan area and to reduce the total scan time.

4.3.2 Equivalent current representation

In contrast to modal expansion, the aim of this method is to determine an equivalent (electric and/or magnetic) current representation of the AUT [119–121]. The far field, if required, can directly be calculated from this representation. The method was first applied to planar geometries [122] using a method of moments procedure to transform the integral equation into a matrix one. It was demonstrated that the method provides accurate results in simulations and measurements [119, 120]. Furthermore, if the sources can be reconstructed from a partial measurement, the far field can be calculated without truncation error. However, the numerical complexity of the transformation is high and, thus, certain approximations were necessary in the beginning to increase the usability [122]. The approach can be straightforward extended to arbitrary sampling geometries which makes the method flexible [120, 123]. Furthermore, a priori knowledge about the AUT can be exploited directly. The drawback of large computation complexity has been overcome by the fast multimode method (FMM) introduced by Rohklin and Greengard [124, 125]. An introduction and further information about the topic can be found in [126, 127]. For the spherical expansion, it was important to diagonalize the translation operator of the spherical waves in order to develop fast transformation algorithms [128–130]. In general, the representation of a single spherical mode in a translated coordinate system is spread over the complete spherical spectrum (see (2.20)) and the evaluation is computationally demanding. However, the complexity is drastically reduced if a first-order probe is used. Furthermore, the calculation needs to be performed only once if the measurement radius stays constant during the measurement. The translation operation can be diagonalized by expanding it into plane waves [130]. A single plane wave is also a single plane wave in a translated coordinate system. The diagonalized FMM and its multilevel version MLFMM have led to the Fast Irregular Antenna Field Transformation Algorithm (FIAFTA) developed by the Technical University of Munich [51, 52, 121].

Nowadays, fast source reconstruction algorithms including probe correction exist and can be used to reduce the truncation error. However, it might be difficult to accurately determine the equivalent currents from a truncated data set. Comprehensive investigations have, up until now, not been performed. Although source reconstruction algorithms do not provide inherently a spherical wave spectrum, they are a useful technique for antenna diagnostics and near-field to far-field transformations.

4.4 Summary

Although not necessary, truncation can be used to accelerate the spherical near-field acquisition. The lost information causes inaccuracies in the calculation of the spherical wave expansion and, hence, in the calculated far field. Therefore, truncated measurements usually give only approximate far-field results. Though the complete far field is affected by the truncation error, the error might be negligible in a certain region. Direct extrapolation (Section 4.1) or the method of alternating orthogonal

projection (Section 4.2) can be used to reduce the error inside the measured region but are generally not capable to determine the far field outside. In addition, the improvement depends on the amount of oversampling. In summary, truncation is a severe problem for the spherical wave expansion and the presented methods can only reduce the effect. A better mitigation might be achieved with other transformation procedures outlined in Section 4.3. In the extreme case when the measurement area is truncated but the number of samples is maintained, Slepian functions (Section 4.3.1) can be used to restore the orthogonality properties on the measured surface. This approach does typically not reduce the acquisition or transformation time. Section 4.3.2 discussed that source reconstruction methods based on equivalent currents exploit a priori information about the AUT and reduce the truncation effect. Though promising results have been shown, a comprehensive truncation error analysis has, up until now, not been performed. Recently, methods based on a priori knowledge gained from simulations have been introduced but are still under investigation.

Overall, truncation is often applied in practice and the reduced accuracy is accepted in many applications. However, the truncation error is scenario dependent and, thus, no generalized theory can be developed. Practical guidelines are derived from experiments and simulation. This might be the reason why truncation error reduction techniques have not yet gained wide acceptance [10]. In conclusion, truncation accelerates the spherical near-field antenna measurements but more elegant methods are desirable.

Non or minimal redundant sampling

As discussed in the previous chapter, truncation of the measurement sphere reduces the accuracy of the spherical wave expansion and, hence, full sphere measurements are required to achieve accurate results. From the theory presented in Chapter 2, it is known that the spherical wave expansion of the electromagnetic field can be band-limited. Consequently, $L = J \propto (kr_0)^2$ measurement samples are required to solve the deterministic linear equation system. However, in contrast to – for example – the point distribution on a line, the problem of an optimal point distribution on the sphere is not uniquely solved for an arbitrary number of samples. For this reason, different sampling point distributions will be discussed in the following Section 5.1 with respect to the number of points (i.e. oversampling), measurement path length and measurement acquisition time in step and continuous scan mode. Next, the presented point distributions are tested in measurement practice (Section 5.2). The measurement uncertainties are discussed in detail in the later Chapter 7. The main result of this chapter is that different sampling grids can be used to reduce the total measurement time while the measurement uncertainty is not significantly affected.

5.1 Point distribution

As previously discussed, it was of utmost importance during the development of spherical near-field antenna measurements to have an efficient transformation algorithm. This was achieved by the Wacker algorithm (Section 2.2.2) using Fourier transforms. For this algorithm, equiangular sampling (Section 5.1.1) was required which is still the most common used sampling scheme. Other sampling schemes such as the thinned equiangular (Section 5.1.2) and the spiral (Section 5.1.3) scheme have been introduced since then. However, these sampling grids require oversampling for an accurate spherical wave expansion. In Section 5.1.4 a numerically optimized point distribution is presented which is non-redundant while the inverse problem is still well-conditioned. Though, it will be shown in Section 5.1.6 that this non-redundant point distribution does not necessarily have the shortest acquisition time. In addition, it is important to emphasize that the electromagnetic near field is a vector field (i.e. it has a polarization). For this reason, point distribution on the sphere means location in θ , ϕ and the rotation angle χ of the probe. However, it turns out that the acquisition of two orthogonal polarizations at each location leads in general to a well-conditioned inverse problem. Nevertheless, this is not mandatory and will

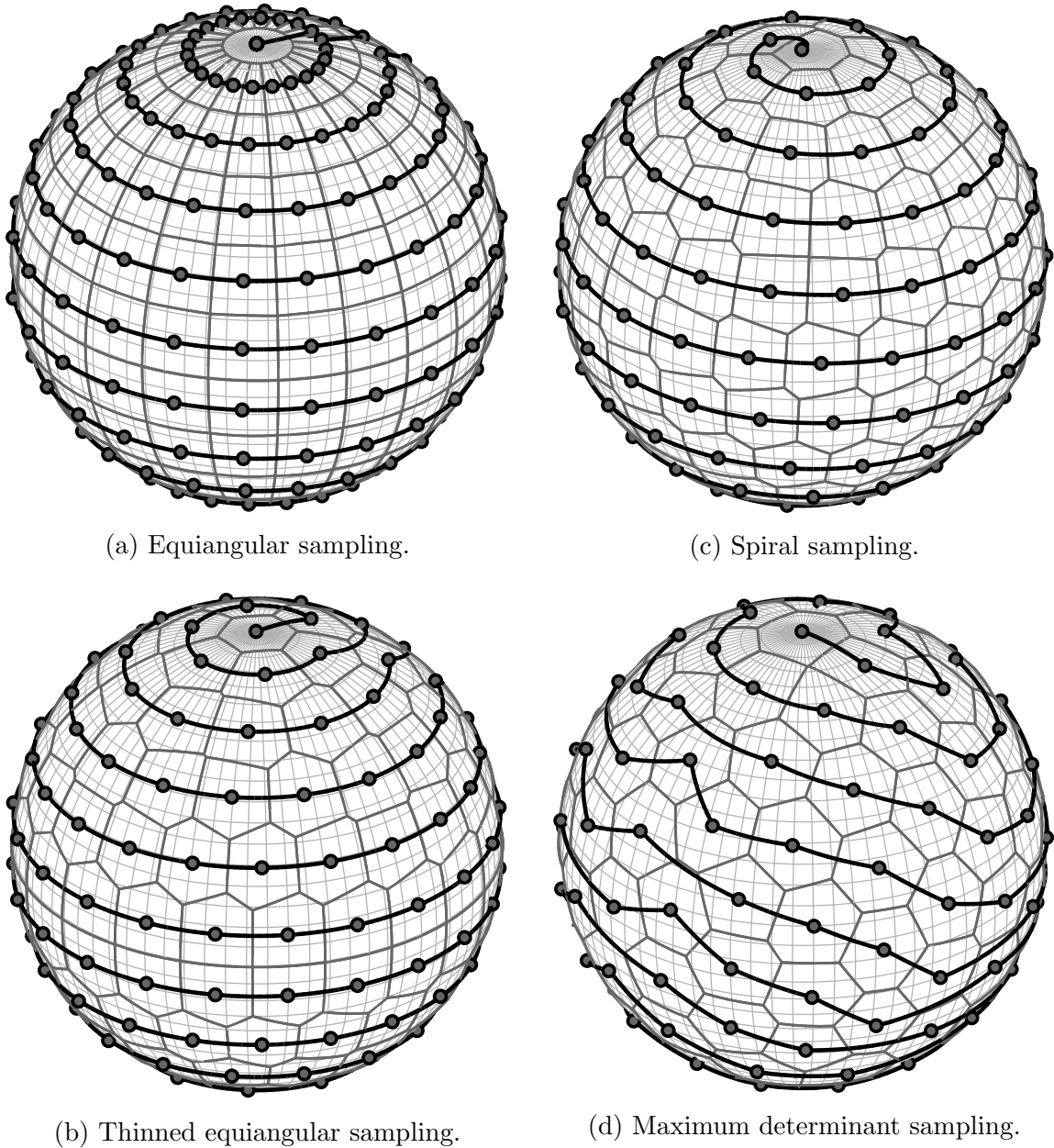


Figure 5.1: Sampling point distributions ($N = M = 10$) with measurement path (solid black) and voronoi tessellation (gray cells).

be highlighted in Section 5.1.3 where an optimized polarization angle is used for a spiral scan.

5.1.1 Equiangular

Probably, the best known and most often used spherical sampling point distribution is the equiangular point distribution in θ and ϕ [21]. The equiangular step sizes are

$$\Delta\theta = \frac{2\pi}{(2N+1)}; \quad \Delta\varphi = \frac{2\pi}{(2M+1)} \geq \frac{2\pi}{(2N+1)}; \quad \chi = \left[0, \frac{\pi}{2}\right]; \quad (5.1)$$

This sampling point distribution leads to a well-conditioned inverse problem and can be efficiently solved with Fourier transforms (see Section 2.2.2). However, as can be seen in Fig. 5.1a the points are concentrated at the poles. Hence, the sphere is highly oversampled in relation to the number of unknown SMC.

5.1.2 Thinned equiangular

A strategy to reduce the concentration of points at the poles is to reduce the number of points in each latitude ring by a $\sin(\theta)$ factor [21]. The step sizes in ϕ are equiangular in each latitude ring i but dependent on the value θ_i .

$$\Delta\theta = \frac{2\pi}{(2N+1)}; \quad \Delta\varphi_i = \frac{2\pi}{\lceil(2M+1)\sin(\theta_i)\rceil} \geq \frac{2\pi}{\lceil(2N+1)\sin(\theta_i)\rceil}; \quad \chi = \left[0, \frac{\pi}{2}\right]; \quad (5.2)$$

This sampling scheme is called thinned equiangular (sometimes also called *igloo*) and is shown in Fig. 5.1b. The concentration at the poles is significantly reduced.

A descriptive explanation for this factor is that the circumference of the latitude ring i is $C(\theta_i) = 2\pi r \sin(\theta_i)$. Consequently, the spacing in ϕ can be increased maintaining a point separation of $\lambda/2$ on the ring. Alternatively, the factor can be derived from the cut-off properties in m of the Legendre functions [21, 76, 131]. An example is shown in Fig. 5.2 where the band-limit of the m spectrum of an dipole array antenna is given for different angles θ . As can be seen, less m modes are required for $\theta = 5^\circ$ compared to $\theta = 90^\circ$. For this reason, the spacing in ϕ can be increased while the linear equation system is still well conditioned. Further reductions in order to find a deterministic sampling scheme as for example proposed by Khalid et. al. [132] lead generally to ill-conditioning of the inverse problem. However, the effect can be partly compensated by a numerically optimized placement of the iso-latitude rings. Overall, since the step sizes in ϕ are equiangular, it is possible to use Fourier transforms to interpolate the data on the equiangular grid presented in Section 5.1.1. By this, the transformation is comparably efficient as for equiangular sampling.

5.1.3 Spirals

Spiral schemes for spherical near-field antenna measurements were introduced by Bucci et. al. in 2001 [23] based on spiral scanning schemes for planar near-field antenna measurements [133, 134]. A comprehensive review with many references can be found in [135]. These approaches use an optimal sampling interpolation scheme [22] to interpolate the near field on a regular equiangular grid which is subsequently used to determine the spherical wave expansion. By this, the transformation complexity is kept low. The accuracy of the interpolation is controlled by oversampling which has to be higher at the poles compared to the equator [23]. However, it is important to emphasize that near-field interpolation is only exact for first order probes (see Section 2.2.3). The proposed spiral scanning scheme was tested extensively and it was shown that the number of measurements can be significantly reduced [23, 136]. However, achievable measurement time reductions have not been stated. As discussed before, a time reduction is certainly achieved in step mode acquisition but it is not obvious for continuous mode acquisition. A recent publication [24] discusses the difficulties of implementing a continuous mode spiral scanning scheme and concluded

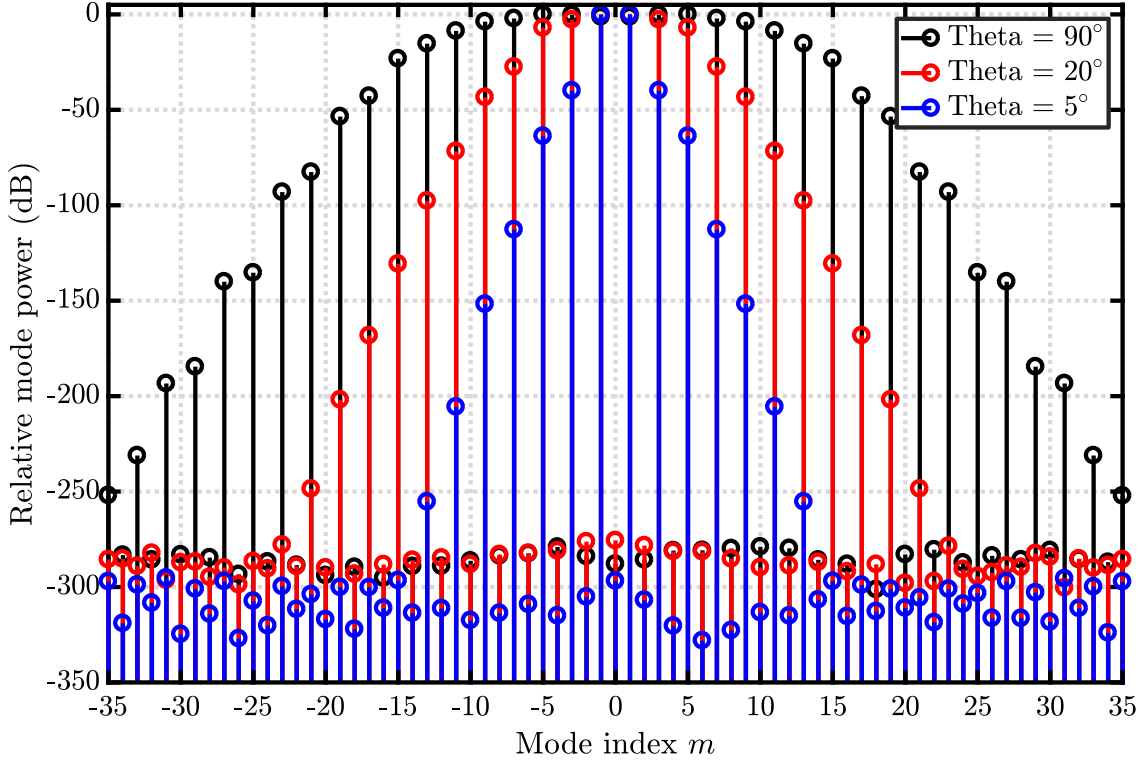


Figure 5.2: Visualisation of the cut-off properties in m of the Legendre functions ($M = 35$) in a latitude ring depending on the angle θ .

that further research is necessary to save measurement time. The publication [24] does not state the measurement times and, thus, it seems that the proposed spiral scanning does not reduce the measurement time in the current implementation.

Besides the established spiral scanning with subsequent interpolation, it is also possible to use the near-field data measured on a spiral path directly for the spherical wave expansion, avoiding drawbacks of the interpolation. Please note, that in this section spherical spirals for the case $M = N$ are investigated but the spiral scan path can be adapted to, for example, an elongated antenna ($M < N$) as described in [135]. Spherical spirals are also used in other research areas as for example in distributing a large number of points on a sphere [137]. The spiral in [137] is created by:

$$\begin{aligned} \theta_p &= \cos^{-1}(h_p); & h_p &= -1 + \frac{2(p-1)}{(L-1)}; & 1 \leq p \leq P; \\ \phi_p &= \left(\phi_{p-1} + \frac{3.6}{\sqrt{L}} \frac{1}{\sqrt{1-h_p^2}} \right); & 2 \leq p \leq P-1; & \phi_1 = \phi_P = 0; \end{aligned} \quad (5.3)$$

where P is the number of measurement locations. Consequently, $P = L/2$ if two polarizations at each location are measured. The value 3.6 is based on numerical experimentation [137]. In [138] a modification is introduced which might be called *generalized spiral points* [139]. While the spiral [23] is designed according to the spatial bandwidth of the field, the spiral in [138] aims to distribute the samples

so that the distance between two adjacent spiral levels is similar to the distance between two adjacent points. The spiral points ($p = 1, \dots, P$) are defined by:

$$\phi_p = g\theta_p; \quad g = \sqrt{\pi P}; \quad \theta_p = \cos^{-1}(h_p); \quad h_p = 1 - \frac{2p-1}{P}; \quad (5.4)$$

The slope (or pitch) g of the spiral leads to an increment $\Delta\theta = 2\pi/g = \sqrt{4\pi/P}$ between two adjacent levels of the spiral ($\Delta\phi = 2\pi$). The total arc length of the spiral [138] is

$$S = \int_0^\pi \sqrt{1 + g^2 \sin^2(\theta)} d\theta = 2\sqrt{1 + g^2} E\left(g/\sqrt{1 + g^2}\right), \quad (5.5)$$

where $E(\cdot)$ is the complete elliptic integral of the second kind. Asymptotically ($L \rightarrow \infty$) S approaches $2g$ so that the spiral is divided into segments of length $2g/P = \sqrt{4\pi/P} = \Delta\theta$. An exact distribution for arbitrary P can be achieved by numerical optimization as described in [140]. The proposed spiral schemes are shown in Fig. 5.3 for $N = M = 10$. It can be seen that all spiral paths are similar but that the sampling points (crosses) are at different locations. Please note that only the spiral according to [137] has points at the poles. Another possibility to compare the point distributions is to investigate the condition of the inverse problem. Fig. 5.4 shows the condition number of the problem ($N = M = 35$, dipole probe, $r = 10\lambda$) depending on oversampling L/J . According to this analysis, the spiral [137] requires the lowest number of samples for a stable reconstruction of the SMC. Furthermore, it can be seen that including points at the poles requires less oversampling. The exact spiral scheme [140] is slightly better than the approximate formulation [138]. Overall, the spiral according to Saff [137] performs best and requires roughly 20% oversampling for a stable reconstruction which is consistent with the oversampling ratios used in [23]. However, the required oversampling increases with N and the acceptable condition number might be selected according to the measurement case at hand. Since the performance of this spiral is best, this spiral scanning scheme is used in later chapter of this thesis and is shown for comparison in Fig. 5.1c. However, a comprehensive study of the behavior of the different spiral definitions and the used constant in (5.3) [137] might be a topic for further research.

Optimized polarization

As already highlighted, it is not required to measure with two or more probe polarization angles, although this leads, in general, to well-conditioned inverse problems. In measurement scenarios where the scan axis velocity is the limiting factor, it would be beneficial if the measurement path had to be scanned only once. Unfortunately, scanning with one fixed probe polarization angle as well as a continuously rotated polarization angle lead to ill-conditioned linear equation systems and can, thus, not be used. Consequently, the probe polarization angle has to be altered as previously shown in [141]. From a practical point of view, this seems to be awkward and indeed it is not obvious how to realize, for example, a different probe polarization angle at every measurement point. Rotation of the probe is expected to be too slow so that electronic switching seems to be required. An approach is to use a dual polarized probe and to excite both ports according to the desired polarization by a switching

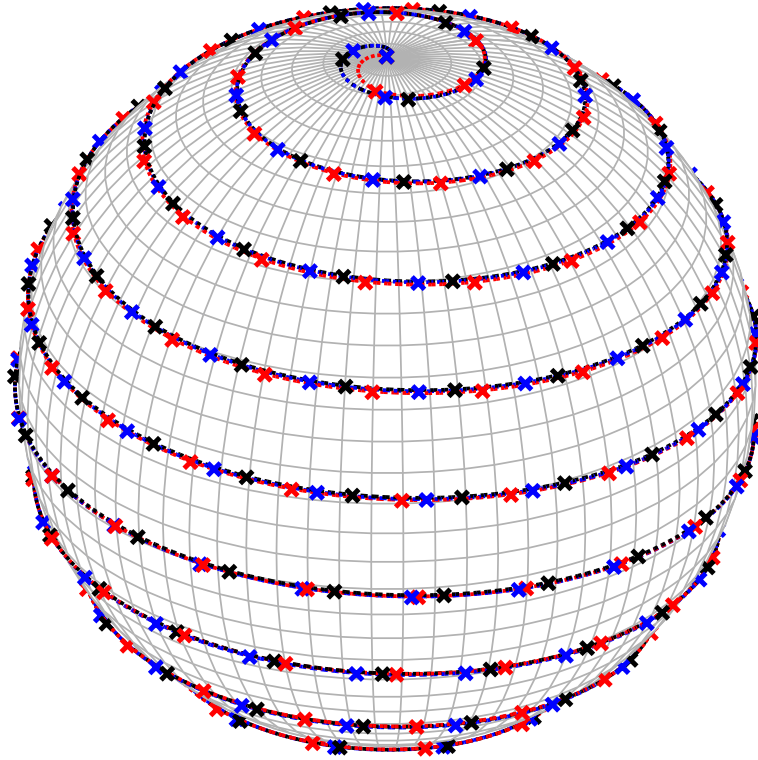


Figure 5.3: Spiral sampling point distributions ($N = M = 10$) with measurement path according to Saff [137] (red), Bauer [138] (black) and Koay [140] (blue).

network. However, in this case both probe ports could be simply switched to measure two polarization angles directly. Therefore, it must be stressed that this measurement scheme is only used for theoretical considerations since a dual polarized probe measurement system is equally fast. Nevertheless, the analysis in this thesis might stimulate some further research and investigation of possible realizations.

As shown in Fig. 5.5 using optimized polarization angles allows to reduce the required oversampling. Up until now, no deterministic way of optimizing the probe polarization angles has been found. For this reason, the optimized angles are determined by calculating the condition number for many polarization vectors where the angles at every measurement point are selected randomly. Fig. 5.6 shows the distribution of the condition numbers for 10^4 trials. The polarization vector with the lowest condition number is stored and selected for the measurement. Please note, that although the polarization vector contains random angles, it is equal for all measurements and has only to be calculated once for the parameter pair $(N, L/J)$. Furthermore, it should be noted that the pitch of the spiral is now lower because the number of locations is doubled ($P = L$) as visualized in Fig. 5.7. As a consequence, the distance between two adjacent points along the spiral path is smaller. This property is relevant for acquisition in continuous mode where the measurement is performed *on the fly* between two points.

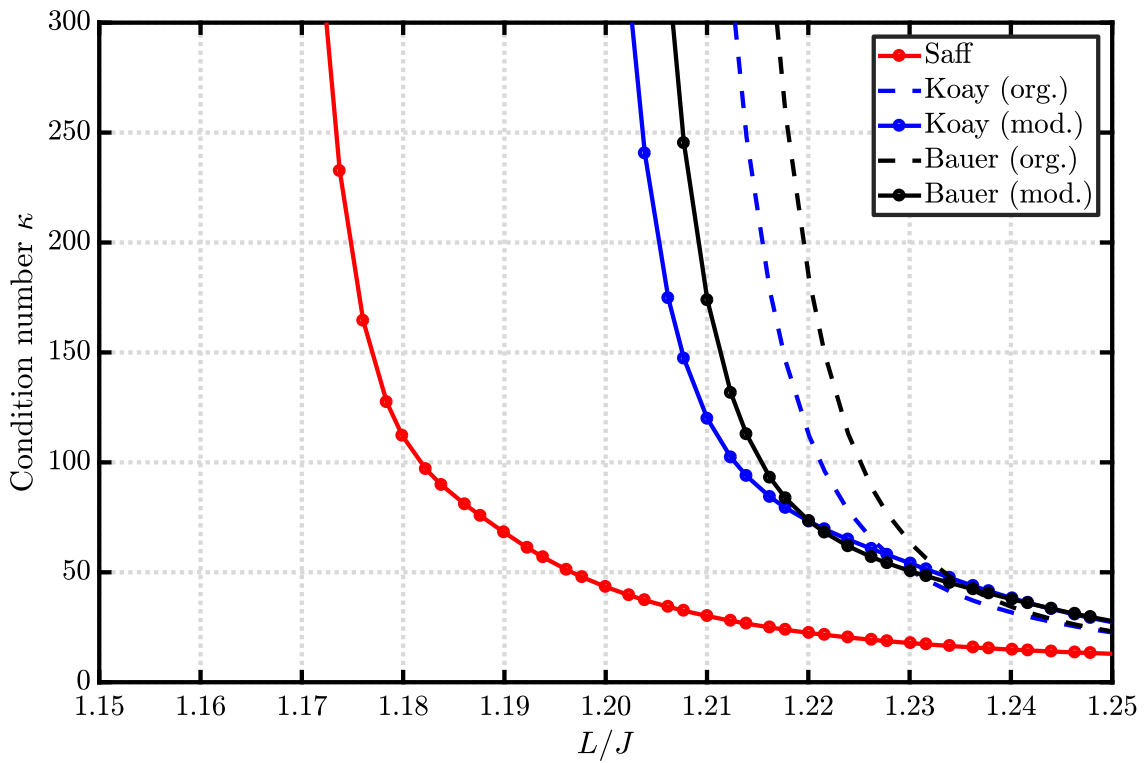


Figure 5.4: Condition number for spiral sampling point distributions ($N = M = 35$) according to Saff [137] (red), Bauer [138] (black) and Koay [140] (blue) depending on oversampling. Modified (mod.) schemes include points on poles.

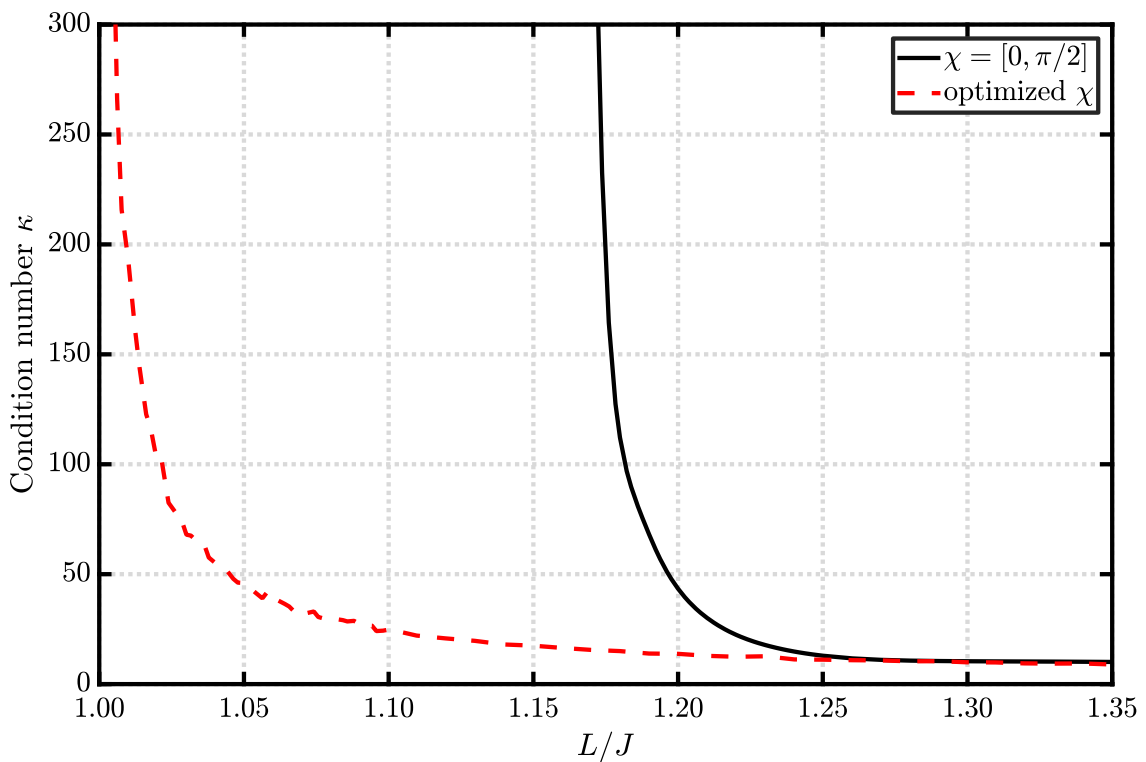


Figure 5.5: Condition number of the spherical wave expansion for spiral sampling point distributions ($N = M = 35$) with $\chi = [0, \pi/2]$ and optimized χ .

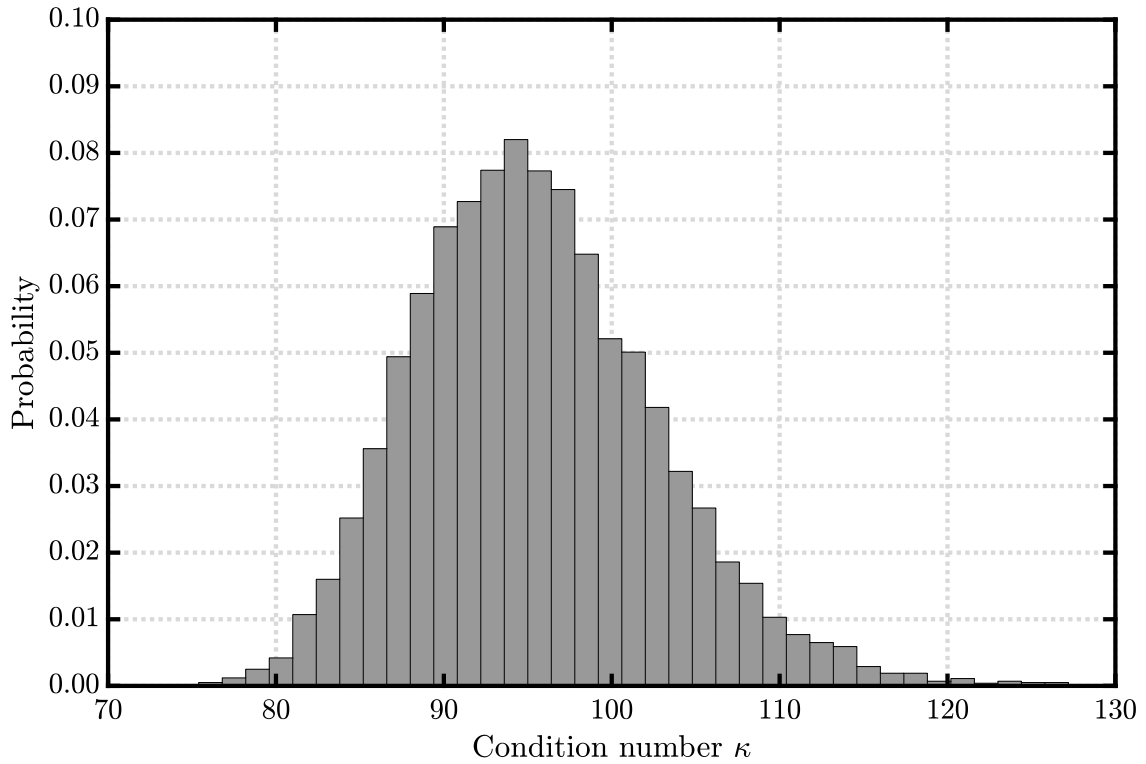


Figure 5.6: Condition number probability for a randomly distributed χ (10^4 trials, $L/J = 1.025$, $N = 35$).

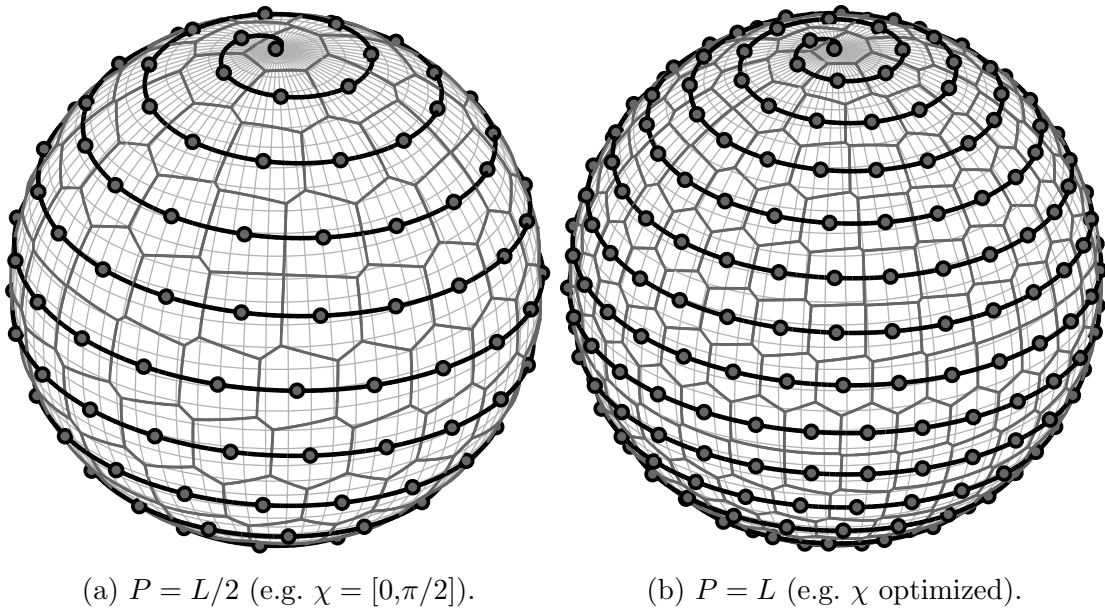


Figure 5.7: Spiral sampling point distributions ($N = M = 10$) with measurement path (solid black) and voronoi tessellation (gray cells) for spiral with two (a) and one (b) polarization measurement(s) at every location.

5.1.4 Maximum determinant

The problem of distributing points on a sphere is not only a problem in electromagnetics but also in many other disciplines such as math or geoscience. A good survey on popular point configurations has been published by Hardin et. al. [139]. In [139] it is pointed out that there is no unique set of points which is optimal in all cases. For this reason, different sets exist which have different properties and might be optimal for certain applications (e.g. numerical integration on the sphere). The spherical wave expansion of an electromagnetic field can be regarded as solving a linear equation system for the unknown SMC of the AUT. Therefore, the point set should be optimal in the sense that the determination of the SMC is stable which can be measured by the condition or the determinant of the matrix. In fact, maximizing the determinant by nonlinear optimization is easier than minimizing the condition number. Optimized point distributions for scalar spherical harmonics up to $N = 165$ are available from <http://web.maths.unsw.edu.au/~rsw/Sphere/Extremal/New/index.html> and are closely related to Fekete Points. Although the point locations are given with double precision, rounding to realistic position accuracies (e.g. 0.01°) does not change the condition number significantly. The point distribution for $N = 10$ is shown in Fig. 5.1d. In order to use the point distribution for vector fields two orthogonal probe angles at every measurement point are used. Since modes with index $n = 0$ only exist for scalar and not for vector spherical harmonics, this leads to a tiny oversampling of 2 samples. In measurement practice two additional samples can be regarded as an irrelevant oversampling. Unfortunately, it is not obvious which points are the least important ones and, therefore, reducing the number of samples by two is not a straightforward task. A possibility to find the two least important samples is to check the condition number for all possible new point sets which is, however, a combinatorial problem with $\binom{J+2}{2}$ possibilities which is not directly solvable in acceptable time. For this reason, one might reduce the point set by one location and both polarizations which is computationally less demanding with $\binom{(J+2)/2}{1}$ possibilities and beneficial from the measurement perspective. In an example for $N = 17$ the deleted point would be $(\theta, \phi) = (117.1^\circ, 153.7^\circ)$ and the condition number raises from 11 to 28. Thus, deleting one point from the point set leads to an increased condition number so that it would be better to adapt the nonlinear optimization routines for the vector case. In addition, including the case $M < N$ is also an issue for the future. Nevertheless, the condition number (point set including the two extra points) is low as shown in Fig. 5.8 for tested cases up to $N = 75$. In contrast to the other point configuration, the optimal scan path is not obvious and is in fact related to the traveling salesman problem known from combinatorial optimization. The approach used to generate the scan path in this thesis is related to a spiral scan from pole to pole. In contrast to spiral scanning, it is allowed to step one level down in θ but the values in ϕ are monotonously increasing. For this reason, the scan path requires θ -rotations in positive and negative direction which complicates the acquisition in continuous mode in the case of a positioning system with two rotational axes. From visual inspection of the scan path and comparison with the scan path length of equiangular sampling, it is concluded that the used approach performs reasonably good. Nevertheless, improvements might be possible but are not the focus of this thesis.

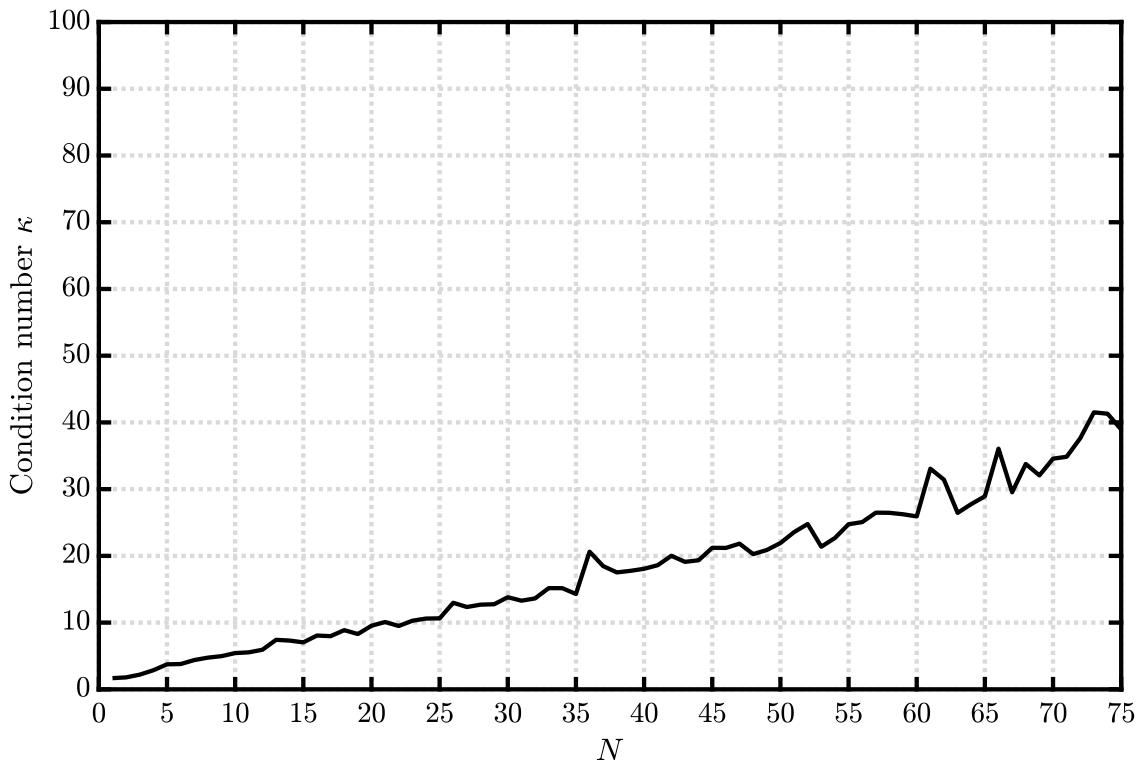


Figure 5.8: Condition number of the spherical wave expansion for maximum determinant sampling point distribution for different N .

In summary, deterministic point sets according to the number of spherical modes exist and allow stable reconstruction of the spherical mode coefficients from spherical near-field data. The non-linear optimization method could further be used to generate non-redundant point set in the case $M < N$ and to optimize the point distribution in the vector case (i.e. without the two additional samples for $n = 0$ in the scalar case).

5.1.5 Others

Besides the presented point configurations, many others exist (see e.g. [139]). They are (optimal) solutions for certain problems such as the equal area partitioning or the minimization of the potential energy. As stated in Section 5.1.4, finding the spherical wave expansion of an electromagnetic field can be regarded as solving a linear equation system for the unknown SMC of the AUT. The maximum determinant point distribution (Section 5.1.4) optimizes the stability and is, for this reason, used in this thesis. However, depending on the considered problem and desired optimization goal, other point distributions might be selected. Furthermore, it should be emphasized that interpolation methods are not investigated in this thesis because the used transformation algorithm allows arbitrary sampling point distributions. In addition, interpolation does not add information and is thus mainly used to accelerate the transformation time which is nowadays less critical. Field interpolation is also restricted to first order probe measurements which is a severe drawback. Overall, the presented point distributions are the most relevant distributions for general

Point distribution	theoretical L	L ($N = 35$)	L/J	κ	S (rad)
Equiangular	$2(N + 1)(2N + 1)$	5328	2.057	8	304
Thinned equiangular	$\frac{2}{\pi}2(N + 1)(2N + 1)$	3264	1.260	2	291
Spiral (both pol.)	-	3108	1.200	7	284
Spiral (opt. pol.)	-	2654	1.025	76	185
Max. determinant	$2N(N + 2)$	2592	1.001	7	330

Table 5.1: Comparison of different sampling point distributions.

spherical antenna measurements. Nevertheless, the methodology of the analysis can be used similarly for other point distribution.

5.1.6 Comparison

In the following, the different point distributions are compared with respect to number of points L , oversampling ratio L/J , measurement path length and measurement acquisition time in step and continuous scan mode. The theoretical and practical ($N = 35$) number of points are stated in Table 5.1. For spiral scanning, there is no general rule for L so that an oversampling L/J of 1.2 was chosen for a spiral scheme with two orthogonal polarization and 1.025 with optimized polarization angles. The factor $2/\pi$ in the case of thinned equiangular is the mean value of $\sin(\theta)$ in the interval $0 \leq \theta \leq \pi$ [21]. It should be mentioned that for both equiangular point distributions the practical number of points are slightly higher because it is common to define the angular step so that the number measurement points is even in the open interval $[0, 2\pi)$ and that measurement points exist for $\theta = 0$ and $\theta = \pi$. Consequently, the number of samples are $2(N + 2)(2N + 2)$ in the equiangular case. Please also note, that the maximum determinant sampling distribution contains the two extra samples. In summary, equiangular sampling causes an oversampling of approximately factor 2 which can be reduced by the presented alternative point distributions. As already discussed in the previous section, the condition number stays low except for the case of the spiral with optimized polarization. However, a higher oversampling would lower the condition number but would increase the number of points. The condition numbers are calculated for the measurement scenario of a BTS antenna ($N = M = 35$, $r \approx 2$ m, $f = 2400$ MHz, HOP with $\mu = \nu = 17$) used in the following Section 5.2.

Spatial aliasing

The condition number is an important key value because it describes how stable the modes up to the considered N can be determined from the field values. A low condition number is thus a prerequisite for an accurate spherical wave expansion. However, this property is not sufficient because more sources of error might affect a spherical near-field measurement. According to Section 2.1, the radiated field by an AUT is quasi-bandlimited according to its electrical size kr_0 and can, for this reason, be described by a limited number of SMC. However, a mode truncation error exist. On the one hand, a certain amount of radiated power is truncated which is

typically reduced to a level comparable to the measurement noise floor by using an exceeded bandwidth (2.13). On the other hand, higher order modes ($n > N$) also affect the spherical mode spectrum for $n \leq N$ by spatial aliasing. The spatial aliasing error can be controlled by oversampling and it can be expected that non-redundant sampling point distributions are more susceptible for this error compared to inherently oversampled point distributions. The issue has, to the best of my knowledge, not been addressed for spherical near-field antenna measurements. The reason might be that in usual measurement scenarios the spatial aliasing error is comparable small and has, therefore, not been studied. In fact the power in higher order modes is typically low because the AUT mode power decays exponentially after the bandlimit and room scattering is suppressed by absorbing materials. However, in the evaluation of new sampling point distributions the effect might be important because spatial aliasing depends on location of the sampling points. In general, literature about spatial aliasing for spherical harmonics is limited but is for example discussed in the context of spherical microphone array design [142] where spatial aliasing is a severe problem. Though acoustic fields are different from electromagnetic field, many research methods and results are comparable. Similarly to [142], the effect of aliasing is investigated by simulating a near field of a single spherical mode with $n > N$ and $|M| \leq n$ for the desired point configuration and the subsequent spherical wave expansion (SWE). If the field of the higher order mode would be orthogonal to the transformation basis, the result would be zero and no aliasing error would exist. However, the point configurations are designed in such a way that only modes up to N are orthogonal to each other and, consequently, sampled higher order modes are, in general, not orthogonal. For this reason, the aliasing error in the determined SMC is non zero. Fig. 5.9 shows the total power of the SMC with $n \leq N = 17$ for specific higher order modes $n > N$ and $|M| \leq n$ for all investigated point configurations. It can be seen that for equiangular sampling (twice oversampled) the effect of higher order modes is smaller compared to other point configurations. The thinned equiangular point distribution has a similar pattern but with higher aliasing power. From that comparison, it can be concluded that the additional samples at the poles allows to distinguish modes with larger m in the dark blue region. Furthermore, it can be seen that spiral scanning with both polarization is susceptible for aliasing from modes with low order m and especially $m = \pm 1$. Since only modes with order $m = \pm 1$ contribute to the field at the poles, this is another argument why the sampling density at the poles is often increased [23]. Spiral scanning with optimized polarization shows poor aliasing properties. Please note, that the power of the aliasing spectrum is larger than the power of the higher order mode. This power amplification might be surprising but spherical harmonic functions are more complex than plane waves and it is difficult to derive analytic functions for the spatial aliasing error [142]. It will be shown later, that it depends on the measurement setup if the error is significant or not. The aliasing effect for maximum determinant sampling is almost uniformly distributed although the values close to the bandlimit are higher. It needs to be stressed that the number of samples in the examples is not equal. For example, maximum determinant sampling with the same number of points as equiangular sampling allows to remove the aliasing error for modes up to $N = 25$ completely. Consequently, the robustness of equiangular

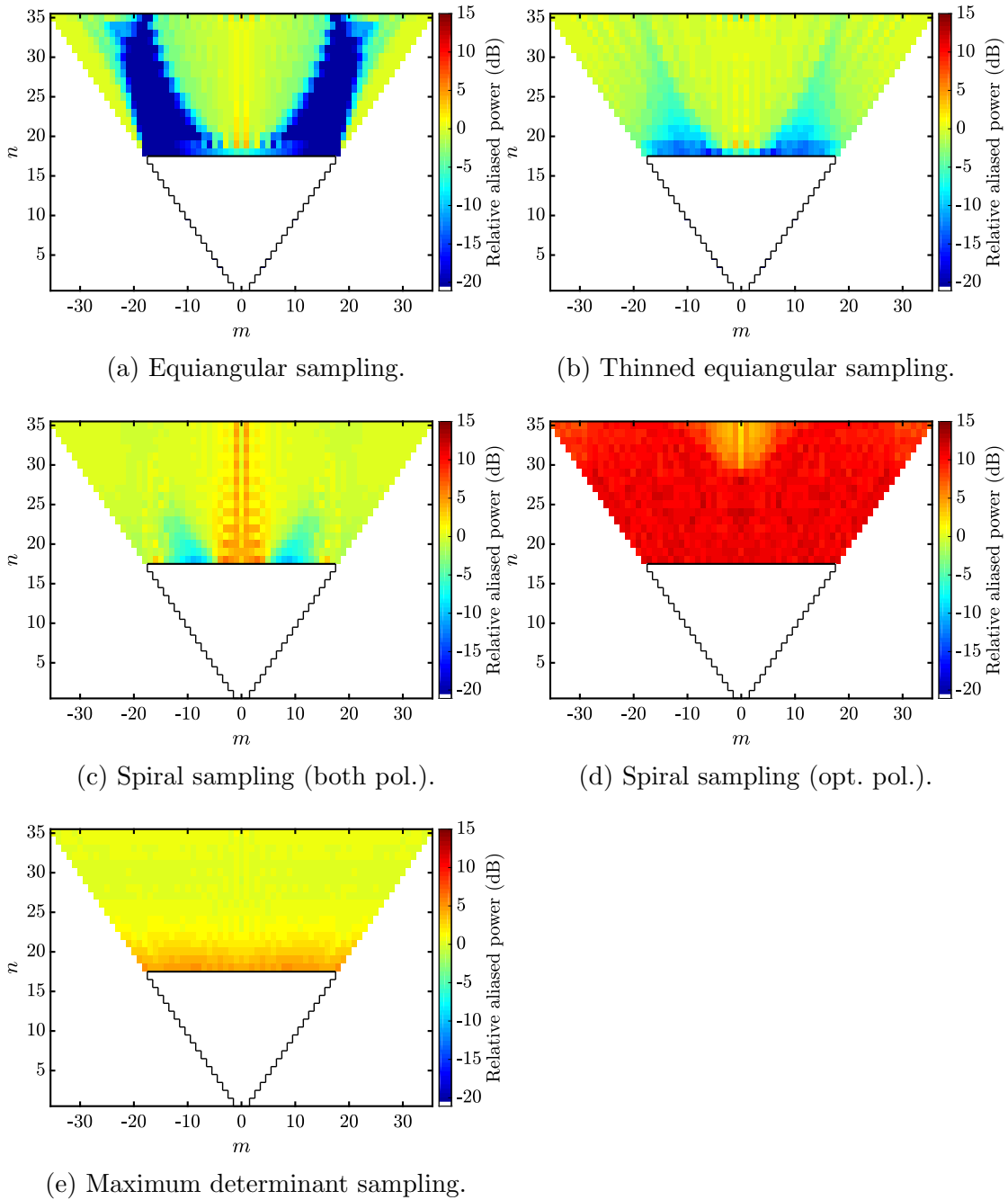


Figure 5.9: Relative mode power aliasing from higher order modes into lower order modes ($N = M = 17$) for different point distributions.

sampling is mainly due to the inherent oversampling and not due to the sampling point distribution.

In summary, spatial aliasing in spherical near-field antenna measurements is, up until now, a not comprehensively studied research area. It is an interesting open research question if spherical anti-aliasing filter [142] can equally be used for electromagnetic vector fields.

Scan path length

Regarding the scan path length S in Table 5.1 (page 55), it is interesting that the number of samples is not directly linked with the scan path length. The path length is calculated on the unit sphere by summation of the shortest paths between adjacent points (geodesic). In the case of equiangular sampling the value 4π has been added in order to include the required rotation at the poles where the path length is zero. This is the main reason for the path length difference between equiangular and thinned equiangular sampling. The spiral scan with two polarization angles reduces the path length only by approximately 7% although the number of points are reduced by around 40%. In addition, the relative path length reduction decreases with increasing N and is for example only 3% for $N = 119$. This is due to the fact, that the distance between two constant latitude rings for equiangular sampling reduces which reduces the influence of the stepping between two levels which is inherently avoided in the spiral scheme. As already pointed out, the points are always distributed over the complete sphere and, consequently, mainly the point separation is increased by spiral sampling. However, in the case of optimized polarization angles the path length is significantly reduced because the spiral path has to be scanned only once. Due to the different spiral pitch (see Fig. 5.7) the path length is not halved compared to spiral scan with two polarization angles as one might expect. Finally, the scan path for maximum determinant sampling is the longest although it has the lowest number of samples. On the one hand side, the used scanning path is not optimal. On the other hand and more important is the fact that the values for θ and ϕ along the path are not monotone (see Fig. 5.1d) which increases the path length.

It has to be mentioned that the investigated scanning scheme is a ϕ -scanning scheme [21] (i.e. $0^\circ \leq \phi < 360^\circ$, $0^\circ \leq \theta \leq 180^\circ$) which is naturally suited for thinned equiangular and spiral scanning. However, a θ -scanning scheme (i.e. $0^\circ \leq \phi < 180^\circ$, $0^\circ \leq \theta < 360^\circ$) might be equally considered for equiangular scanning. The scanning scheme is less important for step mode acquisition but is relevant for a acquisition in continuous mode because it affects the scan path length. Besides, the selected scheme also affects some measurement uncertainty terms such as peak directivity [143]. Throughout this thesis a ϕ -scanning scheme is used for different reasons. First, it is well-suited for all measurement grids and, thus, allows a good comparison. Second, later measurements are performed with a roll-over-azimuth measurement system where the AUT is mounted on the roll (ϕ) axis which allows faster movements and requires less settle time compared to the azimuth positioner. Third, the measurements have to be acquired in step mode due to limitations of the soft- and hardware so that the effect of the scan scheme is less relevant. Finally, the measurement uncertainty assessment is focused on a comparison between different grids and it is beneficial to avoid additional differences due to the scanning scheme. However, a detailed investigation might be performed in the future. It might be for example investigated how the uncertainties are affected by $+\phi$ -scanning for one polarization and a $-\phi$ -scanning (i.e. $0^\circ \leq \phi < 360^\circ$, $-180^\circ \leq \theta \leq 0^\circ$) for the second polarization. In conclusion, it is possible to reduce the number of measurement points but this does not generally reduce the scan path length. This is an important result because depending on the acquisition mode the one or the other parameter dominates the total acquisition time.

Acquisition time in step mode

In step mode acquisition the measurement system (probe and AUT) stands still at each measurement point. This mode is typically used in cases where it is important to measure all configurations (e.g. frequencies) at the exact same location (e.g. determination of broadband impulse response over angle) or where an accurate continuous movement and triggering of the scan axis is not possible. The measurement time is determined by the time to reach the new measurement position, the settling time of the positioners and the sweep time. The acquisition time might thus be estimated by

$$\begin{aligned} T_{\text{step}} &= \sum_{l=1}^L t_{l,\text{step}} = \sum_{l=1}^L (t_{l,\text{move}} + t_{l,\text{settle}} + t_{l,\text{sweep}}) \\ &= \sum_{l=1}^L t_{l,\text{move}} + L(t_{\text{settle}} + t_{\text{sweep}}) = \sum_{l=1}^L t_{l,\text{move}} + Lt_{\text{point}} \end{aligned} \quad (5.6)$$

where the individual times depend on the exact measurement configuration. Nevertheless, this simple formula highlights that the acquisition time is determined by a term related to the scan path and a term which linearly depend on the number of measurement points L . In order to investigate the acquisition time of the different scan schemes, two different positioning systems are evaluated:

- A: Roll-over-azimuth positioning system with equal axis rotation velocity.
- B: Robot arm positioning system with constant track velocity.

For system A, the total path length between two points on the unit sphere with $\Delta\theta = \theta_2 - \theta_1$ and $\Delta\phi = \phi_2 - \phi_1$ is

$$\Delta S_A(\Delta\theta, \Delta\phi) = s_A(\Delta\theta, \Delta\phi) = \Delta\theta + \Delta\phi \quad (5.7)$$

while for system B

$$s_B(\theta_1, \theta_2, \Delta\phi) = \cos^{-1}(\cos(\theta_1)\cos(\theta_2) + \sin(\theta_1)\sin(\theta_2)\cos(\Delta\phi)). \quad (5.8)$$

The time to move to the next measurement point can be calculated by

$$t_{l,\text{move},A} = \frac{\max(\Delta\theta, \Delta\phi)}{\bar{v}_A} \quad \text{and} \quad t_{l,\text{move},B} = \frac{s_B}{\bar{v}_B} \quad (5.9)$$

where $\bar{v}_{A,B}$ is the mean velocity in the segment l and depends on the maximum velocity $v_{\max,A,B}$ and acceleration $a_{\max,A,B}$. It is assumed that the θ and ϕ axis can be rotated simultaneously (otherwise $t_{l,\text{move},A} = t_{l,\text{move},\theta,A} + t_{l,\text{move},\phi,A}$ and $t_{l,\text{settle}} = t_{l,\text{settle},\theta} + t_{l,\text{settle},\phi}$). The model can also be adapted to include different velocities for θ and ϕ though this is not done here. Of course, these formulas are not suitable for exact acquisition time calculation of a specific measurement system. However, the simplification reduces the complexity in order to focus on the main contributions to the acquisition time.

According to the presented acquisition model the acquisition times for the later used measurement scenario ($N = M = 35$, $v_{\max,(A,B)} = a_{\max,(A,B)} = 20^\circ/\text{s}$, $t_{\text{point}} = 3\text{ s}$)

Point distribution	L		$T_{\text{step,A}}$		S_A	
	abs.	rel. (%)	abs. (h)	rel. (%)	abs. (rad)	rel. (%)
Equiangular	5328	100.0	5.9	100.0	467.9	100.0
Thinned equiangular	3264	61.3	3.8	64.4	443.1	94.7
Spiral (both pol.)	3108	58.3	3.7	61.7	443.0	94.7
Spiral (opt. pol.)	2654	49.8	3.0	50.7	289.0	61.8
Max. determinant	2592	48.6	3.1	53.0	443.4	94.8

Table 5.2: Estimated acquisition times in step mode for system A (roll-over-azimuth positioner) with $N = M = 35$, $v_{\text{max,A}} = a_{\text{max,A}} = 20^\circ/\text{s}$, $t_{\text{point}} = 3\text{ s}$.

Point distribution	L		$T_{\text{step,B}}$		S_B	
	abs.	rel. (%)	abs. (h)	rel. (%)	abs. (rad)	rel. (%)
Equiangular	5328	100.0	5.6	100.0	319.4	100.0
Thinned equiangular	3264	61.3	3.6	64.7	293.3	91.9
Spiral (both pol.)	3108	58.3	3.5	61.8	286.5	89.7
Spiral (opt. pol.)	2654	49.8	2.9	51.1	185.3	58.0
Max. determinant	2592	48.6	3.0	53.7	332.2	104.0

Table 5.3: Estimated acquisition times in step mode for system B (robot arm positioning system) with $N = M = 35$, $v_{\text{max,B}} = a_{\text{max,B}} = 20^\circ/\text{s}$, $t_{\text{point}} = 3\text{ s}$.

are estimated for different point distributions and are listed in Table 5.2 for system A and in Table 5.3 for system B. It can be seen that the relative measurement time T_{step} correlates with the relative number of measurement points L . The path length has a minor effect which, however, is noticeable by the fact that the estimated acquisition time for spiral scanning with optimized polarization is lower as for maximum determinant sampling although it has a higher number of samples. The effect of the path length depends on t_{point} and v_{max} . Fig. 5.10 and Fig. 5.11 show the dependency of the relative measurement time on the time t_{point} for measurement system A and B, respectively. Both systems have a similar behavior. For small t_{point} , the relative acquisition time is strongly influenced by the relative path length while the value approaches the relative number of points for large t_{point} . The maximum velocity $v_{\text{max,A}}$ determines how fast the relative acquisition time approaches the relative number of points with increasing t_{point} . In typical measurement configurations, t_{point} is comparably large and, thus, the relative acquisition time can be assumed to be equal to the number of measurement points in step mode acquisition. In summary, reducing the acquisition time in step mode is mainly achieved by reduction of required measurement points. For this reason, maximum determinant sampling can be regarded as the best possible option. Since the long acquisition times in step mode are a severe disadvantage, acceleration of 40% to 50% as achieved by the presented point distributions are a significant improvement.

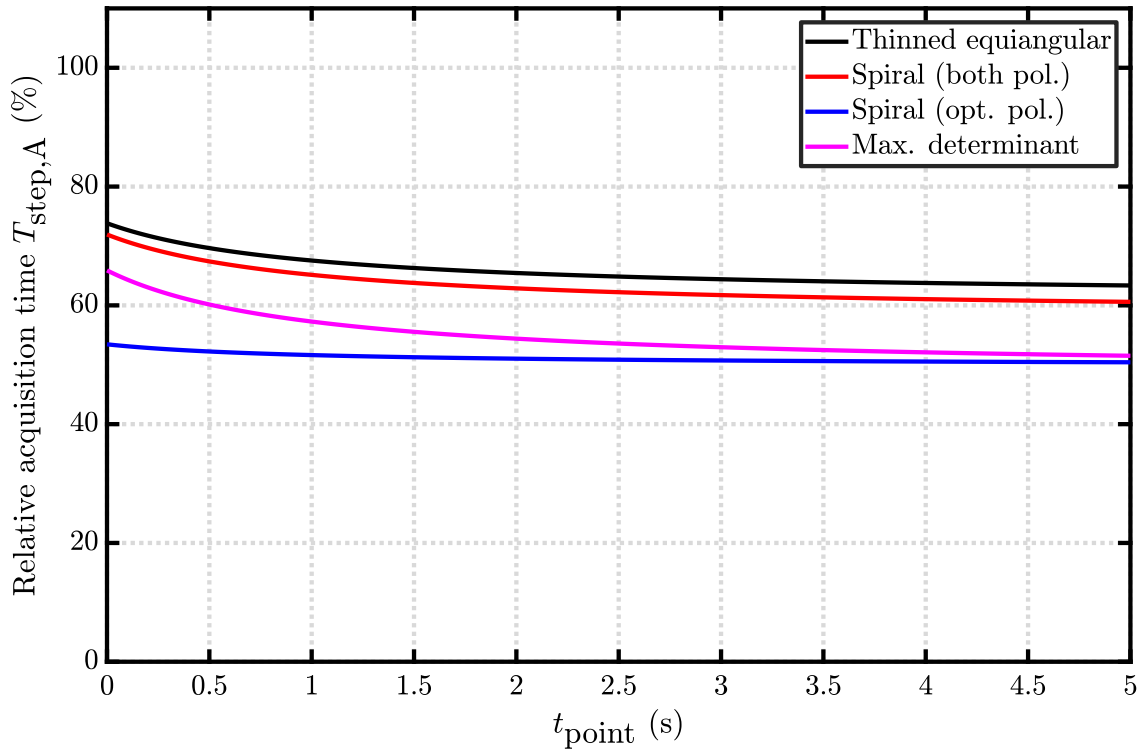


Figure 5.10: Relative acquisition times in step mode for system A (roll-over-azimuth positioner) over t_{point} with $N = M = 35$, $v_{\text{max,A}} = a_{\text{max,A}} = 20^\circ/\text{s}$.

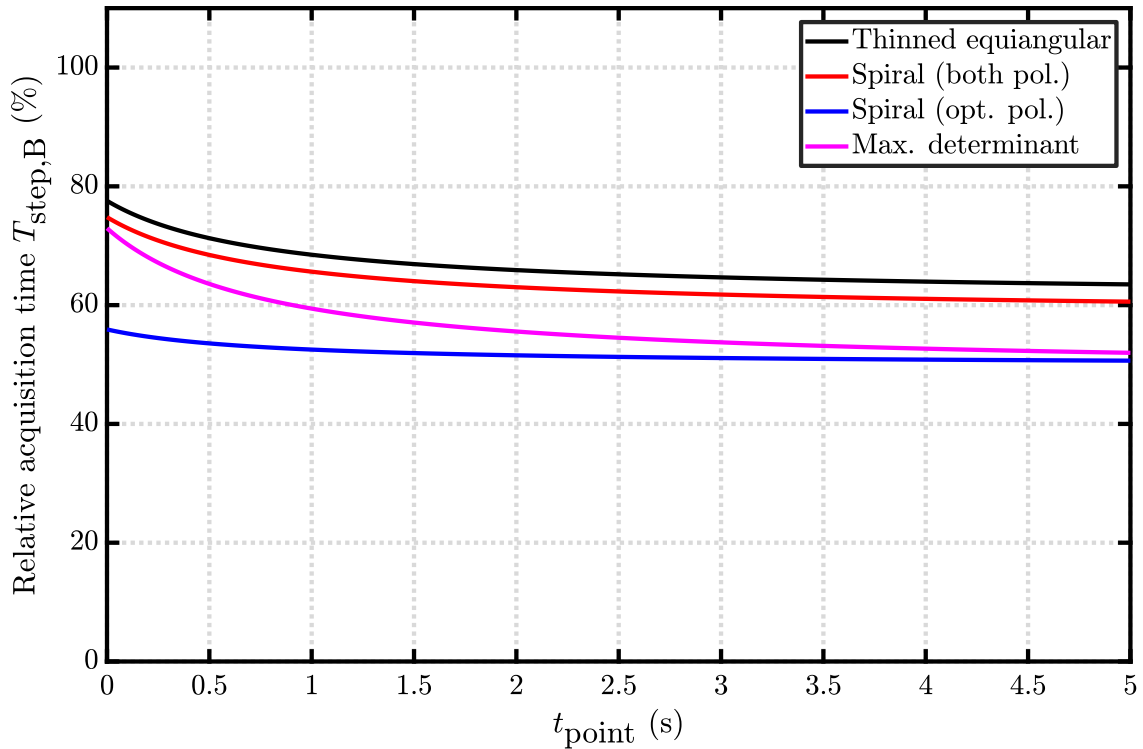


Figure 5.11: Relative acquisition times in step mode for system B (robot arm positioning system) over t_{point} with $N = M = 35$, $v_{\text{max,B}} = a_{\text{max,B}} = 20^\circ/\text{s}$.

Acquisition time in continuous mode

In contrast to step mode acquisition, the scan axes are never stopped in continuous mode acquisition and the acquisition is performed *on the fly*. Consequently, the measurement time is related to the path length of the acquisition path and the velocity along that path. As already shown, the total path lengths are similar for different point distributions because the points are always distributed over the complete sphere. The velocity along the path depends on the length of the segment and the time to measure all required configurations (e.g. frequencies, ports, etc.) but cannot exceed the maximum axis velocity. The acquisition time can thus be approximated by

$$T_{\text{cont}} = \sum_{l=1}^L t_{l,\text{cont}} = \sum_{l=1}^L \max\left(\frac{s_l}{v_{\text{max}}}, t_{\text{sweep}}\right). \quad (5.10)$$

This is a simplification because it neglects time for acceleration and deceleration as well as additional blank times. Nevertheless, some general results can be obtained. The analysis is carried out for the same measurement systems as for step mode acquisition. According to the presented acquisition model the acquisition times for the later used measurement scenario ($N = M = 35$, $v_{\text{max},(A,B)} = 20^\circ/\text{s}$, $t_{\text{sweep}} = 150 \text{ ms}$) are estimated for different point distributions and are listed in Table 5.4 for system A and in Table 5.5 for system B. In the case of a roll-over-azimuth measurement system (Table 5.4), the relative acquisition time is equal to the relative path length. However, if the sweep time gets larger the relative reduction increases as shown in Fig. 5.12 due to larger point separations. Starting from $t_{\text{sweep}} = 250 \text{ ms} = s_l/v_{\text{max},A}$ the absolute measurement time of equiangular sampling (i.e. reference) grows faster as for the other point distributions. Hence, t_{sweep} of the cut-off decreases with smaller point separation (i.e. with increasing N) and with an increased maximum velocity $v_{\text{max},A}$. The slight increase in relative measurement time for spiral sampling with optimized polarization around $t_{\text{sweep}} = 250 \text{ ms}$ is caused by the fact that the measurement spacing is less compared to the spiral with two polarizations (see also Section 5.1.3). Therefore, the scan velocity has to be reduced earlier compared to other grids (see Fig. 5.14). But the effect of a scan velocity reduction on equiangular sampling is larger than on the spiral and, consequently, the relative measurement time falls again. The acquisition times for maximum determinant sampling are not stated because they are certainly larger than for equiangular sampling and cannot be estimated with the simplified model. The reason for this is that the chosen scan path is not well-suited for a roll-over-azimuth positioner because it requires positive and negative rotations in θ . Thus, the axis has to stop which increases the acquisition time. If all θ values are sorted in descending order, the number of rotations in ϕ would be either large or would require rotations in positive and negative directions. The scan path might be optimized numerically but this is a complex problem related to the travelling salesman problem. Please note also that the absolute acquisition times are significantly shorter compared to step mode acquisition.

In the case of a robot arm measurement system (Table 5.5) the relative acquisition time is lower than the relative path length because the point distance s_B (5.8) is shorter at the poles compared to the equator. For this reason, a larger point

Point distribution	L		$T_{\text{cont,A}}$		S_A	
	abs.	rel. (%)	abs. (min)	rel. (%)	abs. (rad)	rel. (%)
Equiangular	5328	100.0	22	100.0	467.9	100.0
Thinned equiangular	3264	61.3	21	94.7	443.1	94.7
Spiral (both pol.)	3108	58.3	21	94.7	443.0	94.7
Spiral (opt. pol.)	2654	49.8	13	61.8	289.0	61.8
Max. determinant	2592	48.6	-	-	443.4	94.8

Table 5.4: Estimated acquisition times in continuous mode for system A (roll-over-azimuth positioner) with $N = M = 35$, $v_{\text{max,A}} = 20^\circ/\text{s}$, $t_{\text{sweep}} = 150$ ms.

Point distribution	L		$T_{\text{cont,B}}$		S_B	
	abs.	rel. (%)	abs. (min)	rel. (%)	abs. (rad)	rel. (%)
Equiangular	5328	100.0	17	100.0	319.4	100.0
Thinned equiangular	3264	61.3	14	80.4	293.3	91.9
Spiral (both pol.)	3108	58.3	13	78.5	286.5	89.7
Spiral (opt. pol.)	2654	49.8	8	50.8	185.3	58.0
Max. determinant	2592	48.6	15	91.0	332.2	104.0

Table 5.5: Estimated acquisition times in continuous mode for system B (robot arm positioning system) with $N = M = 35$, $v_{\text{max,B}} = 20^\circ/\text{s}$, $t_{\text{sweep}} = 150$ ms.

separation is more important as can be also seen in Fig. 5.13. In order to explain the curves, it is useful to look at the total measurement times displayed in Fig. 5.15. Except for the equiangular grid, the measurement times are constant up to a certain sweep-time and start to increase afterward. For this reason, part of the relative measurement time reduction in Fig. 5.13 is explained by an increased acquisition time of the reference (i.e. equiangular) while the convergence level is defined by the number of measurement points. Though the acquisition time reduction is larger, the absolute measurement time increases (increased sweep times are not desirable). In contrast to step mode acquisition, maximum determinant sampling performs worst in this example because the scan path length is even increased compared to equiangular sampling. This result shows that reducing the number of points is not the main goal for fast acquisition in continuous mode.

In most measurement configurations, t_{sweep} is comparably small and, thus, the allowed axis speed is the limiting factor. In this case, the improvements of the proposed sampling grids compared to an equiangular grid in a roll-over-azimuth are around 5% if the more theoretical case of a spiral with optimized polarization is excluded. Considering the robot arm measurement system, the improvements are higher, although, not as high as for step mode acquisition. Independent of the measurement system, an optimized point configuration reduces the acquisition time in cases where the sweep time is the limiting factor and the larger point separation can be exploited by faster scan velocities.

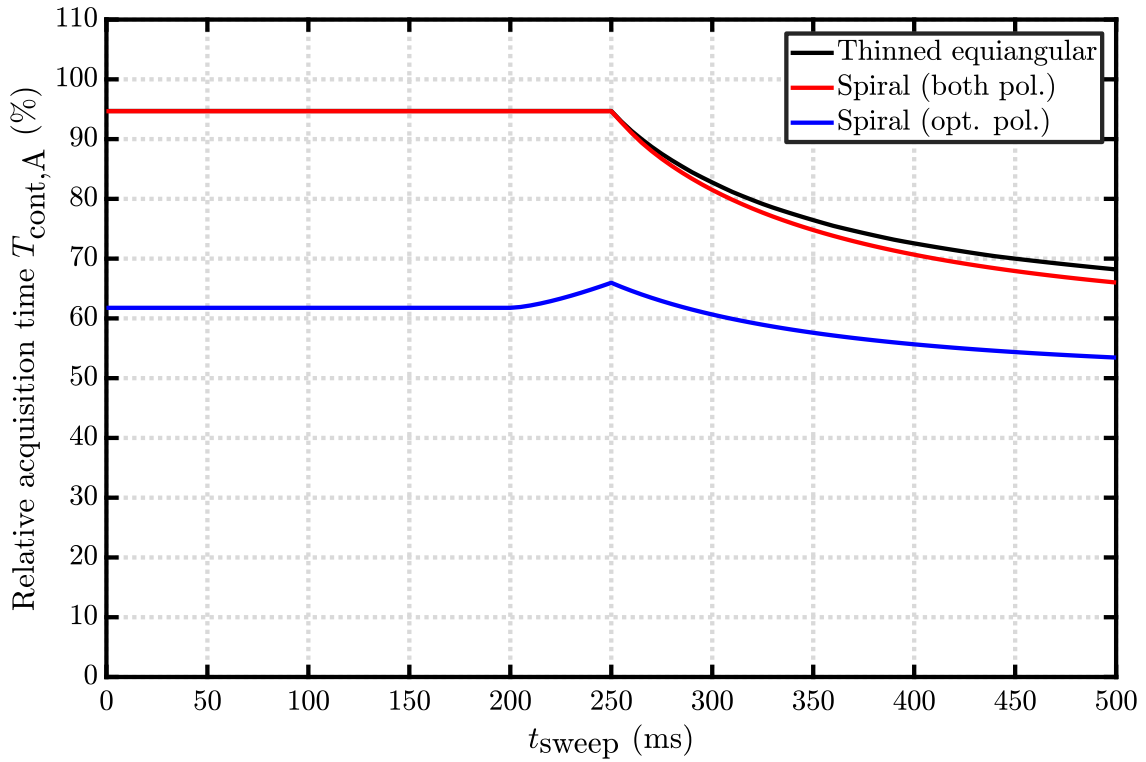


Figure 5.12: Relative acquisition times in continuous mode for system A (roll-over-azimuth positioner) over t_{sweep} with $N = M = 35$, $v_{\text{max},A} = 20^\circ/\text{s}$.

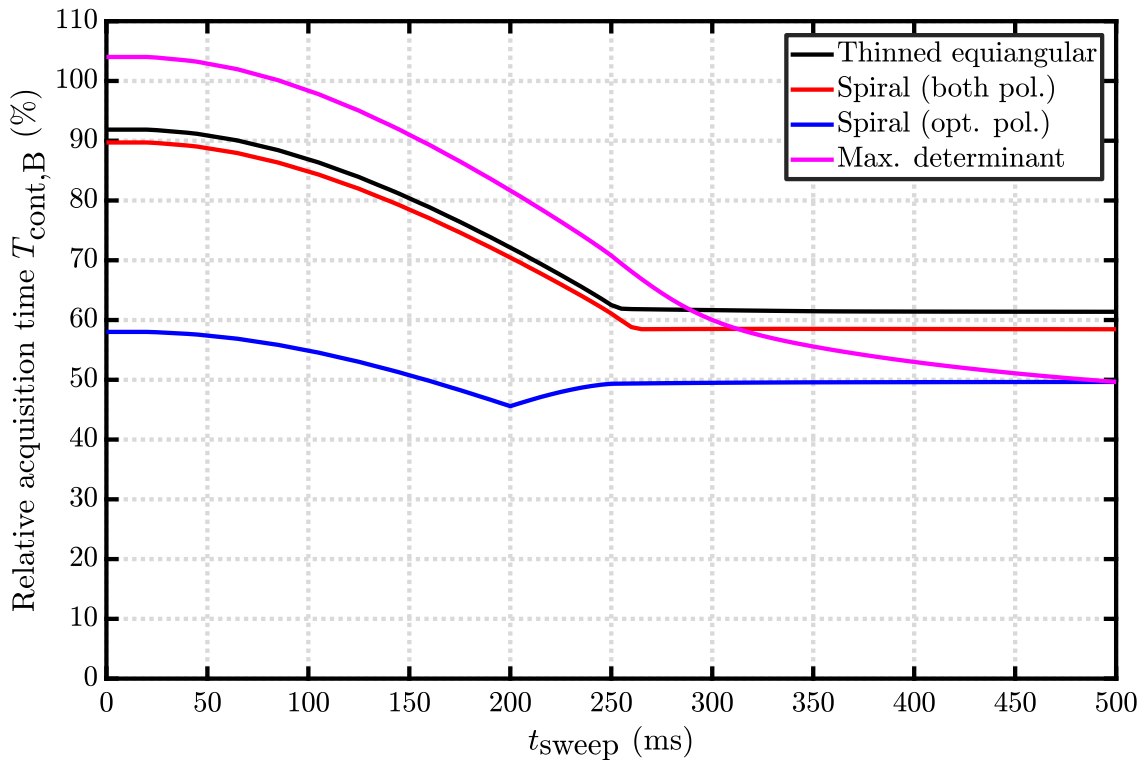


Figure 5.13: Relative acquisition times in continuous mode for system B (robot arm positioning system) over t_{sweep} with $N = M = 35$, $v_{\text{max},B} = 20^\circ/\text{s}$.

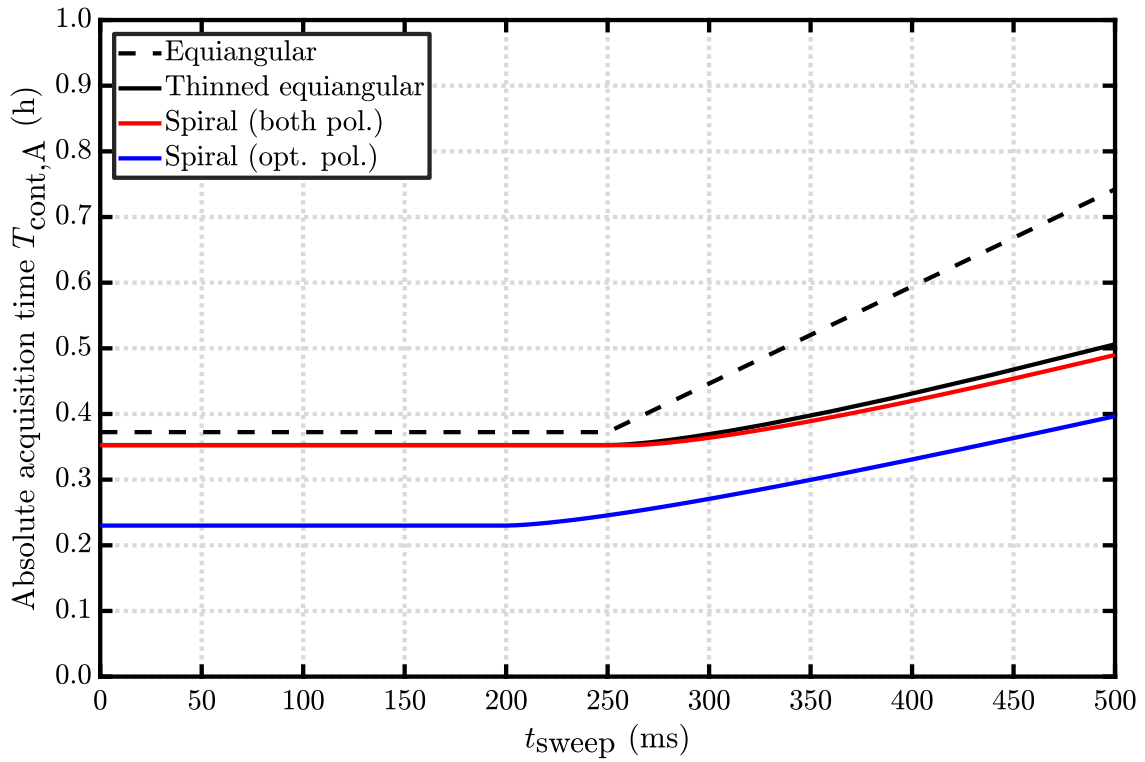


Figure 5.14: Absolute acquisition time for system A (roll-over-azimuth positioner) over t_{sweep} with $N = M = 35$, $v_{\text{max},A} = 20^\circ/\text{s}$.

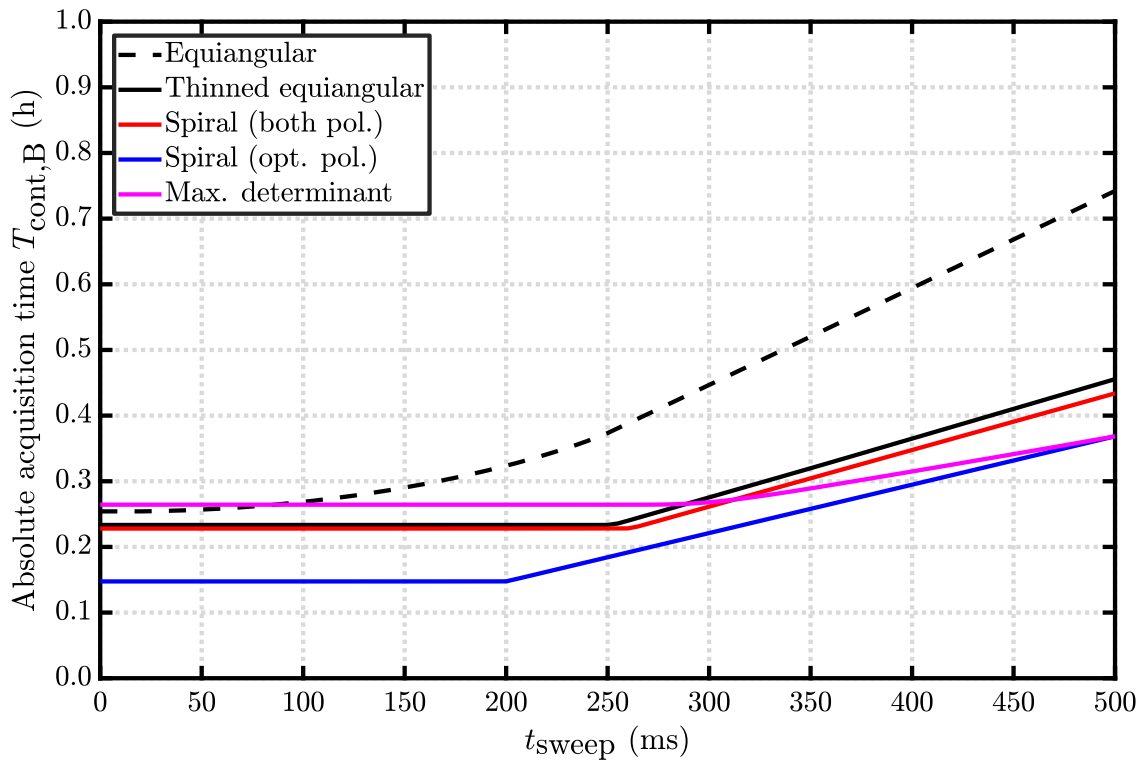


Figure 5.15: Absolute acquisition times in continuous mode for system B (robot arm positioning system) over t_{sweep} with $N = M = 35$, $v_{\text{max},B} = 20^\circ/\text{s}$.

However, this requires accurate and flexible velocity control which is, up until now, not standard for spherical near-field (SNF) measurement setups. Furthermore, thinned equiangular sampling performs almost as well as spiral scanning but has the benefit that it is easier to realize in most measurement ranges and, in addition, the transformation algorithm is numerically more efficient.

In summary, reducing the acquisition time in continuous mode is mainly achieved by reduction of scan path length. However, this is not simply achieved by measurement point reduction and the presented results show that the reduction of the scan path length compared to equiangular sampling is not as high as the possible reduction of measurement points. More acquisition time is saved if the sweep-time is large and point separation is the limiting factor. Although the relative acquisition time reduction is not as large as for step mode acquisition, the acquisition time is reduced. It must be stressed that accelerating measurements in continuous mode is a complex, interdisciplinary task and further research is required to optimize the scan path in conjunction with position triggering and axes control.

5.2 Measurements

It can be concluded from the previous Section 5.1 that, in general, different point configurations can be used for spherical near-field antenna measurements. According to the condition of the inverse problem all point configurations allow a stable determination of the SMC of an AUT. However, besides noise, more sources of error such as aliasing exist in a spherical near-field measurement [10]. In order to evaluate the total performance of the proposed grids, measurements were performed including a complete uncertainty budget calculation (details in Section 7.1).

The used test object is a typical BTS antenna operating in the frequency range from 1710 MHz to 2690 MHz with adjustable electrical tilt. The details are summarized in Appendix B.1. The analysis is performed for the key parameter directivity (D), half-power beam width (HPBW), first sidelobe level (FSL) and angle of the first sidelobe (FSLA) in the vertical cut. The vertical radiation pattern cut of the reference field is shown in Fig. 5.16 and the tilting (-12°) of the pattern is clearly seen. The reference pattern has been calculated by averaging 50 different measurements which were acquired during the measurement campaign. The antenna has been measured in the SNF measurement chamber of the IHF which is shown in Fig. 5.17 and consist of a roll-over-azimuth measurement system with a measurement radius of approximately 2 m. A double ridged broadband horn antenna (SH800) is used as measurement probe. A complete specification of the chamber including the electrical subsystem is given in Appendix A. According to Section 5.1, five different point configurations have been tested. Due to a limited position accuracy of the axes, the sampling point positions are rounded to a precision of 0.01° . The acquisition is performed in step mode and with ϕ -scanning. The data for the spiral scanning with optimized polarization has been derived from a measurement with two orthogonal polarizations by combination. The effect of the chosen optimized polarization vector on the calculated far field can be easily investigated because both orthogonal polarizations have been measured. Fig. 5.18 shows the pattern variation for the three polarization vectors with the lowest condition number. The used polarization vector

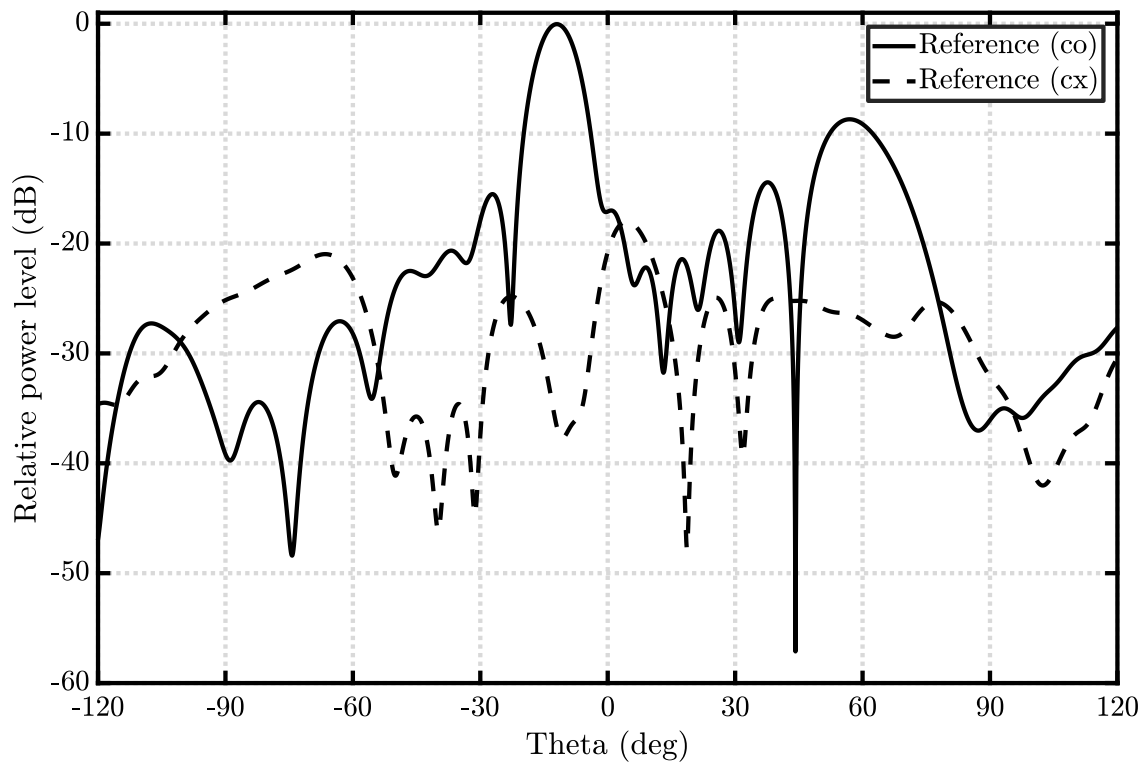


Figure 5.16: BTS antenna reference vertical far-field pattern cut.



Figure 5.17: IHF SNF measurement chamber.

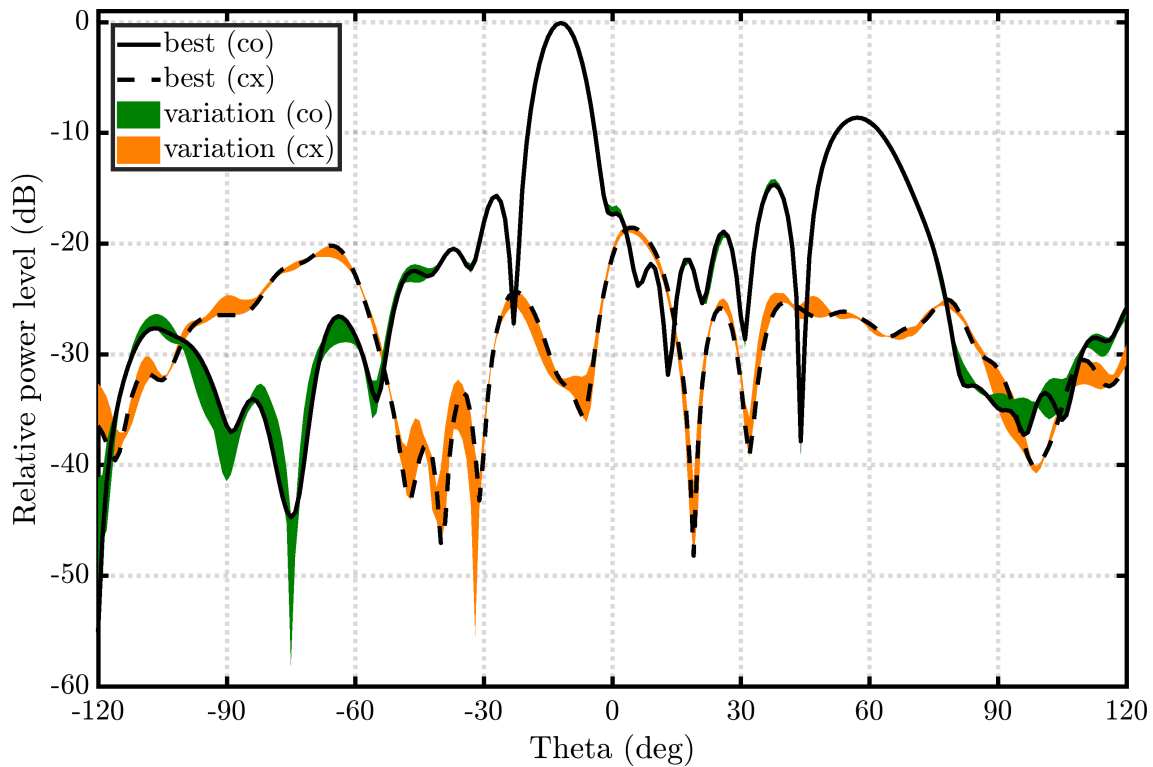


Figure 5.18: BTS antenna vertical far-field pattern cut variations for three different polarization vectors.

has a noticeable effect but further studies are necessary to investigate the dependencies of uncertainty and polarization vector. However, this is a more theoretical investigation since it is not clear how these measurements systems can be realized with reasonable effort.

The measurement results including the 1σ uncertainty for the four key parameter are shown in Fig. 5.19 to 5.22. Except for directivity, the reference value is always contained in the 1σ environment of the measurement. The directivity of the AUT is underestimated by approximately 0.05 dB for all grids and the differences between these values are small (note the displayed range of 0.3 dB). The reason for the systematic offset is mainly the room scattering which has been mitigated in the reference pattern by averaging. Furthermore, the results show that the determined antenna parameters are similar for all measurement grids. However, the uncertainties for the spiral scanning with optimized polarization tend to be slightly larger. In conclusion, the uncertainties of the investigated key antenna parameters are not significantly increased compared to equiangular sampling. Although investigation of uncertainties for individual key antenna parameter is important, it represents only a part of the pattern uncertainty. In order to evaluate the uncertainties more qualitatively, the logarithmic pattern differences according to (3.2) are shown in Fig. 5.23 and Fig. 5.24 for co- and cross-polarization, respectively. The differences between the results for spiral sampling with optimized polarization and the reference are in general larger as for the other point distributions. The relative differences stay mostly below -40 dB which is a reasonable pattern measurement accuracy.

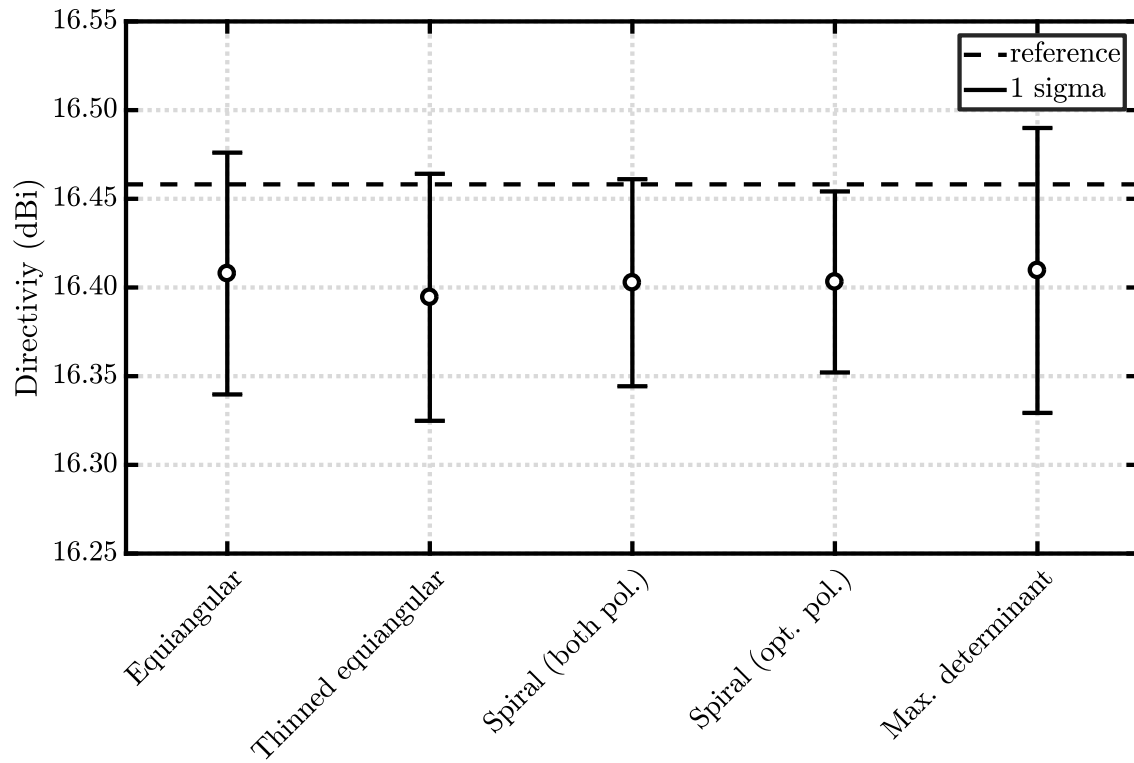


Figure 5.19: Directivity results for BTS measurements.

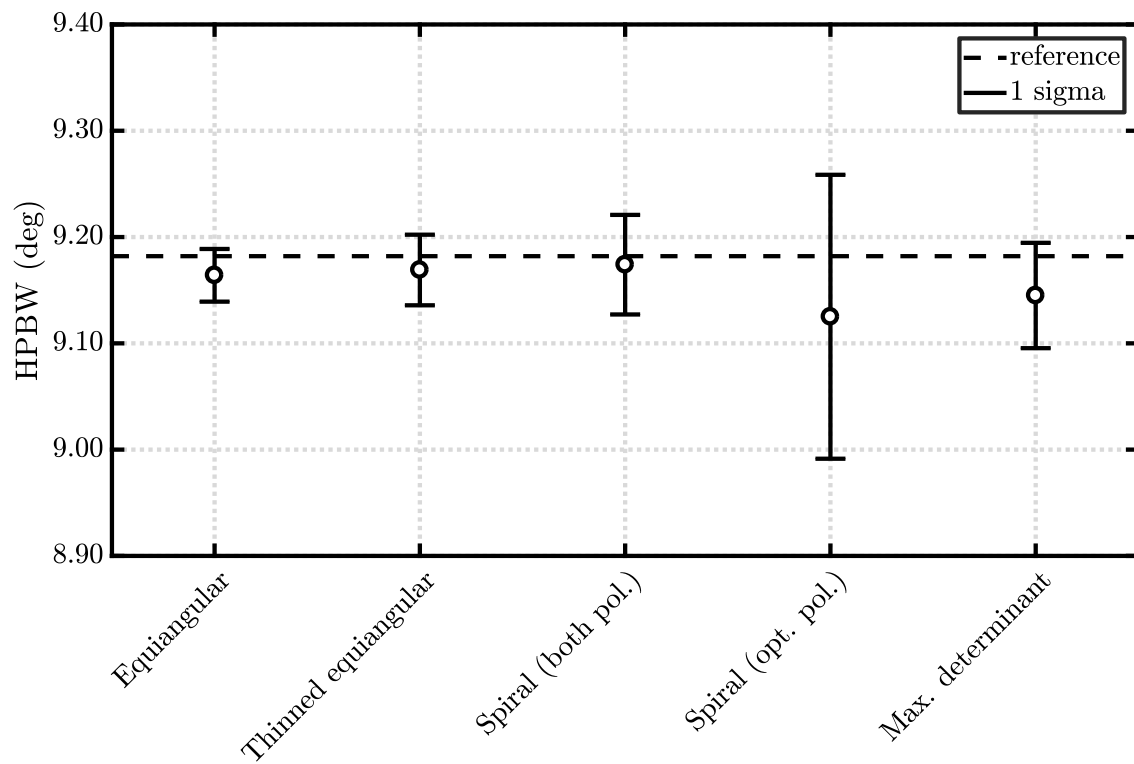


Figure 5.20: Half power beam width results for BTS measurements.

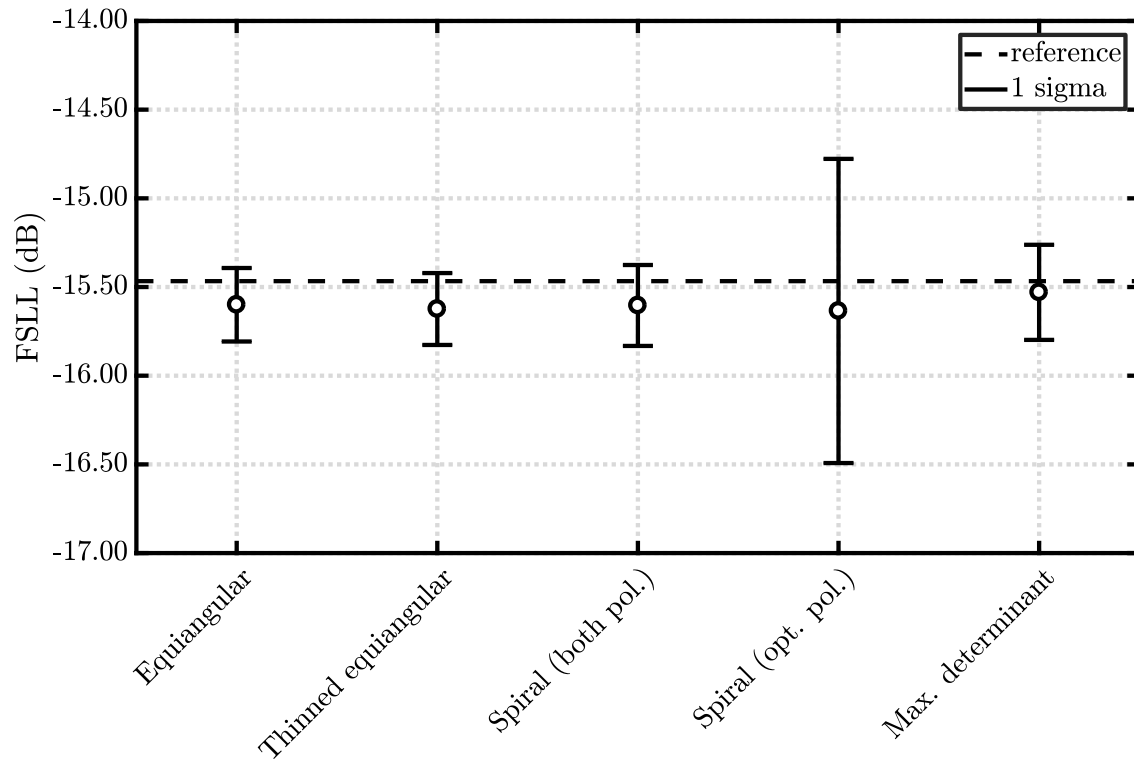


Figure 5.21: First side lobe level results for BTS measurements.

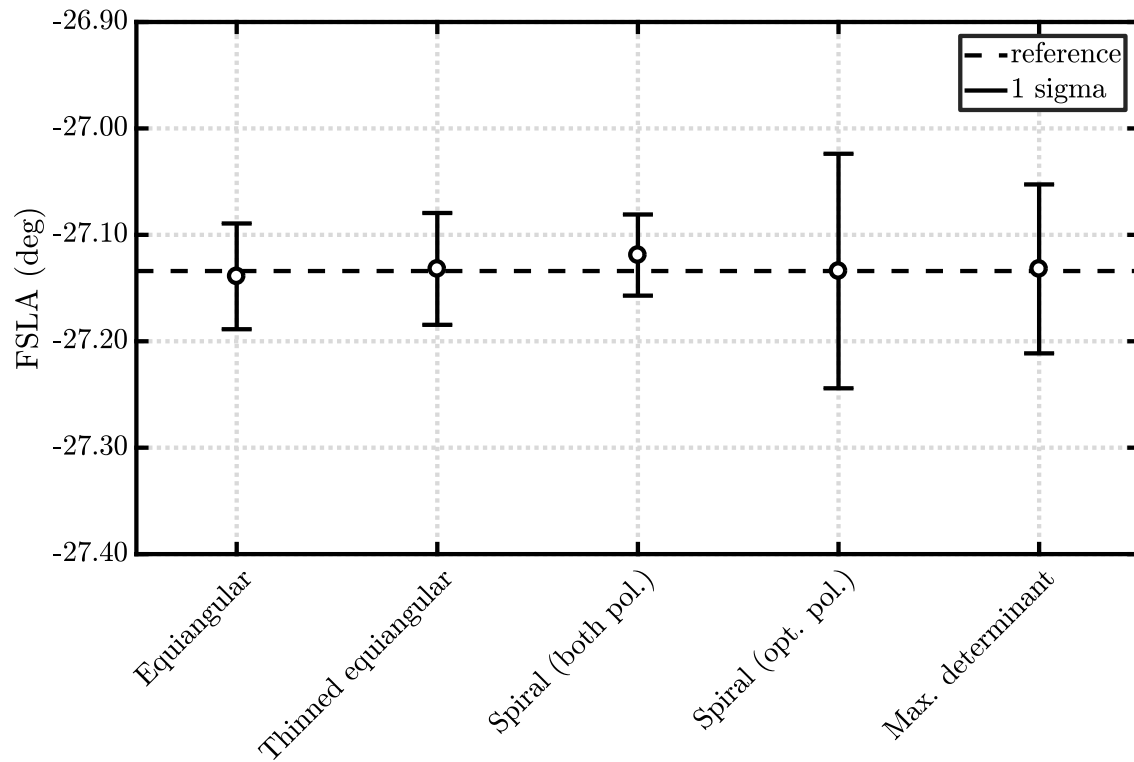


Figure 5.22: First side lobe angle results for BTS measurements.

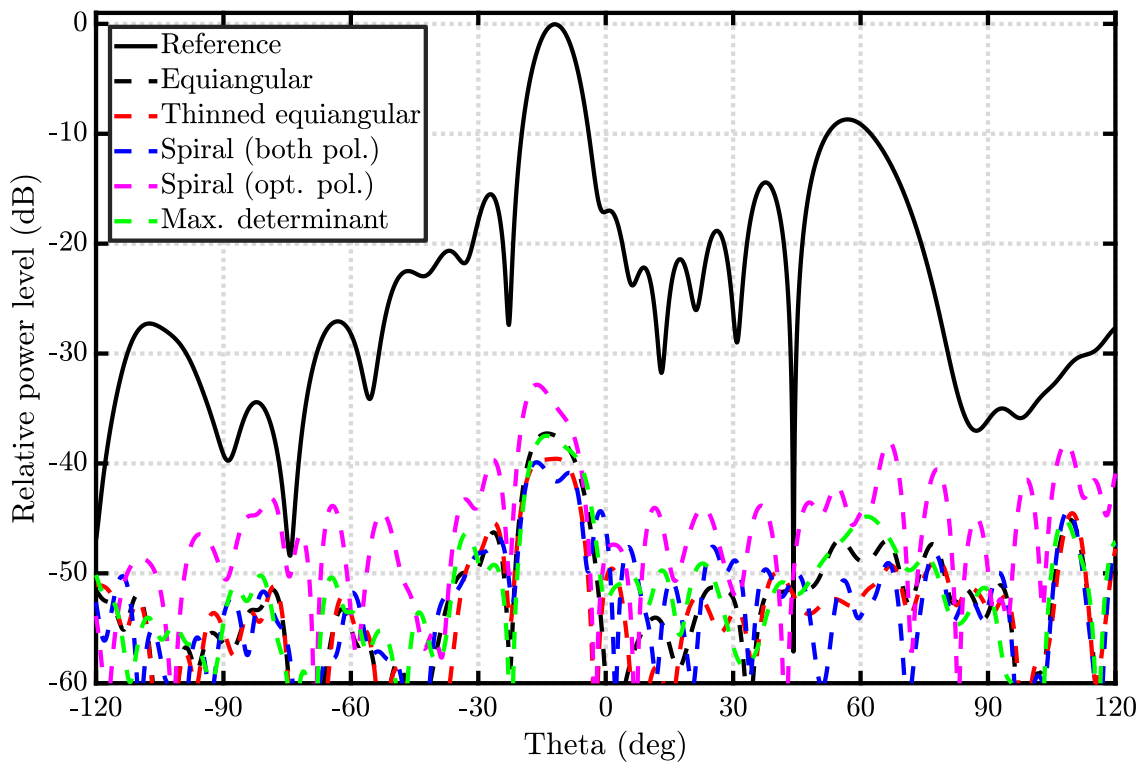


Figure 5.23: Co-polar BTS antenna vertical far-field pattern cut differences for all point configurations.

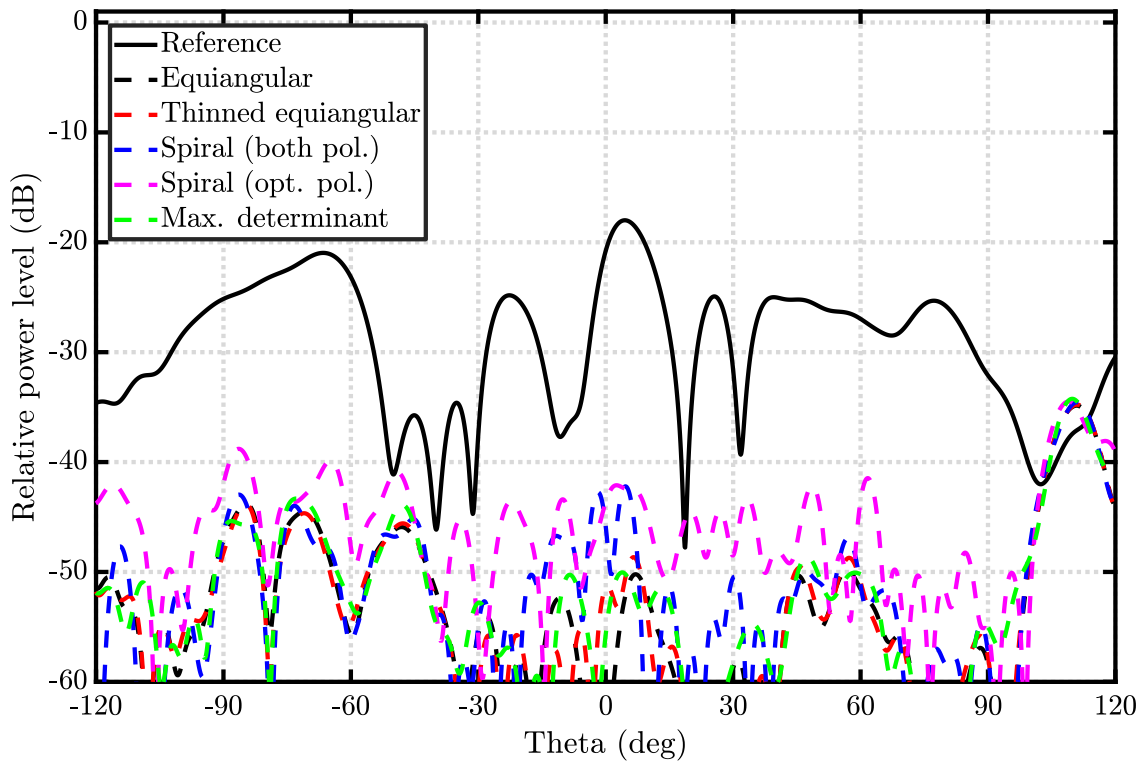


Figure 5.24: Cross-polar BTS antenna vertical far-field pattern cut differences for all point configurations.

Point distribution	L		T_{meas}		$T_{\text{estimated}}$	
	abs.	rel. (%)	abs. (h)	rel. (%)	abs. (h)	rel. (%)
Equiangular	5328	100.0	6.2	100.0	6.2	100.0
Thinned equiangular	3264	61.3	4.2	67.6	4.0	65.0
Spiral (both pol.)	3108	58.3	4.5	71.8	4.4	71.6
Spiral (opt. pol.)	2654	49.8	3.6	57.1	3.6	58.4
Max. determinant	2592	48.6	4.3	69.0	4.1	66.1

Table 5.6: Measured and estimated acquisition times in step mode for BTS antenna measurements.

The absolute and relative measurement times are stated in Table 5.6 together with the number of points. The condition number and path length have been already stated in Table 5.1. The acquisition times are in agreement with the estimated times although it has to be mentioned that the times are different to the estimated times in Table 5.2. The reason is that the axes move sequential and not simultaneously due to software constraints and, thus, $t_{\text{move,A}} = t_{\text{move},\theta,A} + t_{\text{move},\phi,A}$ and $t_{\text{settle}} = t_{\text{settle},\theta} + t_{\text{settle},\phi}$. Since θ is not changed during a scan on a constant latitude ring, equiangular and thinned equiangular measurements are less affected by the sequential axis movement compared to other point distribution because $t_{\text{settle},\theta}$ is zero for most movements. The other parameters are $v_{\text{max},\theta} = a_{\text{max},\theta} = 10^\circ/\text{s}$, $v_{\text{max},\phi} = a_{\text{max},\phi} = 15^\circ/\text{s}$, $t_{\text{settle},\theta} = t_{\text{settle},\phi} = 0.5\text{ s}$ and $t_{\text{sweep}} = 2.5\text{ s}$ where t_{sweep} also includes the blank time used by the software.

In summary, the measurements confirm that measurement point reduction significantly reduces the acquisition time in step mode acquisition. In addition, the measurement uncertainties are similar to the uncertainties for equiangular sampling – even for the non-redundant maximum determinant point distribution. Consequently, the number of required measurement points can be halved and the acquisition time can be reduced more than 40% by using optimized sampling grids.

5.3 Summary

In this chapter the commonly used equiangular, thinned equiangular and spiral sampling point distributions have been investigated. The first two distributions are inherently oversampled with regard to the number of unknown spherical mode coefficients. Although spiral sampling is not inherently oversampled, oversampling is required to keep the condition of the inverse problem low and to guarantee a stable reconstruction. The newly introduced maximum determinant sampling point distribution is non-redundant and the linear equation system is well-conditioned. The point distributions are found by numerical optimization of the determinant and are available¹ for $N < 165$.

In Section 5.1.6, methods for the calculation of the acquisition time were presented and subsequently used to estimate the acquisition times of the proposed point distri-

¹<http://web.maths.unsw.edu.au/~rsw/Sphere/Extremal/New/index.html>

butions. The analysis has been performed for a measurement configuration consisting of two rotational axes, namely roll and azimuth, and for a robot arm measurement configuration. In addition, acquisition in step and continuous mode have been treated separately. It was shown that the relative acquisition time in step mode, compared to regular equiangular sampling, is almost equal to the relative number of sampling points. Consequently, the non-redundant maximum determinant sampling scheme minimizes the total acquisition time. Although this is true for typical measurement scenarios, the results depend on the specific measurement setup. For this reason, the presented procedure should be applied to the specific measurement scenario under investigation in order to evaluate the relative measurement times. In total, the acquisition times in step mode can be nearly halved by using an optimized point configuration.

In contrast to step mode acquisition, the relative measurement time reductions in continuous mode are generally smaller. The scan path length is more important than the number of points. Since the measurement points are distributed over the whole sphere, the relative scan paths length do not correspond to the relative number of measurement points. Nevertheless, reduction of approximately 5% to 20% are estimated for typical measurement scenarios and the considered roll-over-azimuth and robot arm measurement configuration, respectively. Thinned equiangular and spiral scanning perform best whereby the transformation algorithm for thinned equiangular sampling is faster. Furthermore, the specific acquisition time reduction depends strongly on the sweep time because it makes a difference if the velocity of the scan is limited by the maximum velocity of the axis or the sweep time which forces the axis to move slower. In the first case, the relative acquisition time reduction is equal to the relative scan path length reduction which is around 5% to 10% for thinned equiangular and spiral scanning. In the second case larger reduction (depending on the sweep time) can be achieved because the larger and more uniform measurement point separations compared to equiangular sampling can be exploited to increase the average scan velocity. However, in order to fully exploit the benefits of optimized sampling grids in continuous mode, axes control with variable scan velocity and precise position readout are necessary. Up until now, such systems are not commercially available but are under investigation [24, 144].

The theoretically investigated sampling point distributions in Section 5.1 are tested in practice and the results are discussed in Section 5.2. It was verified that an optimized point distribution reduce the acquisition time in step mode as expected. In addition, it was shown that the measurement uncertainties of typical key antenna parameter such as the directivity are not significantly increased.

In conclusion, the point configuration can be optimized for the required measurement task with respect to different goals such as minimal acquisition time. The presented analysis can be directly applied to newly developed point configurations and measurement systems.

Translation and rotation of the transformation origin

In the previous chapter non-redundant sampling on the sphere for a bandlimited number of spherical modes $J \propto (kr_0)^2$ was discussed where r_0 is the radius of the sphere containing all sources. It must be stressed that the radius is measured from the origin of the spherical wave expansion O_{SWE} . In most theoretical investigations the origin is defined in such a way that the sphere has minimal size. However, in measurement practice the origin of the coordinate system is defined by the measurement system and its center of rotation $O_{\text{SWE}} = O_{\text{Meas}}$. In order to minimize the number of unknown spherical modes and, consequently, the measurement time, the AUT center O_{AUT} is typically placed in the center of rotation. But this is not always possible due to the mechanical properties of the AUT or the positioner. In these cases the AUT minimum sphere is offset and, therefore, the radius of the sphere, measured from the center of rotation, containing all sources is enlarged as depicted in Fig. 6.1.

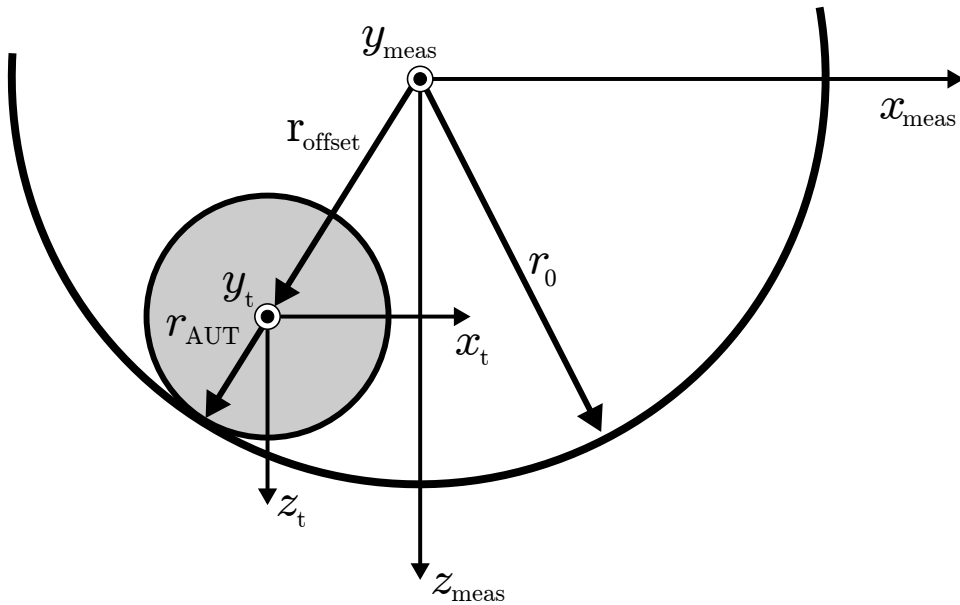


Figure 6.1: Coordinate system for an AUT in offset position.

Though the offset of the AUT does not change the far-field amplitude radiation pattern, it changes its phase. The larger phase variation can only be represented by modes with higher index (m, n) and is the reason for the increased bandlimit. In the following, N_{AUT} and N are the bandlimit of the AUT in the centered and the

offset case, respectively. They are calculated by:

$$N_{\text{AUT}} = kr_{\text{AUT}} + n_1 \quad (6.1)$$

$$N = kr_0 + n_1 \quad (6.2)$$

where

$$r_{\text{AUT}} = \sqrt{(x_{\text{AUT}})^2 + (y_{\text{AUT}})^2 + (z_{\text{AUT}})^2} \quad (6.3)$$

$$r_0 = \sqrt{(x_{\text{AUT}} + x_{\text{offset}})^2 + (y_{\text{AUT}} + y_{\text{offset}})^2 + (z_{\text{AUT}} + z_{\text{offset}})^2}. \quad (6.4)$$

For $kr_{\text{AUT}} \gg n_1$, the bandlimit increases by r_0/r_{AUT} and, consequently, the total number of spherical modes by $(r_0/r_{\text{AUT}})^2$. This increase is severe and an offset mounting of the AUT should be avoided. Typically, a mechanical axis can be used to adjust the AUT position with respect to the center of rotation. Nevertheless, the maximum displacement of the axis might be limited or the AUT is located on a mounting structure (e.g. a satellite) so that the AUT has to be measured in an offset position. In addition, an intentional AUT offset might be used to reduce room scattering effects [10].

Obviously, the AUT is not changed by an offset and, intuitively, it should be possible to measure the AUT with the same number of measurement samples as in the centered case because the information content of the AUT has not been increased. Therefore, the spherical transmission formula used for an arbitrary transformation origin O_{SWE} which fully decouples the transformation from the measurement origin is introduced in Section 6.1. Next, the sampling point distribution for an arbitrary transformation origin is discussed in Section 6.2. It will be shown that the central projection of the measurement points of the minimum sphere onto the enlarged sphere — or onto an arbitrary closed surface — is generally a suitable procedure and allows a stable spherical mode decomposition. The theoretical results are tested in measurement practice (Section 6.3) and it is verified that measurements with an AUT in offset position do not necessarily increase the number of required measurement points. However, the uncertainty generally increases although not dramatically. The individual uncertainty terms have a different dependency on the AUT offset and the used point distribution as will be later discussed in Section 7.1.

6.1 Spherical transmission formula for an arbitrary transformation origin

The spherical transmission formula (2.21) can generally be used for irregular sampling in (r, θ, ϕ, χ) and, thus, also for an arbitrary transformation origin. However, especially the probe correction needs some special attention and will be discussed in detail. If probe correction is neglected, a transformation procedure with an arbitrary origin based on (2.7) requires only a simple translation from the measured to the transformation coordinate system including a rotation of the polarization basis [25] [82]. Alternatively, Wood's method to separate incoming and outgoing waves can be used but requires, in general, two electric and two magnetic tangential field measurements and approximations are used in practical applications [21]. Explicit

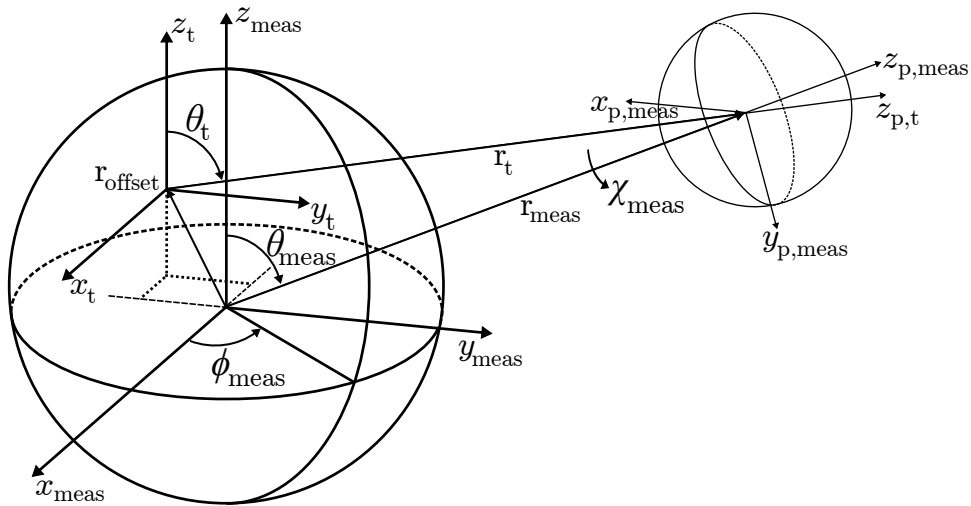


Figure 6.2: Measurement $(x_{\text{meas}}, y_{\text{meas}}, z_{\text{meas}})$ and translated (x_t, y_t, z_t) AUT coordinate system with the corresponding probe coordinate system (x_p, y_p, z_p) .

probe correction formulas for the spherical transmission formula in the case of an AUT z -offset were probably discussed first in the dissertation of J. Christ [145] in the year 1995. Since the dissertation is in German, it might not have been noticed by the community. Curiously, it seems that a publication of Leatherwood in 2007 [146, 147] where probe correction formulas are given for an arbitrary range geometry, has not been noticed by many since it is also not often referenced. The reason might be that the title of the publication and the shown example refer to a conical near-field measurement system, thus, the generality of the formulas is not prominent. The publications investigate the possibilities of arbitrary sampling geometries with full probe correction capabilities. In this thesis, the origin is translated and rotated so that the coordinates for the transformation are irregular although the coordinates lie on a spherical measurement surface. An arbitrary sampling geometry and an arbitrary transformation origin are two different views on the same problem and, thus, have the same solution.

In the following, a similar procedure to [146] is used to derive explicit probe correction formulas but the unnecessary restriction to first order probes is eliminated. The coordinate systems of the measurement $(x_{\text{meas}}, y_{\text{meas}}, z_{\text{meas}})$ and the translated coordinate system used in the transformation (SWE) (x_t, y_t, z_t) are shown in Fig. 6.2. The translation is described by $\mathbf{r}_{\text{offset}}$. In addition, the corresponding probe coordinate system (x_p, y_p, z_p) for a single measurement position is given. The measurement and translated probe position vectors are denoted by \mathbf{r}_{meas} and \mathbf{r}_t , respectively. Due to the offset, the probe z -axis $z_{p,t}$ in the translated coordinate system is not parallel to the original z -axis $z_{p,\text{meas}}$. This means that for a translated origin the probe is not pointing towards the origin. The pointing, only a rotation, can be described by Euler rotations (α, β, γ) . The transmission formula (2.21) for an analytically derived test zone field based on the SMC of the probe is repeated here for convenience and with added coordinate system index

$$\underline{w}^{(l)}(r_t, \theta_t, \phi_t, \chi_t) = \frac{v}{2} \sum_{\substack{smn \\ \sigma\mu\nu}} \underline{T}_{smn} e^{im\phi_t} d_{\mu m}^n(\theta_t) e^{i\mu\chi_t} \underline{C}_{\sigma\mu\nu}^{sn}(kr_t) \underline{R}_{\sigma\mu\nu}^{(l)} \quad . \quad (6.5)$$

Including an arbitrary probe pointing results in

$$\underline{w}^{(l)}(r_t, \theta_t, \phi_t, \chi_t, \alpha, \beta, \gamma) = \frac{v}{2} \sum_{\substack{smn \\ \sigma\mu\nu}} \underline{T}_{smn} e^{im\phi_t} d_{\mu m}^n(\theta_t) e^{i\mu\chi_t} \underline{C}_{\sigma\mu\nu}^{sn}(kr_t) \sum_{-\mu'}^{\mu'} e^{i\mu\alpha} d_{\mu'\mu}^{\nu}(\beta) e^{i\mu'\gamma} \underline{R}_{\sigma\mu'\nu}^{(l)} \quad (6.6)$$

where $e^{i\mu\alpha} d_{\mu'\mu}^{\nu}(\beta) e^{i\mu'\gamma}$ describes the relative rotation of the probe coordinate system and $\underline{R}_{\sigma\mu'\nu}$ are the probe receiving modes in the non-rotated coordinate system. Both formulas are very similar because the rotated probe receiving modes still represent a spherical mode spectrum. As shown in [148] the last summation can also be summarized in a new probe response constant

$$\underline{P}_{\sigma\mu\nu}^{(l)}(kr_t, \alpha, \beta, \gamma) = \frac{1}{2} \sum_{\sigma\nu} \underline{C}_{\sigma\mu\nu}^{sn}(kr_t) \sum_{-\mu'}^{\mu'} e^{i\mu\alpha} d_{\mu'\mu}^{\nu}(\beta) e^{i\mu'\gamma} \underline{R}_{\sigma\mu'\nu}^{(l)} \quad . \quad (6.7)$$

It must be stressed that the rotation of the probe changes the mode spectrum so that, for the general case $\beta \neq 0$, higher-order probe correction is necessary even for $\mu' = \pm 1$ probes. A drawback is that the total transformation time might be dominated by the calculation of the probe rotations in the initialization of the linear equation system. As discussed in Section 2.2.4 the calculations can be performed in parallel and in advance of the measurement. Furthermore, the number of evaluations can be reduced if for example the distance r_t or the Euler angles are the same for multiple measurement points. In addition, if the offset is only along the z -axis and the near field is sampled equiangular in ϕ , the FFT / Matrix method [44] can still be used to accelerate the transformation which has been exploited in [145, 146]. In general, the probe pointing is different for every point and, hence, a pointwise probe correction (Chapter 3) is needed but poses no problem from a theoretical point of view. It needs to be emphasized that the general transmission formula (2.14) and subsequently (2.22) are already suitable for an arbitrary expansion origin although their generality is often overseen. Nevertheless, the presented modification states the explicit probe correction formula for an arbitrary oriented probe which is used in the transformation procedure. It should be noted, that besides a translation, a rotation of the expansion origin is equally possible and does not change the presented formalism. A rotation can be useful in cases where the source volume is of cylindrical shape (i.e. the antenna is elongated and $M < N$) in order to align the z_t -axis with the longest dimension of the cylinder. In total, the arbitrary transformation origin definition can exploit all 6-degrees of freedom (DOF). The presented procedure allows it to define the coordinate system for the transformation independent of the measured coordinate system. By this, an AUT measurement with any point distribution on any closed surface with any probe orientation can be exactly transformed to a spherical mode representation of the AUT. However, limitations exist for practical implementations in order to guarantee accurate measurement results as will be shown in the next sections.

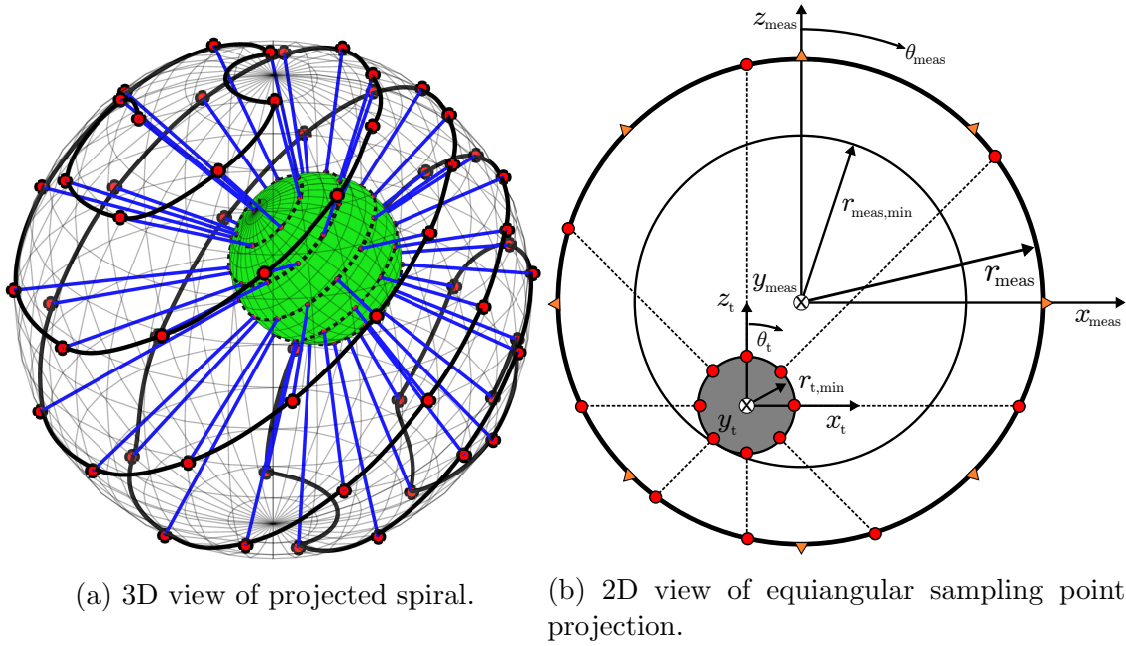


Figure 6.3: Sampling point projection from the minimum to the measurement sphere.

6.2 Sampling point projection

In Chapter 5, different point distributions on the sphere were discussed where it was inherently assumed that the origin of the SWE is the center of the sphere. It can be expected that the point distribution in an offset case should be different in order to guarantee a good condition of the inverse problem. An intuitive approach is to project the point distribution from the AUT minimum sphere to the measured surface which can have an arbitrary shape, in general. For the case of a spherical measurement surface, this is shown in Fig. 6.3. By projection, the relative angle of a sampling point is kept while the radius is changed. The radius mainly affects the phase and no sampling criteria exist for the radius because the spherical harmonics are valid for all $r \geq r_0$. And indeed, this approach performs good for a spherical measurement surface shown in Fig. 6.4. It can be seen that the condition number increases exponentially with increasing offset for constant sampling whereas the condition number stays low for projected sampling point locations. The behavior is the same for all offset directions and, therefore, only one exemplary direction is shown. Please note that for offset $r_{offset}/r_{meas} > 0.9$ the minimum sphere of the AUT intersects with the probe sphere which violates a theoretical requirement of the transformation and has been excluded for this reason.

The results confirm the expectation that the sampling point distribution should be different for an offset configuration. Furthermore, it seems that sampling point projection is optimal in the sense that the condition number is almost unchanged. It can be expected that the results hold for arbitrary surfaces but that needs to be verified by further research. Since rotations of spherical harmonics (3D rotation group or $SO(3)$) do not change the number of spherical modes, a rotation of the coordinate system does not require a change of the sampling point locations and has no effect on the condition number. This means, that only the translation (3-DOF) of the coor-

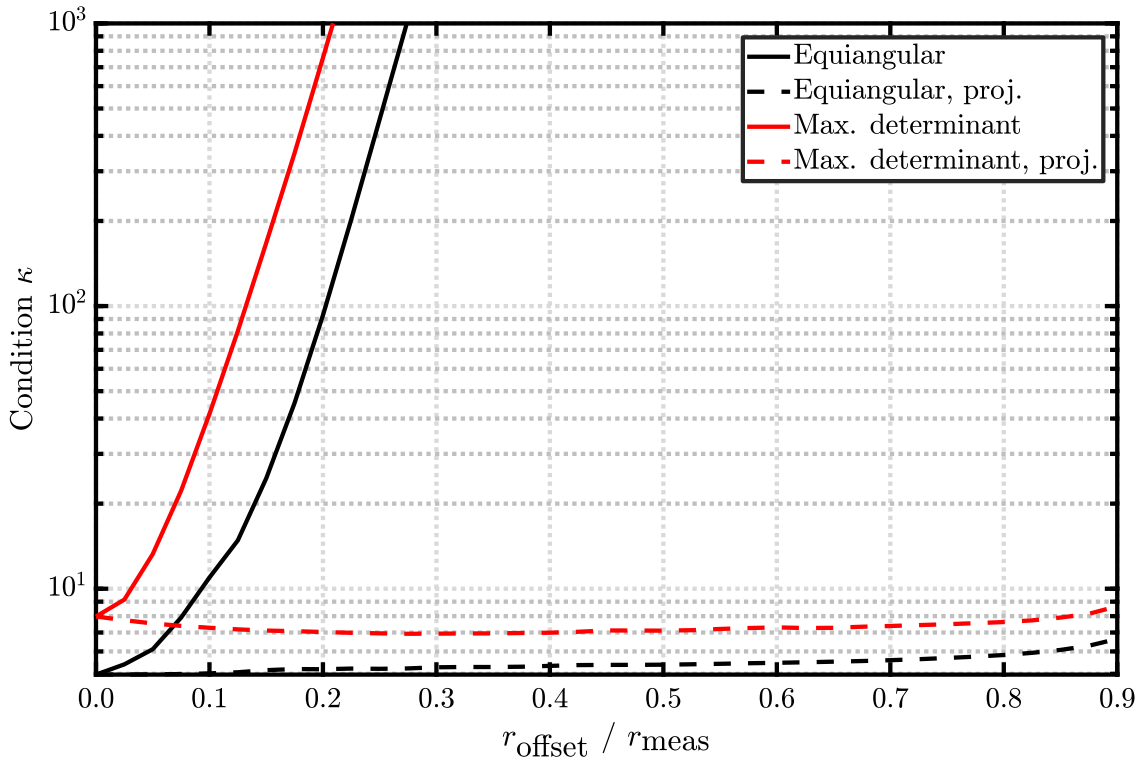


Figure 6.4: Condition number of the linear equation system ($N = M = 17$, $r_{\text{meas}} = 2$ m, dipole probe, $f = 5$ GHz) depending on the offset $r_{\text{offset}}/r_{\text{meas}}$ in xz -direction for equiangular and maximum determinant sampling point distribution with and without projection from the minimum sphere.

ordinate system is important for the point distribution in an offset case. In contrast, if the considered source volume is not a sphere (i.e. $M < N$) the orientation (3-DOF) of the coordinate system is important. Generally, $M < N$ means some sort of cylindrical source volume and the z -axis needs to be aligned with the longest dimension in order to minimize the maximum extend in x and y and, consequently, the number of modes in M . It should be noted, that a rotation of the coordinate system can also be applied if the offset is zero. However, in order to measure these points the measurement systems needs to provide enough degrees of freedom to acquire these points fast. In the case of the roll-over-azimuth measurement system at the IHF, it is for example not easily possible to measure in a 90° rotated coordinate system. Principal cuts are typically easy but others are difficult (e.g. the diagonal cut). If the measurement coordinate system cannot be rotated easily, it might, depending on the specific case, still be possible to reduce the number of points but certainly not by its maximum amount. In contrast, the measurement effort in a robot arm measurement configuration is equal for all coordinate systems. Hence, the flexibility of a robot arm measurement system can be exploited in this case.

It is worth to mention, that additional DOF of a measurement system can be used to rotate the coordinate system in such a way that the offset is only along the new z -axis. By this and in conjunction with equiangular sampling, the FFT / matrix transformation algorithm can be used which accelerates the transformation process for cases $M = N$ as well as $M < N$.

In order to avoid a modification of the measurement coordinate system, [149] proposes to do this in post-processing by interpolating the near-field measurement data on the sphere in the case that $M = N$. The used phase correction term is based on the far-field approximation and a comprehensive investigation of the limitations and the introduced error has not yet been performed. In addition, it is not equally possible to use this procedure with probe correction, and, consequently, longer transformation times must be accepted in most scenarios.

6.3 Measurements

The presented spherical transmission formula for an AUT in offset position is validated by measurements and the results are stated in this section. Preliminary tests have been published in [148]. The used test object is a small open boundary horn antenna (QH2000) mounted on a special mechanical structure which allows a variable offset in x (see Fig. 6.5). The investigated frequency is 5 GHz and the analysis is focused on two principal cuts. The reference radiation pattern is shown in Fig. 6.6 and Fig. 6.7 for the E- and H-plane, respectively. The reference pattern has been calculated by averaging 16 different regular equiangular measurements in continuous mode. After the SWE, the modes are translated and truncated according to the AUT offset and the bandlimit $N = 17$ (encloses the AUT without mounting structure). Although the offset could be equally considered directly in transformation, the transformation time due to the more complex probe correction procedure is longer. Please note that the results would be equal because the transformation procedures are analytically exact and they operate on the same measurement data. Regarding the reference pattern, it might be noted that the pattern is not symmetric, more prominent in the H-plane, which is an effect of the asymmetric mounting structure which shadows part of the radiation and causes reflections. These are not perfectly filtered because the absorber are close to the antenna.

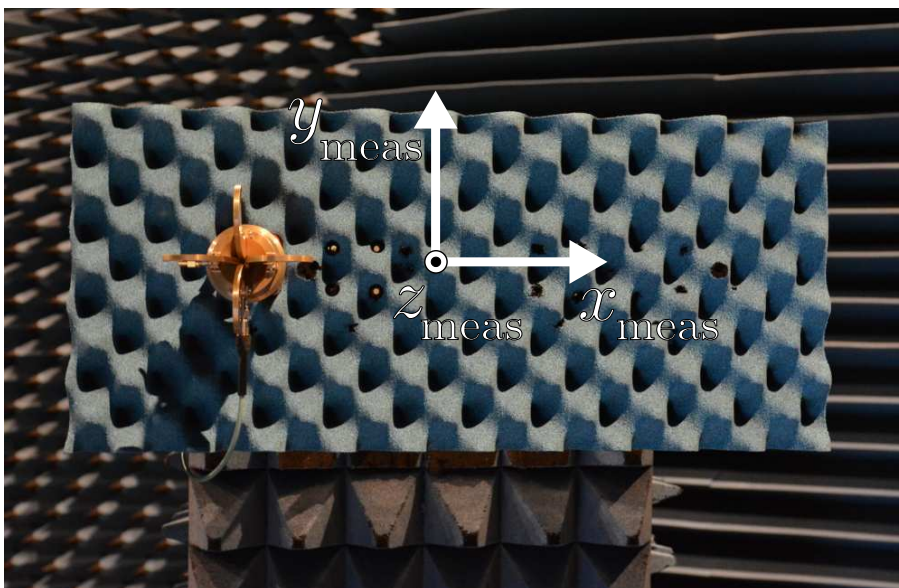


Figure 6.5: QH2000 antenna mounted in the IHF SNF chamber.

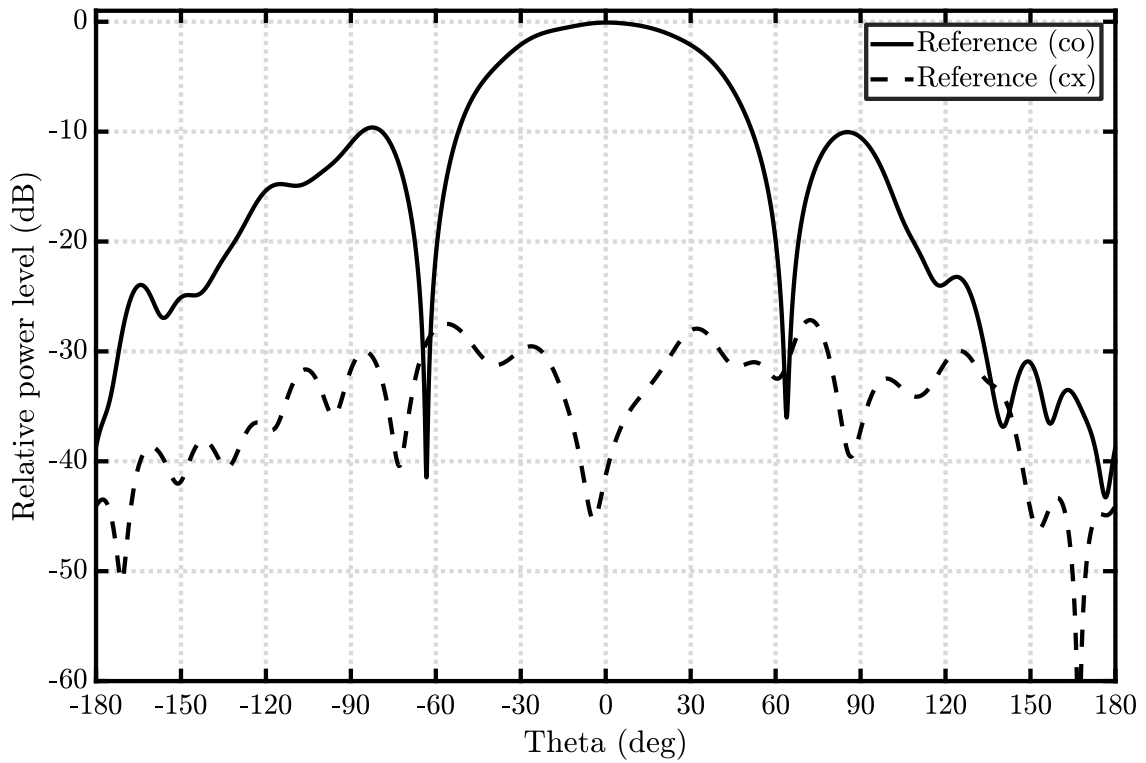


Figure 6.6: QH2000 antenna H-plane ($\phi = 0^\circ$) reference far-field pattern cut.

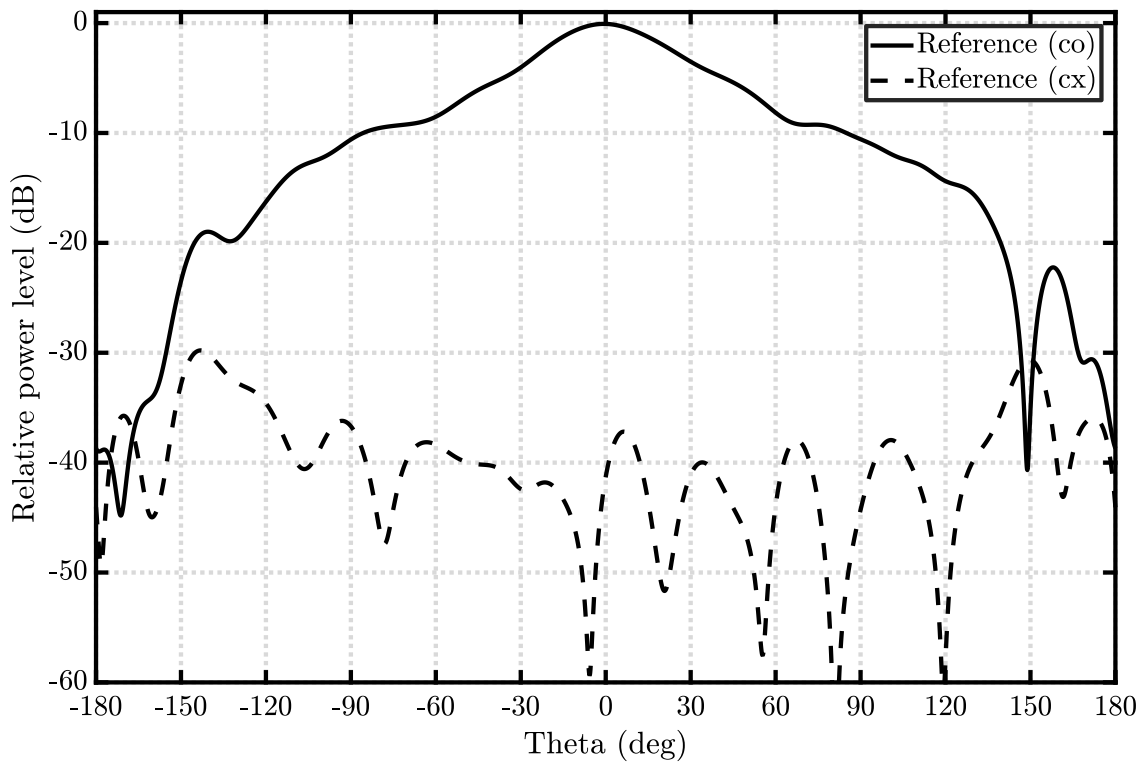


Figure 6.7: QH2000 antenna E-plane ($\phi = 90^\circ$) reference far-field pattern cut.

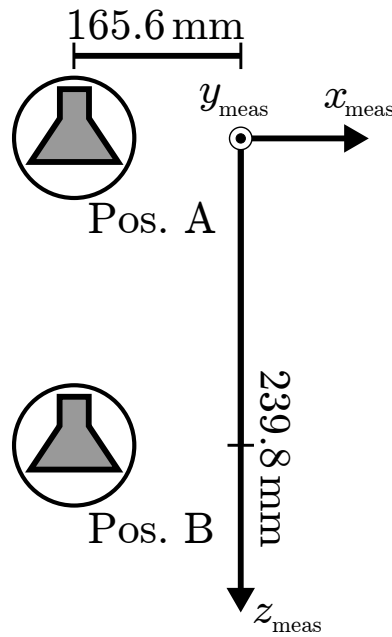


Figure 6.8: QH2000 measurement positions. Position A with AUT center at $(x_{\text{meas}}, y_{\text{meas}}, z_{\text{meas}}) = (-165.6 \text{ mm}, 0, 0)$ and Position B with AUT center at $(x_{\text{meas}}, y_{\text{meas}}, z_{\text{meas}}) = (-165.6 \text{ mm}, 0, 239.8 \text{ mm})$.

The investigation is performed for two different AUT positions in order to investigate the effect of the offset. The first offset is a shift only along the negative x -axis by 165.6 mm using the special mounting structure. Next, the AUT is displaced 239.8 mm $\approx 4\lambda$ in z by a linear slide below the roll axis. These positions are named A and B in the following and are depicted in Fig. 6.8. According to the offsets A and B, the bandlimit N increases from 17 to 35 and 49, respectively.

The AUT is at first measured with regular equiangular sampling without considering the AUT offset (bandlimit N) which is, up until now, the commonly used measurement method. Next, the AUT is measured with equiangular sampling according to $N = N_{\text{AUT}}$ but without projection. Although it has been shown in Section 6.2 that a measurement point projection is beneficial for the condition of the problem, it causes an irregular sampling point distribution which typically increases the measurement time if the measurement setup consists of rotational axes (e.g. roll-over-azimuth). From the previous analysis, it can be expected that the uncertainties without projection are larger but they might be acceptable if the offset is not too large. Finally, the AUT is measured with all five, in Section 5.1 presented, point distributions projected on the measurement sphere. The measurements are listed in Table 6.1 and Table 6.2 for the AUT in position A and B. The absolute number of required measurement points changes only for the regular equiangular sampling. Due to the offset, the projected points at the poles for the equiangular grid get redundant because the probe orientation can only be switched between 0° and 90° . By this, the number of unique measurements reduces by $2(2(N + 1) - 1)$ to 1298. Furthermore, the relative number of points compared to regular equiangular sampling with bandlimit N (total number of modes J) and the total number of modes J_{AUT} required to represent the centered AUT radiation pattern are given. While the regular equiangular

Point distribution (pos. A)	L	L/J	L/J_{AUT}	κ
Equiangular	5328	2.057	8.248	7
Equiangular ($N = N_{AUT}$)	1368	0.528	2.118	7
Equiangular ($N = N_{AUT}$), proj.	1368 ^a	0.528	2.118	5
Thinned equiangular, proj.	812	0.314	1.257	2
Spiral (both pol.), proj.	736	0.284	1.139	8
Spiral (opt. pol.), proj.	692	0.267	1.071	24
Max. determinant, proj.	648	0.250	1.003	5

Table 6.1: Comparison of different sampling point distributions for offset position A. ^a) The projected points do not lie on an equiangular global grid and the number of unique measurements is only 1298 due to the redundant projected pole.

Point distribution (pos. B)	L	L/J	L/J_{AUT}	κ
Equiangular	10200	2.041	15.789	10
Equiangular ($N = N_{AUT}$)	1368	0.274	2.118	19
Equiangular ($N = N_{AUT}$), proj.	1368 ^a	0.274	2.118	5
Thinned equiangular, proj.	812	0.162	1.257	2
Spiral (both pol.), proj.	736	0.147	1.139	9
Spiral (opt. pol.), proj.	692	0.138	1.071	27
Max. determinant, proj.	648	0.130	1.003	5

Table 6.2: Comparison of different sampling point distributions for offset position B. ^a) The projected points do not lie on an equiangular global grid and the number of unique measurements is only 1298 due to the redundant projected pole.

sampling is already oversampled by a factor of 8 for position A, this increases to more than 15 for position B. This shows clearly that an offset has a large effect on the number of required measurement points. In contrast, if the translated origin is considered in the transformation, the required number of samples is independent of the offset. In the case of spiral scanning, an oversampling of approximately 1.14 and 1.07 has been chosen to keep the condition number low which are stated in the last column. Please note that the condition numbers of the projected grids are almost unchanged whereas the condition number for the non projected equiangular sampling has almost tripled.

The measurement times are listed in Table 6.3 and Table 6.4. Since the number of measurements does not change for projected grids, their total measurement times are almost unchanged. Due to the fact that the acquisition time for regular equiangular sampling increases significantly, the relative acquisition time reduces by up to approximately 80% and 90% for position A and B, respectively. Similar to the results for the BTS antenna in Section 5.2 the relative measurement times are closely related to the relative number of measurement points. However, due to the sequential movement of the axes the measurement times are slightly higher compared to a

Point distribution (pos. A)	L		T_{meas}	
	abs.	rel. (%)	abs. (h)	rel. (%)
Equiangular	5328	100.0	6.4	100.0
Equiangular ($N = N_{\text{AUT}}$)	1368	25.7	1.6	25.0
Equiangular ($N = N_{\text{AUT}}$), proj.	1368	25.7	2.0	30.8
Thinned equiangular, proj.	812	15.2	1.4	21.7
Spiral (both pol.), proj.	736	13.8	1.3	20.0
Spiral (opt. pol.), proj.	692	13.0	1.1	17.4
Max. determinant, proj.	648	12.2	1.3	20.7

Table 6.3: QH2000 measurement times in step mode for offset position A.

Point distribution (pos. B)	L		T_{meas}	
	abs.	rel. (%)	abs. (h)	rel. (%)
Equiangular	10200	100.0	10.2	100.0
Equiangular ($N = N_{\text{AUT}}$)	1368	13.4	1.6	15.6
Equiangular ($N = N_{\text{AUT}}$), proj.	1368	13.4	2.0	19.4
Thinned equiangular, proj.	812	8.0	1.4	13.6
Spiral (both pol.), proj.	736	7.2	1.3	12.5
Spiral (opt. pol.), proj.	692	6.8	1.1	10.9
Max. determinant, proj.	648	6.4	1.3	13.0

Table 6.4: QH2000 measurement times in step mode for offset position B.

case where the axes move simultaneously. In summary, the realized acquisition time reductions are as expected based on the analysis in previous chapters. It should be pointed out that acquisition in continuous mode is more complicated for projected grids compared to a centered coordinate system especially if the measurement system consists of rotational axes. Thus, it can be expected that the improvements due to optimized sampling are slightly reduced in continuous mode. As previously discussed, new, flexible measurement systems and further research are necessary to investigate this in practice.

The measurement results including the 1σ uncertainty are discussed in the following. The directivity D is shown in Fig. 6.9 for position A (yellow circle with black uncertainty bar) and position B (yellow diamond with blue uncertainty bar). The reference value is always contained in the 1σ environment which indicates that the estimated uncertainties are plausible. In general, there is no unique dependency of the total measurement uncertainty on the position and the effect is mostly small. Interestingly, the uncertainties for the non projected equiangular grid are slightly smaller than the uncertainty for the projected grid. The reason for this counter-intuitive result is that the projected grid has less ($\approx 9.5\%$) unique measurement points (1298 instead of 1368), especially in the main beam region. Overall, the accuracies are good except for the spiral scheme with optimized polarization. In fact,

the results are quite inaccurate due to spatial aliasing which will be discussed later in detail. Fig. 6.10 visualizes the differences in the HPBW of the H- (yellow marker) and E-plane (red marker) for position A (black uncertainty bar) and position B (blue uncertainty bar). Thus, in total 4 measurement values and their 1σ uncertainty are given for every measurement grid. In general, the uncertainty for H- and E-plane HPBW are similar. For the projected grids, the uncertainties do further not show any clear dependency on the offset. In contrast, the non projected equiangular sampling tend to have a larger uncertainty for position B. The deviation of the angle of the nulls in the H-plane is given in Fig. 6.11. Compared to regular equiangular sampling, the uncertainties are enlarged which indicates that most probably the reflections at the mounting structure affect the position of the null which are only partially filtered by the reduced grids. Nevertheless, the estimated angles are almost all in the range of $\pm 1^\circ$.

It should be noted that the true value of the right null for position B is in most cases not contained in the 1σ environment of the estimated values. This means that a measurement uncertainty is underestimated and most probably the effect of the mounting structure is not accurately considered. The geometrical angles of the mounting structure in the local AUT coordinate system are approximately 110° and -140° in the H-plane and 149° and -144° in the E-plane. Similar to the analysis of the blockage of a positioner, the effect might be estimated by truncating the near-field data. However, this would be an overestimation and furthermore would neglect reflection and diffraction. Simulation of the AUT including the mounting structure might be the most accurate solution but is not the focus of this thesis though definitely an interesting further research topic. Lastly, the maximum cross-polarization in the E- and H-plane HPBW are investigated and the values are given in Fig. 6.12 where the reference values are indicated by dashed lines. Less redundant sampling point distributions show an increased cross-polar uncertainty in offset configurations which can be explained by the fact that redundancy improves the filtering capabilities of the SWE. Hence, reducing redundancy might cause increased uncertainties especially in measurement scenarios where the measurement is affected by contributions from higher order modes (i.e. spatial aliasing). In contrast to the measurement scenario presented in Section 5, these effects are stronger for QH2000 measurements due to the mounting structure and the lower directivity. A detailed discussion will be performed in the following measurement uncertainty section.

Overall, the analysis of the dependency of the offset on the measurement uncertainty is difficult due to the fact that typical uncertainty budgets evaluate only certain key parameters which might have a complex and non-linear dependency on the causing error source. In general, the complete radiation pattern is affected by a measurement error. Therefore, it is difficult to predict the effect of certain antenna parameters because they depend on all SMC representing the radiation pattern which are differently distorted. It might thus happen, that the maximum cross polarization is reduced although the global cross-polarization level is higher or that some other parameters are affected. Consequently, the generalization of the dependency of the uncertainty of antenna parameters on the offset is complicated.

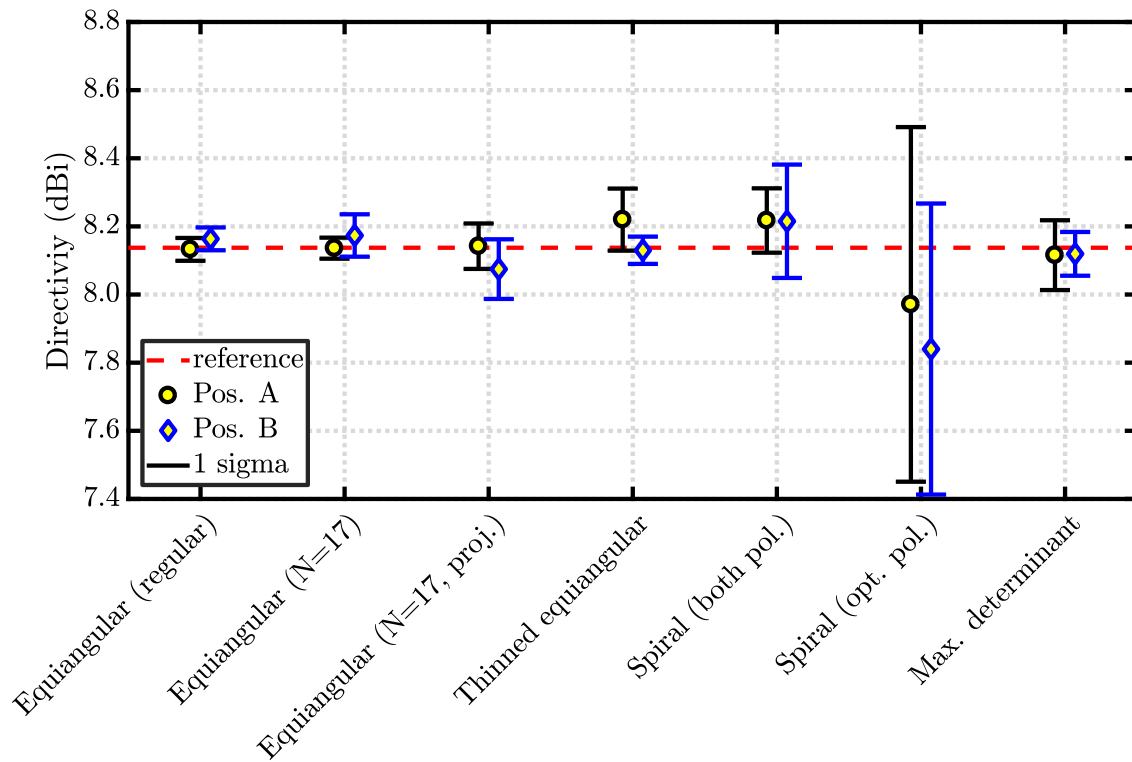


Figure 6.9: Directivity results for QH2000 measurements.

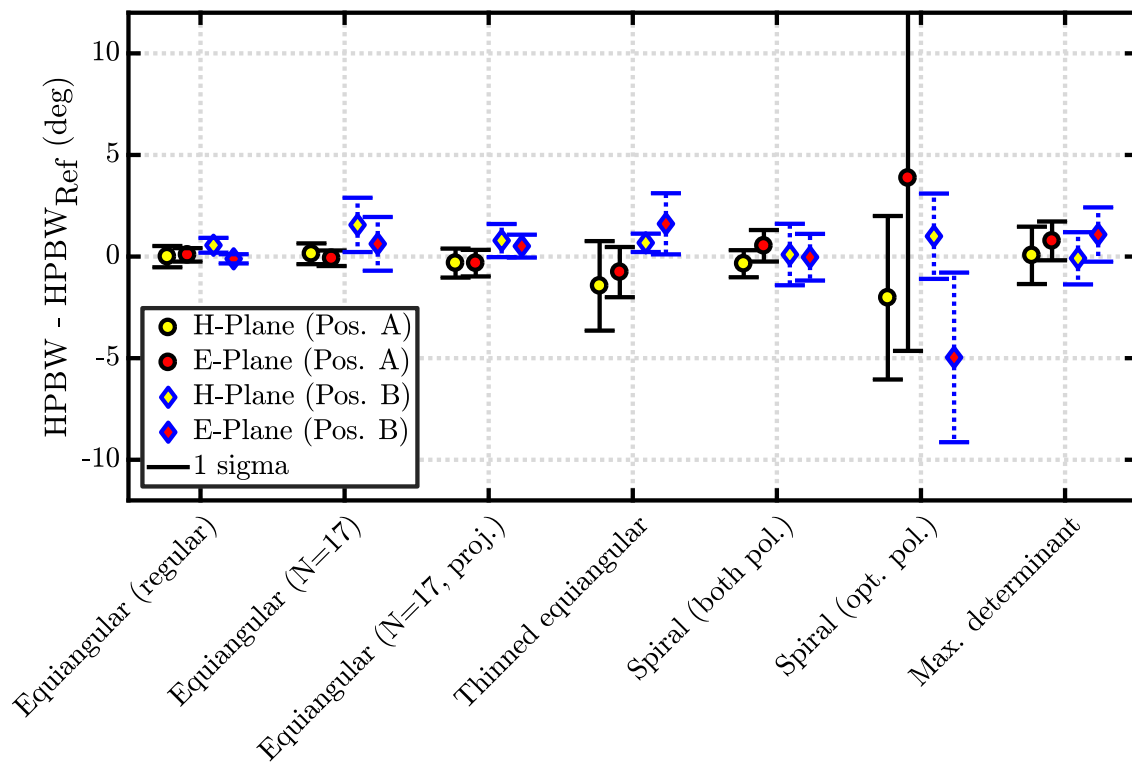


Figure 6.10: Relative half power beam width for QH2000 measurements.

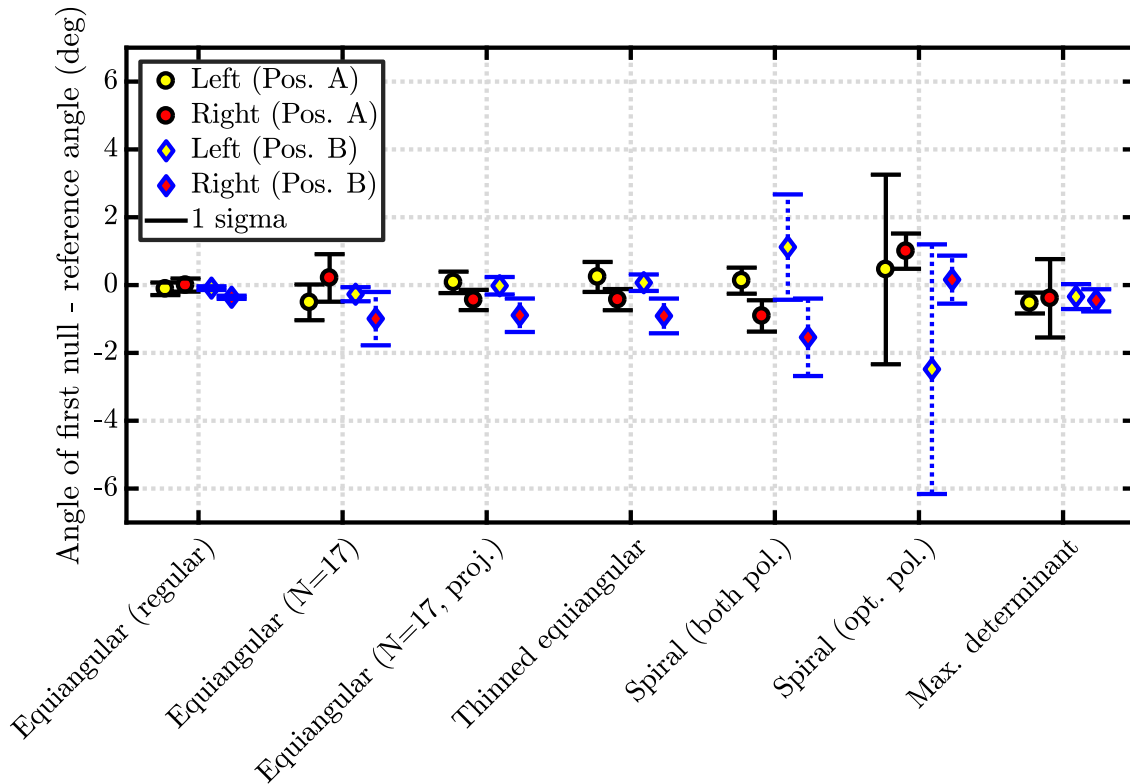


Figure 6.11: Relative position of the first null for QH2000 measurements.

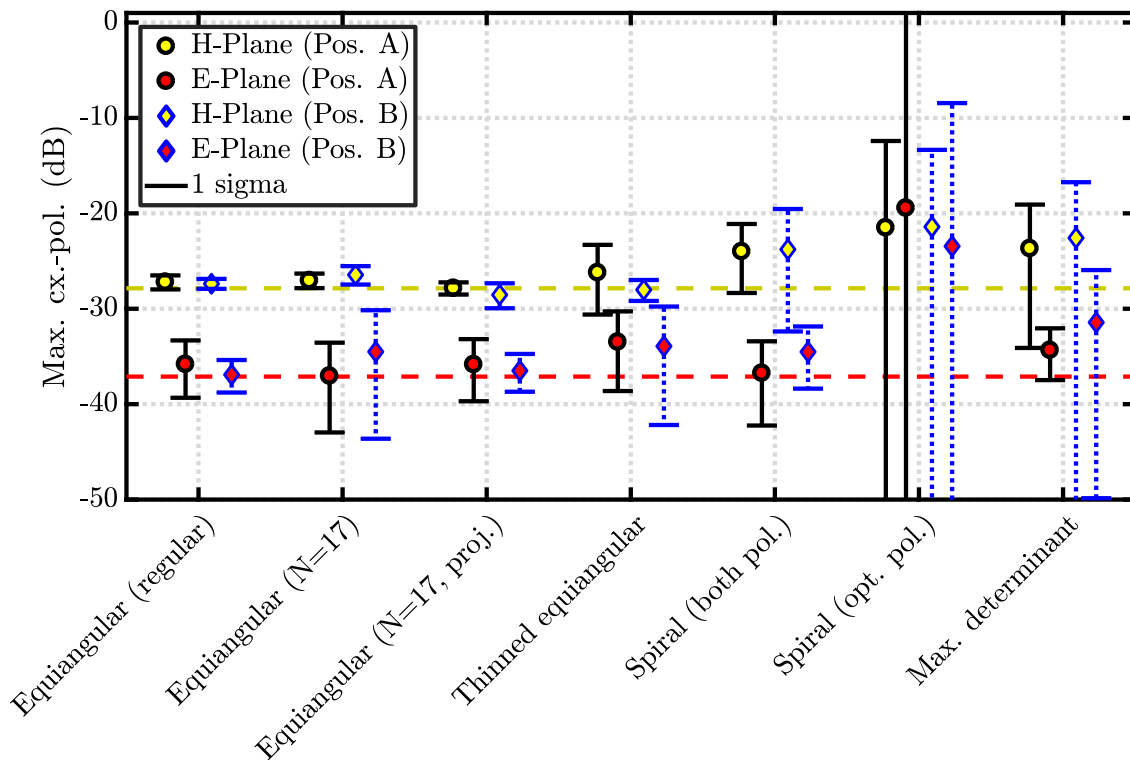


Figure 6.12: Maximum cross-polarization level for QH2000 measurements.

An alternative parameter which provides a sort of global error, is the erroneous power in the mode spectrum. This value is calculated by summing up the power of the differences between the modes of the reference field Q_{smn}^{ref} and the distorted field Q_{smn} according to the following formula

$$\epsilon = \frac{P_\epsilon}{P_{\text{ref}}} = \frac{\frac{1}{2} \sum_{smn} |Q_{smn}^{\text{ref}} - Q_{smn}|^2}{\frac{1}{2} \sum_{smn} |Q_{smn}^{\text{ref}}|^2} \quad (6.8)$$

By this, the global pattern uncertainty is reduced to a single term but has lost its descriptiveness because it cannot be directly linked to the uncertainty of a single antenna parameter. This is a general problem in uncertainty evaluation. It depends on the purpose of the analysis which evaluation method is more suited. In the case of a specific antenna measurement it is beneficial to investigate key parameters directly whereas for a generalization of certain effects the spherical mode differences are more adequate. The total RSS differences are shown in Fig. 6.13 where the contribution from error term 7 has been removed because it is equal for all measurement grids. For equiangular sampling, the uncertainty is reduced or almost equal for position B compared to position A. For all other point distributions, a larger offset increases the global measurement uncertainty. Again, the uncertainties for spiral scanning with optimized polarization are the largest one. The dependencies of the individual error terms will be comprehensively analyzed in Section 7.1.

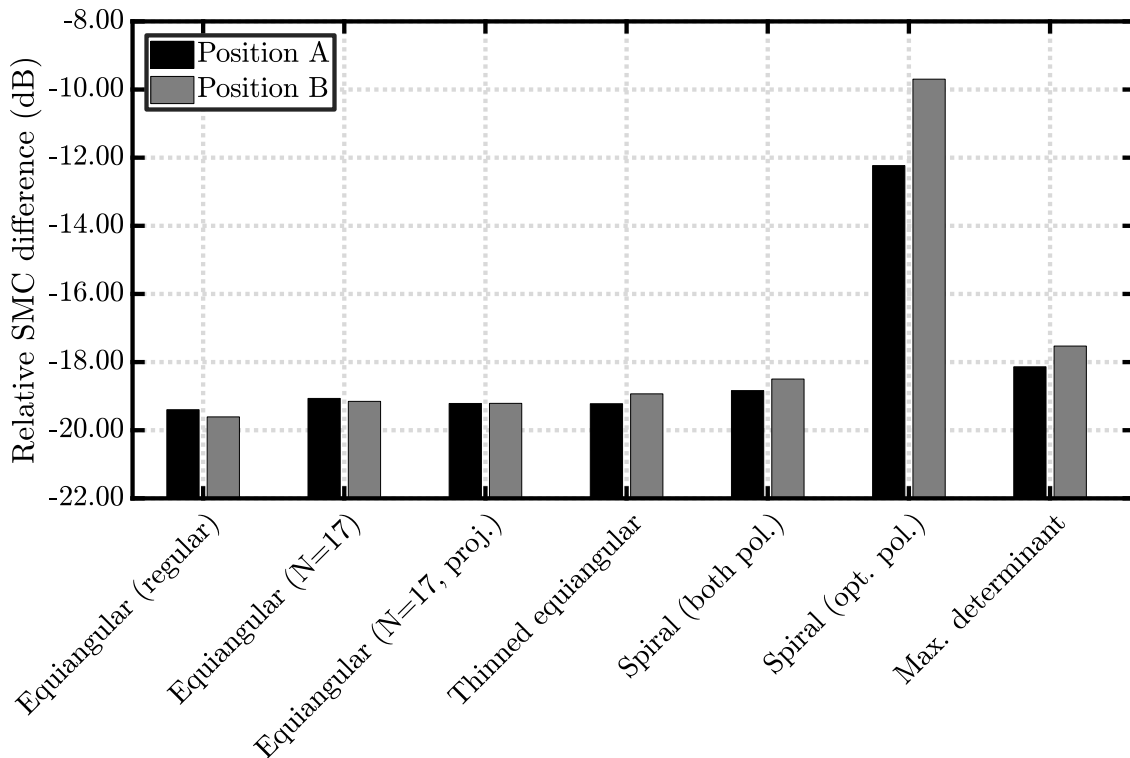
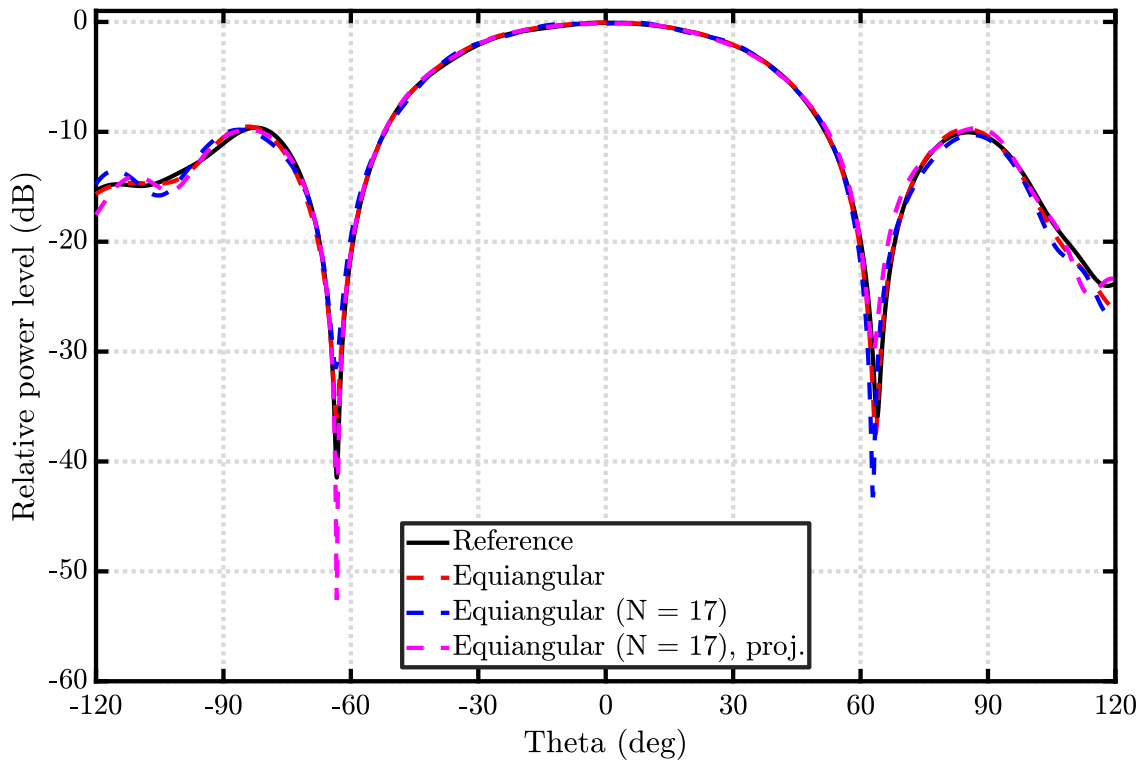


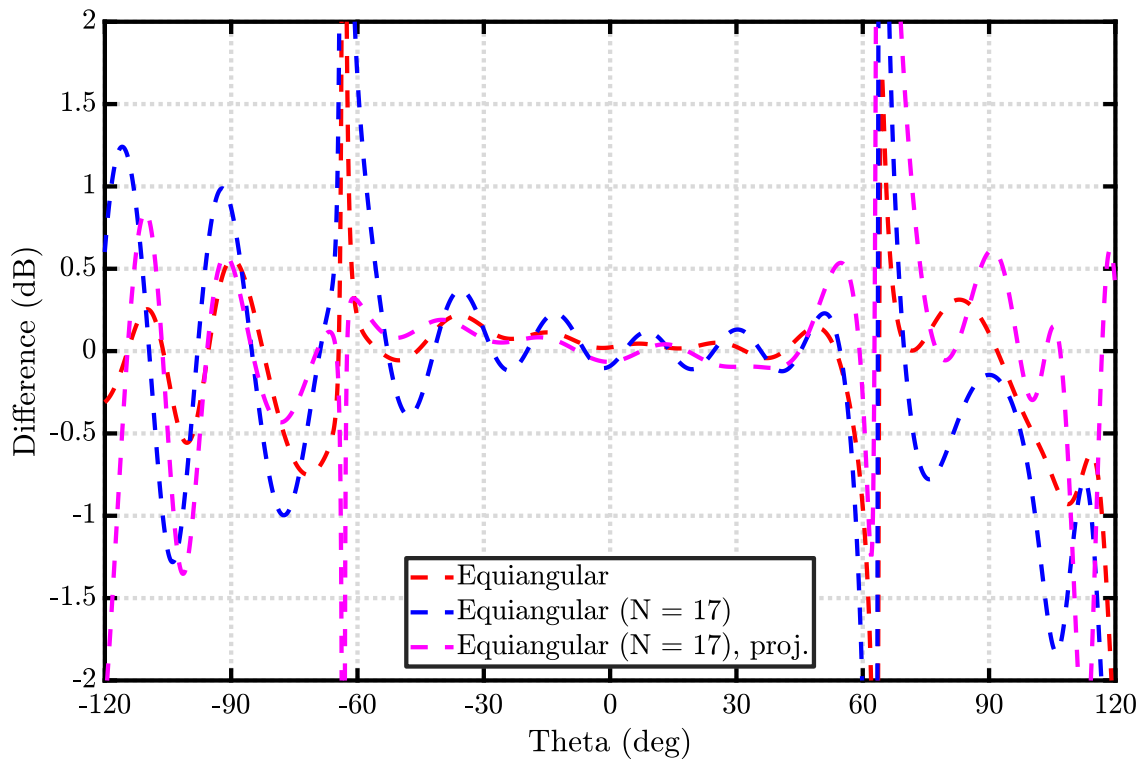
Figure 6.13: QH2000 measurement SMC difference (without term 7) for position A and B for different point configurations.

A more qualitative evaluation can be performed by inspection of the H-plane far-field radiation pattern for the different measurement grids which are shown Fig. 6.14, Fig. 6.15 and Fig. 6.16 for co- and cross-polarization. The general co-polar pattern is similar for all measurement grids although the location and the depth of the null vary for different point distributions. Spiral scanning with optimized polarization shows the largest difference which is consistent with the estimated uncertainty. The cross-polar pattern is significantly distorted if the oversampling is reduced by using for example spiral scanning schemes. However, it is not surprising that oversampling improves the accuracy in cases where measurement errors are noticeable. The perspective should be that a non-redundant measurement has a certain uncertainty which can be reduced by oversampling regardless of the sampling scheme. It must be stressed that a fair comparison requires an equal number of samples. Furthermore, it can be expected that oversampled maximum determinant sampling is more robust against measurement errors compared to equiangular sampling because the points are more uniformly distributed and not concentrated at the poles.

Overall, the measurements confirm again that measurement point reduction significantly reduces the acquisition time in step mode acquisition. Furthermore, the measurement results show reasonable agreement for the investigated point distributions although the spiral scanning scheme with optimized polarization shows large discrepancies which is reflected by the measurement uncertainties. In general, the uncertainties dependent on the offset and different point distributions are not equally sensitive. However, projected, non redundant maximum determinant sampling allows the determination of for example the directivity almost five and seven times faster (position A and B) compared to regular equiangular sampling without considering the offset whereas the uncertainty is still around 0.1 dBi. If higher accuracies are required, more measurement points can be measured so that the desired uncertainty level is reached. By this, the operator has the flexibility to balance measurement time and accuracy in the desired way which is not similarly possible with classical sampling schemes. In summary, the measurements show that the number of required samples can always be minimized according to the electrical size of the AUT and independent of its location inside the measurement sphere. This is a significant result because the dramatically increased acquisition time for offset mounted antennas can be reduced to the acquisition time required for a centered AUT.

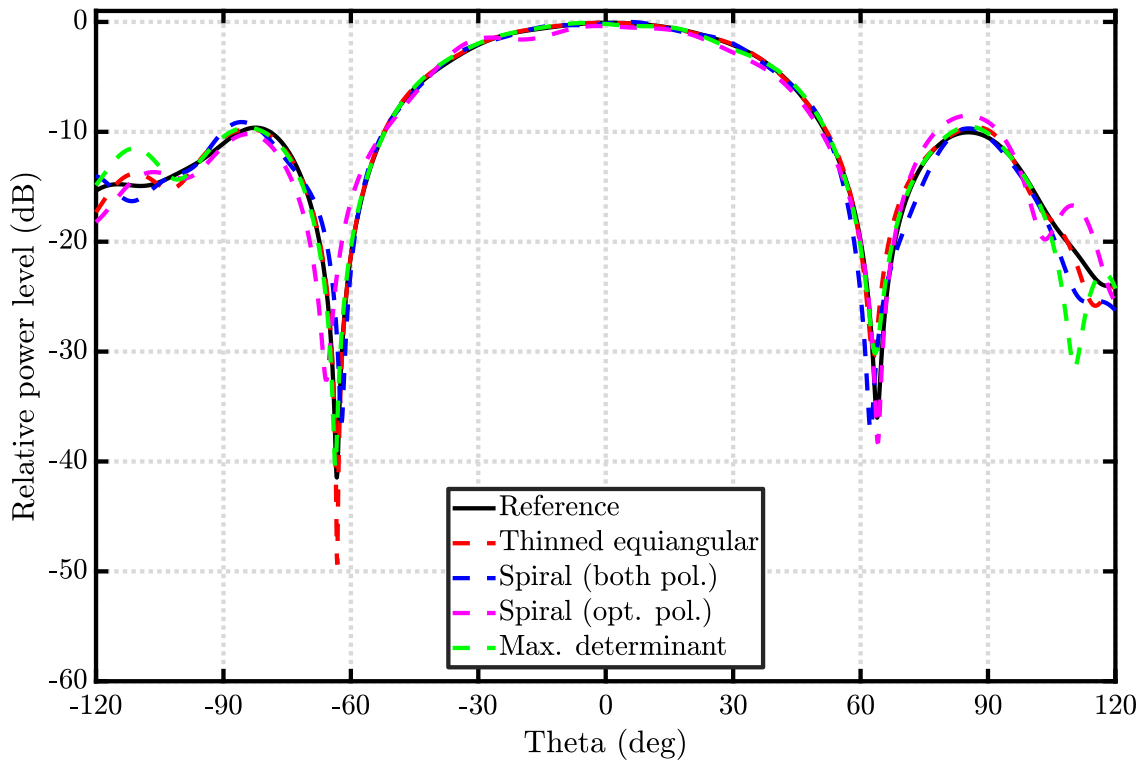


(a) Co-polar H-plane far-field pattern.

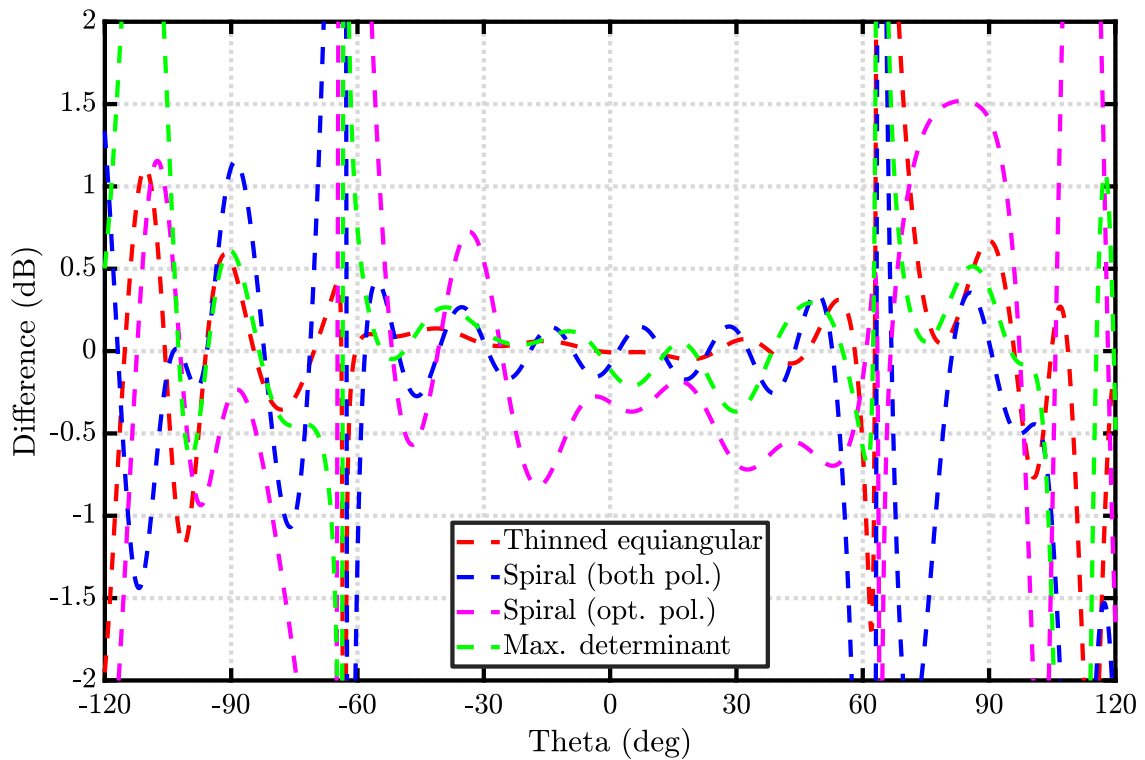


(b) Differences.

Figure 6.14: QH2000 co-polar H-plane far-field pattern (a) and differences (b) for equiangular sampling grids (Pos. B).

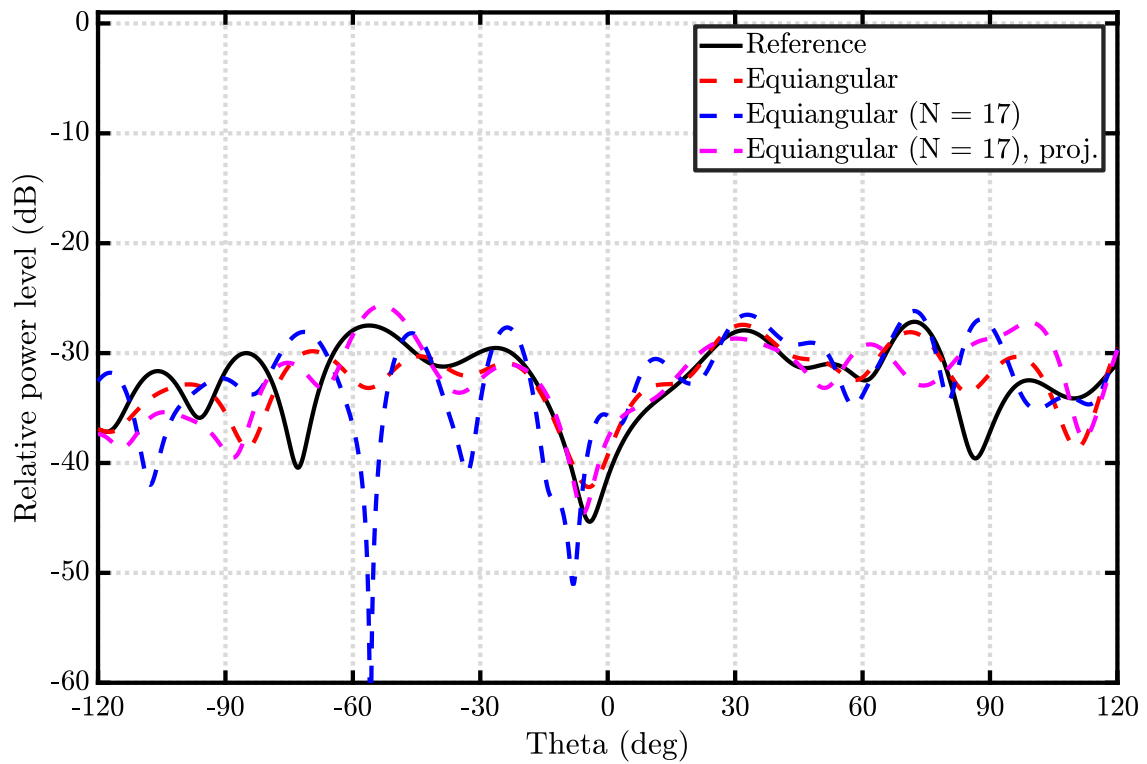


(a) Co-polar H-plane far-field pattern.

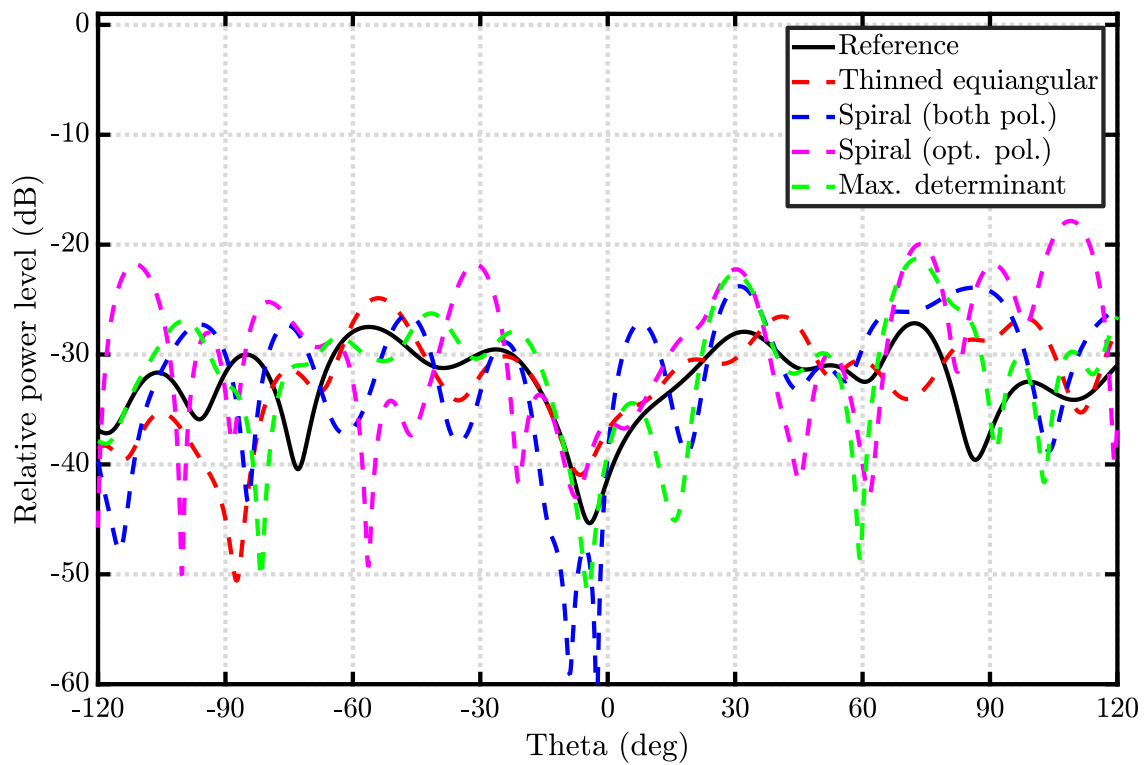


(b) Differences.

Figure 6.15: QH2000 co-polar H-plane far-field pattern (a) and differences (b) for other sampling grids (Pos. B).



(a) Only equiangular sampling.



(b) Other grids.

Figure 6.16: QH2000 cross-polar H-plane far-field pattern for different sampling grids (Pos. B).

6.4 Summary

In this chapter, the previously highlighted generality of the spherical transmission formula was used to define an arbitrary position and orientation of the coordinate system for the spherical wave expansion algorithm. Therefore, the origin of the expansion has not necessarily to be the center of rotation of the measurement range. By this, it is always possible to minimize the sphere containing all sources (e.g. the antenna) so that the number of required measurement points is minimal. The number of measurement points is thus solely dependent on the electrical size of the AUT and not anymore dependent on the position in the measurement range. Although the generality of the transmission formula inherently allows an arbitrary origin, explicit probe correction formulas were derived for the case of a typical measurement configuration with a single probe. Furthermore, it has been shown that the projection of the sampling point distribution from the source volume (i.e. AUT minimum sphere) to the measurement sphere preserves the properties regarding the SWE.

Besides the theoretical investigation, the common measurement scenario of an offset mounted AUT has been investigated. An open boundary horn antenna (QH2000) was measured in two different offset configurations and a full uncertainty budget has been calculated. By this, it was verified that the number of measurements and, consequently, the acquisition time can significantly be reduced by the proposed procedure. It was further pointed out that the uncertainties of an offset mounted AUT are, in general, increased compared to a centered AUT measurement and, hence, centered AUT measurements are preferable. Nevertheless, if the oversampling is increased, errors due to, for example, room scattering can be reduced which is employed by scattering suppression methods. Overall, the measurement uncertainties for the minimum number of samples are reasonable for the IHF SNF measurement chamber which is designed for low frequency operations ($f \leq 2$ GHz). Depending on the requirements, the proposed procedure allows flexible control of the oversampling which can be used to increase the accuracy and to filter scatterers.

Although the shown example is a typical measurement case, the applicability of the procedure is by far more general. In fact, arbitrary scanning geometries are possible while full probe correction is available. Accurate positioning on a spherical surface is mechanical challenging and might affect the maximum scan speed. Using other geometries such as a cube might increase the measurement speed. In summary, the discussed procedure replaces the paradigm of accurate positioning on a sphere ($< \lambda/50$) by the requirement to know the position and orientation of the coordinate systems. If the axis position readout is sufficiently accurate, settling time of the axes can be minimized. In addition, optical measurement devices such as laser trackers can be used to track the relative position of the probe and the AUT. In summary, the antenna measurement range design can profit from the generality of the presented formulas in order to develop measurement systems optimized for the desired measurement task.

Measurement uncertainties

The stated measurement uncertainties for the BTS and QH2000 antenna in the previous chapters are discussed in this section in more detail. The individual uncertainty terms as well as the estimation method are presented in Section 7.1. It will be discussed how the uncertainties depend on the used point distribution and the offset. Tables with the complete uncertainty budget can be found in the Appendix B.2 and Appendix C.2 for the BTS and QH2000 antenna, respectively. In general, the performed uncertainty analysis follows the guidelines of the IEEE standard [10] which is based on the commonly used NIST 18-Terms error budget [150]. However, since the original NIST 18-Term model was developed for planar near-field antenna measurements, modifications are used of which some are described in [10]. For others, especially the estimation of the room scattering (Term 16), new methods are developed and replace older ones. The full NIST 18-Term [10] and the modified uncertainty model used in this thesis are shown in Table 7.1. For convenience, the original numbering is kept for identical terms although this means that certain uncertainty numbers do not exist. Uncertainty terms related to gain (i.e. 3, 5 and 6) are not considered in this thesis because they are independent of the used measurement grid. Measurement area truncation is also not investigated because full sphere measurements were performed. In addition, term 2 (probe polarization ratio) has been included in term 1 and term 10 and 11 are combined in term 10 because in a roll-over-azimuth spherical near-field range the separation in transverse and orthogonal position errors is not as natural as for planar near-field measurements. Detailed explanations are given in the corresponding paragraphs.

Though it is known by most in the research area, it should be emphasized that the used uncertainty estimation methodology [10] is aligned with measurement practice in order to keep the effort reasonable. Therefore, the calculated uncertainties might not be exact but have proven sufficient agreement with experienced differences between measurements. In addition, a near-field antenna measurement is a complex measurement process and affected by many possible error sources. For this reason, the uncertainty models are focused on the major contributions and it turns out that, typically, only a few terms have a significant contribution to the total uncertainty. Hence, the simplifications and assumptions in the methodology might not be theoretically exact, but allow a practical and sufficiently accurate determination of the measurement uncertainty.

In general, the uncertainty is described by a distribution function (e.g. normal, uniform, etc.). Since an unknown systematic error has to be included in the parameters defining the uncertainty function, the mean value of the uncertainty can be assumed to be zero. It is further assumed that all terms are independent and uncorrelated. Usually, the parameter of the distribution function (e.g. standard deviation) is esti-

NIST 18-Term model		Used uncertainty model	
1	Probe relative pattern	1	Probe relative pattern
2	Probe polarization ratio	2	-
3	Gain standard	3	-
4	Probe alignment error	4	Probe alignment error
5	Normalization constant	5	-
6	Impedance mismatch	6	-
7	AUT alignment error	7	AUT alignment error
8	Data point spacing	8	Data point spacing
9	Measurement area truncation	9	-
10	Probe transverse position error	10	Position error
11	Probe orthogonal position error	11	-
12	Multiple reflections	12	Multiple reflections
13	Receiver amplitude non-linearity	13	Receiver amplitude non-linearity
14	System amplitude and phase errors	14	System amplitude and phase errors
15	Receiver dynamic range	15	Receiver dynamic range
16	Room scattering	16	Room scattering
17	Leakage and crosstalk	17	Leakage and crosstalk
18	Miscellaneous random errors	18	Miscellaneous random errors

Table 7.1: Comparison of full NIST 18-Term model and used uncertainty model.

mated by comparing two sets of data where the data is chosen in such a way that the differences are mainly caused by the investigated error source. Hence, the terms can be evaluated independently. Finally, all uncertainties are combined using the root square sum (RSS) procedure. Many antenna parameters are usually specified in logarithmic scale and, consequently, an uncertainty in logarithmic scale is also convenient. However, a linear symmetric uncertainty is not exact symmetric in the logarithmic scale. But the differences can be regarded as negligible for uncertainties below 0.3 dB and, thus, the stated logarithmic uncertainty is the mean value of the absolute lower and upper error if not explicitly stated.

7.1 Uncertainty budget calculation

The evaluation method for every uncertainty term is presented in the following and is equal for both investigated antennas. Therefore, the general procedure is first discussed for the BTS antenna (2400 MHz) which is centered in the measurement coordinate system. As it is common practice, the uncertainty evaluation is performed for a limited number of key antenna parameters. Next, the QH2000 antenna (5 GHz) measurements in two offset positions are used to evaluate the effect of an AUT offset on the measurement uncertainties. As previously discussed (see Section 6.3), it is more appropriate to use the global mode power error (6.8) for this investigation. The uncertainty terms 13, 14, 15, 17 and 18 are related to the measurement system and, for that reason, no dependency on the offset was found. They are not explicitly discussed in this chapter but are listed in Appendix C.2.

7.1.1 Term 1 & 4: Probe related uncertainties

Term 1: Probe relative pattern

For the correction of the probe in the transformation, it is necessary to know the radiation pattern of the probe. The probe pattern is usually determined by numerical simulation for simple probes (e.g. dipole or open ended waveguides) or by measurements. Nevertheless, the probe pattern is never exactly known and, hence, the real probe pattern differs from the assumed probe pattern in the transformation. The related uncertainty can be evaluated by comparing transformation results for two slightly different probe patterns. Here, the simulated (full wave simulation with CST [151]) and the measured probe pattern are used. The principal cuts are shown in Fig. 7.1 for comparison. The second probe (i.e. for measuring the other polarization) is the same probe but 90° rotated.

In contrast to planar near-field antenna measurements, the spherical probe correction procedure uses the SMC of the probe instead of the far-field pattern. For this reason, the probe polarization ratio over the entire radiation pattern is inherently considered in the correction. A separation of the error term related to a finite probe polarization ratio (term 2 in Table 7.1) is not necessary. As can be seen in Fig. 7.1, the simulated probe is perfectly linear polarized so that the polarization ratio error might be slightly overestimated. The estimated uncertainties are given in table Table 7.2.

Besides the absolute error, also the relative error compared to equiangular sampling is interesting to discuss. Although for all point distributions the same probe patterns are used, the errors are not equal. This is a consequence of the higher order modes excited by the probe. If the probe would be a first order probe, the errors would be exactly the same because in this case the probe can be interpreted as an ideal probe measuring an effective field [53].

Term 4: Probe alignment error

The probe alignment error represents the mismatch of the probe coordinate systems in the data and the actual measurement. There are 6 DOF which are separately

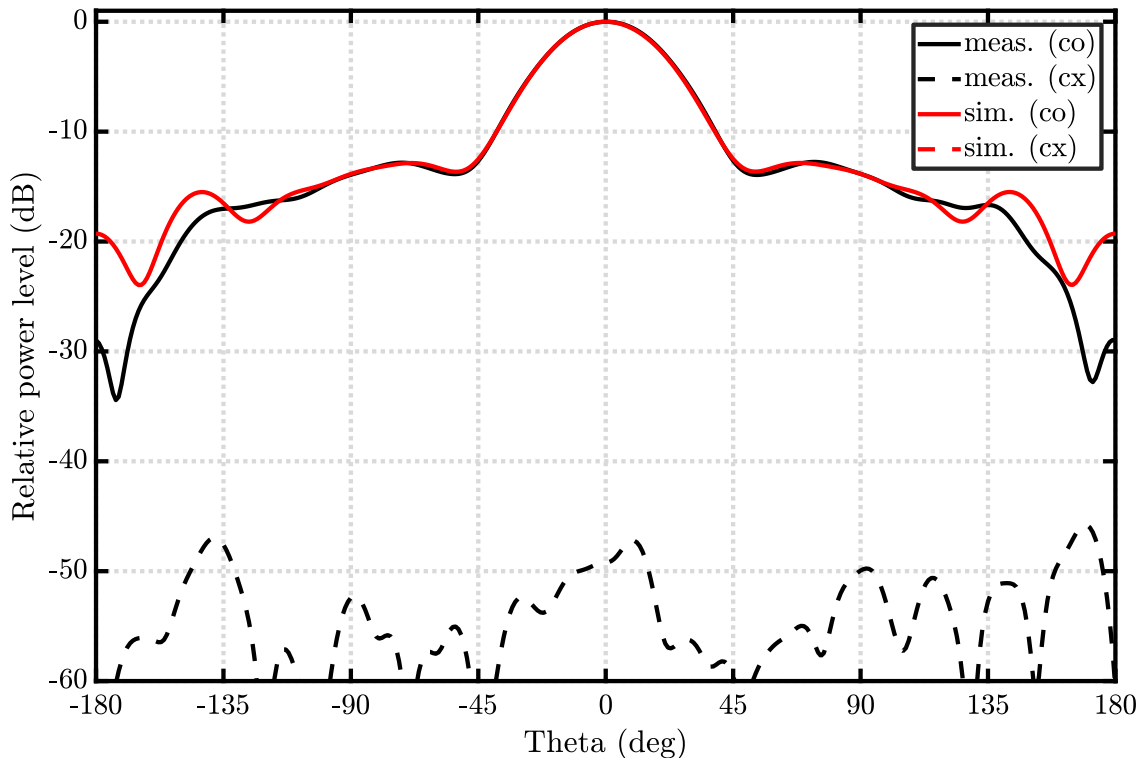


Figure 7.1: Comparison of simulated and measured SH800 E-plane radiation pattern at 2400 MHz. Note, the cx-polar level of the simulated probe pattern is below -100 dB and out of the displayed range.

Point distribution	D (dBi)	HPBW ($^\circ$)	FSL (dB)	FSLA ($^\circ$)
	16.458	9.182	-15.467	-27.134
Equiangular	± 0.006	± 0.013	± 0.053	± 0.013
Thinned equiangular	± 0.006	± 0.013	± 0.054	± 0.014
Spiral (both pol.)	± 0.006	± 0.012	± 0.054	± 0.014
Spiral (opt. pol.)	± 0.005	± 0.006	± 0.060	± 0.013
Max. determinant	± 0.007	± 0.012	± 0.052	± 0.014

Table 7.2: Term 1 (BTS): Probe relative pattern.

evaluated and summed by the RSS procedure. The estimated alignment errors for the IHF spherical near-field chamber are $(0.1^\circ, 0.2^\circ, 0.2^\circ)$ in roll, azimuth and elevation and $(0.1 \text{ mm}, 0.1 \text{ mm}, 1.0 \text{ mm})$ in x , y , z , respectively. The near-field data for a misaligned probe is calculated using a higher order probe correction scheme which has also been used in the analysis presented in [152]. The resulting near-field data is subsequently transformed assuming an ideal probe alignment. The error is evaluated by comparing the far-field data. For a frequency of 2400 MHz, the probe alignment is not crucial and, therefore, the total error is small. An investigation of the individual contributions is not valuable. Similar to term 1, the errors would be exactly equal for

a first order probe. In the case of the investigated HOP the combined uncertainties are given in Table 7.3.

Point distribution	D (dBi)	HPBW ($^\circ$)	FSSL (dB)	FSLA ($^\circ$)
	16.458	9.182	-15.467	-27.134
Equiangular	± 0.001	± 0.001	± 0.004	± 0.004
Thinned equiangular	± 0.001	± 0.002	± 0.004	± 0.004
Spiral (both pol.)	± 0.002	± 0.003	± 0.003	± 0.004
Spiral (opt. pol.)	± 0.001	± 0.001	± 0.006	± 0.004
Max. determinant	± 0.001	± 0.002	± 0.004	± 0.004

Table 7.3: Term 4 (BTS): Probe alignment error.

Offset measurements

An offset AUT measurement can be interpreted as a measurement of an virtually enlarged antenna. Hence, the source volume containing the antenna is enlarged and, consequently, the geometric angles under which the probe *sees* the AUT are larger. Accordingly, it can be expected that the probe related uncertainty terms, namely “probe relative pattern” and “probe alignment error”, increase with increasing offset. However, the results given in Table 7.4 show that this is only correct for term 1 whereas for term 4 the uncertainty decreases. The individual (6-DOF) uncertainties of term 4 are given in Table 7.5 for regular equiangular sampling (similar for other point distributions) and reveal that only the z alignment error decreases. Since it is the dominant term, the total error decreases as well. The reason is that a translation in the probe z direction can be equally regarded as a measurement with the same probe radiation pattern but at a different measurement distance. In the special case of an offset AUT coordinate system, the measurement distance error is not unique. For example an AUT offset in z by $z_{\text{offset,AUT}}$ causes an offset measurement distance $r_{\text{meas,offset}}(\theta, \forall\phi) = r_{\text{meas}} - z_{\text{offset,AUT}} \cos(\theta)$. Since the effect is varying over the number of measurement samples, it is partly filtered out in the transformation by mode truncation. Simulations with different offsets and probes showed that an offset slightly reduces the error due to a probe misalignment in z . All other DOF change the relative probe pattern and, consequently, the error increases as expected. In conclusion, the uncertainty due to the probe relative pattern caused by approximated probe data, rotational misalignment or translation in x , y , increase with the AUT offset. In contrast, an probe z alignment error is slightly reduced by an AUT offset. These results hold for all spherical near-field measurements and not only for transformation procedures which directly include the AUT offset.

Point distribution	Term 1		Term 4	
	ϵ (dB)	$\Delta\epsilon$ (dB)	ϵ (dB)	$\Delta\epsilon$ (dB)
Equiangular	-43.035	+2.624	-19.618	-0.032
Equiangular ($N = N_{\text{AUT}}$)	-43.000	+2.661	-19.618	-0.032
Equiangular ($N = N_{\text{AUT}}$), proj.	-42.962	+2.610	-19.618	-0.032
Thinned equiangular, proj.	-43.021	+2.638	-19.618	-0.032
Spiral (both pol.), proj.	-42.648	+2.523	-19.618	-0.032
Spiral (opt. pol.), proj.	-42.178	+2.719	-19.618	-0.032
Max. determinant, proj.	-42.996	+2.635	-19.618	-0.032

Table 7.4: Mode power differences (see (6.8) on page 89) for probe related uncertainty terms 1 & 4 (QH2000 measurement) and difference between offsets.

probe alignment error	$\epsilon_{\text{pos. A}}$ (dB)	$\epsilon_{\text{pos. B}}$ (dB)	$\Delta\epsilon$ (dB)
x	-67.327	-60.444	+6.883
y	-64.829	-64.360	+0.469
z	-19.618	-19.650	-0.032
roll	-55.278	-55.078	+0.199
azimuth	-50.553	-44.225	+6.327
elevation	-49.638	-47.831	+1.807

Table 7.5: Individual contributions to uncertainty term 4 (QH2000) and difference between offsets.

7.1.2 Term 7: Antenna under test (AUT) alignment error

The AUT alignment error expresses the effect of a non-ideal mounting of the AUT. Since the AUT has not been touched during the measurement campaign, the related uncertainty is equal for all point configurations. In spherical near-field antenna measurements the 6-DOF can easily be evaluated by rotation and translation of the SMC of the AUT. The estimated alignment errors are (0.2° , 0.02° , 0.02°) in roll, azimuth and elevation and (2 mm, 2 mm, 5 mm) in x , y , z , respectively. The combined uncertainty is small and an investigation of the individual contributions is not valuable.

Point distribution	D (dBi)	HPBW ($^\circ$)	FSL (dB)	FSLA ($^\circ$)
	16.458	9.182	-15.467	-27.134
All grids	± 0.001	± 0.001	± 0.001	± 0.012

Table 7.6: Term 7 (BTS): AUT alignment error.

7.1.3 Term 8: Data point spacing

It has been discussed in Section 2.1 that the radiated field by an AUT can be regarded as quasi-bandlimited. Hence, by increasing the number of modes the error rapidly decreases although it is not zero. Furthermore, scattering close to the antenna (e.g. caused by the mounting structure) increases the error if the scattering sources are not inside the considered minimum sphere. A typical procedure to estimate the error is to repeat the measurement with an smaller step size than required (increases the considered minimum sphere) and to compare the results to the regular sampling step size. For comparing different point distributions this approach is time consuming and, more important, no unique reference exists so that other error sources make it difficult to evaluate the differences. For this reason, an alternative approach is used here. An oversampled near-field measurement is used to calculate a spherical mode representation of the AUT with $N > N_{\text{AUT}}$. Next, the reference spherical mode spectrum is used to generate near-field data for the investigated point distributions which contains also the information of the higher order modes. The generated data is transformed to the far field and compared with the reference in order to evaluate the variations due to aliasing and mode truncation. The uncertainties are shown in Table 7.7. The uncertainties are generally low but are slightly higher for maximum determinant sampling and spiral sampling with optimized polarization. This behavior was expected because the number of redundant samples is low and spatial aliasing occurs as discussed in Section 5.1.6. However, the effect in this measurement scenario is not significant although redundancy will always improve the accuracy.

Point distribution	D (dBi)	HPBW ($^{\circ}$)	FSSL (dB)	FSLA ($^{\circ}$)
	16.458	9.182	-15.467	-27.134
Equiangular	± 0.002	± 0.013	± 0.030	± 0.034
Thinned equiangular	± 0.001	± 0.013	± 0.023	± 0.042
Spiral (both pol.)	± 0.001	± 0.007	± 0.037	± 0.029
Spiral (opt. pol.)	± 0.016	± 0.066	± 0.031	± 0.055
Max. determinant	± 0.010	± 0.035	± 0.057	± 0.055

Table 7.7: Term 8 (BTS): Data point spacing.

Offset measurement

The uncertainty due to the data point spacing in a measurement scenario with AUT offset is given in Table 7.8. In relation to the BTS antenna measurement, the uncertainty term is large except for regular equiangular sampling. The reason is that the mounting structure of the antenna is not well enough separated from the AUT so that significant higher order modes exist which cause spatial aliasing. The n-spectrum (all modes m and s are summed up) of the centered QH2000 SMC is shown in Fig. 7.2. It can be seen that most of the power is concentrated in the lowest modes which indicates that the origin of the expansion is close to the radiation center of

Point distribution	$\epsilon_{\text{pos. A}}$ (dB)	$\epsilon_{\text{pos. B}}$ (dB)	$\Delta\epsilon$ (dB)
Equiangular	-55.358	-56.415	-1.057
Equiangular ($N = N_{\text{AUT}}$)	-25.536	-23.983	+1.553
Equiangular ($N = N_{\text{AUT}}$), proj.	-25.626	-24.254	+1.372
Thinned equiangular, proj.	-25.129	-22.917	+2.212
Spiral (both pol.), proj.	-22.923	-21.606	+1.317
Spiral (opt. pol.), proj.	-12.961	-10.835	+2.126
Max. determinant, proj.	-20.710	-19.542	+1.168

Table 7.8: Uncertainty term 8 for QH2000 measurement and difference between offsets.

the AUT. However, a second peak around $n = 22$ can be observed which represents the scattering of the mounting structure. With regular equiangular sampling, the full spectrum is calculated first and afterwards modes with $n > N_{\text{AUT}} = 17$ are discarded. In the considered test cases, N is equal to 35 and 49 for position A and B, respectively. Thus, the scattering by the mounting structure can be partially filtered and do not cause spatial aliasing. In contrast, the reduced sampling schemes can only resolve modes up to $N = N_{\text{AUT}} = 17$ and are, consequently, affected by the spatial aliasing of the higher order modes. In total, the power contained in the spectrum $n > 17$ relatively to the power for $n \leq 17$ is approximately -23 dB which is close to the stated differences in Table 7.8 except for spiral scanning with optimized polarization. As discussed in Section 5.1.6, spiral scanning with optimized polarization is very susceptible for spatial aliasing errors which is the main reason for the inaccurate results in the considered QH2000 measurement scenario. In this measurement scenario the error increases with the offset but it need to be pointed out that the reference measurements for position A and position B are different which permits a generalization. In addition, the reduction for regular equiangular sampling cannot be generalized too, because the chosen bandlimit N has been rounded so that the ratio N/kr_0 is 1.48 and 1.33 for position A and B, respectively.

In summary, the measurement example shows that mode truncation and spatial aliasing might be a problem if the AUT is mounted in an offset position and close to a reflective surface. Thus, similarly to a centered measurement scenario, it cannot be expected that direct and scattering sources can be separated by modal filtering if they are close to each other. However, in contrast to regular equiangular sampling, the oversampling can be chosen by the operator and is not dictated by the transformation routine. The accuracy might be sufficient for a preliminary antenna test even if the final testing is performed with high oversampling.

7.1.4 Term 10: Position error

In uncertainty analysis for planar near-field measurements the position error is commonly separated in transverse and orthogonal position errors terms due to the specific measurement geometry of a planar scanning in x and y [10]. In the case of SNF antenna measurements, the separation in two separate uncertainty terms is not prac-

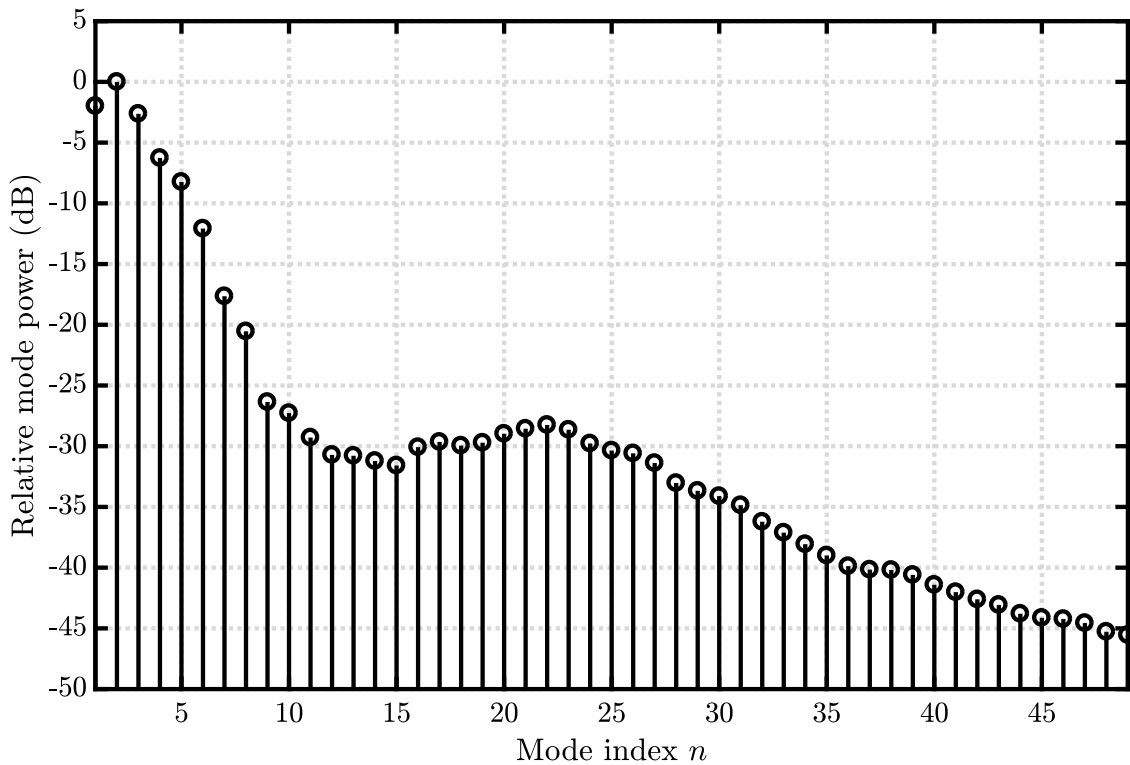


Figure 7.2: QH2000 SMC n-spectrum.

tical because some typical mechanical misalignments (e.g. non-intersecting of axes) causes an position error in all three spherical coordinates θ , ϕ and r which are, in addition, dependent on the specific position. For this reason, all position errors are combined in one uncertainty term whereas each contribution has been calculated separately. In the case of the considered roll-over-azimuth measurement system of the IHF the following individual terms are evaluated:

1. Non-intersecting of axes (0.1 mm).
2. Theta-zero error (0.01°).
3. Elevation error of roll axis (0.01°).
4. Elevation error of azimuth axis (0.01°).
5. Random angular (θ , ϕ) error (0.03°).
6. Probe rotation error (0.08°).

As pointed out in [21], the individual terms may vary for different measurement systems (e.g. a gantry arm measurement system). Please note, that the systematic probe mounting misalignment errors (e.g. measurement distance, angular misalignment) have been already considered in term 4. It should be emphasized, that the evaluation of the error term is a complex task because it requires the simulation of the near-field at irregular points. In addition, care must be taken in order to correctly simulate the irregular measurement coordinates because they depend on the specific measurement setup. For example in a roll-over-azimuth configuration, an elevation error of the roll axis is independent of the roll position. Consequently, the constant elevation error in the global coordinate system causes a changing azimuth and elevation error in the local AUT coordinate system — for example, the

elevation cut is measured as azimuth cut for roll= 90°. It is of utmost importance to correctly represent the actual measurement procedure in the uncertainty evaluation. It makes for example a difference whether the scan is performed as ϕ or θ scanning although the desired measurement locations are the same. The reason is that while the θ position error is constant for all angles ϕ on a ring with constant θ in the ϕ -scanning case, it is inverse for a θ -scanning scheme. The combined uncertainties for the different grids and the used measurement configuration are:

Point distribution	D (dBi)	HPBW (°)	FSSL (dB)	FSLA (°)
	16.458	9.182	-15.467	-27.134
Equiangular	± 0.003	± 0.008	± 0.028	± 0.010
Thinned equiangular	± 0.004	± 0.007	± 0.020	± 0.006
Spiral (both pol.)	± 0.004	± 0.006	± 0.025	± 0.010
Spiral (opt. pol.)	± 0.005	± 0.013	± 0.064	± 0.016
Max. determinant	± 0.006	± 0.005	± 0.008	± 0.006

Table 7.9: Term 10 (BTS): Position error.

In general, the random angular and the theta-zero errors have the largest importance as can be seen from Fig. 7.3 to 7.6 where the relative contribution of each part is shown for the four different parameters. Interestingly, the relative importance of different error sources depends on the used point distributions. However, further studies are needed to investigate these correlations in order to check if these are general casualties of the point distributions or specific for the investigated AUT. Though the total combined uncertainty for different point distributions is similar, they are not similarly affected by different error terms.

Offset measurement

In Section 6.2 it was pointed out that the condition of the problem gets worse without sampling point projection from the minimum sphere to the measurement sphere. Hence, the sampling position is important and it can be expected that the error due

Point distribution	$\epsilon_{\text{pos. A}}$ (dB)	$\epsilon_{\text{pos. B}}$ (dB)	$\Delta\epsilon$ (dB)
Equiangular	-42.655	-42.312	+0.343
Equiangular ($N = N_{\text{AUT}}$)	-42.627	-41.815	+0.812
Equiangular ($N = N_{\text{AUT}}$), proj.	-42.638	-41.897	+0.740
Thinned equiangular, proj.	-42.635	-41.477	+1.158
Spiral (both pol.), proj.	-42.501	-41.425	+1.075
Spiral (opt. pol.), proj.	-38.706	-34.922	+3.784
Max. determinant, proj.	-42.527	-40.803	+1.724

Table 7.10: Uncertainty term 10 for QH2000 measurement and difference between offsets.

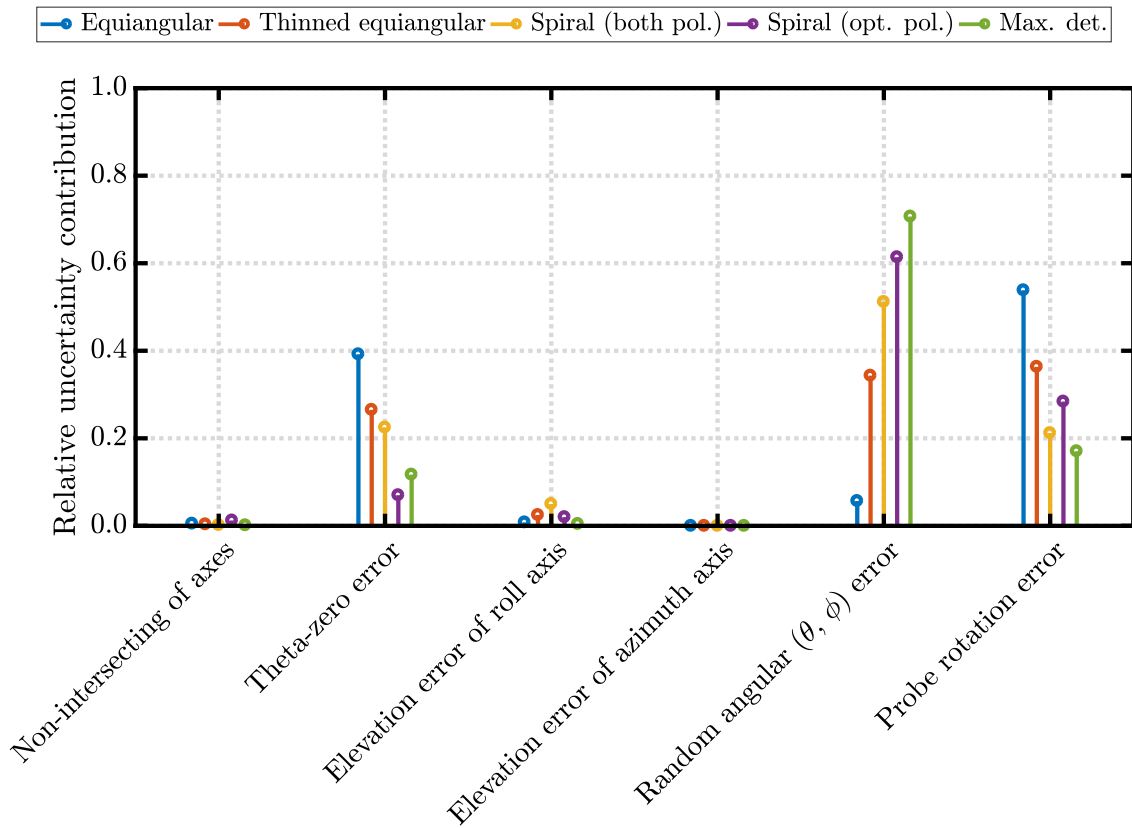


Figure 7.3: Individual directivity uncertainty contributions of uncertainty term 10 (position error) for the BTS antenna measurement (2400 MHz).

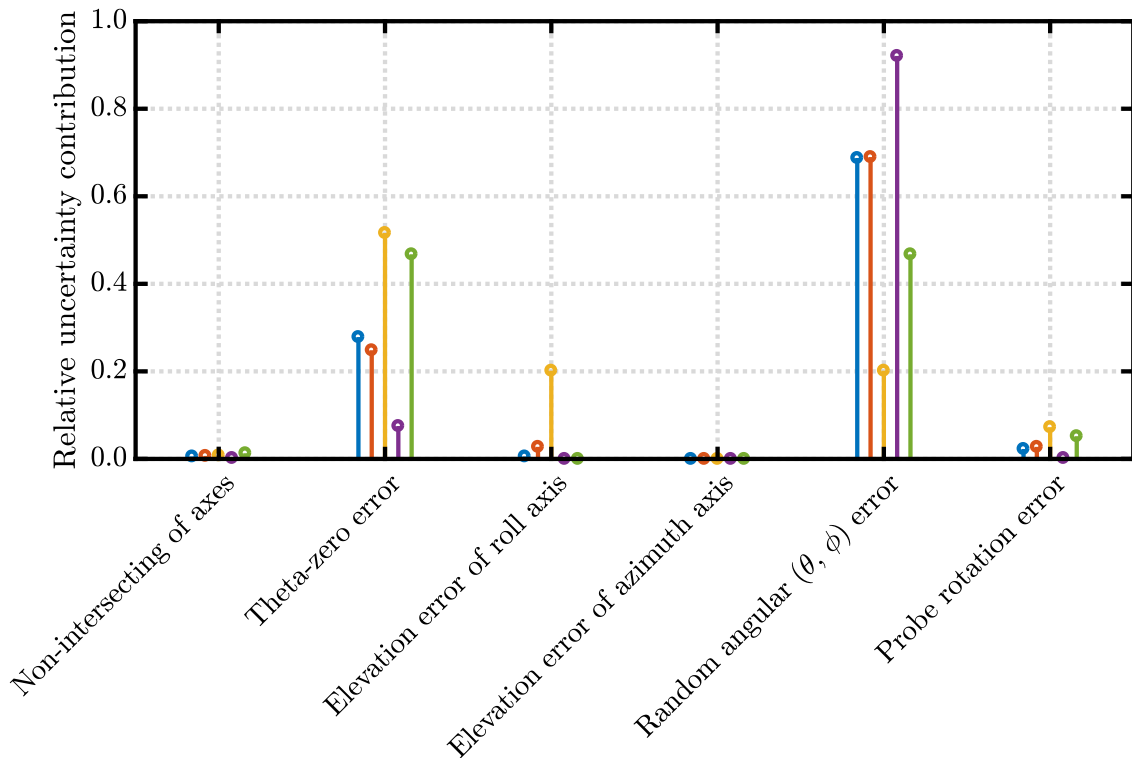


Figure 7.4: Individual HPBW uncertainty contributions of uncertainty term 10 (position error) for the BTS antenna measurement (2400 MHz).

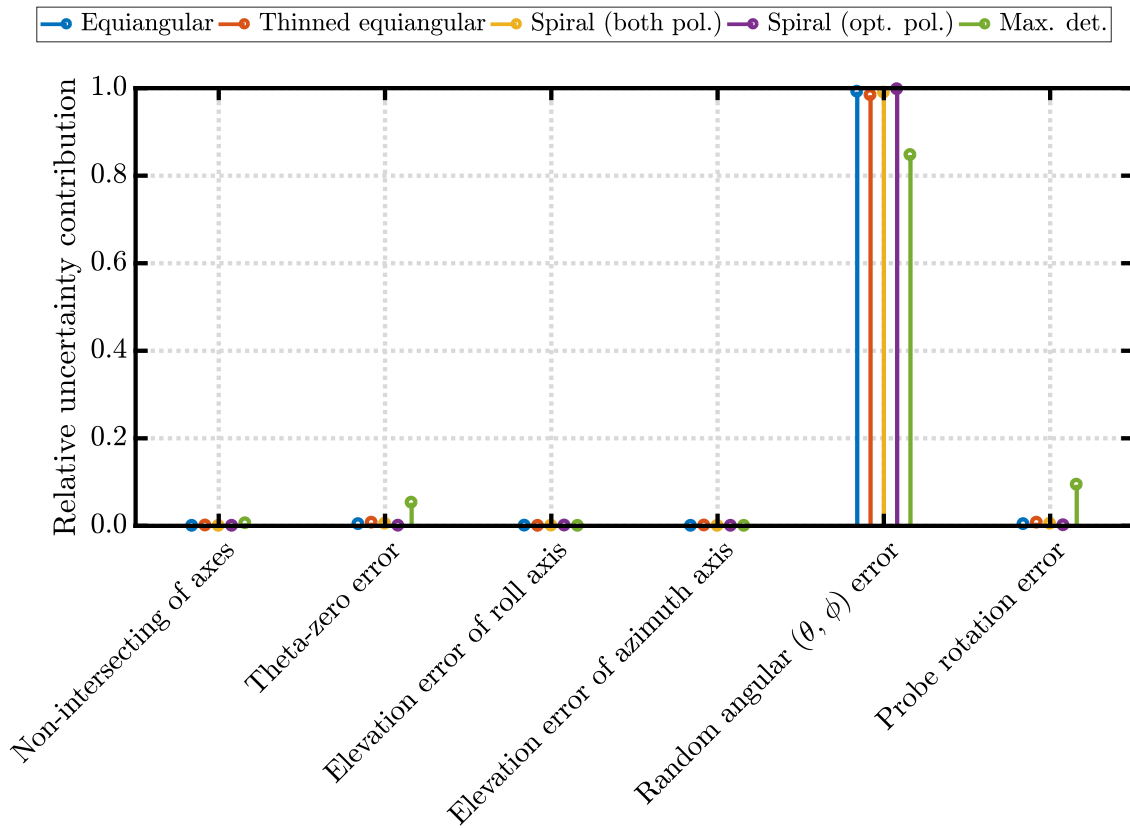


Figure 7.5: Individual FSSL uncertainty contributions of uncertainty term 10 (position error) for the BTS antenna measurement (2400 MHz).

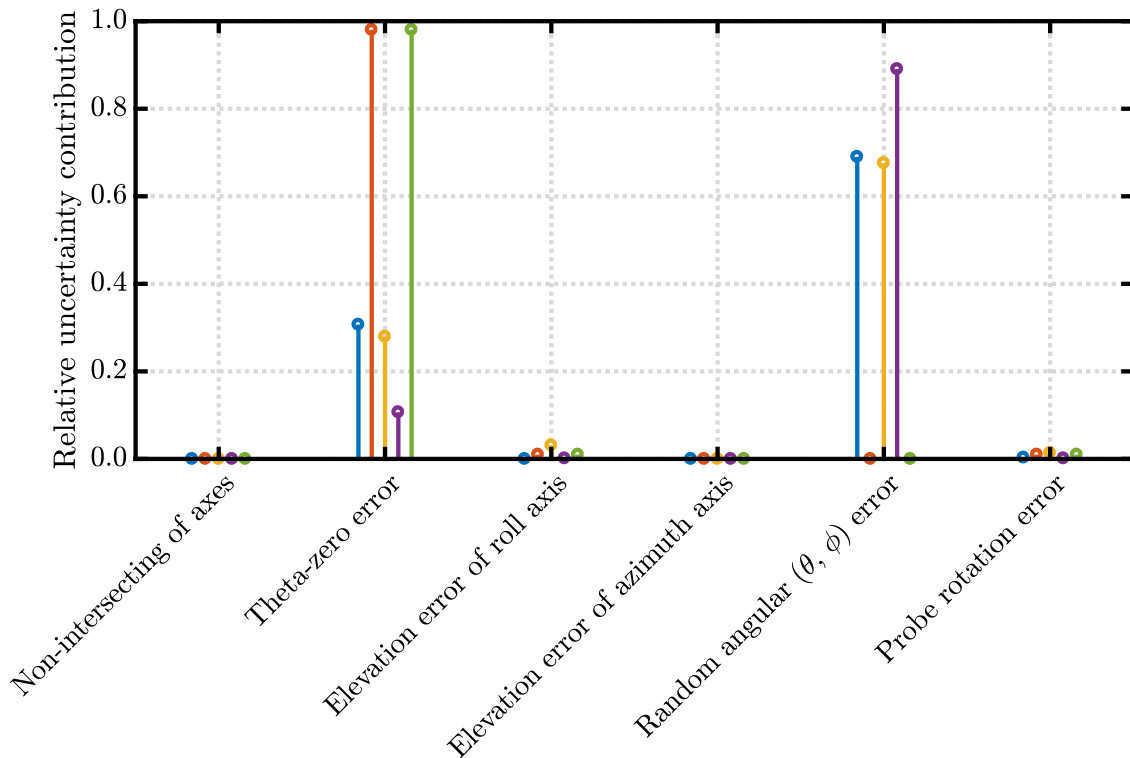


Figure 7.6: Individual FSLA uncertainty contributions of uncertainty term 10 (position error) for the BTS antenna measurement (2400 MHz).

to positioning errors increases simultaneously with the offset. Especially, rotational misalignment in azimuth and elevation lead to increased absolute position errors in x , y and z if the offset is larger. The assumption is confirmed by the results given in Table 7.10. First, it can be noticed that the error increases if the redundancy in the point configuration is reduced. Next, the error for the non projected equiangular measurement grid is slightly larger which indicates that this point configuration is more sensitive for position errors compared to its projected counterpart.

7.1.5 Term 12: Multiple reflections

The uncertainty term describes the effect of the signal $\text{AUT} \rightarrow \text{probe} \rightarrow \text{AUT} \rightarrow \text{probe}$. The uncertainty is typically evaluated by comparing multiple repeated measurements where the measurement radius is varied in $\lambda/8$ steps. However, in many SNF measurement ranges the probe is mounted at a fixed measurement radius and cannot be easily translated. This is also the case at the IHF and, therefore, the probe mounting was extended by an additional spacer of $\lambda/4$ as shown in Fig. 7.7. However, inserting and removing the spacer requires dismounting of the probe which causes additional uncertainties due to limited reproducibility. Even more severe is the correlation with the error term 16 for room scattering because if the probe location is shifted the reflected waves from the walls sum up differently. Errors due to multiple reflections and room scattering are difficult to separate, especially at low frequencies. According to the common practice of repeated measurements at two measurement distances $\lambda/4$ apart, the following differences have been determined

Point distribution	D (dBi)	HPBW ($^\circ$)	FSSL (dB)	FSLA ($^\circ$)
	16.458	9.182	-15.467	-27.134
Equiangular	± 0.006	± 0.006	± 0.177	± 0.005
Thinned equiangular	± 0.002	± 0.021	± 0.176	± 0.004
Spiral (both pol.)	± 0.001	± 0.033	± 0.203	± 0.003
Spiral (opt. pol.)	± 0.019	± 0.099	± 0.845	± 0.087
Max. determinant	± 0.002	± 0.030	± 0.256	± 0.008

Table 7.11: Term 12 (BTS): Multiple reflections.

According to the results, multiple reflections have a strong effect on the first side lobe level and are highest for spiral sampling with optimized polarization. As mentioned above, errors due to room scattering and multiple reflections are difficult to separate and, thus, the total error might be overestimated. In order to investigate the correlation in detail, different additional measurements have been performed to measure the effect of multiple reflections.

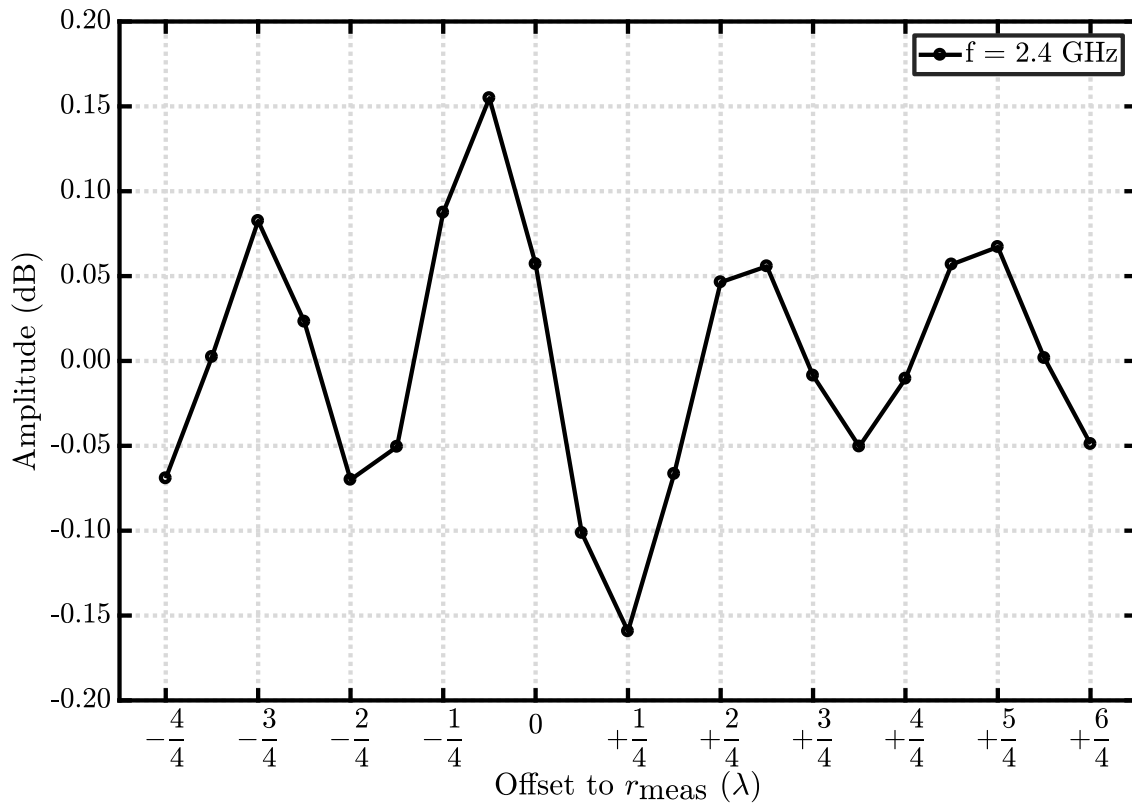
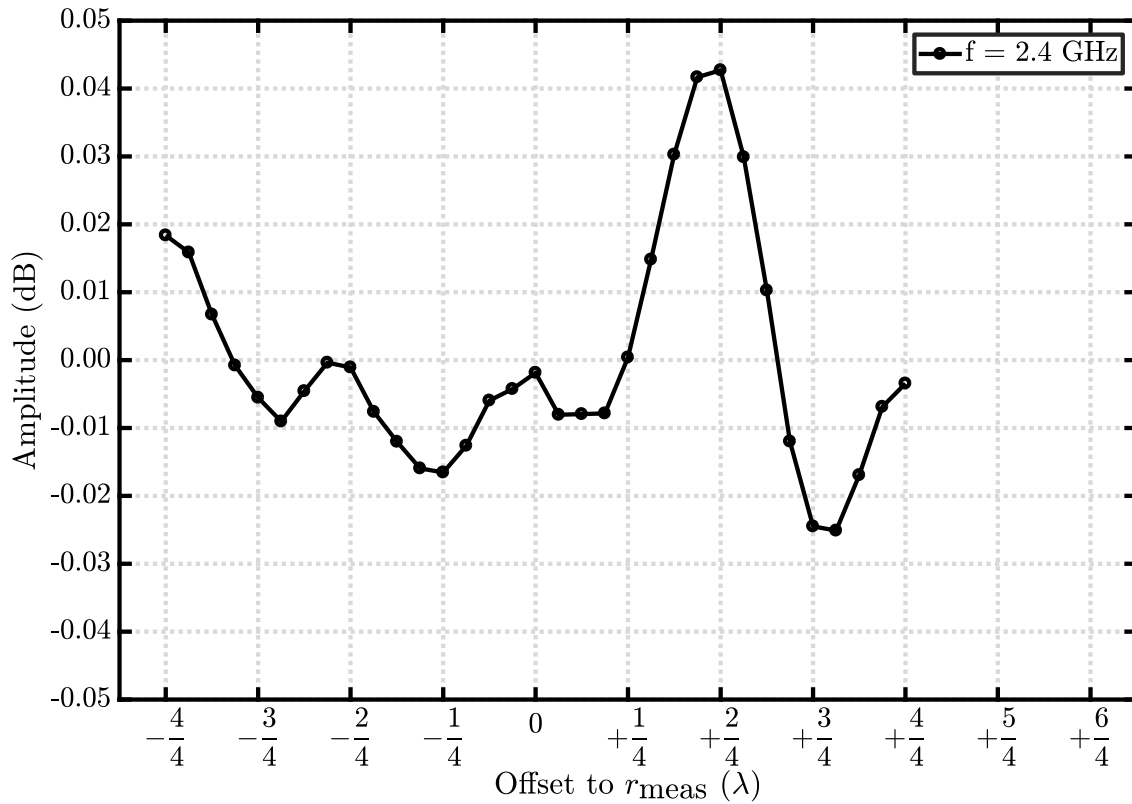
At first, it was tried to measure the near-field standing wave due to multiple reflection. For this purpose, additional near-field measurements with varying AUT-probe distances have been performed in mechanical boresight direction by using a linear slide below the roll axis which is usually used to position the AUT in the center of rotation. Please note, that this configuration cannot be used for a full SNF measurement because the AUT is moved out of the center of rotation but the near-field



Figure 7.7: Probe displaced by $\lambda/4$ with additional spacer.

measurement distance is not changed. However, for mechanical boresight ($\theta = 0^\circ$) and only for mechanical boresight a translation of the probe is equal to a translation of the AUT because both z axes are coincident. The results are shown in Fig. 7.8. Although a standing wave can be seen, the frequency of the oscillation does not fit to the AUT-probe distance. The distance between two maximums should be $\lambda/2$ but is around $5\lambda/8$. For this reason, the reflection is most likely not produced by the probe but by something else. It is also important to mention, that the AUT does not radiate in mechanical boresight but has an electrical downtilt of 12° . Repeating the measurements for electrical boresight give the results shown in Fig. 7.9. Please note that this measurement was only possible by using an available linear floor side axes (below the azimuth positioner) which compensated the angle between the AUT and probe z -axis. The standing wave is not clearly seen in this measurement although some small oscillations (< 0.05 dB) exist. It might be, however, that the reflections are reduced due to the mechanical orientation of the AUT which's aperture is not anymore orthogonal to the probe z axis but tilted by 12° . Hence, the scattered signal might not return to the probe but be reflected somewhere else.

Next, time domain measurements were performed in order to identify a multiple reflection. Fig. 7.10 shows the received signal in time domain for angles $\theta = [-12^\circ, 0^\circ]$. As can be seen, reflected signals are present but again cannot be well matched to the multiple reflection between AUT and probe which should have a relative path length of $2r_{\text{meas}} \approx 4$ m. The large reflection around 2 m for $\theta = 0^\circ$ is likely to come from the walls at the sides or behind the probe. Since the absorbers on the wall are in the near field of the AUT and probe, the assumption of a reflected plane wave is not valid and, consequently, is not exactly possible to locate the scatterer

Figure 7.8: Near-field standing wave for BTS antenna at $\theta = 0^\circ$.Figure 7.9: Near-field standing wave for BTS antenna at $\theta = -12^\circ$.

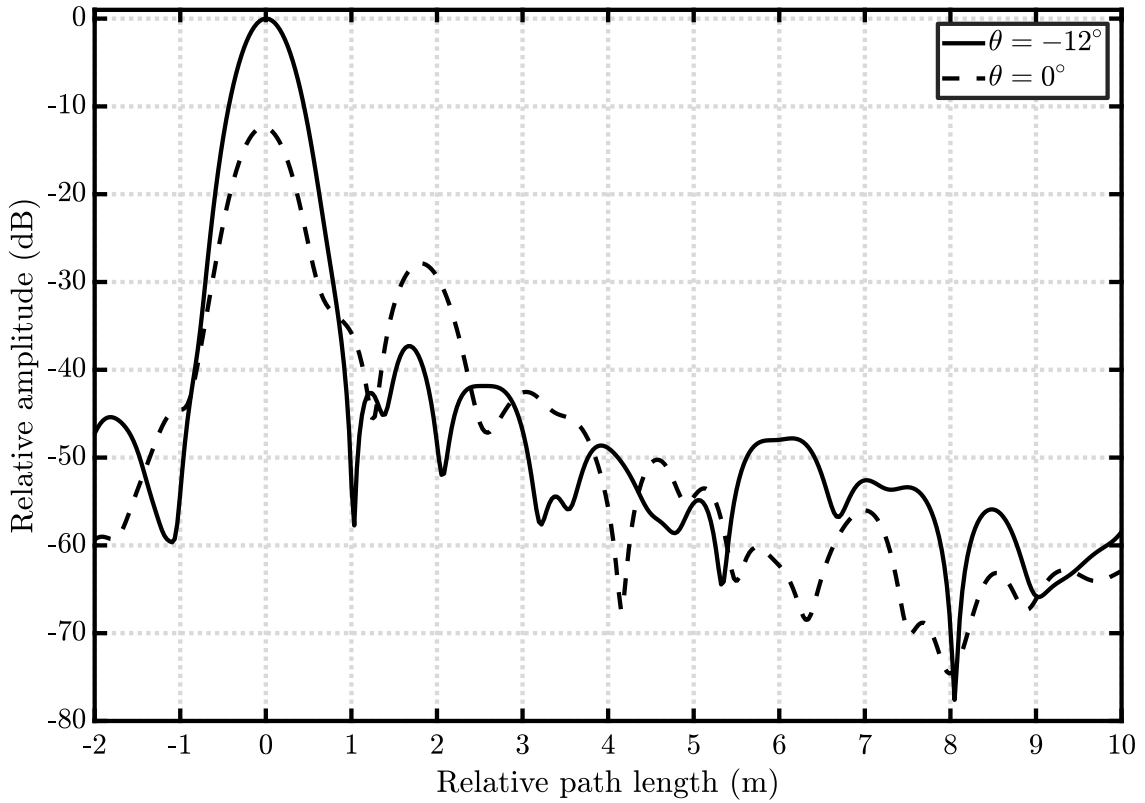


Figure 7.10: Near-field time domain analysis for BTS antenna (Blackman window, $f = [1.7 \text{ GHz}, 2.7 \text{ GHz}]$, $\Delta f = 2 \text{ MHz}$).

by ray-tracing. Overall, additional measurements have not clearly shown a standing wave between AUT and probe although the measurement results for two different measurement distances are not equal.

Since errors due to room scattering and multiple reflections are inevitable coupled by the measurements, another approach was used in order to point out the correlations of room scattering and multiple reflections. The chamber is partly simulated with the full wave simulation tool FEKO [153]. More details about the simulation are given in Section 7.1.9 and Appendix D. In summary, the compact range reflector of the hybrid measurement chamber as well as the absorber close to the spherical near-field setup have been modeled and two simulations have been conducted where the probe location has been translated by $\lambda/4$. Since the simulation does not take into account multiple reflections between the AUT and probe, the differences are only due to the room scattering. The resulting differences for an AUT measurement with equiangular sampling in this simulated measurement chamber are:

	D (dBi)	HPBW ($^{\circ}$)	FSL (dB)	FSLA ($^{\circ}$)
Only Absorber (sim.)	± 0.013	± 0.005	± 0.090	± 0.018
Only Reflector (sim.)	± 0.004	± 0.001	± 0.033	± 0.004
Room and mult. reflection (meas.)	± 0.006	± 0.006	± 0.177	± 0.005

The simulated differences for a measurement with a displaced probe without multiple reflections are comparably large as the measured differences which include multiple reflections as well as the different room scattering. The results and the analysis emphasize that errors due to room scattering and multiple reflections are difficult to separate by measurements and that the common practice of uncertainty evaluation for these terms needs to be enhanced in order to correct for that correlation. It is surprising, that this issue has not been addressed comprehensively before. The reason might be that the effect is overestimated and relatively small for the common used method so that it can be seen as a conservative approach and that a more accurate method is, up until now, not available. In addition, the non-symmetric measurement range design with the probe mounting in a corner of the hybrid IHF measurement range has an effect on these results. Nevertheless, this fact must be taken into account when the presented results of the commonly applied method are compared for different measurement grids.

Offset measurement

The relative mode power error levels for the comparison of two measurements with a $\lambda/4$ different measurement radius in an offset measurement scenario are given in Table 7.12 and show that the error levels are reduced (except for spiral scanning with optimized polarization) if the offset is increased. Due to a larger offset, the AUT probe distance changes rapidly for different angles and this will affect the standing wave between them. According to the results, the effect is positive and the uncertainties due to multiple reflections can be reduced. However, the correlation with room scattering is still a problem and most probably the reason for the increased error for spiral scanning with optimized polarization due to spatial aliasing.

Point distribution	$\epsilon_{\text{pos. A}}$ (dB)	$\epsilon_{\text{pos. B}}$ (dB)	$\Delta\epsilon$ (dB)
Equiangular	-25.660	-28.448	-2.787
Equiangular ($N = N_{\text{AUT}}$)	-24.743	-28.910	-4.166
Equiangular ($N = N_{\text{AUT}}$), proj.	-24.773	-29.643	-4.870
Thinned equiangular, proj.	-25.351	-28.553	-3.203
Spiral (both pol.), proj.	-24.750	-27.688	-2.938
Spiral (opt. pol.), proj.	-19.862	-17.507	+2.355
Max. determinant, proj.	-24.310	-25.699	-1.389

Table 7.12: Uncertainty term 12 for QH2000 measurement and difference between offsets.

7.1.6 Term 13: Receiver amplitude nonlinearity

Modern microwave receivers are very linear and the error due to the amplitude non-linearity is difficult to measure [10,154]. Typically, the measurement is repeated with different power levels while the signal to noise ratio is kept fixed. Since the errors are most often negligible compared to other error sources and a comparison between

different measurement grids might, thus, be difficult due to other errors, a different strategy is used here. The receiver nonlinearity is approximated by a polynomial based on multiple full sphere near-field measurements with different power levels. This nonlinearity distortion is applied to the simulated near-field data of each point distribution. The uncertainties are estimated from the far-field comparison and are tabulated in Table 7.13. The term is independent of the offset and, thus, no investigation has been performed with respect to the AUT offset.

Point distribution	D (dBi)	HPBW ($^\circ$)	FSSL (dB)	FSLA ($^\circ$)
	16.458	9.182	-15.467	-27.134
Equiangular	± 0.002	± 0.002	± 0.004	± 0.003
Thinned equiangular	± 0.002	± 0.002	± 0.004	± 0.004
Spiral (both pol.)	± 0.002	± 0.001	± 0.004	± 0.003
Spiral (opt. pol.)	± 0.002	± 0.002	± 0.012	± 0.001
Max. determinant	± 0.002	± 0.002	± 0.004	± 0.004

Table 7.13: Term 13 (BTS): Receiver amplitude nonlinearity.

7.1.7 Term 14: System amplitude and phase errors

From experience it has been learned, that the systematic amplitude and phase errors for measurements in the IHF SNF measurement chamber are mainly caused by drift due to the long acquisition times in step mode. The amplitude and phase variation over 48 h are shown in Fig. 7.11. In order to reduce the effect of the drift on the measurements, one near-field point is remeasured multiple times during the acquisition (approximately every 20 min). The amplitude and phase variations are interpolated and used for correction of the phase and the amplitude of the measurement data. The residual error after drift correction is estimated by comparing the results for spline and linear drift interpolation as shown in Fig. 7.12. The resulting uncertainties are listed in Table 7.14.

Point distribution	D (dBi)	HPBW ($^\circ$)	FSSL (dB)	FSLA ($^\circ$)
	16.458	9.182	-15.467	-27.134
Equiangular	± 0.000	± 0.000	± 0.001	± 0.000
Thinned equiangular	± 0.000	± 0.000	± 0.000	± 0.001
Spiral (both pol.)	± 0.000	± 0.000	± 0.000	± 0.000
Spiral (opt. pol.)	± 0.004	± 0.000	± 0.008	± 0.003
Max. determinant	± 0.001	± 0.000	± 0.002	± 0.001

Table 7.14: Term 14 (BTS): System amplitude and phase errors.

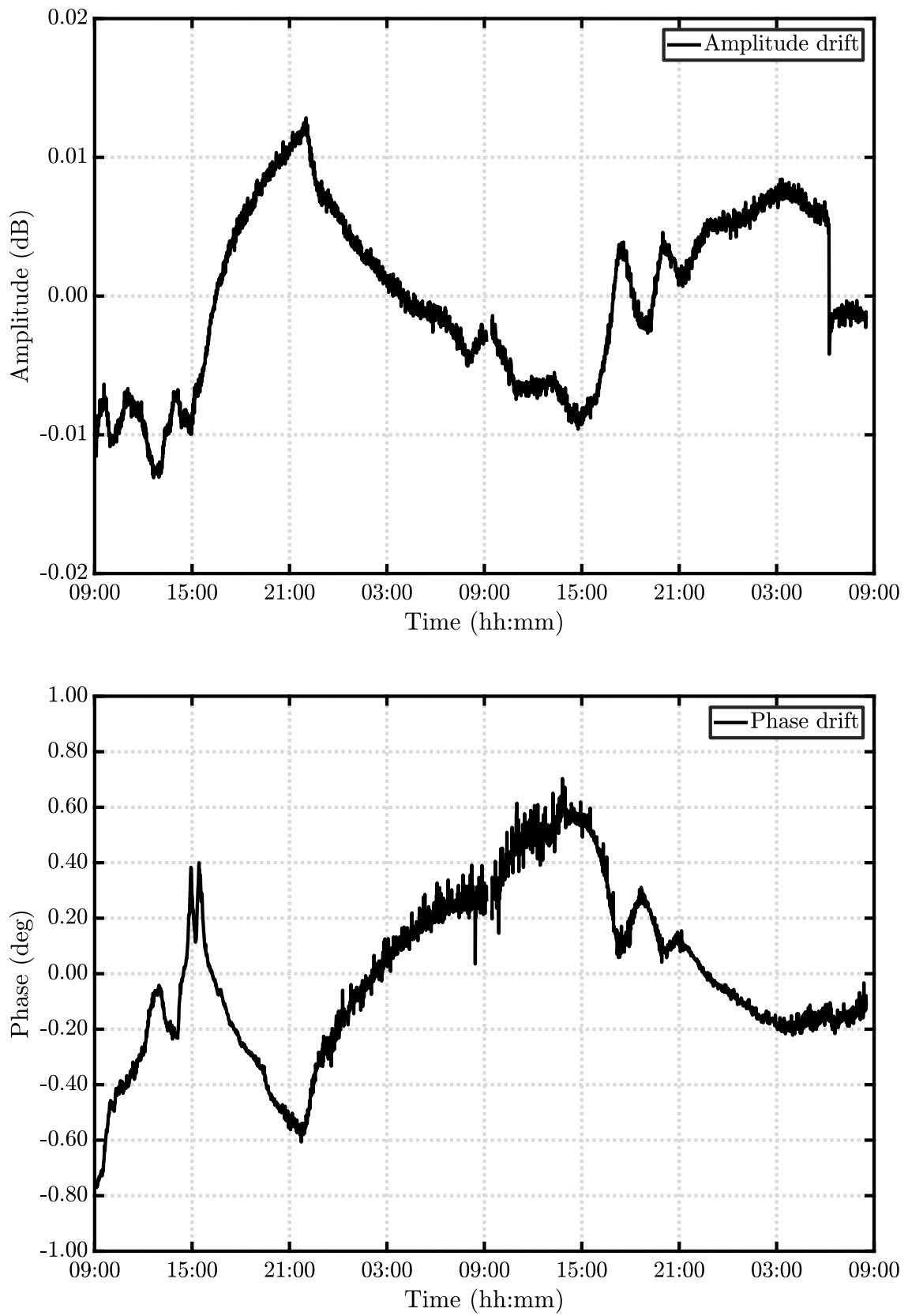


Figure 7.11: Amplitude and phase drift over 48 h at 2400 MHz.

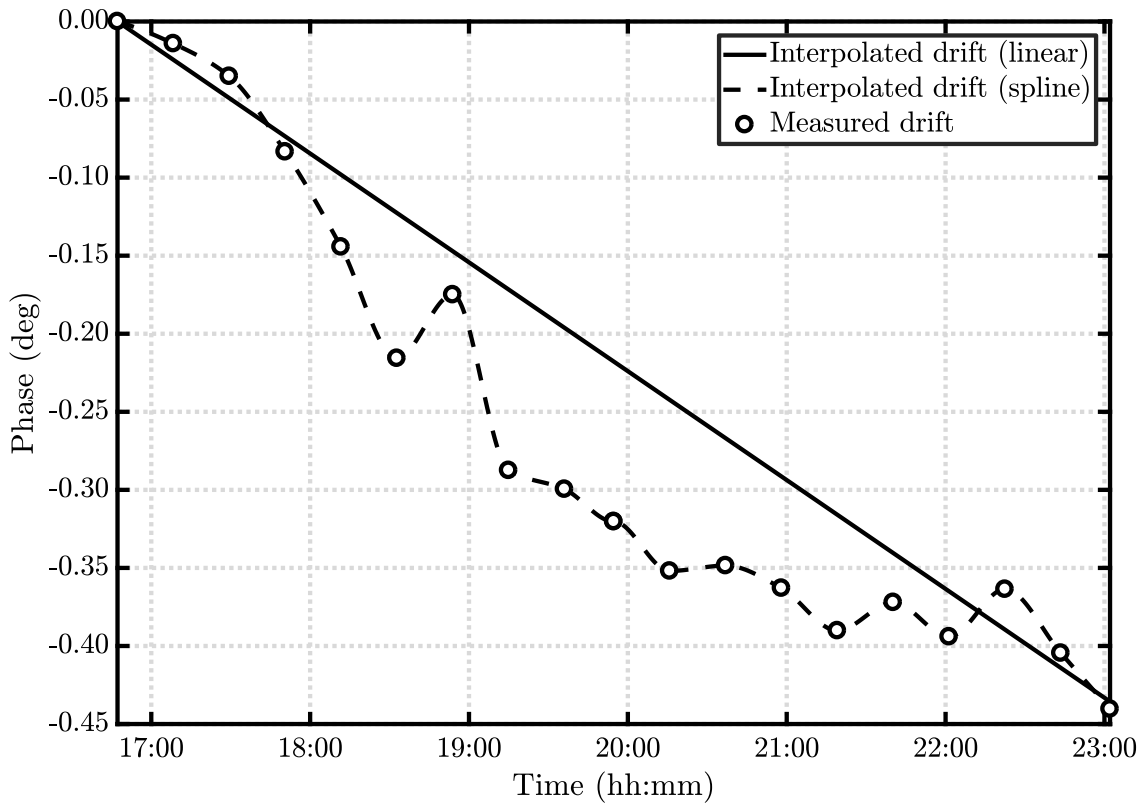


Figure 7.12: Phase drift correction function (linear and spline interpolation) for a BTS near-field measurement at 2400 MHz.

7.1.8 Term 15: Receiver dynamic range

The effect of limited dynamic range is simulated by distorting the near-field data with random noise according to the measured signal to noise ratio of the measurement system ($\text{SNR} \approx 5.6 \cdot 10^{-05} \approx -85 \text{ dB}$, $1\sigma \approx 2.36 \cdot 10^{-05}$). Table 7.15 lists the calculated uncertainty values.

Point distribution	D (dBi)	HPBW ($^\circ$)	FSL (dB)	FSLA ($^\circ$)
	16.458	9.182	-15.467	-27.134
Equiangular	± 0.000	± 0.000	± 0.001	± 0.000
Thinned equiangular	± 0.000	± 0.000	± 0.001	± 0.000
Spiral (both pol.)	± 0.000	± 0.000	± 0.002	± 0.001
Spiral (opt. pol.)	± 0.000	± 0.001	± 0.001	± 0.001
Max. determinant	± 0.000	± 0.001	± 0.001	± 0.001

Table 7.15: Term 15 (BTS): Receiver dynamic range.

7.1.9 Term 16: Room scattering

Due to the limited reflection suppression of microwave absorbing material, reflected signals enter the test zone which contains the AUT. These extraneous signals cause

measurement errors because the probe correction in the transformation assumes that the test zone field is determined only by the direct path between probe and AUT. The error term might be evaluated by translating the probe and AUT in the measurement chamber while keeping the relative alignment constant. However, this is typically not possible in a SNF antenna measurement range and, thus, other methods are frequently used. The extraneous sources are most often located well outside of the AUT minimum sphere so that they cause an error field with a high spatial variation. Therefore, they are partly filtered by the transformation due to the mode truncation and the filtering can be enhanced by oversampling. Consequently, comparing results for a regular and a highly oversampled measurement allow a rough estimation of the room scattering. Post-processing methods are another possibility to estimate the effect of room scattering [10]. These methods are available in most commercial software and were developed for reflection suppression but can be equally used to estimate room scattering. They are based on modal filtering where, in addition, the AUT is moved out of the center of rotation in order to improve the filtering capabilities. In general, estimating room scattering by measurements is time consuming because highly oversampled measurements are required. In the context of this thesis, another drawback is that no unique reference field exists and, thus, a comparison between different point distributions is difficult. Simulation of the measurement chamber represent a more general and more powerful approach and is getting more frequently used because the computational resources are nowadays available. This approach has already been used to investigate the performance of reflection suppression methods [155]. Nevertheless, simulations are still limited by the available hardware and up until now full measurement chamber simulations are only feasible for low frequencies (some GHz [156, 157]). For this reason, the simulation model used in this thesis is limited to the compact range reflector and the absorbers in the corner of the near-field probe because they are most important. The schematic is shown in Fig. 7.13 where the shown coordinate system represents the location of the near-field probe and the blue sphere represents the test zone with a radius of 1 m. The evaluation is performed on a sphere because it is a closed volume containing all information about the field inside and is naturally suited for a spherical mode representation. This approach is closely related to spherical near-field scanning [36] where the quality of a test zone is investigated. However, in the context of this thesis this method is applied for the first time to spherical near-field test zones and, in addition, used for measurement uncertainty evaluation. The absorber on the wall are typical pyramidal absorber AEP-24 and AEP-18 on the one and wedge absorber AEPW-12 on the other side [158]. Since the exact dielectric properties of the absorbing material are not available, $\epsilon'_r = 1.95$, $\epsilon''_r = 1.4$ and $\tan \delta = 0.71795$ [159] are used. Although this is not exact, it is assumed that the used values are close to the true value and experience showed that small changes in the parameters do not significantly change the scattered field. The compact range reflector geometry is imported as CAD file and its material in the simulation is PEC. The simulation software is FEKO [153] and runs on a computer with 24 cores (2.2 GHz) and 256 GB RAM (see Appendix D for more details).

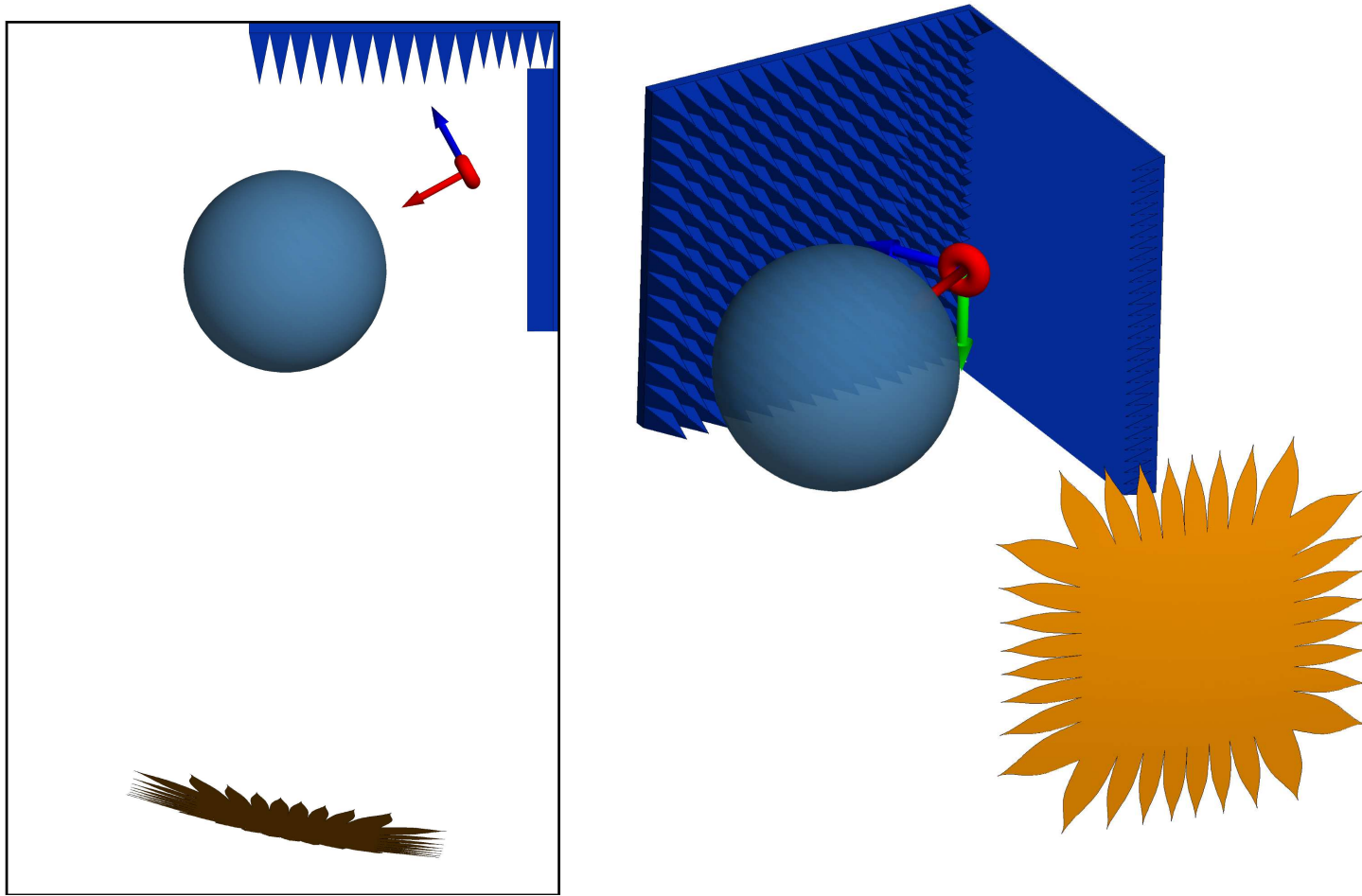


Figure 7.13: IHF measurement chamber schematic in top (left) and perspective (right) view.

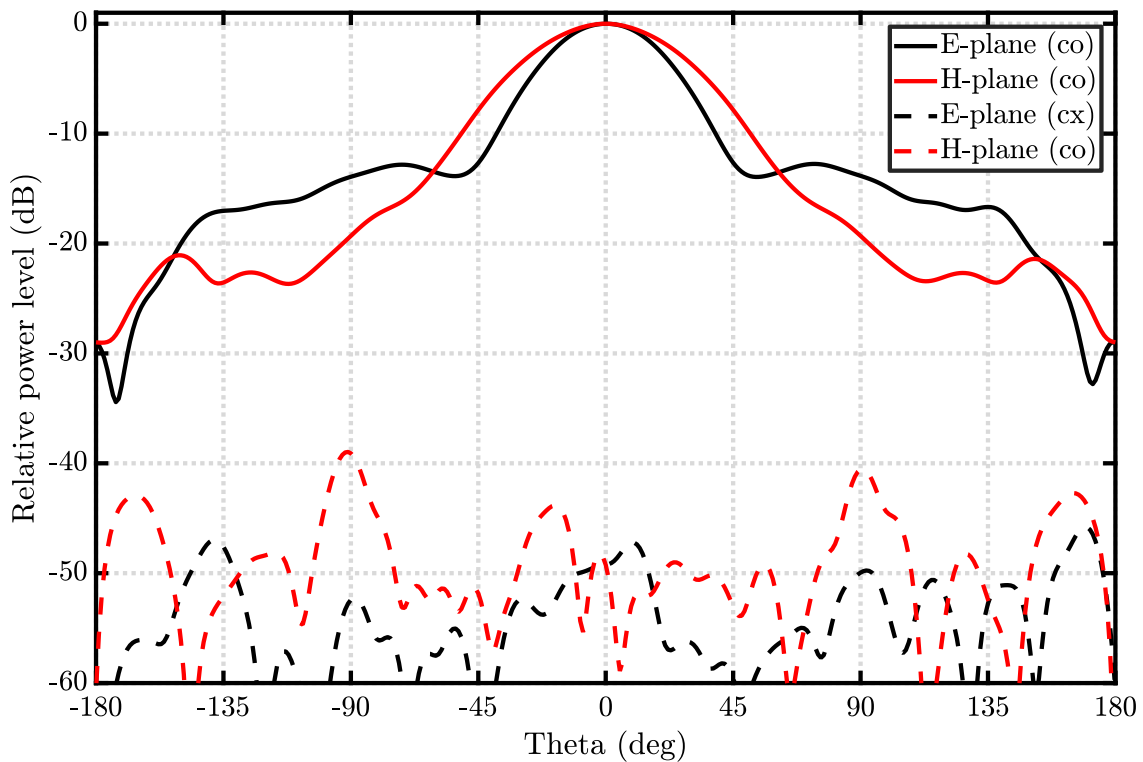


Figure 7.14: SH800 E-plane and H-plane radiation pattern at 2400 MHz.

The individual test zone field contributions ($r = 1$ m, 2400 MHz) of the direct probe field and the scattered field of the absorber and the reflector are shown in Fig. 7.15 and Fig. 7.16 for horizontal and vertical probe polarization. The coordinate system is defined in the way that the coordinates $(EL, AZ) = (0^\circ, 0^\circ)$ point in the direction of the probe. A positive azimuth angle means a rotation in the direction of the compact range reflector. Please note, that the waves may have traveled through the test zone. It can be seen that the scattered waves from the reflector have, as expected, a higher amplitude than the scattered field from the absorbers. In total, the power levels ($[H, V]$ probe polarization) relative to the direct signal power entering the test zone volume are approximately $[-23.1$ dB, -18.7 dB] and $[-47.2$ dB, -46.5 dB] for the scattered waves coming from the reflector and the absorber, respectively. Hence, the scattered power reflected to the test zone differs around 4 dB for the reflector while it changes less than 1 dB for the absorber when the probe is rotated. This effect is due to the probe pattern which has at this frequency (different at higher frequencies) a larger beamwidth in the H-plane compared to the E-plane (Fig. 7.14). Consequently, for a vertical orientation the probe radiation towards the reflector (angles of approximately 35° to 55°) and subsequently the scattered field is higher. Fig. 7.17 and Fig. 7.18 show the normalized surface currents on the absorber which also show a dependency on the probe pattern, mainly the backward radiation. Furthermore, fields scattered by the reflector are higher in the lower hemisphere which can be explained by the geometry of the reflector. The range reflector is designed for a double offset feed position so that the normal vectors on the reflector surface are tilted towards the bottom of the chamber as well as towards the chamber side of the near-field probe.

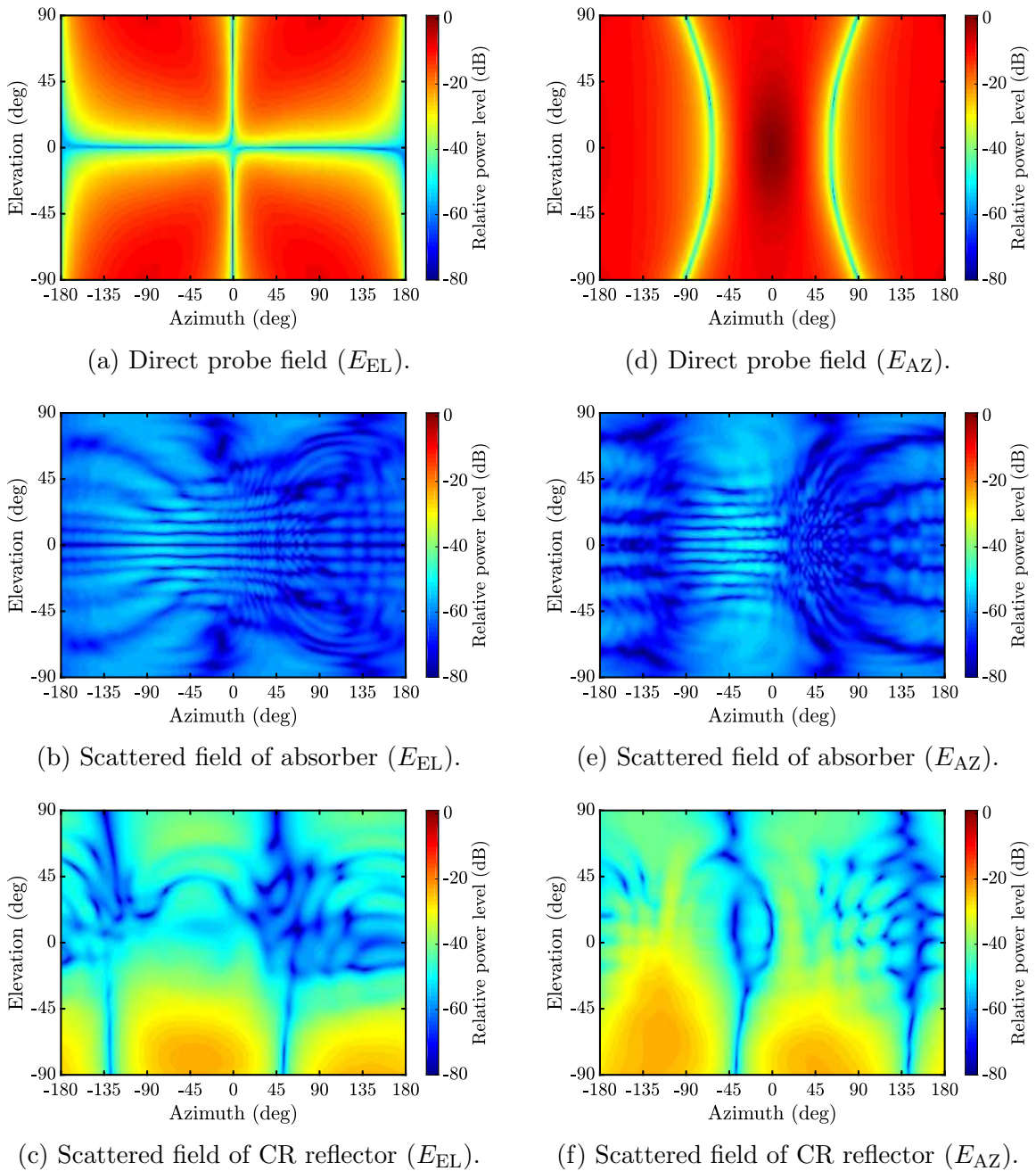


Figure 7.15: Test zone field contributions (2400 MHz) for horizontal polarized (E_{AZ}) probe.

Overall, it is important to emphasize that the room scattering is different for the horizontal and vertical oriented probe because the probe radiation pattern is not rotational symmetric. For this reason, the test zone field distortions are not equal for both polarizations which has to be considered in the simulation of the received AUT signal. In order to calculate the effect of distorted test zone fields on the AUT measurement, first, the test zone fields for horizontal and vertical probe orientation are transformed to spherical mode spectra which represent the incoming spherical waves for the specific probe orientation (see (2.18)). Next, the known AUT reference SMC are used to determine the received signal for every measurement point of the

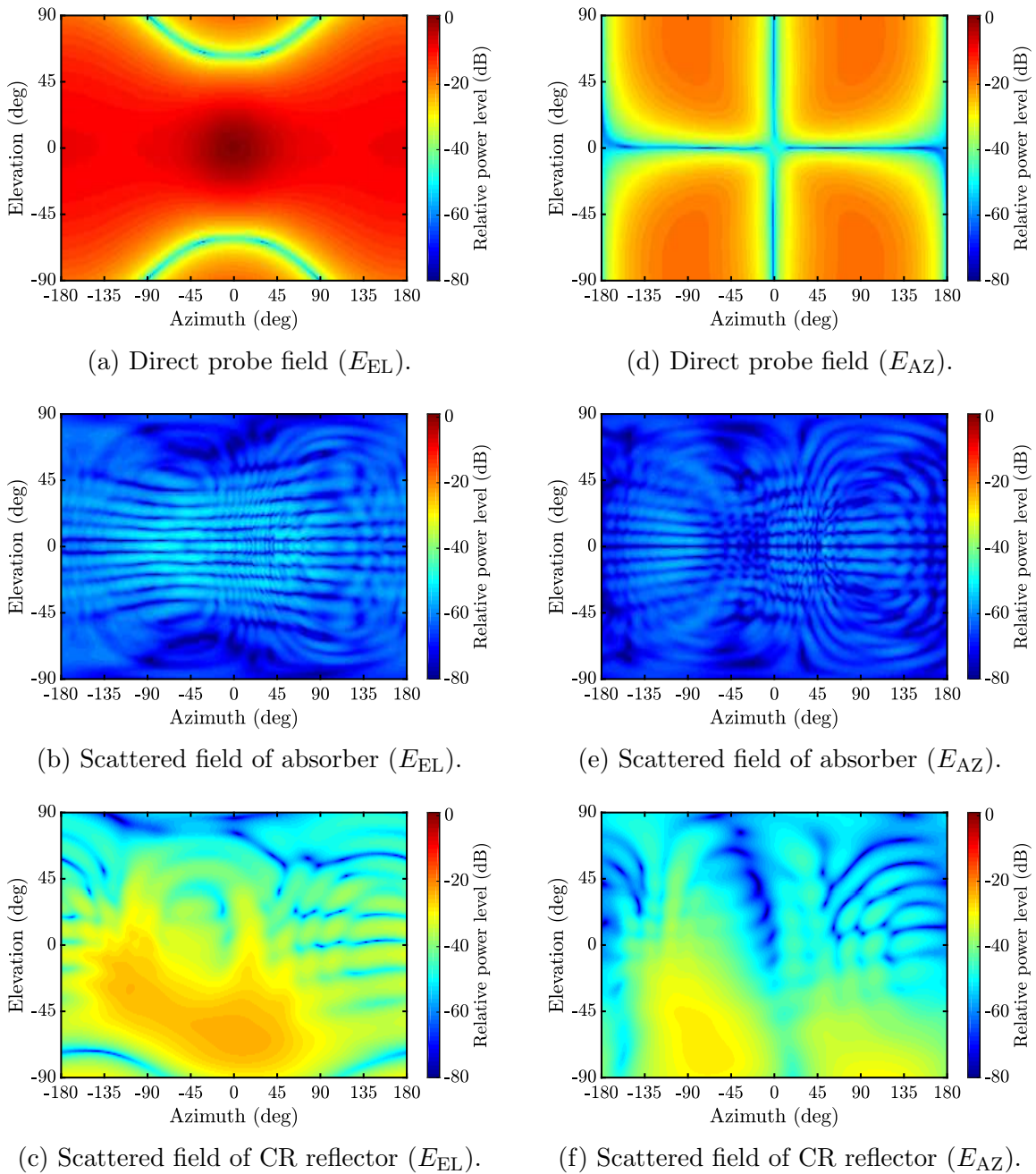


Figure 7.16: Test zone field contributions (2400 MHz) for vertical polarized (E_{EL}) probe.

considered point distribution. Similar to the evaluation of the uncertainty term 10, is important to correctly represent the measurement configuration. According to the roll-over-azimuth configuration at the IHF the AUT is only rotated in roll and azimuth which means that the mechanical boresight direction of the AUT is never directed towards the ceiling or bottom of the measurement range. It is convenient for the simulation to rotate the AUT SMC according to the mechanical rotation angles in roll and azimuth and to keep the test zone field fixed. The estimated uncertainties (RSS of both contributions) based on the simulations are given in Table 7.16.

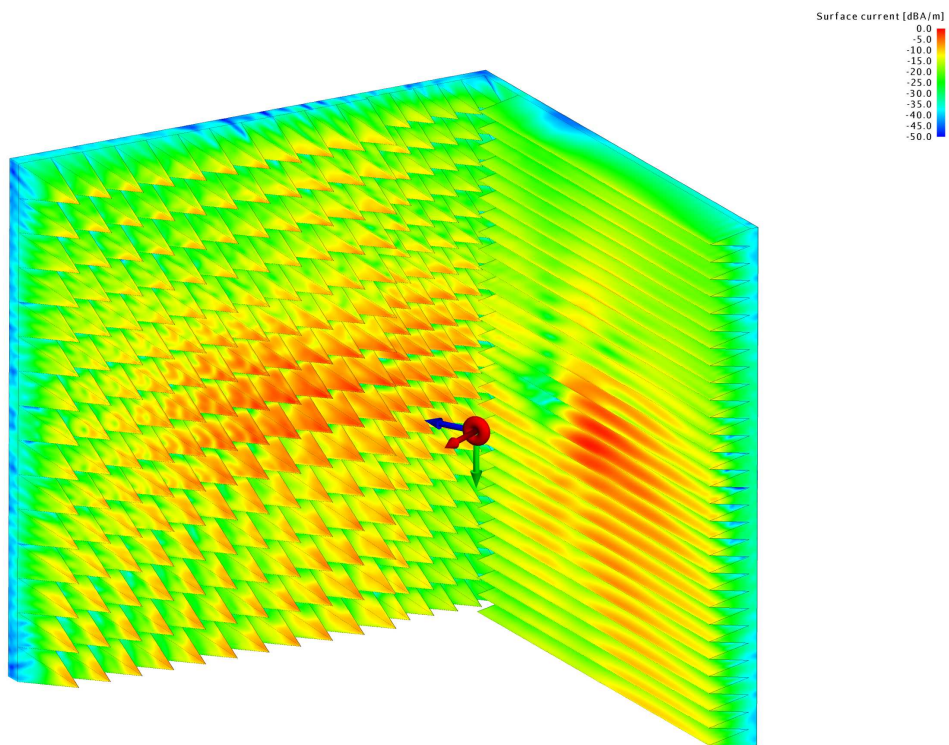


Figure 7.17: Normalized surface currents for probe H-polarization (2400 MHz).

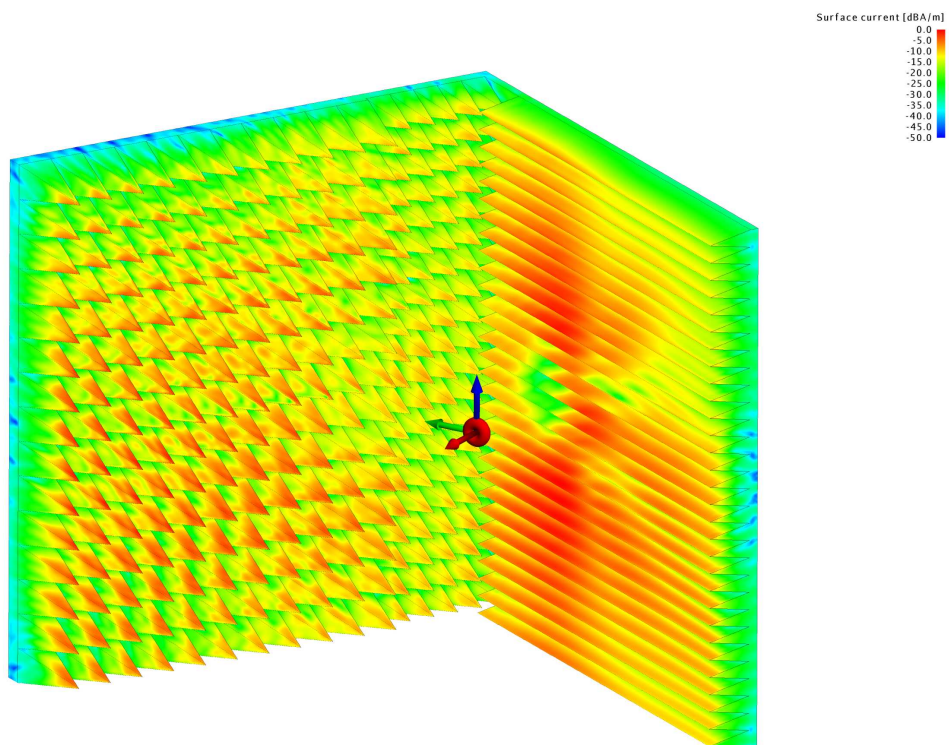


Figure 7.18: Normalized surface currents for probe V-polarization (2400 MHz).

Point distribution	D (dBi)	HPBW ($^\circ$)	FSSL (dB)	FSLA ($^\circ$)
	16.458	9.182	-15.467	-27.134
Equiangular	± 0.067	± 0.013	± 0.084	± 0.029
Thinned equiangular	± 0.069	± 0.016	± 0.078	± 0.024
Spiral (both pol.)	± 0.058	± 0.029	± 0.076	± 0.012
Spiral (opt. pol.)	± 0.044	± 0.059	± 0.112	± 0.031
Max. determinant	± 0.079	± 0.013	± 0.022	± 0.053

Table 7.16: Term 16 (BTS): Room scattering.

From the relative power levels of the reflected signals, it can be expected that the effect of the compact range reflector is more significant than the effect from the absorber. This is verified by the investigation of the individual terms shown in Fig. 7.19. The individual contributions are added (i.e. worst case) instead of using the RSS procedure in order to compensate for underestimation of the error by the simplified simulation model. Similar to the individual contribution for error term 10 (multiple reflections) the effect of the individual contributions depends on the point distributions. However, the results are only valid for the investigated AUT and can, thus, not easily be generalized. Further research is necessary to investigate possible dependencies but it can be expected that the analysis is difficult due to the fact that the full spherical mode spectra of the AUT and test zone have to be analyzed in amplitude and phase. A starting point could be to investigate simulated aperture antennas with electrical symmetry planes so that certain modes are zero.

Besides the investigation by means of simulation, the effect was also investigated by measurements. For this purpose, oversampled measurements with a redundant equiangular sampling ($-180^\circ \leq \theta \leq 180^\circ$, $0^\circ \leq \phi < 360^\circ$, $N = 44$) were performed for five different AUT z -positions ($-\lambda/2$ to $\lambda/2$). The far-field results are averaged after correcting the phase according to the z -position in order to mitigate the room scattering effect and to create the reference data. The uncertainty is estimated by the difference of the considered measurements to the reference data. The estimated uncertainties based on simulation and measurements are compared in Table 7.17.

Simulated	D (dBi)	HPBW ($^\circ$)	FSSL (dB)	FSLA ($^\circ$)
Reference value	16.458	9.182	-15.467	-27.134
Est. uncertainty	± 0.067	± 0.013	± 0.084	± 0.029
Measured				
Reference value	16.473	9.188	-15.486	-27.134
Est. uncertainty	± 0.070	± 0.033	± 0.128	± 0.041

Table 7.17: Comparison of simulated and measured room scattering (term 16) uncertainties for the BTS antenna.

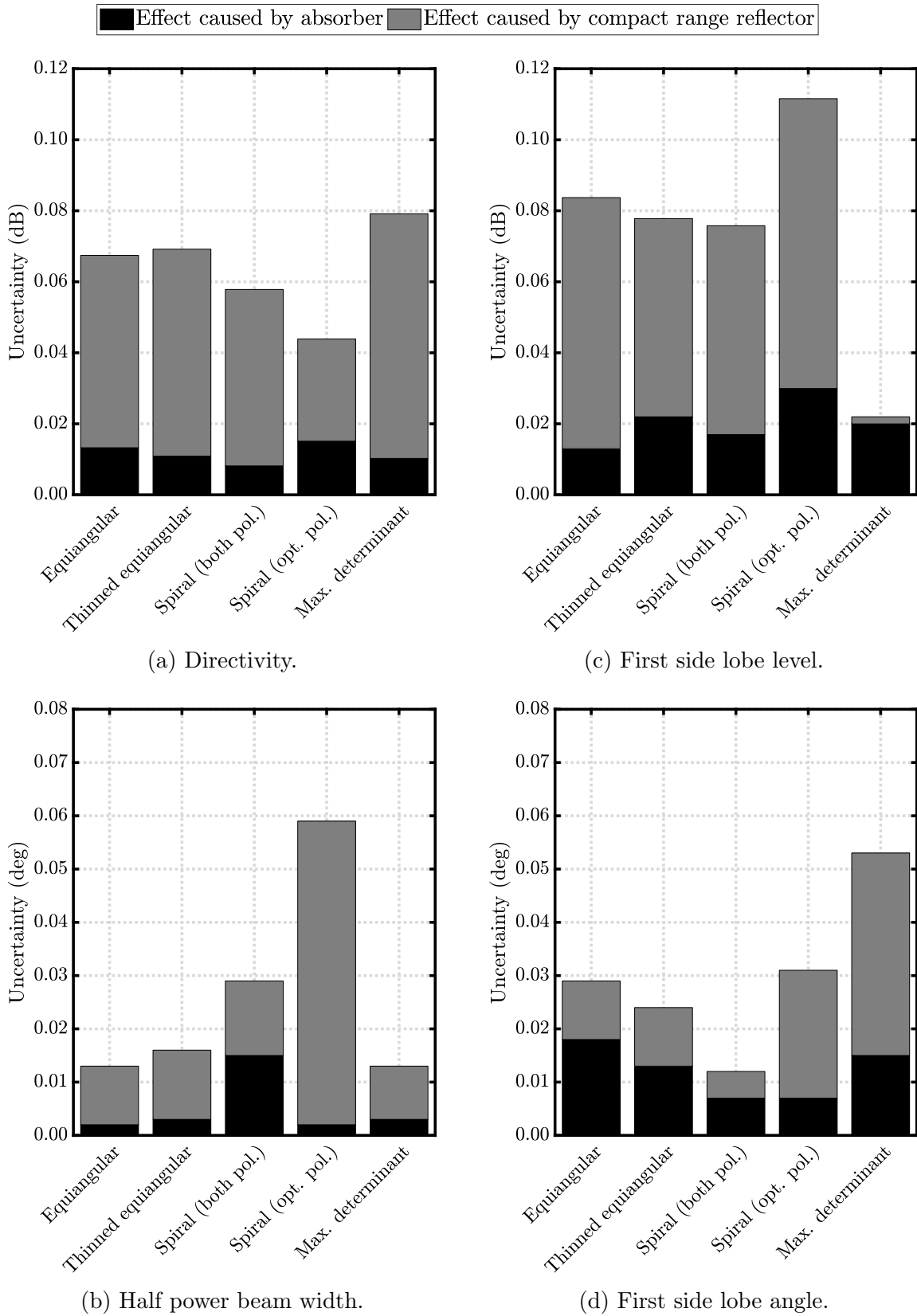


Figure 7.19: Individual term 16 (room scattering) uncertainty contributions for the BTS antenna measurement.

The estimated uncertainties based on measurement are slightly higher compared to the calculation based on simulations. However, both methods are affected by different sources of errors. The simulation does not exactly represent the measurement environment because it is only partly modeled, is based on the designed chamber geometry and is solved numerically with certain assumption (e.g. PEC). In contrast, the measurements are affected by other error sources (e.g. multiple reflections, alignment and position errors, ...) which might be neither constant nor canceling out each other for the repeated measurements. Furthermore, five redundant measurements are probably not a sufficiently large number in order to accurately estimate the reference value and the uncertainty distribution by statistics. This is one reason why the reference value in the measured case does not correspond exactly to the reference value for the simulation which has been determined from the averaged SMC of all performed measurements during the campaign. It is further possible to investigate this behavior by means of simulation. With the presented method, it is possible to simulate an AUT with an offset position inside the erroneous test zone. For comparison, this has been performed for the z -positions used in the measurements. The results are shown in Table 7.18. As expected, the error due to room scattering is significantly reduced by averaging multiple measurements (SUM 2) at different locations which is consistent with findings of other researcher [10]. However, the proposed method shows also that the error due to the reflector is reduced more than the error due to reflections at the absorbers. The residual uncertainty indicates that the number of samples and its location is not sufficient to determine the true value. Similarly, the average value of the measurements has a residual error. This residual error affects also the accuracy of the room scattering uncertainty estimation from the limited set of data as shown at the bottom of the table (SUM 3). In the light

	D (dBi)	HPBW ($^\circ$)	FSSL (dB)	FSLA ($^\circ$)
Reference value	16.458	9.182	-15.467	-27.134
Absorber	± 0.013	± 0.002	± 0.013	± 0.018
Reflector	± 0.054	± 0.011	± 0.071	± 0.011
SUM 1	± 0.067	± 0.013	± 0.084	± 0.029
Averaged				
Absorber	± 0.006	± 0.003	± 0.010	± 0.010
Reflector	± 0.005	± 0.001	± 0.014	± 0.000
SUM 2	± 0.010	± 0.004	± 0.024	± 0.010
Est. based on avg.				
Absorber	± 0.006	± 0.001	± 0.006	± 0.009
Reflector	± 0.054	± 0.004	± 0.085	± 0.019
SUM 3	± 0.060	± 0.005	± 0.091	± 0.028

Table 7.18: Estimated room scattering (term 16) uncertainties for the BTS antenna by using multiple datasets.

of this discussion, the agreement of the results can be regarded as acceptable for the purpose of uncertainty estimation in this thesis. It is also possible to use both, simulation and measurement, in order to improve the quality of the uncertainty estimation. Alternatively, simulations can be used to optimize the number and location of the measurements with respect to the residual error of the room scattering which can finally be added to the uncertainty. By this, the efficiency of averaging, which always costs measurement time, can be improved. It should be pointed out that it is also possible to replace the simulated test zone field data by measured test zone field data which for example has been acquired with a spherical near-field scanning setup [36] [160].

In summary, simulation of the test zone fields is an extremely powerful tool for the analysis of the room scattering effect or more generally of the measurement environment on the AUT. If multiple reflections and mutual coupling between the AUT and the measurement environment can be regarded as negligible, the test zone field is independent of the AUT and, thus, the same test zone field can be used for all measured AUTs. By this, it becomes possible to estimate uncertainties due to room scattering in advance and to check if the desired upper-bound of uncertainties can be fulfilled. Furthermore, it can be investigated if certain scan range configurations allow lower uncertainties. Four commonly used roll-over-azimuth scan ranges are listed in Table 7.19 together with the estimated uncertainties due to room scattering. According to the results, it is best to measure the directivity of a medium directive antenna in a configuration where the AUT never points towards the reflector with its main beam (i.e. $-180^\circ \leq \theta \leq 0^\circ$, $0^\circ \leq \phi < 360^\circ$). This is plausible but the presented method allows a detailed and quantitative investigation of every parameter

Scan range	D (dBi)	HPBW ($^\circ$)	FSL (dB)	FSLA ($^\circ$)
	16.458	9.182	-15.467	-27.134
$0^\circ \leq \theta \leq 180^\circ$, $0^\circ \leq \phi < 360^\circ$	-0.013	+0.002	-0.013	+0.018
$-180^\circ \leq \theta \leq 0^\circ$, $0^\circ \leq \phi < 360^\circ$	+0.002	-0.009	-0.014	+0.001
$-180^\circ \leq \theta < 180^\circ$, $0^\circ \leq \phi < 180^\circ$	+0.001	-0.006	-0.012	+0.004
$-180^\circ \leq \theta < 180^\circ$, $180^\circ \leq \phi < 360^\circ$	-0.012	+0.000	-0.016	+0.015

(a) Room scattering errors due to absorber (BTS).

Scan range	D (dBi)	HPBW ($^\circ$)	FSL (dB)	FSLA ($^\circ$)
	16.458	9.182	-15.467	-27.134
$0^\circ \leq \theta \leq 180^\circ$, $0^\circ \leq \phi < 360^\circ$	-0.055	-0.011	-0.071	+0.011
$-180^\circ \leq \theta \leq 0^\circ$, $0^\circ \leq \phi < 360^\circ$	-0.005	-0.002	+0.037	-0.002
$-180^\circ \leq \theta < 180^\circ$, $0^\circ \leq \phi < 180^\circ$	-0.032	+0.002	+0.018	+0.000
$-180^\circ \leq \theta < 180^\circ$, $180^\circ \leq \phi < 360^\circ$	-0.028	-0.015	-0.051	+0.008

(b) Room scattering errors due to range reflector (BTS).

Table 7.19: Room scattering errors for different scan configurations.

under study. Please note that many other scan position ranges are possible since every relative AUT/probe orientation can be measured at the positions (θ, ϕ) and $(-\theta, \phi + \pi)$. In addition, the rotation angle of the probe might be optimized as well. Overall, the presented methodology of using full wave simulations of the test zone field in order to evaluate measurement uncertainties offers great flexibility. For the first time, a method exists which allows an individual error contribution analysis (e.g. of an additional range reflector, a door, different types of absorber, etc.). Therefore, the method can also be used during the design process of an antenna measurement range in order to derive range specifications. In addition, the methodology is similarly applicable to all types of range (e.g. far-field ranges) due to the generality of the underlying concept. It can be expected that with further increasing performance of computers and available simulation tools the method gets more accurate and more frequently used.

Offset measurement

Possible methods to evaluate room scattering were comprehensively discussed in the previous section and the following results are obtained by using test zone fields generated by a full wave simulation of the measurement chamber. Table 7.20 show the combined effect of the absorber and the compact range reflector on the AUT measurement. As expected, the effect is reduced for regular equiangular sampling. Unfortunately, this property is due to the oversampling and, thus, is not available for other point configurations with less oversampling. This might be surprising because measurement results in [161] indicated that the suppression capabilities are equal. However, according to the analysis of spatial aliasing presented in Section 5.1.6, there is no theoretical justification that higher order modes are generally filtered if no oversampling is used because they cannot be separated. Numerical simulations with different offsets in various directions have shown in every example that the error due to higher order modes caused by room scattering (e.g represented by a plane wave, multiple higher order modes, simulated test zone field) increases. It is therefore concluded, that, in general, offset AUT measurements reduce the effect of room scattering only in conjunction with oversampling.

Point distribution	$\epsilon_{\text{pos. A}}$ (dB)	$\epsilon_{\text{pos. B}}$ (dB)	$\Delta\epsilon$ (dB)
Equiangular	-30.893	-33.934	-3.041
Equiangular ($N = N_{\text{AUT}}$)	-26.006	-24.507	+1.499
Equiangular ($N = N_{\text{AUT}}$), proj.	-26.213	-24.796	+1.417
Thinned equiangular, proj.	-26.154	-23.733	+2.421
Spiral (both pol.), proj.	-24.218	-22.502	+1.716
Spiral (opt. pol.), proj.	-15.504	-11.851	+3.653
Max. determinant, proj.	-22.573	-20.980	+1.593

Table 7.20: Uncertainty term 16 for QH2000 measurement and difference between offsets.

7.1.10 Term 17: Leakage and crosstalk

The distortion due to leakage and crosstalk are below the noise floor of the measurement system and, thus, have been regarded as negligible for all measurement grids.

Point distribution	D (dBi)	HPBW ($^\circ$)	FSSL (dB)	FSLA ($^\circ$)
	16.458	9.182	-15.467	-27.134
All grids	± 0.000	± 0.000	± 0.000	± 0.000

Table 7.21: Term 17 (BTS): Leakage and crosstalk.

7.1.11 Term 18: Miscellaneous random errors

The term is usually assessed by repeated measurements without any change and represents some sort of safety margin. In order to avoid effects of the amplitude and phase drift, the repeated measurements are performed in continuous mode and for equiangular sampling. It is further assumed, that the error is equal for all measurement grids because it has no theoretical relation to the measurement grid.

Point distribution	D (dBi)	HPBW ($^\circ$)	FSSL (dB)	FSLA ($^\circ$)
	16.458	9.182	-15.467	-27.134
All grids	± 0.001	± 0.001	± 0.001	± 0.001

Table 7.22: Term 18 (BTS): Miscellaneous random errors.

7.2 NF pattern averaging

In general, every measurement is affected by measurement errors and, consequently, has only a limited accuracy. Depending on the error source, different countermeasures can be used to reduce the error and to improve the accuracy. A well-known method is averaging and it has been shown in Section 7.1 that multiple measurements of a displaced AUT reduce the error due to room scattering. Typically, the AUT can be displaced along its z -axis by an often available linear slide, for example below the roll axis. With typical SWE algorithms it is required that the AUT and probe z -axis are coincident for $\theta = 0$, so that other displacements (e.g. in x) are not allowed by the transformation. However, the presented procedure for an arbitrary transformation origin (see Chapter 6) can equally be applied to measurement scenarios where the complete AUT positioner is translated. By this, the local AUT offset depends on the measurement coordinate system because, for example, the roll axis does not anymore rotate around the global z axis. This example should emphasize that any additional range translation or rotation axis can be utilized for generating different measurements to average. Former unused axes in a spherical near-field measurement setup can now be used to improve the measurement accuracy. At the IHF,

a translation axis (floor slide) below the roll-over-azimuth positioner exists which is usually used for averaging in the compact range measurement setup. For this reason, the slide is aligned with the coordinates of the far-field setup and, consequently, is slanted in the SNF setup. However, by considering the offset in the SWE it is possible to use the slide for near-field pattern averaging. As a measurement example, the BTS antenna was measured at three different positions in x and z . The measurement grid has not been adjusted because the offsets are small ($< \lambda$). Fig. 7.20 shows the complex averaged pattern including absolute min and max values of the individual measurements. It can be observed that the regions of large variation are not perfectly equal (e.g. $\theta \approx -60^\circ$). Since the translations are along different directions, the relative phase variation of the scatterers is different. Please note the region around 110° where the phases cancel out each other for averaging in x , only.

In conclusion, near-field pattern averaging can generally be used to improve the measurement accuracy. The proposed SWE with arbitrary transformation origin allows to displace the AUT in all possible directions and even together with the positioning system. By this, all available range axes can be utilized for averaging. Using displacements by multiple axes has often the benefit that the filtering is improved because it provides different variations of the scattered signal.

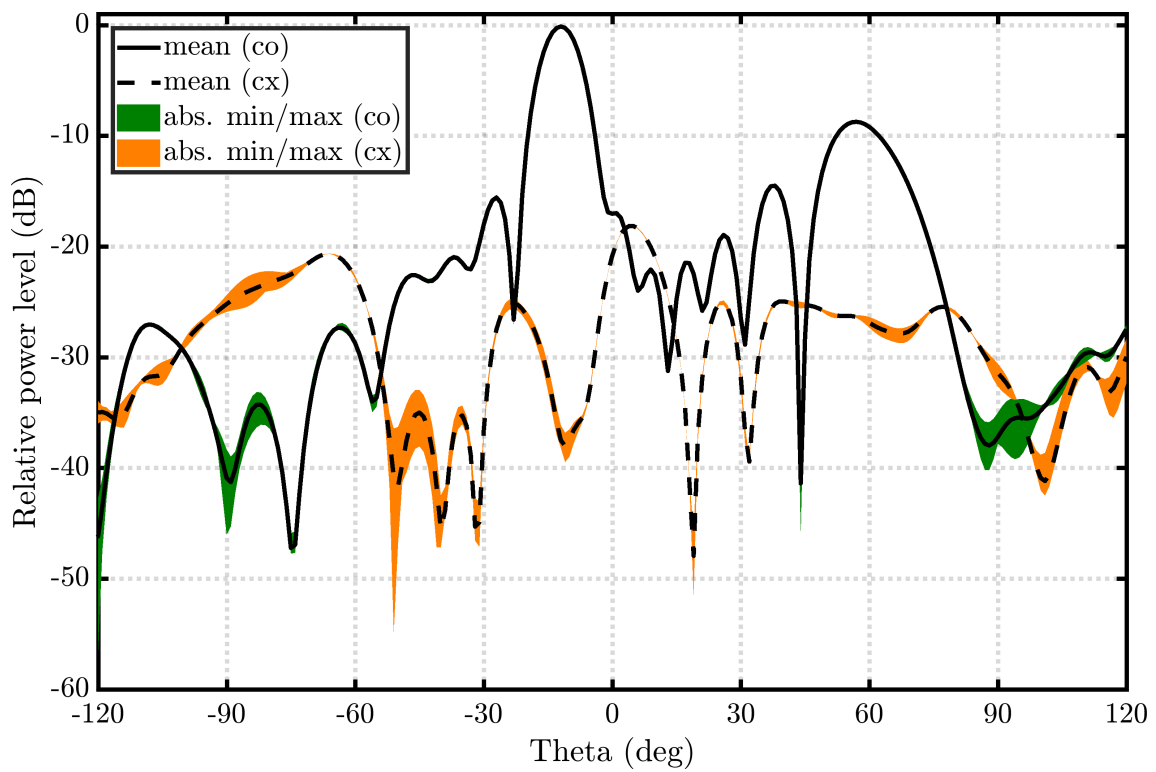
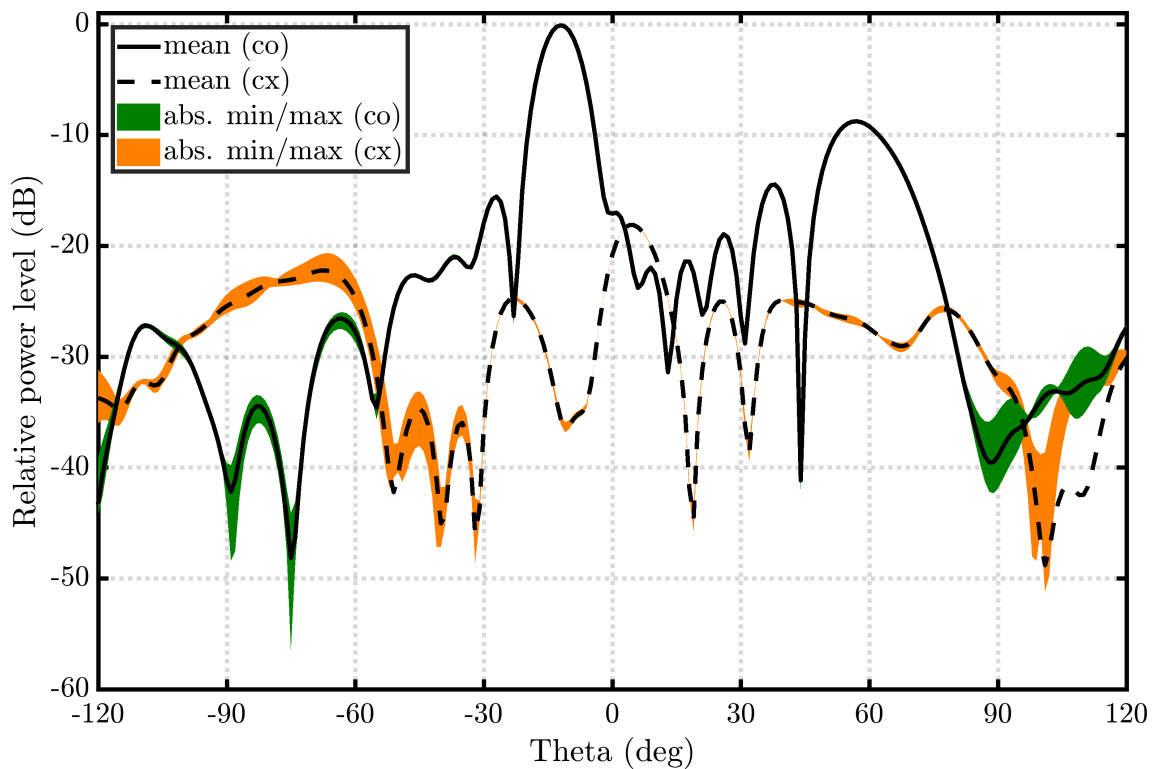
(a) Three z positions.(b) Three x positions.

Figure 7.20: Average pattern for BTS antenna measured at three different positions.

7.3 Summary

In this chapter, the uncertainties of the previously presented measurements are discussed. It was pointed out that uncertainties due to multiple reflections (term 12) and room scattering (term 16) are difficult to evaluate separately by measurements. For this reason, a new method for evaluating the room scattering uncertainties is presented in Section 7.1.9 which is based on full wave simulations of the test zone field. It was shown that the uncertainties estimated by a simulated test zone field and by measurements are in acceptable agreement. In addition, the proposed uncertainty estimation method provides unique features such as the possibility to investigate the effect of different scattering sources separately or the analysis of optimal measurement configurations. It is further pointed out, that the method is not only useful in the context of the uncertainty estimation in this thesis but also for many other application (e.g. measurement range design) due to the generality of the underlying concept.

According to the results for the BTS antenna, the measurement uncertainties are not significantly affected by the used point configuration. Thus, the point distribution has only a minor effect on the measurement uncertainty. However, the analysis of the QH2000 antenna measurements showed that different point configurations are not equally susceptible to different error sources. Especially errors due to spatial aliasing and room scattering depend strongly on the used point configuration and the amount of oversampling. Inherently oversampled point configurations such as equiangular sampling perform consequently better. But, this is mainly an effect of the oversampling and not of the point distribution. It can be expected that maximum determinant sampling with the same number of measurement points as equiangular sampling perform better than equiangular sampling because the measurement points are less redundant. In general, oversampling reduces the measurement uncertainty but increases the measurement time. It was further shown, that most uncertainty terms increase with an increased AUT offset independent of the point configuration. In particular, it was found that the error due to room scattering generally increases if the number of measurements is not increased. For that reason, offset AUT measurements do not inherently reduce this uncertainty term.

Overall, no significant increase in the measurement uncertainty can be observed except for spiral scanning with optimized polarization. Consequently, the effect of the point distribution is marginal for most uncertainty terms and measurement scenarios. Therefore, the presented point distribution are well suited for SNF antenna measurement and have the advantage of a faster near-field acquisition.

Sub-Nyquist sampling

In Chapter 2 the bandlimit of antennas was introduced. Subsequently, the minimal required number of samples was stated to be equal to the number of unknown spherical mode coefficients. In general, no further reduction is possible without adding a-priori knowledge. In measurement practice, it can often be observed that the spherical mode spectrum of an AUT is well compressible and, furthermore, a certain amount of modes is often zero. Antennas are man made devices and have often electrical or magnetic symmetry planes. Due to these symmetry planes, only modes with certain indices exist and others are forced to zero. If a mode cannot exist, the coefficient is irrelevant and, thus, the number of unknown SMC reduces. Similar to near-field measurements over an infinite large perfectly conduction half space, the number of measurement points can be consequently reduced. However, it is often only known that some percentage of the modes do not exist and not which indices they have. Therefore, it is not directly possible to reduce the size of the unknown SMC vector to generate a deterministic linear equation system. Instead, different methods have to be used. The framework of compressed sensing (CS) (or compressive sampling) provides theoretical fundamentals and practical reconstruction methods.

Beginning with the work of Donoho [162] and Candès, Romberg and Tao [163], who are widely regarded as the founders of the theory of compressed sensing, there has been a rapid development in the theoretical and practical aspects of the subject over the last decade. CS deals with the conditions under which signals sampled below the classical Nyquist rate can be reconstructed completely without error or within specified error bounds. A crucial prerequisite for the use of CS is that a sparse representation of the observed signal exists in a known basis.

A signal $\underline{\mathbf{q}} \in \mathbb{C}^L$ is called k -sparse if it has at most k non-zero components. This is usually expressed using the so-called ℓ_0 pseudonorm: $\underline{\mathbf{q}}$ is k -sparse $\Leftrightarrow \|\underline{\mathbf{q}}\|_0 = |\{i \mid q_i \neq 0\}| \leq k$. Since this is often a too stringent signal model for practical purposes, so-called compressible signals are used. A signal is called compressible if the error of the best k -sparse approximation

$$\min_{\|\underline{\mathbf{z}}\|_0 \leq k} \|\underline{\mathbf{z}} - \underline{\mathbf{q}}\|_p \quad (8.1)$$

with respect to the ℓ_p (quasi) norm ($p > 0$) quickly tends to zero with increasing k . This model is often better suited for practical purposes than the model of exactly k -sparse signals, since real signals are not often sparse even in optimal transformation bases. In this case, besides the k dominating signal coefficients, the measurements include other non-zero components, which in comparison have only a small influence on the actual characteristics of the signal.

Similar to the sampling process in Section 2.2.1.1, the L -dimensional signal $\underline{\mathbf{w}}$ is described in the context of compressed sensing as a linear mapping through the so-called measuring or sampling matrix $\underline{\Phi} \in \mathbb{C}^{L \times J}$

$$\underline{\mathbf{w}} = \underline{\Phi} \underline{\mathbf{q}} \quad . \quad (8.2)$$

In CS, in contrast to previous investigations, the focus lies on the underdetermined case $L < J$, especially with $L \ll J$, where infinitely many solutions exist.

The fundamental idea of CS is to integrate the knowledge that the signal is sparse or compressible directly into the, usually nonlinear, reconstruction process. Under certain restrictions for the signal $\underline{\mathbf{q}}$, as well as the sampling matrix $\underline{\Phi}$, it is then possible to reconstruct the signal from the compressed measurement $\underline{\mathbf{w}}$ error-free or in compliance with predetermined error bounds. For this purpose, the so-called ℓ_0 minimization problem

$$\min \|\underline{\mathbf{q}}\|_0 \text{ subject to } \underline{\mathbf{w}} = \underline{\Phi} \underline{\mathbf{q}} \quad (8.3)$$

is formulated, in which the solution $\underline{\mathbf{q}}$ is sought so that the non-zero entries are minimal. Since the ℓ_0 minimization problem is combinatorial in nature and belongs to the class of NP-hard problems, there is no algorithm that efficiently solves (8.3). However, it can be shown that the solution of the ℓ_0 problem is under certain conditions equal with the solution of the closely related ℓ_1 minimization problem

$$\min \|\underline{\mathbf{q}}\|_1 \text{ subject to } \underline{\mathbf{w}} = \underline{\Phi} \underline{\mathbf{q}} \quad . \quad (8.4)$$

This problem is convex and, hence, can be efficiently solved, for example, by interior-point methods. Measurements are usually affected by additive noise which can be incorporated by replacing the equality condition in the optimization problem

$$\min \|\underline{\mathbf{q}}\|_1 \text{ subject to } \|\underline{\mathbf{w}} - \underline{\Phi} \underline{\mathbf{q}}\|_2 \leq \epsilon \quad (8.5)$$

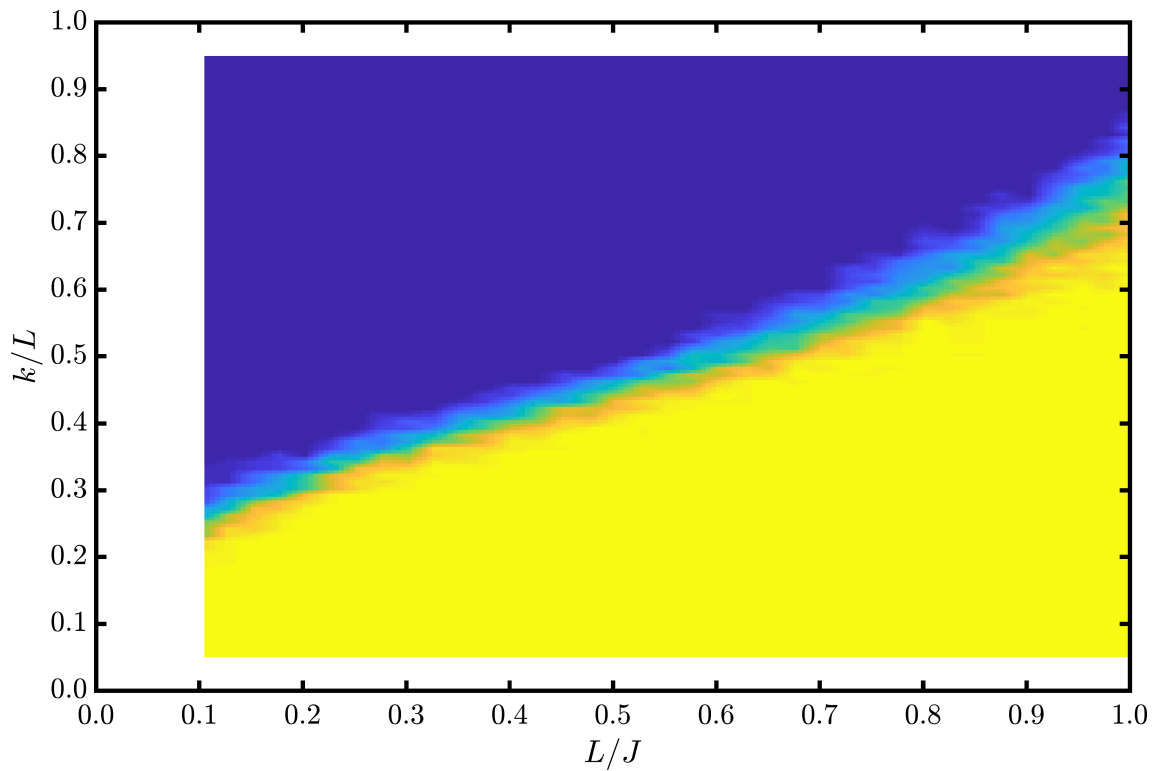
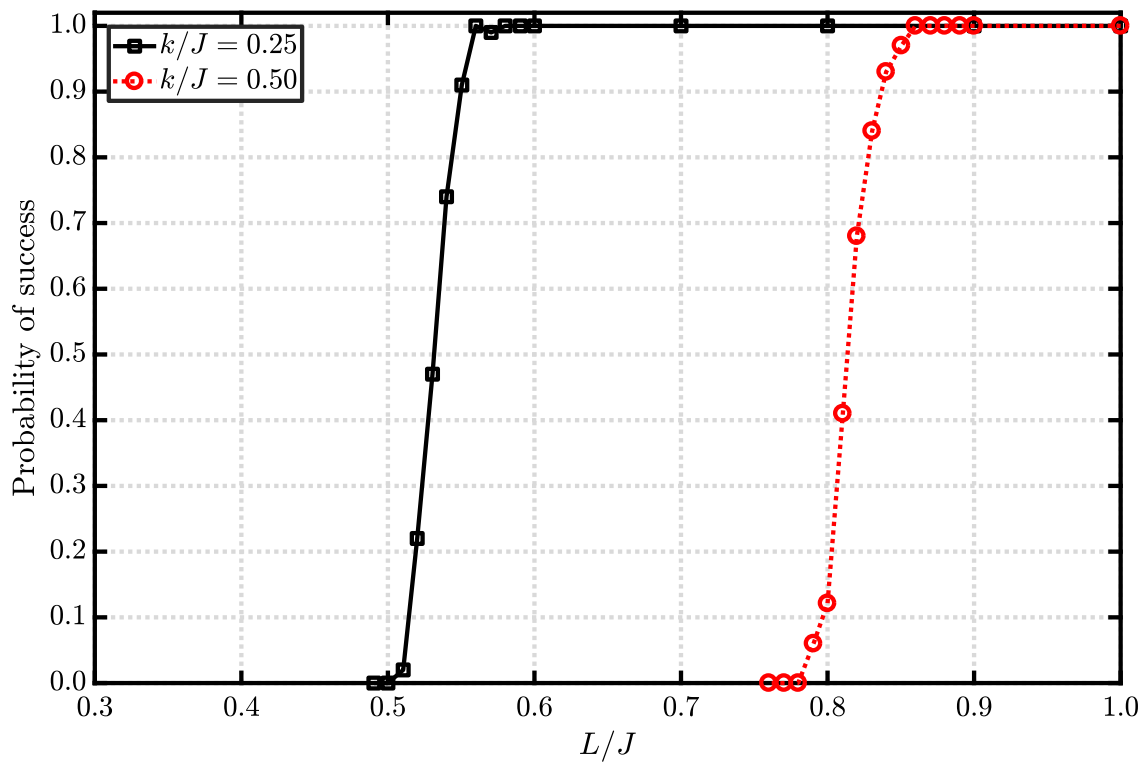
where ϵ is the maximum allowed reconstruction error. The design of the sensing matrix $\underline{\Phi}$ plays an important role for the recoverability of $\underline{\mathbf{q}}$. In the literature, a variety of properties and conditions for the sensing matrix have been proposed which provide sufficient and/or necessary conditions for perfect signal recovery. The most significant conditions are based on the coherence of the sampling matrix, the null space property (NSP) or the restricted isometry property (RIP). Coherence has a special significance because it can always be calculated explicitly for a given sensing matrix $\underline{\Phi}$, while checking the NSP or RIP are itself NP-hard problems [164]. Notwithstanding this, results based on the RIP are of great interest for practical applications. While coherence-based reconstruction criteria always require $\mathcal{O}(k^2)$ measurements [165], only $\mathcal{O}(k \ln(L/k))$ measurement points are needed for RIP-based results [166, 167]. However, the deterministic construction of such matrices is still an unsolved problem. Only randomly constructed or random subsampled orthonormal matrices are highly likely to fulfill the RIP under certain conditions. But, due to the fact that it is not efficiently possible to verify that a given matrix complies with the RIP, the reconstruction guarantees are of probabilistic nature in this case. In other words, the probability of successfully reconstructing a signal measured with a random matrix by ℓ_1 minimization corresponds to the probability that the randomly constructed measurement matrix fulfills the RIP.

Instead of convex reconstruction algorithms, greedy or iterative hard and soft thresholding algorithms can be used. There are also various conditions for these classes of algorithms, under which the original signal can be reconstructed without error or with the required accuracy. However, these conditions are often more stringent than those required when using ℓ_1 -based convex methods. Nevertheless, these algorithms represent an attractive alternative in practical application since they mostly have favorable convergence properties compared to convex methods.

Methods of compressed sensing have already been used in various areas of antenna technology, such as direction of arrival estimation and group antenna analysis [168–170] as well as for scalar spherical harmonics [171]. In [172] methods of compressed sensing were for the first time applied to spherical near-field antenna measurements. At the IHF the research is continued in a research project founded by the German Research Foundation (DFG) while also other international research groups are working on the subject [173, 174]. Regarding the QH2000 antenna it can be shown that the spectrum is compressible by evaluating the number of modes which contain a certain amount of power as given in the following table:

$\frac{P}{P_{\text{total}}}$	Absolute	Relative
95.00%	28	4.3%
99.00%	59	9.1%
99.90%	303	46.9%
99.99%	521	80.7%

This analysis motivates that CS might allow further measurement point reductions. This assumption is further supported by numerical simulations. A random mode spectra with $J = 390$ ($N = 13$) was used as a test case. The sampling points are randomly distributed and the reconstruction is performed by ℓ_1 minimization (SPGL1 [175]). The simulation is repeated 50 times. The phase transition diagram in Fig. 8.1 shows the reconstruction error depending on the sampling ratio L/J and the sparsity k/L , relative to the number of measurements. Perfect reconstruction and failure are indicated by the yellow and blue (darker) region, respectively. As typical for CS applications, the transition is very steep and it confirms that perfect reconstruction from undersampled measurements is possible as long as the sparsity does not exceed a certain threshold. Since the simulations are time consuming, the phase transition diagram has only been calculated for $N = 13$. Results for another example with $N = 23$ ($J = 1150$, 100 trials) is given in Fig. 8.2. An amplitude RMS error below 10^{-4} is regarded as successful reconstruction. It can be seen that a mode spectrum with a sparsity of $k/J = 0.25$ can be reconstructed from almost a twice undersampled measurement. The improvement reduces with decreased sparsity as shown by the second curve for $k/J = 0.50$. Nevertheless, still 15% of the measurement points can be saved.

Figure 8.1: Phase transition diagram ($J = 390$).Figure 8.2: Probability of success ($J = 1150$, $\text{RMSE} < 10^{-4}$).

Besides the angular dimensions, also the frequency dimension might be sub-sampled. The sweep time and, as a result, the acquisition time increases if many frequencies are measured. However, if the frequency step is small, it might be possible to approximate the frequency dependency of the SMC by a low order model (Model-Based Parameter Estimation (MBPE) [176–180]) because the radiation pattern change is often small between two adjacent frequencies. Nevertheless, uncertainty evaluations have to be performed in order to verify the performance and to check required conditions and prerequisites.

In summary, sub-sampled acquisition is possible to some extent which further allows to reduce the required number of measurement points. Although preliminary results showed the potential, further research is necessary to validate the methods in typical measurement applications. Most importantly the question how the sampling point distribution has to be in order to guarantee good reconstruction while the measurement time is reduced. Random point distributions might be a useful assumption for theoretical considerations but are generally not beneficial for measurement practice. Hence, deterministic sampling point distributions are desirable which, however, may not provide theoretical bounds on the number of points and the reconstruction error. In conclusion, sub-Nyquist sampling approaches have to verify how much acquisition time can be saved and how the measurement uncertainties are affected in order to bring the theory into measurement practice.

Conclusion

The goal of this thesis was to investigate fast spherical near-field antenna measurement methods in order to reduce the usually long measurement times in SNF. In conclusion, most spherical near-field antenna measurement could be performed in less measurement time if the presented procedures are applied. A prerequisite for some procedures, especially the most general ones, is a universal spherical wave expansion algorithm which is not limited to, for example, equiangular sampling or first order probe correction. In fact, it was shown that most of the measurement limitations are due to the requirements of the used transformation algorithm and not due to theoretical limitations. It needs to be emphasized that the generality of the spherical wave expansion for antenna measurements offers a plethora of possibilities. Here, the gained flexibility of modern transformations algorithms is used for accelerating the acquisition process.

The main limitation of the commonly used transformation algorithm based on Fourier transforms is that equiangular sampling on the sphere is required which is inherently highly oversampled. Spiral point configurations are able to reduce the oversampling factor from approximately 2 for equiangular sampling to around 1.2. The numerical optimized point configuration of maximum determinate nodes does not require oversampling at all. Furthermore, it has been presented that by including a translation and rotation of the transformation origin in the transformation process the number of required measurement points depends only on the size of the AUT. Thus, the number of points does not depend anymore (previously quadratically) on the AUT position inside the measurement sphere and can be minimized in every measurement configuration. In addition, it has been shown that it is beneficial to project the sampling point distribution from the AUT source volume to the spherical measurement surface. Full probe correction is available and explicit formulas for the typical case of a single measurement probe have been derived.

It needs to be emphasized that all presented point configurations allow an analytical exact spherical wave decomposition and do not add any constraints on the transformation. For this reason, using a different point distribution does not introduce a reconstruction error by itself. In contrast, the acceleration of antenna measurements by truncation, i.e. performing only partial spherical measurements, distort the orthogonality of the spherical modes and, consequently, introduce an approximation error. Nevertheless, truncation is useful in measurement scenarios where only certain antenna key parameters are of interest. In addition, the approximation error can be reduced by different methods such as extrapolation or source reconstruction. Nevertheless, the approximation error depends strongly on the investigated AUT and, thus, a theoretical generalization is not possible. For this reason, the applicability of truncation has to be investigated for every measurement task anew. Though trun-

cation is not ideal, it can significantly reduce the measurement time and can also be combined with the presented point configurations.

Other methods to decrease the absolute measurement time are the usage of faster measurement equipment such as a faster scan axes, a faster measurement receiver or the usage of multiple measurement channels. Multiple channel measurements are typically performed using one or more dual-polarized measurement probes. It has been pointed out in this thesis that probe correction is possible by using the proposed pointwise probe correction scheme. Although these methods decrease the absolute measurement time, the relative measurement time compared to equiangular sampling is more or less unchanged. Therefore, the acquisition is faster but not more efficient. Nevertheless, especially a dual-polarized probe reduces the measurement time by nearly 50% and can be used together with optimized point configurations. However, additional channel calibrations are required which increase the measurement setup time and needs to be taken into account in an overall measurement time estimation. In summary, different approaches are possible to accelerate spherical near-field antenna measurements. The main contribution of this thesis is the investigation of more efficient sampling point configurations.

In total, the number of measurement points can always be minimized according to the number of unknown spherical mode coefficients. Accordingly, a measurement time reduction of up to 50% compared to equiangular sampling is possible in step mode acquisition. Since the scan axis stops at every measurement point, the acquisition time is proportional to the number of points. In addition, antenna measurements in step mode take often hours so that a reduction is highly desirable. However, measurement systems operate more frequently in continuous mode acquisition which is in general faster than an acquisition in step mode because the scan axis does not stop during the measurement. In this acquisition mode the length of the measurement path is more important than the number of points along that path. For this reason, the achievable acquisition time reduction depends on the acquisition time for every measurement point, the distances between two adjacent measurement points and the axis velocity. In general, the acquisition times reduce around 5-10% if the velocity of the axis is the limiting factor. If the acquisition time for every measurement point increases, the scan axis cannot travel anymore with its maximum velocity and optimized sampling point configuration can achieve measurement time reductions similar to the values in step mode acquisition. In practice, acquisition time reductions somewhere in between (e.g. 20%) seem realistic. Overall, accelerating antenna measurements in continuous mode by adapting the sampling is not as efficient as in step mode and, furthermore, requires accurate and flexible velocity control of the scan axis which is, up until now, not standard for SNF measurement setups. The design of such systems is a complex interdisciplinary task and further research is required to optimize the scan path in conjunction with position triggering and axes control.

Measurement results have verified that acquisition times in step mode can be significantly reduced by using optimized sampling grids. In addition, the measurement uncertainties are not generally larger than for equiangular sampling. However, oversampling improves the accuracy of the measurement results but can be used more flexible with non-equiangular sampling grids which are not inherently oversampled. By this, the operator can balance measurement accuracy and measurement time.

Although it is not the focus of this thesis, methods for uncertainty estimation in SNF are discussed and improved. By this, properties of different point configurations such as the susceptibility to spatial aliasing or room scattering can be well compared. Especially the evaluation of room scattering by full wave simulations of the measurement chamber shows great potential for a variety of applications such as measurement range design or determination of an optimal scan scheme.

Overall, the theory of the spherical wave expansion for antenna measurement provides a very general basis for the description of antenna measurements which is by far not yet exploited. Continuously improving computer performances will allow a more realistic and, hence, more accurate representation of the actual antenna measurement scenario. In this thesis, the generality was used to derive efficient sampling point configurations on the sphere in order to accelerate the spherical near-field acquisition. However, a spherical wave expansion can generally be applied to measurements on arbitrary surfaces while full probe correction is available. Consequently, measuring on a spherical surface is not required to determine the SMC of an AUT. Instead, every closed surface can be used. Therefore, new measurement range concepts such as a cube or closed cylinder measurement range might be investigated in the future because their mechanical realization can be expected to be simpler compared to spherical geometries. In addition, optical measurement devices, e.g. laser tracker, can be used to track the position and orientation of the AUT and probe coordinate system. By this, new degrees of freedom are available in the range design and could be used to further accelerate antenna measurements. Of course, other design goals such as costs of the measurement range or adaption to a specific measurement task can be considered as well. As discussed, using universal spherical wave expansion algorithms, almost no limitations exist. However, this does not imply that all systems are equally sensitive to measurement errors and provide the same measurement accuracy. The investigation of measurement uncertainties will also be an important aspects for the analysis of the briefly discussed sub-Nyquist sampling methods. Numerical experiments have shown that a priori knowledge can be used for more efficient near-field sampling but rigorous investigations are still missing. Another interesting aspect is how good numerically simulated data of the antenna, which is nowadays always available, can be used to support the antenna measurement process.

In conclusion, increased sampling efficiency by the proposed point distributions decreases the acquisition time of spherical near-field antenna measurements. In addition, the measurement uncertainties are generally not significantly affected. Overall, the theory of spherical wave expansion can be used in a much more broad sense and is not restricted to a spherical measurement geometry. It can be expected that this generality can be beneficial for future antenna measurement range designs.

IHF measurement chamber

The antenna measurement chamber at the IHF is a hybrid antenna measurement chamber and is a compact antenna test range (CATR) as well as a spherical near-field (SNF) antenna test range. General information can be found at www.ihf.rwth-aachen.de.

A.1 SNF range

The SNF range shown in Fig. A.1 consists of a roll-over-azimuth positioner which rotates the AUT in roll (ϕ) and azimuth (θ) and a probe polarization axis to switch between the two measurement polarizations ($E_\theta = E_H$ and $E_\phi = E_V$). In addition, a manually controlled elevation axis below the roll positioner and a linear slide above the azimuth axis can be used to translate the AUT in the z -direction and to compensate the bending of the positioner. Furthermore, a linear floor slide below the azimuth axis exists which can move the complete AUT tower. Since this axis is aligned with the far-field range coordinate system, the orientation in the SNF range is slanted by approximately 29° . Further range specifications are listed in Table A.1. The used probe antenna is a dual ridged broadband horn antenna (SH800) from Satimo (MVG) [181] and is described in Appendix A.2.

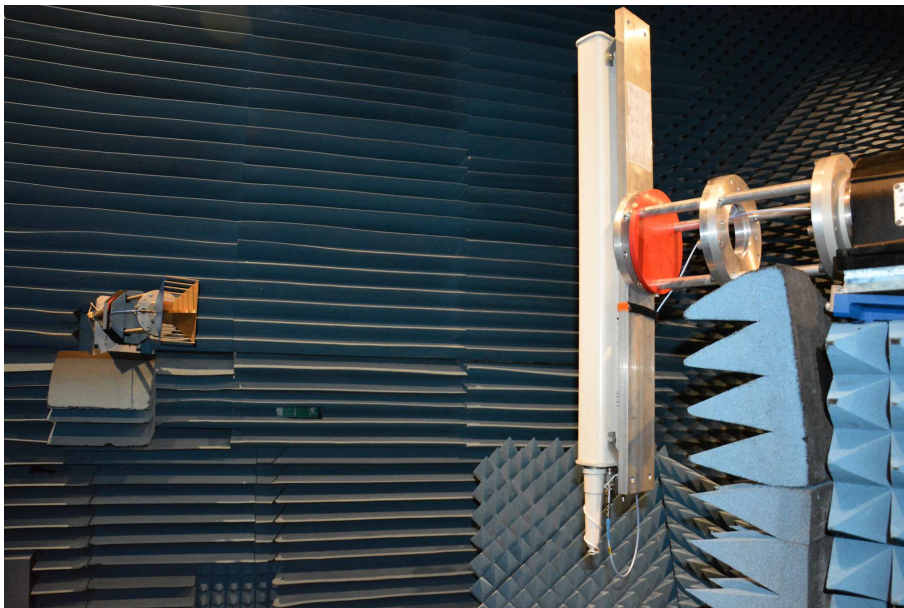


Figure A.1: IHF SNF measurement chamber.

Frequency range:
0.8 - 12 GHz
AUT positioner:
Roll-over-Azimuth plus elevation squint and pick-up Max. AUT mass: 100 kg Optional dielectric tower for low-gain antennas up to 12 kg
RF instrumentation:
Rohde & Schwarz ZVA24 VNA
Shielded anechoic room:
5 m x 5 m x 9 m
Control and post-processing software:
ActiveCell 4 by Orbit/FR Europe

Table A.1: IHF SNF measurement chamber specifications.

A.2 SH800 near-field probe

Satimo SH800 specifications:	
Frequency:	0.8 - 12 GHz
Gain:	7 - 15 dBi
Polarization:	Linear (cx-pol < -45 dB)
Dimensions:	270 mm, 146 mm, 225 mm

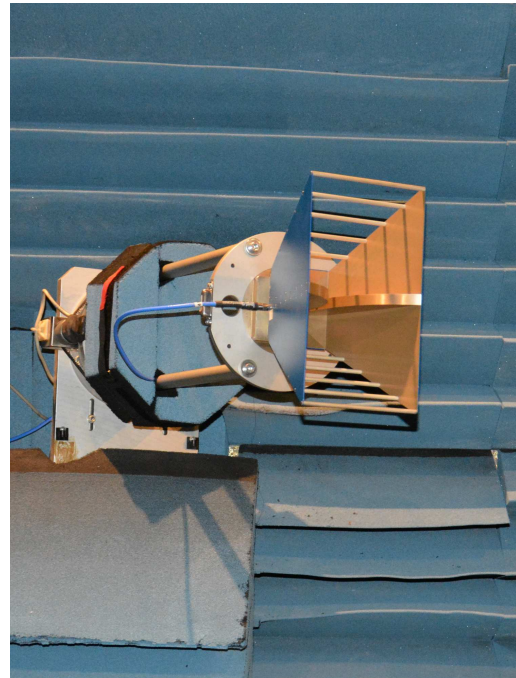


Figure A.2: SH800 near-field probe mounted in IHF chamber.

Appendix B

BTS measurements

B.1 BTS specifications

BTS specifications:	
Frequency:	1710 - 2690 MHz
Tilt:	0 - 12°
Gain:	16.5 dBi (tilt: 0°)
HPBW:	8.8° (tilt: 0°)
Polarization:	Slanted $\pm 45^\circ$
Dimensions:	851 mm, 172 mm, 92 mm



Figure B.1: BTS antenna mounted in IHF chamber.

B.2 BTS measurement uncertainties

The uncertainty budgets for the BTS antenna measurements are summarized in this chapter. A detailed discussion can be found in Section 7.1. Table B.1 shows the combined measurement uncertainty (1σ) of the measurements for different point distributions. The individual complete uncertainty budgets are given in Table B.2 to Table B.6. In general, the uncertainty is described by a distribution function (i.e. normal (term 1, 2, 8, 13, 14, 15, 16, 17, 18), uniform (term 4, 7, 10) and u-shaped (term 12)). Please note, that the listed uncertainties are already converted to an equivalent normal distribution uncertainty value depending on the distribution function. It is further assumed that all terms are independent and uncorrelated

Point distribution	D (dBi)	HPBW ($^\circ$)	FSSL (dB)	FSLA ($^\circ$)
	16.458	9.182	-15.467	-27.134
Equiangular	± 0.068	± 0.025	± 0.207	± 0.050
Thinned equiangular	± 0.070	± 0.033	± 0.203	± 0.053
Spiral (both pol.)	± 0.058	± 0.047	± 0.228	± 0.038
Spiral (opt. pol.)	± 0.051	± 0.134	± 0.857	± 0.110
Max. determinant	± 0.080	± 0.050	± 0.268	± 0.079

Table B.1: Uncertainty budget for BTS antenna measurement (2.4 GHz) for different point distributions.

Uncertainty term		D (dBi)	HPBW (deg)	FSSL (dB)	FSLA (deg)
1.	Probe relative pattern	0.006	0.013	0.053	0.013
4.	Probe alignment error	0.001	0.001	0.004	0.004
7.	AUT alignment error	0.001	0.001	0.001	0.012
8.	Data point spacing	0.002	0.013	0.030	0.034
9.	Measurement area truncation	-	-	-	-
10.	Position error	0.003	0.008	0.028	0.010
12.	Multiple reflections	0.006	0.006	0.177	0.005
13.	Receiver amplitude nonlinearity	0.002	0.002	0.004	0.003
14.	System amplitude and phase error	0.000	0.000	0.001	0.000
15.	Receiver dynamic range	0.000	0.000	0.001	0.000
16.	Room scattering	0.067	0.013	0.084	0.029
17.	Leakage and crosstalk	0.000	0.000	0.000	0.000
18.	Miscellaneous random errors	0.001	0.001	0.001	0.001
RSS		0.068	0.025	0.207	0.050
exp. RSS (k = 3)		0.205	0.074	0.622	0.149

Table B.2: Uncertainty budget for BTS antenna measurement (2.4 GHz) with equiangular sampling.

so that they can be combined using the root square sum (RSS) procedure. Many antenna parameters are usually specified in logarithmic scale and, consequently, an uncertainty in logarithmic scale is also convenient. However, a linear symmetric uncertainty is not exact symmetric in the logarithmic scale. But the differences are typically negligible for uncertainties below 0.3 dB and, thus, the stated logarithmic uncertainty is the mean value of the absolute lower and upper error.

Uncertainty term		D (dBi)	HPBW (deg)	FSL (dB)	FSLA (deg)
1.	Probe relative pattern	0.006	0.013	0.054	0.014
4.	Probe alignment error	0.001	0.002	0.004	0.004
7.	AUT alignment error	0.001	0.001	0.001	0.012
8.	Data point spacing	0.001	0.013	0.023	0.042
9.	Measurement area truncation	-	-	-	-
10.	Position error	0.004	0.007	0.020	0.006
12.	Multiple reflections	0.002	0.021	0.176	0.004
13.	Receiver amplitude nonlinearity	0.002	0.002	0.004	0.004
14.	System amplitude and phase error	0.000	0.000	0.000	0.001
15.	Receiver dynamic range	0.000	0.000	0.001	0.000
16.	Room scattering	0.069	0.016	0.078	0.024
17.	Leakage and crosstalk	0.000	0.000	0.000	0.000
18.	Miscellaneous random errors	0.001	0.001	0.001	0.001
RSS		0.070	0.033	0.203	0.053
exp. RSS ($k = 3$)		0.209	0.100	0.609	0.158

Table B.3: Uncertainty budget for BTS antenna measurement (2.4 GHz) with thinned equiangular sampling.

Uncertainty term		D (dBi)	HPBW (deg)	FSL (dB)	FSLA (deg)
1.	Probe relative pattern	0.006	0.012	0.054	0.014
4.	Probe alignment error	0.002	0.003	0.003	0.004
7.	AUT alignment error	0.001	0.001	0.001	0.012
8.	Data point spacing	0.001	0.007	0.037	0.029
9.	Measurement area truncation	-	-	-	-
10.	Position error	0.004	0.006	0.025	0.010
12.	Multiple reflections	0.001	0.033	0.203	0.003
13.	Receiver amplitude nonlinearity	0.002	0.001	0.004	0.003
14.	System amplitude and phase error	0.000	0.000	0.000	0.000
15.	Receiver dynamic range	0.000	0.000	0.002	0.001
16.	Room scattering	0.058	0.029	0.076	0.012
17.	Leakage and crosstalk	0.000	0.000	0.000	0.000
18.	Miscellaneous random errors	0.001	0.001	0.001	0.001
RSS		0.058	0.047	0.228	0.038
exp. RSS ($k = 3$)		0.175	0.141	0.686	0.114

Table B.4: Uncertainty budget for BTS antenna measurement (2.4 GHz) with spiral sampling using two orthogonal polarizations.

Uncertainty term		D (dBi)	HPBW (deg)	FSL (dB)	FSLA (deg)
1.	Probe relative pattern	0.005	0.006	0.060	0.013
4.	Probe alignment error	0.001	0.001	0.006	0.004
7.	AUT alignment error	0.001	0.001	0.001	0.012
8.	Data point spacing	0.016	0.066	0.031	0.055
9.	Measurement area truncation	-	-	-	-
10.	Position error	0.005	0.013	0.064	0.016
12.	Multiple reflections	0.019	0.099	0.845	0.087
13.	Receiver amplitude nonlinearity	0.002	0.002	0.012	0.001
14.	System amplitude and phase error	0.004	0.000	0.008	0.003
15.	Receiver dynamic range	0.000	0.001	0.001	0.001
16.	Room scattering	0.044	0.059	0.112	0.031
17.	Leakage and crosstalk	0.000	0.000	0.000	0.000
18.	Miscellaneous random errors	0.001	0.001	0.001	0.001
RSS		0.051	0.134	0.857	0.110
exp. RSS (k = 3)		0.153	0.401	2.643	0.331

Table B.5: Uncertainty budget for BTS antenna measurement (2.4 GHz) with spiral sampling using one optimized polarizations.

Uncertainty term		D (dBi)	HPBW (deg)	FSL (dB)	FSLA (deg)
1.	Probe relative pattern	0.007	0.012	0.052	0.014
4.	Probe alignment error	0.001	0.002	0.004	0.004
7.	AUT alignment error	0.001	0.001	0.001	0.012
8.	Data point spacing	0.010	0.035	0.057	0.055
9.	Measurement area truncation	-	-	-	-
10.	Position error	0.006	0.005	0.008	0.006
12.	Multiple reflections	0.002	0.030	0.256	0.008
13.	Receiver amplitude nonlinearity	0.002	0.002	0.004	0.004
14.	System amplitude and phase error	0.001	0.000	0.002	0.001
15.	Receiver dynamic range	0.000	0.001	0.001	0.001
16.	Room scattering	0.079	0.013	0.022	0.053
17.	Leakage and crosstalk	0.000	0.000	0.000	0.000
18.	Miscellaneous random errors	0.001	0.001	0.001	0.001
RSS		0.080	0.050	0.268	0.079
exp. RSS (k = 3)		0.241	0.149	0.806	0.238

Table B.6: Uncertainty budget for BTS antenna measurement (2.4 GHz) with maximum determinant sampling.

QH2000 measurements

C.1 QH2000 specifications

Satimo QH2000 specifications:	
Frequency:	2 - 32 GHz
Gain:	3 - 16 dBi
Polarization:	Dual linear
max. cx-pol.:	< -30 dB (on-axis)
Dimensions:	110 mm, 105 mm, 105 mm

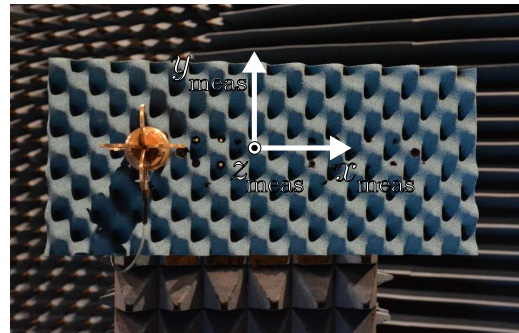


Figure C.1: QH2000 antenna mounted in IHF chamber.

C.2 QH2000 measurement uncertainties

The uncertainty budgets for the QH2000 antenna measurements are summarized in this chapter. A detailed discussion can be found in Section 7.1. Table C.1 shows the combined measurement uncertainty (1σ) of the measurements for different point distributions and both offset positions. Please note that the mode power differences do not include the uncertainty due to term 7 (AUT misalignment) because it is equal for all point distributions. However, the value can be found in the detailed uncertainty budgets given in Table C.2 to Table C.15. In general, the uncertainty is described by a distribution function (i.e. normal (term 1, 2, 8, 13, 14, 15, 16, 17, 18), uniform (term 4, 7, 10) and u-shaped (term 12)). Please note, that the listed uncertainties are already converted to an equivalent normal distribution uncertainty value depending on the distribution function. It is further assumed that all terms are independent and uncorrelated so that they can be combined using the root square sum (RSS) procedure. Many antenna parameter are usually specified in logarithmic scale and, consequently, an uncertainty in logarithmic scale is also convenient. However, a linear symmetric uncertainty is not exact symmetric in the logarithmic scale. But the differences are typically negligible for uncertainties below 0.3 dB and, thus, the stated logarithmic uncertainty of the directivity D is the mean value of the absolute lower and upper error. In contrast, only the upper bound is stated for the maximum cross-polarization levels in the E- and H-plane.

Point distribution (pos. A)	D (dBi)	HPBW _H (deg)	HPBW _E (deg)	Null _{Left} (deg)	Null _{Right} (deg)	max(CX _H) (dB)	max(CX _E) (dB)	ϵ^* (dB)
	8.137	69.838	52.201	-63.310	63.900	-27.856	-37.111	
Equiangular	± 0.034	± 0.523	± 0.331	± 0.186	± 0.193	+0.704	+2.496	-19.398
Equiangular ($N = N_{\text{AUT}}$)	± 0.031	± 0.496	± 0.331	± 0.521	± 0.701	+0.727	+1.648	-19.067
Equiangular ($N = N_{\text{AUT}}$), proj.	± 0.065	± 0.704	± 0.637	± 0.315	± 0.299	+0.615	+2.659	-19.215
Thinned equiangular, proj.	± 0.091	± 2.204	± 1.235	± 0.436	± 0.311	+2.890	+3.198	-19.223
Spiral (both pol.), proj.	± 0.094	± 0.662	± 0.739	± 0.373	± 0.470	+2.926	+3.189	-18.837
Spiral (opt. pol.), proj.	± 0.519	± 3.971	± 8.509	± 2.795	± 0.520	+9.087	+21.565	-12.233
Max. determinant, proj.	± 0.098	± 1.398	± 0.945	± 0.316	± 1.155	+4.614	+2.301	-18.139

(a) Position A with $(x_{\text{meas}}, y_{\text{meas}}, z_{\text{meas}}) = (-165.6 \text{ mm}, 0, 0)$.

Point distribution (pos. B)	D (dBi)	HPBW _H (deg)	HPBW _E (deg)	Null _{Left} (deg)	Null _{Right} (deg)	max(CX _H) (dB)	max(CX _E) (dB)	ϵ^* (dB)
	8.137	69.838	52.201	-63.310	63.900	-27.856	-37.111	
Equiangular	± 0.034	± 0.365	± 0.226	± 0.055	± 0.047	+0.505	+1.538	-19.609
Equiangular ($N = N_{\text{AUT}}$)	± 0.062	± 1.341	± 1.321	± 0.207	± 0.785	+0.912	+4.349	-19.153
Equiangular ($N = N_{\text{AUT}}$), proj.	± 0.078	± 0.722	± 0.397	± 0.240	± 0.495	+1.207	+1.756	-19.212
Thinned equiangular, proj.	± 0.039	± 0.472	± 1.431	± 0.249	± 0.512	+1.034	+4.167	-18.933
Spiral (both pol.), proj.	± 0.160	± 1.440	± 1.070	± 1.540	± 1.142	+4.227	+2.639	-18.498
Spiral (opt. pol.), proj.	± 0.428	± 1.992	± 4.164	± 3.656	± 0.710	+8.058	+14.733	-9.696
Max. determinant, proj.	± 0.062	± 1.261	± 1.337	± 0.366	± 0.329	+5.839	+5.477	-17.530

(b) Position B with $(x_{\text{meas}}, y_{\text{meas}}, z_{\text{meas}}) = (-165.6 \text{ mm}, 0, 239.8 \text{ mm})$.

Table C.1: Total uncertainty budgets for QH2000 measurements (*: without term 7).

Uncertainty term (pos. A)		D (dBi)	HPBW _H (deg)	HPBW _E (deg)	Null _{Left} (deg)	Null _{Right} (deg)	max(CX _H) (dB)	max(CX _E) (dB)	ϵ (dB)
		8.137	69.838	52.201	-63.310	63.900	-27.856	-37.111	
1.	Probe relative pattern	± 0.005	± 0.097	± 0.059	± 0.020	± 0.010	+0.077	+0.750	-43.035
4.	Probe alignment error	± 0.008	± 0.071	± 0.049	± 0.012	± 0.012	+0.187	+0.602	-19.618
7.	AUT alignment error	± 0.002	± 0.027	± 0.017	± 0.020	± 0.015	+0.406	+1.134	-8.612
8.	Data point spacing	± 0.007	± 0.062	± 0.045	± 0.010	± 0.010	+0.096	+0.154	-55.358
9.	Measurement area truncation	-	-	-	-	-	-	-	-
10.	Position error	± 0.008	± 0.054	± 0.091	± 0.020	± 0.008	+0.014	+0.281	-42.655
12.	Multiple reflections	± 0.023	± 0.434	± 0.005	± 0.085	± 0.021	+0.087	+0.783	-25.660
13.	Receiver amplitude nonlinearity	± 0.017	± 0.049	± 0.076	± 0.010	± 0.000	+0.034	+0.000	-50.419
14.	System amplitude and phase error	± 0.008	± 0.074	± 0.217	± 0.010	± 0.010	+0.051	+1.854	-26.666
15.	Receiver dynamic range	± 0.000	± 0.000	± 0.002	± 0.000	± 0.000	+0.001	+0.003	-71.625
16.	Room scattering	± 0.005	± 0.235	± 0.199	± 0.160	± 0.190	+0.532	+0.870	-30.893
17.	Leakage and crosstalk	± 0.000	± 0.000	± 0.000	± 0.000	± 0.000	+0.000	+0.000	-
18.	Miscellaneous random errors	± 0.002	± 0.019	± 0.022	± 0.003	± 0.010	+0.017	+0.057	-50.810
RSS		± 0.034	± 0.523	± 0.331	± 0.186	± 0.193	+0.704	+2.496	-8.597
exp. RSS (k = 3)		± 0.101	± 1.570	± 0.992	± 0.557	± 0.580	+1.960	+6.015	-3.825

Table C.2: Uncertainty budget for QH2000 antenna measurement (5 GHz) for regular equiangular $N = 35$ sampling (pos. A).

Uncertainty term (pos. B)		D (dBi)	HPBW _H (deg)	HPBW _E (deg)	Null _{Left} (deg)	Null _{Right} (deg)	max(CX _H) (dB)	max(CX _E) (dB)	ϵ (dB)
		8.137	69.838	52.201	-63.310	63.900	-27.856	-37.111	
1.	Probe relative pattern	± 0.008	± 0.140	± 0.067	± 0.020	± 0.020	+0.023	+0.466	-40.411
4.	Probe alignment error	± 0.019	± 0.127	± 0.147	± 0.006	± 0.013	+0.298	+0.612	-19.650
7.	AUT alignment error	± 0.002	± 0.026	± 0.017	± 0.020	± 0.015	+0.406	+1.132	-8.612
8.	Data point spacing	± 0.003	± 0.022	± 0.016	± 0.000	± 0.010	+0.030	+0.053	-56.415
9.	Measurement area truncation	-	-	-	-	-	-	-	-
10.	Position error	± 0.010	± 0.167	± 0.093	± 0.012	± 0.013	+0.022	+0.281	-42.312
12.	Multiple reflections	± 0.013	± 0.199	± 0.050	± 0.014	± 0.000	+0.030	+0.709	-28.448
13.	Receiver amplitude nonlinearity	± 0.018	± 0.055	± 0.082	± 0.010	± 0.000	+0.034	+0.006	-50.035
14.	System amplitude and phase error	± 0.001	± 0.044	± 0.025	± 0.000	± 0.010	+0.020	+0.126	-49.267
15.	Receiver dynamic range	± 0.000	± 0.001	± 0.002	± 0.010	± 0.000	+0.005	+0.011	-74.744
16.	Room scattering	± 0.009	± 0.153	± 0.074	± 0.040	± 0.030	+0.034	+0.292	-33.934
17.	Leakage and crosstalk	± 0.000	± 0.000	± 0.000	± 0.000	± 0.000	+0.000	+0.000	-
18.	Miscellaneous random errors	± 0.002	± 0.019	± 0.022	± 0.003	± 0.010	+0.017	+0.057	-50.810
RSS		± 0.034	± 0.365	± 0.226	± 0.055	± 0.047	+0.505	+1.538	-8.598
exp. RSS (k = 3)		± 0.101	± 1.094	± 0.678	± 0.164	± 0.140	+1.435	+3.980	-3.827

Table C.3: Uncertainty budget for QH2000 antenna measurement (5 GHz) for regular equiangular $N = 49$ sampling (pos B).

Uncertainty term (pos. A)		D (dBi)	HPBW _H (deg)	HPBW _E (deg)	Null _{Left} (deg)	Null _{Right} (deg)	max(CX _H) (dB)	max(CX _E) (dB)	ϵ (dB)
		8.137	69.838	52.201	-63.310	63.900	-27.856	-37.111	
1.	Probe relative pattern	± 0.004	± 0.086	± 0.046	± 0.020	± 0.010	+0.113	+0.699	-43.000
4.	Probe alignment error	± 0.007	± 0.053	± 0.037	± 0.008	± 0.012	+0.179	+0.590	-19.618
7.	AUT alignment error	± 0.002	± 0.027	± 0.018	± 0.015	± 0.015	+0.406	+1.134	-8.612
8.	Data point spacing	± 0.001	± 0.086	± 0.268	± 0.500	± 0.650	+0.363	+0.476	-25.536
9.	Measurement area truncation	-	-	-	-	-	-	-	-
10.	Position error	± 0.005	± 0.029	± 0.080	± 0.015	± 0.013	+0.020	+0.329	-42.627
12.	Multiple reflections	± 0.023	± 0.223	± 0.086	± 0.099	± 0.000	+0.038	+0.458	-24.743
13.	Receiver amplitude nonlinearity	± 0.016	± 0.050	± 0.073	± 0.010	± 0.000	+0.032	+0.007	-50.415
14.	System amplitude and phase error	± 0.007	± 0.004	± 0.095	± 0.010	± 0.000	+0.016	+0.537	-25.208
15.	Receiver dynamic range	± 0.000	± 0.002	± 0.009	± 0.000	± 0.000	+0.023	+0.046	-66.287
16.	Room scattering	± 0.004	± 0.417	± 0.070	± 0.100	± 0.260	+0.452	+0.191	-26.006
17.	Leakage and crosstalk	± 0.000	± 0.000	± 0.000	± 0.000	± 0.000	+0.000	+0.000	-
18.	Miscellaneous random errors	± 0.002	± 0.019	± 0.022	± 0.003	± 0.010	+0.017	+0.057	-50.810
RSS		± 0.031	± 0.496	± 0.331	± 0.521	± 0.701	+0.727	+1.648	-8.594
exp. RSS (k = 3)		± 0.093	± 1.487	± 0.992	± 1.562	± 2.102	+2.021	+4.227	-3.823

Table C.4: Uncertainty budget for QH2000 antenna measurement (5 GHz) for equiangular $N = 17$ sampling (pos A).

Uncertainty term (pos. B)		D (dBi)	HPBW _H (deg)	HPBW _E (deg)	Null _{Left} (deg)	Null _{Right} (deg)	max(CX _H) (dB)	max(CX _E) (dB)	ϵ (dB)
		8.137	69.838	52.201	-63.310	63.900	-27.856	-37.111	
1.	Probe relative pattern	± 0.007	± 0.168	± 0.051	± 0.020	± 0.020	+0.117	+0.366	-40.338
4.	Probe alignment error	± 0.017	± 0.137	± 0.141	± 0.006	± 0.013	+0.277	+0.589	-19.650
7.	AUT alignment error	± 0.002	± 0.027	± 0.018	± 0.020	± 0.015	+0.406	+1.134	-8.612
8.	Data point spacing	± 0.026	± 1.141	± 1.155	± 0.150	± 0.760	+0.749	+4.068	-23.983
9.	Measurement area truncation	-	-	-	-	-	-	-	-
10.	Position error	± 0.004	± 0.127	± 0.042	± 0.010	± 0.008	+0.053	+0.276	-41.815
12.	Multiple reflections	± 0.039	± 0.297	± 0.254	± 0.106	± 0.092	+0.026	+0.882	-28.910
13.	Receiver amplitude nonlinearity	± 0.016	± 0.012	± 0.059	± 0.010	± 0.010	+0.031	+0.066	-50.020
14.	System amplitude and phase error	± 0.004	± 0.009	± 0.093	± 0.000	± 0.000	+0.008	+0.033	-50.115
15.	Receiver dynamic range	± 0.001	± 0.013	± 0.006	± 0.010	± 0.000	+0.011	+0.043	-65.772
16.	Room scattering	± 0.032	± 0.587	± 0.556	± 0.090	± 0.170	+0.202	+1.313	-24.507
17.	Leakage and crosstalk	± 0.000	± 0.000	± 0.000	± 0.000	± 0.000	+0.000	+0.000	-
18.	Miscellaneous random errors	± 0.002	± 0.019	± 0.022	± 0.003	± 0.010	+0.017	+0.057	-50.810
RSS		± 0.062	± 1.341	± 1.321	± 0.207	± 0.785	+0.912	+4.349	-8.595
exp. RSS (k = 3)		± 0.186	± 4.024	± 3.963	± 0.622	± 2.355	+2.492	+9.395	-3.824

Table C.5: Uncertainty budget for QH2000 antenna measurement (5 GHz) for equiangular $N = 17$ sampling (pos. B).

Uncertainty term (pos. A)		D (dBi)	HPBW _H (deg)	HPBW _E (deg)	Null _{Left} (deg)	Null _{Right} (deg)	max(CX _H) (dB)	max(CX _E) (dB)	ϵ (dB)
		8.137	69.838	52.201	-63.310	63.900	-27.856	-37.111	
1.	Probe relative pattern	± 0.012	± 0.173	± 0.115	± 0.020	± 0.010	+0.092	+1.111	-42.962
4.	Probe alignment error	± 0.009	± 0.088	± 0.054	± 0.010	± 0.013	+0.184	+0.696	-19.618
7.	AUT alignment error	± 0.002	± 0.027	± 0.018	± 0.015	± 0.015	+0.406	+1.134	-8.612
8.	Data point spacing	± 0.049	± 0.113	± 0.421	± 0.210	± 0.200	+0.323	+1.977	-25.626
9.	Measurement area truncation	-	-	-	-	-	-	-	-
10.	Position error	± 0.013	± 0.127	± 0.132	± 0.015	± 0.008	+0.042	+0.221	-42.638
12.	Multiple reflections	± 0.025	± 0.409	± 0.223	± 0.035	± 0.014	+0.176	+0.629	-24.773
13.	Receiver amplitude nonlinearity	± 0.023	± 0.113	± 0.138	± 0.010	± 0.000	+0.039	+0.026	-50.406
14.	System amplitude and phase error	± 0.015	± 0.140	± 0.027	± 0.010	± 0.000	+0.001	+0.215	-44.224
15.	Receiver dynamic range	± 0.000	± 0.007	± 0.005	± 0.000	± 0.000	+0.013	+0.012	-66.241
16.	Room scattering	± 0.006	± 0.478	± 0.354	± 0.230	± 0.220	+0.213	+0.865	-26.213
17.	Leakage and crosstalk	± 0.000	± 0.000	± 0.000	± 0.000	± 0.000	+0.000	+0.000	-
18.	Miscellaneous random errors	± 0.002	± 0.019	± 0.022	± 0.003	± 0.010	+0.017	+0.057	-50.810
RSS		± 0.065	± 0.704	± 0.637	± 0.315	± 0.299	+0.615	+2.659	-8.595
exp. RSS (k = 3)		± 0.195	± 2.113	± 1.912	± 0.946	± 0.896	+1.728	+6.339	-3.824

Table C.6: Uncertainty budget for QH2000 antenna measurement (5 GHz) for projected equiangular $N = 17$ sampling (pos. A).

Uncertainty term (pos. B)		D (dBi)	HPBW _H (deg)	HPBW _E (deg)	Null _{Left} (deg)	Null _{Right} (deg)	max(CX _H) (dB)	max(CX _E) (dB)	ϵ (dB)
		8.137	69.838	52.201	-63.310	63.900	-27.856	-37.111	
1.	Probe relative pattern	± 0.001	± 0.224	± 0.000	± 0.010	± 0.020	+0.064	+0.827	-40.353
4.	Probe alignment error	± 0.019	± 0.148	± 0.150	± 0.012	± 0.014	+0.292	+0.714	-19.650
7.	AUT alignment error	± 0.002	± 0.027	± 0.018	± 0.020	± 0.015	+0.406	+1.134	-8.612
8.	Data point spacing	± 0.063	± 0.163	± 0.264	± 0.040	± 0.490	+0.928	+0.527	-24.254
9.	Measurement area truncation	-	-	-	-	-	-	-	-
10.	Position error	± 0.018	± 0.130	± 0.128	± 0.010	± 0.048	+0.020	+0.199	-41.897
12.	Multiple reflections	± 0.000	± 0.489	± 0.101	± 0.163	± 0.042	+0.131	+0.684	-29.643
13.	Receiver amplitude nonlinearity	± 0.024	± 0.115	± 0.144	± 0.010	± 0.000	+0.040	+0.036	-50.031
14.	System amplitude and phase error	± 0.007	± 0.073	± 0.035	± 0.000	± 0.000	+0.010	+0.021	-46.235
15.	Receiver dynamic range	± 0.000	± 0.000	± 0.004	± 0.000	± 0.000	+0.019	+0.017	-65.928
16.	Room scattering	± 0.029	± 0.383	± 0.126	± 0.170	± 0.020	+0.635	+0.401	-24.796
17.	Leakage and crosstalk	± 0.000	± 0.000	± 0.000	± 0.000	± 0.000	+0.000	+0.000	-
18.	Miscellaneous random errors	± 0.002	± 0.019	± 0.022	± 0.003	± 0.010	+0.017	+0.057	-50.810
RSS		± 0.078	± 0.722	± 0.397	± 0.240	± 0.495	+1.207	+1.756	-8.595
exp. RSS (k = 3)		± 0.234	± 2.165	± 1.190	± 0.721	± 1.486	+3.211	+4.466	-3.824

Table C.7: Uncertainty budget for QH2000 antenna measurement (5 GHz) for projected equiangular $N = 17$ sampling (pos. B).

Uncertainty term (pos. A)		D (dBi)	HPBW _H (deg)	HPBW _E (deg)	Null _{Left} (deg)	Null _{Right} (deg)	max(CX _H) (dB)	max(CX _E) (dB)	ϵ (dB)
		8.137	69.838	52.201	-63.310	63.900	-27.856	-37.111	
1.	Probe relative pattern	± 0.009	± 0.122	± 0.084	± 0.020	± 0.010	+0.022	+1.271	-43.021
4.	Probe alignment error	± 0.008	± 0.067	± 0.042	± 0.010	± 0.013	+0.188	+0.703	-19.618
7.	AUT alignment error	± 0.002	± 0.027	± 0.018	± 0.015	± 0.015	+0.406	+1.134	-8.612
8.	Data point spacing	± 0.052	± 1.705	± 0.609	± 0.370	± 0.280	+2.216	+0.317	-25.129
9.	Measurement area truncation	-	-	-	-	-	-	-	-
10.	Position error	± 0.004	± 0.037	± 0.063	± 0.015	± 0.013	+0.028	+0.224	-42.635
12.	Multiple reflections	± 0.023	± 0.296	± 0.342	± 0.064	± 0.028	+0.556	+0.095	-25.351
13.	Receiver amplitude nonlinearity	± 0.023	± 0.108	± 0.145	± 0.010	± 0.000	+0.041	+0.119	-50.444
14.	System amplitude and phase error	± 0.001	± 0.042	± 0.078	± 0.000	± 0.000	+0.003	+0.091	-49.403
15.	Receiver dynamic range	± 0.001	± 0.005	± 0.006	± 0.000	± 0.010	+0.012	+0.045	-64.777
16.	Room scattering	± 0.066	± 1.352	± 0.998	± 0.220	± 0.130	+1.962	+2.796	-26.154
17.	Leakage and crosstalk	± 0.000	± 0.000	± 0.000	± 0.000	± 0.000	+0.000	+0.000	-
18.	Miscellaneous random errors	± 0.002	± 0.019	± 0.022	± 0.003	± 0.010	+0.017	+0.057	-50.810
RSS		± 0.091	± 2.204	± 1.235	± 0.436	± 0.311	+2.890	+3.198	-8.595
exp. RSS (k = 3)		± 0.273	± 6.612	± 3.704	± 1.309	± 0.934	+6.787	+7.367	-3.824

Table C.8: Uncertainty budget for QH2000 antenna measurement (5 GHz) for projected thinned equiangular sampling (pos. A).

Uncertainty term (pos. B)		D (dBi)	HPBW _H (deg)	HPBW _E (deg)	Null _{Left} (deg)	Null _{Right} (deg)	max(CX _H) (dB)	max(CX _E) (dB)	ϵ (dB)
		8.137	69.838	52.201	-63.310	63.900	-27.856	-37.111	
1.	Probe relative pattern	± 0.005	± 0.150	± 0.051	± 0.020	± 0.020	+0.029	+1.066	-40.383
4.	Probe alignment error	± 0.018	± 0.123	± 0.139	± 0.006	± 0.014	+0.298	+0.726	-19.650
7.	AUT alignment error	± 0.002	± 0.027	± 0.018	± 0.020	± 0.015	+0.406	+1.134	-8.612
8.	Data point spacing	± 0.009	± 0.314	± 0.955	± 0.110	± 0.510	+0.614	+0.972	-22.917
9.	Measurement area truncation	-	-	-	-	-	-	-	-
10.	Position error	± 0.015	± 0.209	± 0.076	± 0.012	± 0.013	+0.025	+0.217	-41.477
12.	Multiple reflections	± 0.011	± 0.061	± 0.542	± 0.127	± 0.014	+0.246	+0.434	-28.553
13.	Receiver amplitude nonlinearity	± 0.024	± 0.112	± 0.154	± 0.010	± 0.000	+0.041	+0.038	-50.067
14.	System amplitude and phase error	± 0.002	± 0.063	± 0.162	± 0.000	± 0.010	+0.075	+0.379	-50.030
15.	Receiver dynamic range	± 0.001	± 0.004	± 0.011	± 0.010	± 0.000	+0.020	+0.004	-65.021
16.	Room scattering	± 0.010	± 0.147	± 0.874	± 0.180	± 0.020	+0.657	+3.873	-23.733
17.	Leakage and crosstalk	± 0.000	± 0.000	± 0.000	± 0.000	± 0.000	+0.000	+0.000	-
18.	Miscellaneous random errors	± 0.002	± 0.019	± 0.022	± 0.003	± 0.010	+0.017	+0.057	-50.810
RSS		± 0.039	± 0.472	± 1.431	± 0.249	± 0.512	+1.034	+4.167	-8.593
exp. RSS (k = 3)		± 0.116	± 1.416	± 4.293	± 0.746	± 1.535	+2.794	+9.088	-3.822

Table C.9: Uncertainty budget for QH2000 antenna measurement (5 GHz) for projected thinned equiangular sampling (pos. B).

Uncertainty term (pos. A)		D (dBi)	HPBW _H (deg)	HPBW _E (deg)	Null _{Left} (deg)	Null _{Right} (deg)	max(CX _H) (dB)	max(CX _E) (dB)	ϵ (dB)
		8.137	69.838	52.201	-63.310	63.900	-27.856	-37.111	
1.	Probe relative pattern	± 0.013	± 0.190	± 0.143	± 0.020	± 0.000	+0.136	+0.399	-42.648
4.	Probe alignment error	± 0.008	± 0.067	± 0.046	± 0.008	± 0.013	+0.190	+0.620	-19.618
7.	AUT alignment error	± 0.002	± 0.027	± 0.018	± 0.015	± 0.015	+0.406	+1.134	-8.612
8.	Data point spacing	± 0.029	± 0.012	± 0.601	± 0.120	± 0.460	+2.380	+2.311	-22.923
9.	Measurement area truncation	-	-	-	-	-	-	-	-
10.	Position error	± 0.008	± 0.091	± 0.048	± 0.015	± 0.018	+0.023	+0.362	-42.501
12.	Multiple reflections	± 0.083	± 0.605	± 0.044	± 0.198	± 0.057	+0.290	+1.774	-24.750
13.	Receiver amplitude nonlinearity	± 0.022	± 0.100	± 0.132	± 0.010	± 0.000	+0.035	+0.109	-50.238
14.	System amplitude and phase error	± 0.007	± 0.033	± 0.127	± 0.010	± 0.010	+0.002	+0.211	-55.853
15.	Receiver dynamic range	± 0.000	± 0.002	± 0.021	± 0.000	± 0.010	+0.012	+0.125	-63.877
16.	Room scattering	± 0.016	± 0.108	± 0.351	± 0.290	± 0.070	+1.858	+1.214	-24.218
17.	Leakage and crosstalk	± 0.000	± 0.000	± 0.000	± 0.000	± 0.000	+0.000	+0.000	-
18.	Miscellaneous random errors	± 0.002	± 0.019	± 0.022	± 0.003	± 0.010	+0.017	+0.057	-50.810
RSS		± 0.094	± 0.662	± 0.739	± 0.373	± 0.470	+2.926	+3.189	-8.592
exp. RSS (k = 3)		± 0.283	± 1.986	± 2.217	± 1.118	± 1.409	+6.855	+7.350	-3.821

Table C.10: Uncertainty budget for QH2000 antenna measurement (5 GHz) for projected spiral (both pol.) sampling (pos. A).

Uncertainty term (pos. B)		D (dBi)	HPBW _H (deg)	HPBW _E (deg)	Null _{Left} (deg)	Null _{Right} (deg)	max(CX _H) (dB)	max(CX _E) (dB)	ϵ (dB)
		8.137	69.838	52.201	-63.310	63.900	-27.856	-37.111	
1.	Probe relative pattern	± 0.002	± 0.250	± 0.040	± 0.010	± 0.000	+0.080	+0.814	-40.125
4.	Probe alignment error	± 0.018	± 0.122	± 0.140	± 0.012	± 0.014	+0.296	+0.614	-19.650
7.	AUT alignment error	± 0.002	± 0.027	± 0.018	± 0.020	± 0.015	+0.406	+1.134	-8.612
8.	Data point spacing	± 0.111	± 0.835	± 0.194	± 1.170	± 1.110	+4.012	+1.548	-21.606
9.	Measurement area truncation	-	-	-	-	-	-	-	-
10.	Position error	± 0.011	± 0.080	± 0.093	± 0.016	± 0.024	+0.287	+0.559	-41.425
12.	Multiple reflections	± 0.093	± 0.991	± 0.003	± 0.148	± 0.057	+0.601	+0.664	-27.688
13.	Receiver amplitude nonlinearity	± 0.023	± 0.099	± 0.137	± 0.010	± 0.000	+0.035	+0.029	-49.847
14.	System amplitude and phase error	± 0.010	± 0.043	± 0.126	± 0.000	± 0.000	+0.006	+0.135	-50.811
15.	Receiver dynamic range	± 0.000	± 0.011	± 0.009	± 0.000	± 0.000	+0.022	+0.128	-63.602
16.	Room scattering	± 0.060	± 0.546	± 1.021	± 0.990	± 0.260	+1.552	+1.624	-22.502
17.	Leakage and crosstalk	± 0.000	± 0.000	± 0.000	± 0.000	± 0.000	+0.000	+0.000	-
18.	Miscellaneous random errors	± 0.002	± 0.019	± 0.022	± 0.003	± 0.010	+0.017	+0.057	-50.810
RSS		± 0.160	± 1.440	± 1.070	± 1.540	± 1.142	+4.227	+2.639	-8.589
exp. RSS (k = 3)		± 0.481	± 4.320	± 3.211	± 4.620	± 3.426	+9.189	+6.298	-3.818

Table C.11: Uncertainty budget for QH2000 antenna measurement (5 GHz) for projected spiral (both pol.) sampling (pos. B).

Uncertainty term (pos. A)		D (dBi)	HPBW _H (deg)	HPBW _E (deg)	Null _{Left} (deg)	Null _{Right} (deg)	max(CX _H) (dB)	max(CX _E) (dB)	ϵ (dB)
		8.137	69.838	52.201	-63.310	63.900	-27.856	-37.111	
1.	Probe relative pattern	± 0.022	± 0.251	± 0.143	± 0.020	± 0.010	+0.222	+0.726	-42.178
4.	Probe alignment error	± 0.008	± 0.078	± 0.031	± 0.012	± 0.012	+0.203	+0.583	-19.618
7.	AUT alignment error	± 0.002	± 0.027	± 0.018	± 0.015	± 0.015	+0.406	+1.134	-8.612
8.	Data point spacing	± 0.323	± 2.961	± 7.251	± 1.410	± 0.430	+8.499	+20.520	-12.961
9.	Measurement area truncation	-	-	-	-	-	-	-	-
10.	Position error	± 0.013	± 0.182	± 0.098	± 0.036	± 0.013	+0.225	+0.921	-38.706
12.	Multiple reflections	± 0.398	± 1.866	± 3.685	± 1.273	± 0.290	+0.134	+0.048	-19.862
13.	Receiver amplitude nonlinearity	± 0.012	± 0.017	± 0.045	± 0.020	± 0.000	+0.024	+0.055	-49.980
14.	System amplitude and phase error	± 0.004	± 0.033	± 0.150	± 0.010	± 0.000	+0.028	+0.023	-45.831
15.	Receiver dynamic range	± 0.001	± 0.014	± 0.019	± 0.020	± 0.000	+0.053	+0.047	-56.423
16.	Room scattering	± 0.063	± 1.847	± 2.487	± 2.050	± 0.020	+5.132	+15.962	-15.504
17.	Leakage and crosstalk	± 0.000	± 0.000	± 0.000	± 0.000	± 0.000	+0.000	+0.000	-
18.	Miscellaneous random errors	± 0.002	± 0.019	± 0.022	± 0.003	± 0.010	+0.017	+0.057	-50.810
RSS		± 0.519	± 3.971	± 8.509	± 2.795	± 0.520	+9.087	+21.565	-8.236
exp. RSS (k = 3)		± 1.621	± 11.912	± 25.526	± 8.386	± 1.559	+16.312	+30.610	-3.465

Table C.12: Uncertainty budget for QH2000 antenna measurement (5 GHz) for projected spiral (opt. pol.) sampling (pos. A).

Uncertainty term (pos. B)		D (dBi)	HPBW _H (deg)	HPBW _E (deg)	Null _{Left} (deg)	Null _{Right} (deg)	max(CX _H) (dB)	max(CX _E) (dB)	ϵ (dB)
		8.137	69.838	52.201	-63.310	63.900	-27.856	-37.111	
1.	Probe relative pattern	± 0.001	± 0.225	± 0.134	± 0.020	± 0.030	+0.110	+0.729	-39.459
4.	Probe alignment error	± 0.015	± 0.101	± 0.159	± 0.006	± 0.008	+0.306	+0.851	-19.650
7.	AUT alignment error	± 0.002	± 0.027	± 0.018	± 0.020	± 0.015	+0.406	+1.134	-8.612
8.	Data point spacing	± 0.315	± 0.176	± 2.529	± 2.250	± 0.570	+6.126	+13.460	-10.835
9.	Measurement area truncation	-	-	-	-	-	-	-	-
10.	Position error	± 0.007	± 0.106	± 0.176	± 0.116	± 0.041	+0.675	+1.093	-34.922
12.	Multiple reflections	± 0.010	± 0.673	± 1.746	± 0.226	± 0.000	+0.702	+1.010	-17.507
13.	Receiver amplitude nonlinearity	± 0.021	± 0.078	± 0.072	± 0.010	± 0.000	+0.027	+0.169	-49.661
14.	System amplitude and phase error	± 0.001	± 0.042	± 0.072	± 0.010	± 0.000	+0.020	+0.075	-52.068
15.	Receiver dynamic range	± 0.000	± 0.042	± 0.010	± 0.030	± 0.000	+0.021	+0.129	-54.942
16.	Room scattering	± 0.288	± 1.844	± 2.795	± 2.870	± 0.420	+6.556	+10.754	-11.851
17.	Leakage and crosstalk	± 0.000	± 0.000	± 0.000	± 0.000	± 0.000	+0.000	+0.000	-
18.	Miscellaneous random errors	± 0.002	± 0.019	± 0.022	± 0.003	± 0.010	+0.017	+0.057	-50.810
RSS		± 0.428	± 1.992	± 4.164	± 3.656	± 0.710	+8.058	+14.733	-7.582
exp. RSS (k = 3)		± 1.319	± 5.975	± 12.493	± 10.968	± 2.130	+14.943	+23.143	-2.810

Table C.13: Uncertainty budget for QH2000 antenna measurement (5 GHz) for projected spiral (opt. pol.) sampling (pos. B).

Uncertainty term (pos. A)		D (dBi)	HPBW _H (deg)	HPBW _E (deg)	Null _{Left} (deg)	Null _{Right} (deg)	max(CX _H) (dB)	max(CX _E) (dB)	ϵ (dB)
		8.137	69.838	52.201	-63.310	63.900	-27.856	-37.111	
1.	Probe relative pattern	± 0.012	± 0.135	± 0.101	± 0.020	± 0.010	+0.066	+1.718	-42.996
4.	Probe alignment error	± 0.008	± 0.053	± 0.039	± 0.010	± 0.006	+0.175	+0.881	-19.618
7.	AUT alignment error	± 0.002	± 0.027	± 0.018	± 0.015	± 0.015	+0.406	+1.134	-8.612
8.	Data point spacing	± 0.091	± 1.354	± 0.783	± 0.300	± 1.110	+3.956	+0.729	-20.710
9.	Measurement area truncation	-	-	-	-	-	-	-	-
10.	Position error	± 0.005	± 0.051	± 0.065	± 0.012	± 0.006	+0.025	+0.214	-42.527
12.	Multiple reflections	± 0.003	± 0.267	± 0.304	± 0.028	± 0.170	+0.096	+0.261	-24.310
13.	Receiver amplitude nonlinearity	± 0.024	± 0.116	± 0.148	± 0.010	± 0.000	+0.044	+0.078	-50.408
14.	System amplitude and phase error	± 0.013	± 0.035	± 0.171	± 0.000	± 0.000	+0.000	+0.247	-53.157
15.	Receiver dynamic range	± 0.001	± 0.006	± 0.006	± 0.000	± 0.000	+0.003	+0.044	-63.285
16.	Room scattering	± 0.019	± 0.109	± 0.347	± 0.090	± 0.270	+2.889	+0.468	-22.573
17.	Leakage and crosstalk	± 0.000	± 0.000	± 0.000	± 0.000	± 0.000	+0.000	+0.000	-
18.	Miscellaneous random errors	± 0.002	± 0.019	± 0.022	± 0.003	± 0.010	+0.017	+0.057	-50.810
RSS		± 0.098	± 1.398	± 0.945	± 0.316	± 1.155	+4.614	+2.301	-8.585
exp. RSS (k = 3)		± 0.294	± 4.195	± 2.836	± 0.948	± 3.465	+9.836	+5.620	-3.814

Table C.14: Uncertainty budget for QH2000 antenna measurement (5 GHz) for projected max. determinant sampling (pos. A).

Uncertainty term (pos. B)		D (dBi)	HPBW _H (deg)	HPBW _E (deg)	Null _{Left} (deg)	Null _{Right} (deg)	max(CX _H) (dB)	max(CX _E) (dB)	ϵ (dB)
		8.137	69.838	52.201	-63.310	63.900	-27.856	-37.111	
1.	Probe relative pattern	± 0.001	± 0.176	± 0.029	± 0.020	± 0.020	+0.050	+1.550	-40.361
4.	Probe alignment error	± 0.018	± 0.108	± 0.131	± 0.008	± 0.008	+0.279	+0.930	-19.650
7.	AUT alignment error	± 0.002	± 0.027	± 0.018	± 0.020	± 0.015	+0.406	+1.134	-8.612
8.	Data point spacing	± 0.017	± 0.690	± 1.108	± 0.340	± 0.060	+4.684	+4.470	-19.542
9.	Measurement area truncation	-	-	-	-	-	-	-	-
10.	Position error	± 0.012	± 0.143	± 0.181	± 0.021	± 0.041	+0.174	+0.242	-40.803
12.	Multiple reflections	± 0.045	± 0.419	± 0.535	± 0.120	± 0.000	+0.404	+1.105	-25.699
13.	Receiver amplitude nonlinearity	± 0.025	± 0.120	± 0.156	± 0.010	± 0.000	+0.041	+0.019	-50.036
14.	System amplitude and phase error	± 0.006	± 0.046	± 0.131	± 0.010	± 0.000	+0.026	+0.147	-50.979
15.	Receiver dynamic range	± 0.000	± 0.002	± 0.003	± 0.000	± 0.000	+0.032	+0.110	-62.697
16.	Room scattering	± 0.021	± 0.926	± 0.425	± 0.050	± 0.320	+4.264	+3.396	-20.980
17.	Leakage and crosstalk	± 0.000	± 0.000	± 0.000	± 0.000	± 0.000	+0.000	+0.000	-
18.	Miscellaneous random errors	± 0.002	± 0.019	± 0.022	± 0.003	± 0.010	+0.017	+0.057	-50.810
RSS		± 0.062	± 1.261	± 1.337	± 0.366	± 0.329	+5.839	+5.477	-8.576
exp. RSS (k = 3)		± 0.187	± 3.782	± 4.012	± 1.098	± 0.988	+11.767	+11.212	-3.805

Table C.15: Uncertainty budget for QH2000 antenna measurement (5 GHz) for projected max. determinant sampling (pos. B).

Appendix D

Test zone simulation

The simulations of the SNF test zone are performed with FEKO [153] and executed on a computer with 24 cores (2.2 GHz) and 256 GB RAM. The range geometry is shown in Fig. 7.13 on page 116. The absorber on the wall are typical pyramidal absorber AEP-24 and AEP-18 on the one and wedge absorber AEPW-12 on the other side [158]. The size of each wall is approximately 3 m by 3 m. Since the exact dielectric properties of the absorbing material are not available, $\epsilon'_r = 1.95$, $\epsilon''_r = 1.4$ and $\tan \delta = 0.71795$ [159] are used. Although this is not exact, it is assumed that the used values are close to the true value and experience showed that small changes in the parameters do not significantly change the scattered field. The compact range reflector geometry is imported as CAD file and its material in the simulation is PEC. The radiation pattern of the probe is defined by its SMC. The simulations are performed for two probe polarizations (H and V) separately. Details of the simulations are given in the following tables:

Simulation	Mesh size	No. of unknowns	RAM (GB)	Time (h)
Probe only	-	-	<0.1	<0.1
Absorber	$\lambda/8$	3080358	104.2	4.6
CATR reflector	$\lambda/8$	94648	2.8	<0.1

Table D.1: Test zone simulations at 2400 MHz with residual $1e^{-8}$.

Simulation	Mesh size	No. of unknowns	RAM (GB)	Time (h)
Probe only	-	-	<0.1	<0.1
Absorber	$\lambda/6$	7560282	234.1	32.2
CATR reflector	$\lambda/6$	232728	8.0	0.2

Table D.2: Test zone simulations at 5 GHz with residual $1e^{-8}$.

The test zone field is calculated on a sphere with radius $r = 1$ m and a spatial resolution of 1° in θ and ϕ . The individual test zone fields are combined by superposition. Thus, interactions between probe, absorber and CATR reflector are neglected.

List of abbreviations

AUT	antenna under test
BTS	base transceiver station
CG	conjugate gradient
CS	compressed sensing
DOF	degrees of freedom
EES	equivalent error signal
FOP	first order probe
FSLA	first sidelobe angle
FSL	first sidelobe level
HOP	higher-order probe
HPBW	half power beam width
IEEE	Institute of Electrical and Electronics Engineers
IHF	Institute of High Frequency Technology
IOT	internet of things
LES	linear equation system
MIMO	multiple input multiple output
MRE	maximum radial extend
NSP	null space property
PEC	perfect electric conductor
RIP	restricted isometry property
RSS	root mean square
SMC	spherical mode coefficients
SNF	spherical near-field
SWE	spherical wave expansion
TE	transverse electric
TM	transverse magnetic
5G	fifth generation cellular network

Bibliography

- [1] *Mobility Report*. Stockholm, Sweden: Ericsson, 2016. [Online]. Available: <http://www.ericsson.com/res/docs/2016/ericsson-mobility-report-2016.pdf> 1
- [2] *Cisco Visual Networking Index: Global Mobile Data Traffic Forecast Update, 2016–2021 (White paper)*. San Jose, USA: Cisco Systems Inc., 2017. [Online]. Available: <http://www.cisco.com/c/en/us/solutions/collateral/service-provider/visual-networking-index-vni/mobile-white-paper-c11-520862.pdf> 1
- [3] A. Osseiran, F. Boccardi, V. Braun, K. Kusume, P. Marsch, M. Maternia, O. Queseth, M. Schellmann, H. Schotten, H. Taoka, H. Tullberg, M. A. Uusitalo, B. Timus, and M. Fallgren, “Scenarios for 5G mobile and wireless communications: the vision of the METIS project,” *IEEE Communications Magazine*, vol. 52, no. 5, pp. 26–35, May 2014. 1
- [4] F. Boccardi, R. W. Heath, A. Lozano, T. L. Marzetta, and P. Popovski, “Five disruptive technology directions for 5G,” *IEEE Communications Magazine*, vol. 52, no. 2, pp. 74–80, Feb. 2014. 1
- [5] *Towards the Connected Community: Accelerating Wireless Broadband with Small Cell Ingenuity (White paper)*. Richardson, USA: Kathrein USA, 2016. [Online]. Available: <http://www.kathreinusa.com/wp-content/uploads/2016/10/Kathrein-Whitepaper-Small-Cell-Ingenuity-v1.pdf> 1
- [6] *The Role of Antenna Quality in Meeting Mobile Data Demand (White paper)*. Richardson, USA: Kathrein USA, 2015. [Online]. Available: <http://www.kathreinusa.com/wp-content/uploads/2015/12/The-Role-of-Antenna-Quality-Kathrein-USA-Whitepaper-v3.pdf> 1
- [7] D. Gray, “How to choose an antenna range configuration,” in *AMTA 24th Annual Meeting and Symposium*, 2002. 1
- [8] J. S. Hollis, T. J. Lyon, and L. Clayton, *Microwave antenna measurement*, 3rd ed. Atlanta, USA: Scientific-Atlanta, 1985. 1
- [9] *IEEE Standard Test Procedures for Antennas*, IEEE Std. 149-1979, 2008. 1
- [10] *Recommended Practice for Near-Field Antenna Measurements*, IEEE Std. 1720-2012, 2012. 1, 2, 5, 9, 17, 23, 43, 66, 76, 95, 102, 111, 115, 123
- [11] R. C. Johnson, H. A. Ecker, and J. S. Hollis, “Determination of far-field antenna patterns from near-field measurements,” *Proceedings of the IEEE*, vol. 61, no. 12, pp. 1668–1694, Dec. 1973. 1
- [12] W. H. Kummer and E. S. Gillespie, “Antenna measurements – 1978,” *Proceedings of the IEEE*, vol. 66, no. 4, pp. 483–507, Apr. 1978. 1
- [13] A. D. Yaghjian, “An overview of near-field antenna measurements,” *IEEE Transactions on Antennas and Propagation*, vol. 34, no. 1, pp. 30–45, Jan. 1986. 1
- [14] P. J. Wood, “Some special advantages of spherical near-field testing,” in *7th International Conference on Antennas and Propagation (ICAP)*, 1991, pp. 527–530. 2

- [15] O. Breinbjerg, “Spherical near-field antenna measurements — the most accurate antenna measurement technique,” in *IEEE AP-S Symposium on Antennas and Propagation*, 2016, pp. 1019–1020. 2, 5, 13
- [16] G. P. Rodrigue and C. P. Burns, “Cost comparison of near-field measurements and far-field measurements for far-field patterns,” in *IEEE AP-S Symposium on Antennas and Propagation*, 1974, pp. 165–168. 2
- [17] G. Hickman, “Economy of near field antenna measurements,” in *AMTA 1st Annual Meeting and Symposium*, 1979. 2
- [18] J. R. Jones, C. E. Green, D. W. Hess, and K. H. Teegardin, “A low cost spherical near-field range facility,” in *AMTA 9th Annual Meeting and Symposium*, 1987. 2
- [19] J. Way and K. Haner, “A low cost spherical near-field system,” in *AMTA 16th Annual Meeting and Symposium*, 1994. 2
- [20] J.-C. Bolomey and F. E. Gardiol, *Engineering Applications of the Modulated Scatterer Technique*. London, UK: Artech House, 2001. 2, 23
- [21] J. E. Hansen, Ed., *Spherical Near-field Antenna Measurements*. London, UK: Peter Peregrinus, Ltd., 1988. 2, 5, 6, 8, 9, 11, 12, 13, 16, 17, 23, 25, 29, 30, 31, 33, 46, 47, 55, 58, 76, 103
- [22] O. M. Bucci, C. Gennarelli, and C. Savarese, “Representation of electromagnetic fields over arbitrary surfaces by a finite and nonredundant number of samples,” *IEEE Transactions on Antennas and Propagation*, vol. 46, no. 3, pp. 351–359, Mar. 1998. 2, 33, 47
- [23] O. M. Bucci, C. Gennarelli, F. D’Agostino, and C. Savarese, “A new and efficient NF-FF transformation with spherical spiral scanning,” in *IEEE AP-S Symposium on Antennas and Propagation*, 2001, pp. 629–632. 2, 47, 48, 49, 56
- [24] B. T. Walkenhorst and S. T. McBride, “Acquisition, reconstruction, and transformation of a spiral near-field scan,” in *AMTA 39th Annual Meeting and Symposium*, 2017, pp. 289–294. 3, 47, 48, 73
- [25] L. J. Foged, F. Saccardi, F. Mioc, and P. O. Iversen, “Spherical near field offset measurements using downsampled acquisition and advanced NF/FF transformation algorithm,” in *10th European Conference on Antennas and Propagation (EuCAP)*, 2016, pp. 1–3. 3, 76
- [26] W. W. Hansen, “A new type of expansion in radiation problems,” *Physical Review*, vol. 47, no. 2, pp. 139–143, Jan. 1935. 5
- [27] C. G. Montgomery, R. H. Dicke, and E. M. Purcell, *Principles of Microwave Circuits*. Institution of Engineering and Technology, 1948. 5
- [28] F. Jensen, “Electromagnetic near-field – far-field correlations,” Ph.D. thesis, Technical University of Denmark, 1970. 5, 14
- [29] P. F. Wacker, “Near-field antenna measurements using a spherical scan: Efficient data reduction with probe correction,” in *Conference on Precision Electromagnetic Measurements*, 1974. 5, 13, 16
- [30] —, “Non-planar near-field measurements: Spherical scanning,” National Bureau of Standards, Boulder, CO, Tech. Rep., 1975. 5, 13, 16, 17
- [31] F. H. Larsen, “Probe-corrected spherical near-field antenna measurements,” Ph.D. thesis, Technical University of Denmark, 1980. 5, 15, 16

- [32] D. W. Hess, "A note to show how an alternative spherical mode normalization simplified the relationship between transmitting and receiving characteristics," in *AMTA 28th Annual Meeting and Symposium*, 2006. 9
- [33] O. M. Bucci and G. Franceschetti, "On the spatial bandwidth of scattered fields," *IEEE Transactions on Antennas and Propagation*, vol. 35, no. 12, pp. 1445–1455, Dec. 1987. 9, 33
- [34] —, "On the degrees of freedom of scattered fields," *IEEE Transactions on Antennas and Propagation*, vol. 37, no. 7, pp. 918–926, Jul. 1989. 9
- [35] F. Jensen and A. Frandsen, "On the number of modes in spherical wave expansions," in *AMTA 26th Annual Meeting and Symposium*, 2004, pp. 489–494. 9
- [36] R. C. Wittmann, "Spherical near-field scanning: determining the incident field near a rotatable probe," in *IEEE AP-S Symposium on Antennas and Propagation*, 1990, pp. 224–227. 12, 115, 124
- [37] D. N. Black, "Test zone field compensation," Ph.D. thesis, Georgia Institute of Technology, 1994. 12
- [38] E. B. Joy, "Antenna measurement range characterization and compensation," in *4th European Conference on Antennas and Propagation (EuCAP)*, 2010, pp. 1–5. 12
- [39] R. J. Pogorzelski, "Extended probe instrument calibration (EPIC) for accurate spherical near-field antenna measurements," *IEEE Transactions on Antennas and Propagation*, vol. 57, no. 10, pp. 3366–3371, Oct. 2009. 13
- [40] —, "Experimental demonstration of the extended probe instrument calibration (EPIC) technique," *IEEE Transactions on Antennas and Propagation*, vol. 58, no. 6, pp. 2093–2097, Jun. 2010. 13
- [41] T. Laitinen, J. Toivanen, and P. Vainikainen, "Toward accurate antenna measurements using multi-probe systems," in *URSI General Assembly and Scientific Symposium*, 2011, pp. 1–4. 13
- [42] D. A. Leatherwood, "Plane wave, pattern subtraction, range compensation for spherical surface antenna pattern measurements," Ph.D. thesis, Georgia Institute of Technology, 1998. 13
- [43] F. Jensen and F. H. Larsen, "Spherical near-field far-field techniques," in *6th European Microwave Conference*, 1976, pp. 98–102. 15
- [44] T. Laitinen, S. Pivnenko, J. M. Nielsen, and O. Breinbjerg, "Theory and practice of the FFT / matrix inversion technique for probe-corrected spherical near-field antenna measurements with high-order probes," *IEEE Transactions on Antennas and Propagation*, vol. 58, no. 8, pp. 2623–2631, Aug. 2010. 15, 18, 78
- [45] Y. Saad, *Iterative Methods for Sparse Linear Systems*, 2nd ed. Philadelphia, PA, USA: Society for Industrial and Applied Mathematics SIAM, 2003. 15
- [46] A. C. Ludwig, "Calculation of orthogonal-function expansion from imperfect data," Electromagnetics Institute Technical University of Denmark, Lyngby, Tech. Rep., 1972. 15, 16
- [47] R. C. Wittmann, B. K. Alpert, and M. H. Francis, "Spherical near field antenna measurements using non-ideal measurement locations," in *AMTA 24th Annual Meeting and Symposium*, 2002. 16

- [48] ———, “Near-field, spherical-scanning antenna measurements with nonideal probe locations,” *IEEE Transactions on Antennas and Propagation*, vol. 52, no. 8, pp. 2184–2186, Aug. 2004. 16
- [49] A. Dutt and V. Rokhlin, “Fast Fourier transforms for nonequispaced data,” *SIAM Journal on Scientific Computing*, vol. 14, no. 6, pp. 1368–1393, Nov. 1993. 16
- [50] T. B. Hansen, “Spherical near-field scanning with higher-order probes,” *IEEE Transactions on Antennas and Propagation*, vol. 59, no. 11, pp. 4049–4059, Nov. 2011. 16, 18
- [51] C. H. Schmidt, M. M. Leibfritz, and T. F. Eibert, “Fully probe-corrected near-field far-field transformation employing plane wave expansion and diagonal translation operators,” *IEEE Transactions on Antennas and Propagation*, vol. 56, no. 3, pp. 737–746, Mar. 2008. 16, 42
- [52] C. H. Schmidt and T. F. Eibert, “Multilevel plane wave based near-field far-field transformation for electrically large antennas in free-space or above material halfspace,” *IEEE Transactions on Antennas and Propagation*, vol. 57, no. 5, pp. 1382–1390, May 2009. 16, 42
- [53] R. C. Wittmann, “Probe correction in spherical near-field scanning, viewed as an ideal probe measuring an effective field,” in *IEEE AP-S Symposium on Antennas and Propagation*, 1984, pp. 674–677. 17, 97
- [54] L. J. Foged, A. Giacomini, R. Morbidini, and A. Potenza, “Wideband field probes for advanced measurement applications,” in *IEEE International Conference on Microwaves, Communications, Antennas and Electronic Systems (COMCAS)*, 2011, pp. 1–7. 18
- [55] F. Saccardi, A. Giacomini, and L. J. Foged, “Probe correction technique of arbitrary order for high accuracy spherical near field antenna measurements,” in *AMTA 38th Annual Meeting and Symposium*, 2016. 18
- [56] L. J. Foged, F. Saccardi, and A. Giacomini, “Higher order versus first order probe correction techniques applied to experimental spherical NF antenna measurements,” in *10th European Conference on Antennas and Propagation (EuCAP)*, 2016, pp. 1–4. 18
- [57] A. C. Newell and S. F. Gregson, “Estimating the effect of higher order modes in spherical near-field probe correction,” in *AMTA 34th Annual Meeting and Symposium*, 2012. 18
- [58] ———, “Estimating the effect of higher order azimuthal modes in spherical near-field probe correction,” in *8th European Conference on Antennas and Propagation (EuCAP)*, 2014, pp. 2486–2490. 18
- [59] R. C. Wittmann and M. H. Francis, “Probe sensitivity in near-field, spherical-scanning, antenna measurements,” in *AMTA 34th Annual Meeting and Symposium*, 2012. 18
- [60] J. Jerauld, “Insights into spherical near field probe correction gained from examining the probe response constants,” in *AMTA 38th Annual Meeting and Symposium*, 2016. 18, 25
- [61] F. H. Larsen and J. E. Hansen, “A dual-polarized probe system for near-field measurements,” in *IEEE AP-S Symposium on Antennas and Propagation*, 1979, pp. 557–560. 23

- [62] T. Laitinen, “Advanced spherical antenna measurements,” Ph.D. thesis, Helsinki University of Technology, 2005. 23
- [63] J.-C. Bolomey, B. J., D. Picard, G. Fine, and M. Mostafavi, “Reduction of near-field techniques duration,” in *AMTA 8th Annual Meeting and Symposium*, 1986. 23
- [64] J.-C. Bolomey, B. J. Cown, G. Fine, L. Jofre, M. Mostafavi, D. Picard, J. P. Estrada, P. G. Friederich, and F. L. Cain, “Rapid near-field antenna testing via arrays of modulated scattering probes,” *IEEE Transactions on Antennas and Propagation*, vol. 36, no. 6, pp. 804–814, Jun. 1988. 23
- [65] L. Duchesne, P. Garreau, N. Robic, A. Gandois, P. O. Iversen, and G. Barone, “Compact multiprobe antenna test station for rapid testing of antennas and wireless terminals,” in *Joint Conference of the 10th Asia-Pacific Conference on Communications and the 5th International Symposium on Multi-Dimensional Mobile Communications Proceeding*, 2004, pp. 553–557. 23
- [66] P. O. Iverson, E. Pasalic, G. Engblom, K. Englund, O. Edvardsson, and P. Garreau, “Real-time spherical near-field antenna test range for wireless applications,” in *AMTA 21th Annual Meeting and Symposium*, 1999. 23
- [67] L. Durand, L. Duchesne, and L. J. Foged, “Fast antenna testing using advanced probe array technology,” in *4th European Conference on Antennas and Propagation (EuCAP)*, 2010, pp. 1–4. 23
- [68] E. Szpindor, P. O. Iversen, D. Frey, and J. Stamm, “Multi-probe spherical near-field antenna test system for an aircraft rotodome,” in *AMTA 37th Annual Meeting and Symposium*, 2015. 23
- [69] P. Garreau, L. Duchesne, A. Gandois, L. J. Foged, and P. O. Iversen, “Probe array concepts for fast testing of large radiating structures,” in *AMTA 26th Annual Meeting and Symposium*, 2004. 23
- [70] R. Cornelius and D. Heberling, “Spherical near-field scanning with pointwise probe correction,” *IEEE Transactions on Antennas and Propagation*, vol. 65, no. 2, pp. 995–997, Feb 2017. 24, 25
- [71] S. Pivnenko, J. J. Besada, A. Ruiz, and C. Rizzo, “On the probe pattern correction in spherical near-field antenna measurements,” in *AMTA 37th Annual Meeting and Symposium*, 2015. 25
- [72] D. Slepian, “Some comments on Fourier analysis, uncertainty and modeling,” *SIAM Review*, vol. 25, no. 3, pp. 379–393, Jul. 1983. 29, 41
- [73] F. Jensen and F. Larsen, “Spherical near-field technique,” in *IEEE AP-S Symposium on Antennas and Propagation*, 1977, pp. 378–381. 29
- [74] A. C. Newell and A. Repjar, “Results of spherical near-field measurements on narrow-beam antennas,” in *IEEE AP-S Symposium on Antennas and Propagation*, 1977, pp. 382–385. 29
- [75] R. L. Lewis, “Spherical scanning data processing; an algorithm for halving the data processing effort when the radiation into the back hemisphere is negligible,” in *IEEE AP-S Symposium on Antennas and Propagation*, Los Angeles, (USA), 1981, pp. 246–249. 29
- [76] S. Pivnenko, “Time-saving scanning schemes for measurement of electrically large antennas by spherical near-field technique,” in *5th European Conference on Antennas and Propagation (EuCAP)*, 2011, pp. 2009–2013. 31, 47

- [77] H. Shakhtour, R. Cornelius, and D. Heberling, “Effect of different truncation angles in spherical near-field measurements,” in *Loughborough Antennas and Propagation Conference (LAPC)*, Loughborough (UK), 2012, pp. 1–4. 32
- [78] R. Cornelius, H. Shakhtour, and D. Heberling, “Extrapolation of truncated spherical near-field measurements,” in *42th European Microwave Conference (EuMC)*, Amsterdam (Netherlands), 2012, pp. 301–304. 32, 36
- [79] P. R. Rousseau, “Development of a near-field data window function for measuring standard gain horns, the,” in *AMTA 19th Annual Meeting and Symposium*, 1997. 33
- [80] E. D. Giampaolo, “A numerical filter to remove the field scattered by the edges of a finite ground plane from measured data,” *Progress In Electromagnetics Research B (PIER B)*, vol. 9, p. 165, 2008. 33
- [81] R. Mauermayer and T. F. Eibert, “Spherical field transformation for hemispherical antenna measurements above perfectly conducting ground planes,” in *AMTA 38th Annual Meeting and Symposium*, 2016. 33
- [82] R. Cornelius, D. Heberling, and D. Pototzki, “Spherical near-field far-field transformation with infinite ground plane at arbitrary height z ,” in *11th European Conference on Antennas and Propagation (EuCAP)*, Paris (France), 2017, pp. 1472–1474. 33, 76
- [83] J. L. C. Sanz and T. Huang, “Some aspects of band-limited signal extrapolation: Models, discrete approximations, and noise,” *IEEE Transactions on Acoustics, Speech, and Signal Processing*, vol. ASSP-31, no. 6, pp. 1492–1501, Dec. 1983. 33, 35
- [84] H. J. Landau, “Extrapolating a band-limited function from its samples taken in a finite interval,” *IEEE Transactions on Information Theory*, vol. 32, no. 4, pp. 464–470, Jul. 1986. 33, 35, 41
- [85] B. J. Sullivan and B. Liu, “On the use of singular value decomposition and decimation in discrete-time bandlimited signal extrapolation,” *IEEE Transactions on Acoustics, Speech, and Signal Processing*, vol. 32, no. 6, pp. 1201–1212, Dec. 1984. 33
- [86] O. M. Bucci, G. D’Elia, and M. D. Migliore, “A new strategy to reduce the truncation error in near-field/far-field transformations,” *Radio Science*, vol. 35, no. 1, pp. 3–17, Feb. 2000. 33
- [87] J.-C. Bolomey, O. M. Bucci, L. Casavola, G. D’Elia, M. D. Migliore, and A. Ziyat, “Reduction of truncation error in near-field measurements of antennas of base-station mobile communication systems,” *IEEE Transactions on Antennas and Propagation*, vol. 52, no. 2, pp. 593–602, Feb. 2004. 33
- [88] O. M. Bucci and M. D. Migliore, “A new method for avoiding the truncation error in near-field antennas measurements,” *IEEE Transactions on Antennas and Propagation*, vol. 54, no. 10, pp. 2940–2952, Oct. 2006. 34
- [89] F. D’Agostino, F. Ferrara, C. Gennarelli, R. Guerriero, and G. Riccio, “An effective technique for reducing the truncation error in the near-field-far-field transformation with plane-polar scanning,” *Progress In Electromagnetics Research (PIER)*, vol. 73, pp. 213–238, 2007. 34
- [90] —, “An OSI-SVD based method for estimating the data falling in the blind zone of a NF spherical facility,” in *IEEE AP-S Symposium on Antennas and Propagation*, 2005, pp. 420–423. 34

- [91] A. Papoulis, "A new algorithm in spectral analysis and band-limited extrapolation," *IEEE Transactions on Circuits and Systems*, vol. 22, no. 9, pp. 735–742, Sep. 1975. 35
- [92] R. W. Gerchberg, "Super-resolution through error energy reduction," *Optica Acta*, vol. 21, no. 9, pp. 709–720, 1974. 35
- [93] D. C. Youla, "Generalised image restoration by the method of alternating projections," *IEEE Transactions on Circuits and Systems*, vol. CAS-25, no. 9, pp. 694–702, Sep. 1978. 35
- [94] Y. Rahmat-Samii, "Surface diagnosis of large reflector antennas using microwave holographic metrology an iterative approach," *Radio Science*, vol. 19, no. 5, pp. 1205–1217, Sep. 1984. 35
- [95] E. Martini, O. Breinbjerg, and S. Maci, "Reduction of truncation errors in planar near-field aperture antenna measurements using the gerchberg-papoulis algorithm," *IEEE Transactions on Antennas and Propagation*, vol. 56, no. 11, pp. 3485–3493, Nov. 2008. 35, 36, 37
- [96] —, "A convergence criterion for the iterative gerchberg-papoulis algorithm applied to truncation error reduction in planar near-field measurements," in *2nd European Conference on Antennas and Propagation (EuCAP)*, 2007, p. 793. 36
- [97] E. Martini, S. Maci, and L. J. Foged, "Reduction of truncation errors in spherical near field measurements," in *AMTA 32th Annual Meeting and Symposium*, 2010. 36
- [98] F. J. Cano-Fácil and S. Pivnenko, "A new method to reduce truncation errors in partial spherical near-field measurements," in *5th European Conference on Antennas and Propagation (EuCAP)*, 2011, pp. 3259–3263. 37
- [99] C. Cappellin, "Antenna diagnostics for spherical near-field antenna," Ph.D. thesis, Technical University of Denmark, 2007. 37
- [100] F. J. Cano-Fácil, S. Pivnenko, and M. Sierra-Castañer, "Reduction of truncation errors in planar, cylindrical, and partial spherical near-field antenna measurements," *International Journal of Antennas and Propagation*, pp. 1–19, 2012. 37
- [101] F. J. Cano-Fácil, "Contribution to the quality improvement of the antenna measurement using post-processing techniques," Ph.D. thesis, Universidad Politécnica de Madrid, 2012. 37
- [102] S. F. Gregson, "Measuring wide angle antenna performance using small planar scanners," in *10th International Conference on Antennas and Propagation (ICAP)*, 1997, pp. 451–455. 40
- [103] R. C. Wittmann, C. Stubenrach, and M. H. Francis, "Spherical scanning measurements using truncated data sets," in *AMTA 24th Annual Meeting and Symposium*, 2002. 40
- [104] G. Giordanengo, M. Righero, F. Vipiana, G. Vecchi, and M. Sabbadini, "Fast antenna testing with reduced near field sampling," *IEEE Transactions on Antennas and Propagation*, vol. 62, no. 5, pp. 2501–2513, May 2014. 40
- [105] K. Wu and S. Parekh, "Methods of transforming antenna fresnel region fields to far region fields," in *AMTA 11th Annual Meeting and Symposium*, 1989. 41
- [106] R. Cornelius, T. Salmerón-Ruiz, F. Saccardi, L. J. Foged, D. Heberling, and M. Sierra-Castañer, "A comparison of different methods for fast single-cut

- near-to-far-field transformation,” *IEEE Antennas and Propagation Magazine*, vol. 56, no. 2, pp. 252–261, Apr. 2014. 41
- [107] D. Slepian and H. O. Pollak, “Prolate spheroidal wave functions, Fourier analysis and uncertainty — I,” *The Bell System Technical Journal*, vol. 40, no. 1, pp. 43–63, Jan. 1961. 41
- [108] H. J. Landau and H. O. Pollak, “Prolate spheroidal wave functions, Fourier analysis and uncertainty — II,” *The Bell System Technical Journal*, vol. 40, no. 1, pp. 65–84, Jan. 1961. 41
- [109] —, “Prolate spheroidal wave functions, Fourier analysis and uncertainty — III: The dimension of the space of essentially time- and band-limited signals,” *The Bell System Technical Journal*, vol. 41, no. 4, pp. 1295–1336, Jul. 1962. 41
- [110] D. Slepian, “Prolate spheroidal wave functions, Fourier analysis and uncertainty — IV: Extensions to many dimensions; generalized prolate spheroidal functions,” *The Bell System Technical Journal*, vol. 43, no. 6, pp. 3009–3057, Nov. 1964. 41
- [111] —, “Prolate spheroidal wave functions, fourier analysis, and uncertainty — V: the discrete case,” *The Bell System Technical Journal*, vol. 57, no. 5, pp. 1371–1430, Jun. 1978. 41
- [112] A. Albertella, F. Sanso, and N. Sneeuw, “Band-limited functions on a bounded spherical domain: the slepian problem on the sphere,” *Journal of Geodesy*, vol. 73, no. 9, pp. 436–447, Oct. 1999. 41
- [113] F. J. Simons, F. A. Dahlen, and M. A. Wieczorek, “Spatiospectral concentration on a sphere,” *SIAM Review*, vol. 48, no. 3, pp. 504–536, Aug. 2006. 41
- [114] A. Plattner and F. J. Simons, “Spatiospectral concentration of vector fields on a sphere,” *Applied and Computational Harmonic Analysis*, vol. 36, no. 1, pp. 1–22, Jan. 2014. 41
- [115] A. P. Bates, Z. Khalid, and R. A. Kennedy, “Slepian spatial-spectral concentration problem on the sphere: Analytical formulation for limited colatitude–longitude spatial region,” *IEEE Transactions on Signal Processing*, vol. 65, no. 6, pp. 1527–1537, Mar. 2017. 41
- [116] K. T. Kim, “Truncation-error reduction in spherical near-field scanning using slepian sequences: Formulation for scalar waves,” *IEEE Transactions on Antennas and Propagation*, vol. 59, no. 8, pp. 2813–2823, Jun. 2011. 41
- [117] —, “Slepian transverse vector spherical harmonics and their application to near-field scanning,” in *IEEE AP-S Symposium on Antennas and Propagation*, 2011, pp. 2138–2141. 41
- [118] —, “Validation of the slepian approach to truncation-error reduction in spherical near-field scanning,” in *IEEE AP-S Symposium on Antennas and Propagation*, 2012, pp. 1–2. 41
- [119] P. Petre and T. K. Sarkar, “Differences between modal expansion and intergral equation methods for planar near-field to far-field transformation,” *Progress In Electromagnetics Research (PIER)*, vol. 12, pp. 37–56, 1996. 42
- [120] Y. Alvarez, F. Las-Heras, and M. R. Pino, “Reconstruction of equivalent currents distribution over arbitrary three-dimensional surfaces based on inte-

- gral equation algorithms,” *IEEE Transactions on Antennas and Propagation*, vol. 55, no. 12, pp. 3460–3468, Dec. 2007. 42
- [121] T. F. Eibert, E. Kilic, C. Lopez, R. A. M. Mauermayer, O. Neitz, and G. Schnattinger, “Electromagnetic field transformations for measurements and simulations (invited paper),” *Progress In Electromagnetics Research (PIER)*, vol. 151, pp. 127–150, May 2015. 42
- [122] P. Petre and T. K. Sarkar, “Planar near-field to far-field transformation using an equivalent magnetic current approach,” *IEEE Transactions on Antennas and Propagation*, vol. 40, no. 11, pp. 1348–1356, Nov. 1992. 42
- [123] A. Taaghola and T. K. Sarkar, “Near-field to near/far-field transformation for arbitrary near-field geometry, utilizing an equivalent magnetic current,” *IEEE Transactions on Electromagnetic Compatibility*, vol. 38, no. 3, pp. 536–542, Aug. 1996. 42
- [124] V. Rokhlin, “Rapid solution of integral equations of classical potential theory,” *Journal of Computational Physics*, vol. 60, no. 2, pp. 187–207, 1985. 42
- [125] L. Greengard and V. Rokhlin, “A fast algorithm for particle simulations,” *Journal of Computational Physics*, vol. 73, no. 2, pp. 325–348, 1987. 42
- [126] R. Coifman, V. Rokhlin, and S. Wandzura, “The fast multipole method for the wave equation: A pedestrian prescription,” *IEEE Antennas and Propagation Magazine*, vol. 35, no. 3, pp. 7–12, Jun. 1993. 42
- [127] W. Chew, E. Michielssen, J. M. Song, and J. M. Jin, Eds., *Fast and Efficient Algorithms in Computational Electromagnetics*. Norwood, MA, USA: Artech House, Inc., 2001. 42
- [128] V. Rokhlin, “Diagonal forms of translation operators for the helmholtz equation in three dimensions,” *Applied and Computational Harmonic Analysis*, vol. 1, no. 1, pp. 82–93, 1993. 42
- [129] M. A. Epton and B. Dembart, “Multipole translation theory for the three-dimensional Laplace and Helmholtz equations,” *SIAM Journal on Scientific Computing*, vol. 16, no. 4, pp. 865–897, Jul. 1995. 42
- [130] T. F. Eibert, “A diagonalized multilevel fast multipole method with spherical harmonics expansion of the k-space integrals,” *IEEE Transactions on Antennas and Propagation*, vol. 53, no. 2, pp. 814–817, Feb. 2005. 42
- [131] S. Pivnenko and T. Laitinen, “Spherical near-field antenna measurements with theta-scanning with reduced number of phi-steps,” in *AMTA 31th Annual Meeting and Symposium*, 2009, pp. 383–388. 47
- [132] Z. Khalid, R. A. Kennedy, and J. D. McEwen, “An optimal-dimensionality sampling scheme on the sphere with fast spherical harmonic transforms,” *IEEE Transactions on Signal Processing*, vol. 62, no. 17, pp. 4597–4610, Sep. 2014. 47
- [133] R. G. Yaccarino, L. I. Williams, and Y. Rahmat-Samii, “Linear spiral sampling for the bipolar planar near-field antenna measurement technique,” *IEEE Transactions on Antennas and Propagation*, vol. 44, no. 7, pp. 1049–1051, Jul. 1996. 47
- [134] L. I. Williams, R. G. Yaccarino, and Y. Rahmat-Samii, “Polar, thinned-polar, and linear spiral sampling using the UCLA bipolar planar near-field measurement system – a comparative-study,” in *IEEE AP-S Symposium on Antennas and Propagation*, 1994, pp. 548–551. 47

- [135] R. Cicchetti, F. D’Agostino, F. Ferrara, C. Gennarelli, R. Guerriero, and M. Migliozi, “Near-field to far-field transformation techniques with spiral scanning: A comprehensive review,” *International Journal of Antennas and Propagation*, pp. 1–13, 2014. 47, 48
- [136] F. D’Agostino, F. Ferrara, J. A. Fordham, C. Gennarelli, R. Guerriero, and M. Migliozi, “An experimental validation of the near-field - far-field transformation with spherical spiral scan,” *IEEE Antennas and Propagation Magazine*, vol. 55, no. 3, pp. 228–235, Aug. 2013. 47
- [137] E. B. Saff and A. B. J. Kuijlaars, “Distributing many points on a sphere,” *The Mathematical Intelligencer*, vol. 19, no. 1, pp. 5–11, 1997. 48, 49, 50, 51
- [138] R. Bauer, “Distribution of points on a sphere with application to star catalogs introduction,” *Journal of Guidance, Control, and Dynamics*, vol. 23, no. 1, pp. 130–137, Jan. 2000. 48, 49, 50, 51
- [139] D. P. Hardin, T. J. Michaels, and E. B. Saff, “A comparison of popular point configurations on S^2 ,” *Dolomites Research Notes on Approximation*, vol. 9, pp. 16–49, 2016. 48, 53, 54
- [140] C. G. Koay, “Analytically exact spiral scheme for generating uniformly distributed points on the unit sphere,” *Journal of Computational Science*, vol. 2, no. 1, pp. 88–91, Mar. 2011. 49, 50, 51
- [141] R. Cornelius and D. Heberling, “Analysis of sampling grids for spherical near-field antenna measurements,” in *Progress In Electromagnetics Research Symposium (PIERS)*, Prague (Czech Republic), 2015, pp. 923–927. 49
- [142] B. Rafaely, B. Weiss, and E. Bachmat, “Spatial aliasing in spherical microphone arrays,” *IEEE Transactions on Signal Processing*, vol. 55, no. 3, pp. 1003–1010, Mar. 2007. 56, 57
- [143] P. Pelland, G. Hindman, and D. van Rensburg, “Spherical near-field alignment sensitivity for polar and equatorial antenna measurements,” in *AMTA 38th Annual Meeting and Symposium*, 2016. 58
- [144] A. Capozzoli, L. Celentano, C. Curcio, A. Liseno, and S. Savarese, “Optimized near field with an optimized controller,” in *12th European Conference on Antennas and Propagation (EuCAP)*, 2018, pp. 1–5. 73
- [145] J. Christ, *Korrektur prinzipbedingter und durch die Messumgebung verursachter Fehler bei der Nahfeld-Fernfeld-Transformation*, ser. Berichte aus der Hochfrequenztechnik. Aachen: Shaker, 1995. 77, 78
- [146] D. A. Leatherwood, “Conical near-field antenna measurement system,” in *AMTA 29th Annual Meeting and Symposium*, 2007, pp. 29–35. 77, 78
- [147] —, “Conical near-field antenna measurement system,” *IEEE Antennas and Propagation Magazine*, vol. 50, no. 6, pp. 212–218, Dec. 2008. 77
- [148] R. Cornelius and D. Heberling, “Spherical wave expansion with arbitrary origin for near-field antenna measurements,” *IEEE Transactions on Antennas and Propagation*, vol. 65, no. 8, pp. 4385–4388, Aug. 2017. 78, 81
- [149] F. Saccardi, F. Mioc, P. O. Iversen, and L. J. Foged, “Theory and validation of reduced complexity translated-SWE algorithm with applications to automotive measurements with minimum sampling,” in *12th European conference on Antennas and Propagation (EuCAP)*, 2018, pp. 1–5. 81

- [150] A. C. Newell, "Error analysis techniques for planar near-field measurements," *IEEE Transactions on Antennas and Propagation*, vol. 36, no. 6, pp. 754–768, Jun. 1988. 95
- [151] CST AG, <http://www.cst.com>, CST Microwave Studio. 97
- [152] R. Cornelius and D. Heberling, "Correction of non-ideal probe orientations for spherical near-field antenna measurements," in *AMTA 39th Annual Meeting and Symposium*, Atlanta (USA), 2017, pp. 394–398. 98
- [153] Altair Engineering, Inc., <http://altairhyperworks.com/product/FEKO>, FEKO 14.0.4. 110, 115, 163
- [154] A. C. Newell, "Reducing measurement time and estimated uncertainties for the nist 18 term error technique," in *AMTA 28th Annual Meeting and Symposium*, 2006. 111
- [155] S. F. Gregson and A. C. Newell, "Verification of spherical mathematical absorber reflection suppression in a combination spherical near-field and compact antenna test range," in *AMTA 39th Annual Meeting and Symposium*, 2017, pp. 415–420. 115
- [156] D. Campbell, "Simulating antenna measurements in an anechoic chamber," in *AMTA 35th Annual Meeting and Symposium*, 2013. 115
- [157] V. Rodriguez, "Comparing predicted performance of anechoic chambers to free space VSWR measurements," in *AMTA 39th Annual Meeting and Symposium*, 2017, pp. 137–142. 115
- [158] Advanced ElectroMagnetics, Inc. (AEMI), http://www.mvg-world.com/en/products/field_product_family/absorber-6. 115, 163
- [159] D. Campbell, G. Gampala, C. J. Reddy, M. Winebrand, and J. Aubin, "Modeling and analysis of anechoic chamber using CEM tools," *ACES Journal*, vol. 28, no. 9, pp. 755–762, Sep. 2013. 115, 163
- [160] M. Dirix, R. Cornelius, and D. Heberling, "Determining measurement uncertainty in a CATR using quiet zone spherical near-field scanning," in *AMTA 37th Annual Meeting and Symposium*, Long Beach (USA), 2015, pp. 76–81. 124
- [161] F. Saccardi, L. J. Foged, and F. Mioc, "Echo reduction with minimum sampling in spherical near field measurements using translated-SWE algorithm," in *AMTA 38th Annual Meeting and Symposium*, 2016. 125
- [162] D. L. Donoho, "Compressed sensing," *IEEE Transactions on Information Theory*, vol. 52, no. 4, pp. 1289–1306, April 2006. 131
- [163] E. J. Candes, J. Romberg, and T. Tao, "Robust uncertainty principles: exact signal reconstruction from highly incomplete frequency information," *IEEE Transactions on Information Theory*, vol. 52, no. 2, pp. 489–509, Jan. 2006. 131
- [164] A. M. Tillmann and M. E. Pfetsch, "The computational complexity of the restricted isometry property, the nullspace property, and related concepts in compressed sensing," *IEEE Transactions on Information Theory*, vol. 60, no. 2, pp. 1248–1259, Feb. 2014. 132
- [165] D. L. Donoho and M. Elad, "Optimally sparse representation in general (nonorthogonal) dictionaries via ℓ_1 minimization," *Proceedings of the National Academy of Sciences*, vol. 100, no. 5, pp. 2197–2202, Mar. 2003. 132

- [166] Y. F. Alem, S. M. A. Salehin, D. H. Chae, and R. A. Kennedy, "Sparse recovery of spherical harmonic expansions from uniform distribution on sphere," in *7th International Conference on Signal Processing and Communication Systems (ICSPCS)*, 2013, pp. 1–5. 132
- [167] M. A. Davenport, "Random observations on random observations: Sparse signal acquisition and processing," Ph.D. thesis, Rice University, 2010. 132
- [168] M. D. Migliore, "A compressed sensing approach for array diagnosis from a small set of near-field measurements," *IEEE Transactions on Antennas and Propagation*, vol. 59, no. 6, pp. 2127–2133, Jun. 2011. 133
- [169] —, "A simple introduction to compressed sensing/sparse recovery with applications in antenna measurements," *IEEE Antennas and Propagation Magazine*, vol. 56, no. 2, pp. 14–26, Feb. 2014. 133
- [170] A. Massa, P. Rocca, and G. Oliveri, "Compressive sensing in electromagnetics — a review," *IEEE Antennas and Propagation Magazine*, vol. 57, no. 1, pp. 224–238, Feb. 2015. 133
- [171] H. Rauhut and R. Ward, "Sparse recovery for spherical harmonic expansions," in *9th International Conference on Sampling Theory and Applications*, 2011, pp. 1–4. 133
- [172] R. Cornelius, D. Heberling, N. Koep, A. Behboodi, and R. Mathar, "Compressed sensing applied to spherical near-field to far-field transformation," in *10th European Conference on Antennas and Propagation (EuCAP)*, Davos (Switzerland), 2016, pp. 1–4. 133
- [173] D. Löschenbrand and C. Mecklenbrauker, "Fast antenna characterization via a sparse spherical multipole expansion," in *4th International Workshop on Compressed Sensing Theory and its Applications to Radar, Sonar and Remote Sensing (CoSeRa)*, 2016, pp. 212–216. 133
- [174] B. Fuchs, L. L. Coq, S. Rondineau, and M. D. Migliore, "Fast antenna far-field characterization via sparse spherical harmonic expansion," *IEEE Transactions on Antennas and Propagation*, vol. 65, no. 10, pp. 5503–5510, Oct. 2017. 133
- [175] E. van den Berg and M. P. Friedlander, "SPGL1: A solver for large-scale sparse reconstruction," <http://www.cs.ubc.ca/labs/scl/spgl1>, 2007. 133
- [176] E. K. Miller, "Model-based parameter estimation in electromagnetics: Part I. Background and theoretical development," *IEEE Antennas and Propagation Magazine*, vol. 40, no. 1, pp. 42–52, Feb. 1998. 135
- [177] D. H. Werner and R. J. Allard, "The simultaneous interpolation of antenna radiation patterns in both the spatial and frequency domains using model-based parameter estimation," *IEEE Transactions on Antennas and Propagation*, vol. 48, no. 3, pp. 383–392, Mar. 2000. 135
- [178] R. J. Allard and D. H. Werner, "The model-based parameter estimation of antenna radiation patterns using windowed interpolation and spherical harmonics," *IEEE Transactions on Antennas and Propagation*, vol. 51, no. 8, pp. 1891–1906, Aug. 2003. 135
- [179] W. Dullaert and H. Rogier, "Novel compact model for the radiation pattern of UWB antennas using vector spherical and slepian decomposition," *IEEE Transactions on Antennas and Propagation*, vol. 58, no. 2, pp. 287–299, Feb. 2010. 135

- [180] N. Mutoonkole, E. R. Samuel, D. I. L. de Villiers, and T. Dhaene, "Parametric modeling of radiation patterns and scattering parameters of antennas," *IEEE Transactions on Antennas and Propagation*, vol. 64, no. 3, pp. 1023–1031, Mar. 2016. 135
- [181] Microwave Vision Group, <http://www.mvg-world.com>. 141

List of publications

- R. Cornelius and D. Heberling, “Correction of non-ideal probe orientations for spherical near-field antenna measurements,” in *AMTA 39th Annual Meeting and Symposium*, Atlanta (USA), 2017, pp. 394–398.
- R. Cornelius and D. Heberling, “Fast spherical near-field antenna measurements by advanced sampling and direct spherical wave expansion,” in *Kleinheubacher Tagung*, Miltenberg (Germany), 2017.
- R. Cornelius and D. Heberling, “Spherical wave expansion with arbitrary origin for near-field antenna measurements,” *IEEE Transactions on Antennas and Propagation*, vol. 65, no. 8, pp. 4385–4388, Aug. 2017.
- M. A. Saporetti, L. J. Foged, M. S. Castañer, S. Pivnenko, R. Cornelius, and D. Heberling, “Description and results: Antenna measurement facility comparisons [measurements corner],” *IEEE Antennas and Propagation Magazine*, vol. 59, no. 3, pp. 108–116, Jun. 2017.
- T. M. Gemmer, R. Cornelius, J. Pamp, and D. Heberling, “Full-wave analysis of a compact antenna test range including probe effect,” in *11th European Conference on Antennas and Propagation (EuCAP)*, Paris (France), 2017, pp. 2577–2581.
- R. Cornelius, D. Heberling, and D. Pototzki, “Spherical near-field far-field transformation with infinite ground plane at arbitrary height z ,” in *11th European Conference on Antennas and Propagation (EuCAP)*, Paris (France), 2017, pp. 1472–1474.
- R. Cornelius, A. Narbudowicz, M. J. Ammann, and D. Heberling, “Calculating the envelope correlation coefficient directly from spherical modes spectrum,” in *11th European Conference on Antennas and Propagation (EuCAP)*, Paris (France), 2017, pp. 3014–3017.
- R. Cornelius and D. Heberling, “Spherical near-field scanning with pointwise probe correction,” *IEEE Transactions on Antennas and Propagation*, vol. 65, no. 2, pp. 995–997, Feb 2017.
- A. Giacomini, L. J. Foged, A. Riccardi, J. Pamp, R. Cornelius, and D. Heberling, “Improving the cross-polar discrimination of compact antenna test range using the CXR feed,” in *AMTA 38th Annual Meeting and Symposium*, Austin (USA), 2016, pp. 411–415.
- K. Menzel, R. Cornelius, and D. Heberling, “Vergleich zwischen dem neuen NF-Huygens-Verfahren und der etablierten Modenentwicklung zur Berechnung des Gesamtfeldes aus Antennennahfeldmessungen,” in *Kleinheubacher Tagung*, Miltenberg (Germany), 2016.
- R. Cornelius, D. Heberling, N. Koep, A. Behboodi, and R. Mathar, “Compressed sensing applied to spherical near-field to far-field transformation,” in *10th European Conference on Antennas and Propagation (EuCAP)*, Davos (Switzerland), 2016, pp. 1–4.
- M. Dirix, R. Cornelius, and D. Heberling, “Calculating arbitrarily located sampling data from quiet zone spherical near-field scanning measurements,” *IEEE*

- Transactions on Antennas and Propagation*, vol. 64, no. 3, pp. 865–871, Mar. 2016.
- J. Pamp, A. Giacomini, R. Cornelius, A. Riccardi, L. J. Foged, and D. Heberling, “Reduction of the cross polarization component in the quiet zone of a single reflector CATR,” in *AMTA 37th Annual Meeting and Symposium*, Long Beach (USA), 2015, pp. 71–75.
 - M. Dirix, R. Cornelius, and D. Heberling, “Determining measurement uncertainty in a CATR using quiet zone spherical near-field scanning,” in *AMTA 37th Annual Meeting and Symposium*, Long Beach (USA), 2015, pp. 76–81.
 - R. Cornelius, A. A. Bangun, and D. Heberling, “Investigation of different matrix solver for spherical near-field to far-field transformation,” in *9th European Conference on Antennas and Propagation (EuCAP)*, Lisbon (Portugal), 2015, pp. 1–4.
 - R. Cornelius and D. Heberling, “Analysis of sampling grids for spherical near-field antenna measurements,” in *Progress In Electromagnetics Research Symposium (PIERS)*, Prague (Czech Republic), 2015, pp. 923–927.
 - R. Cornelius, M. Dirix, H. Shakhtour, and D. Heberling, “Comparison of horizontal and vertical feed scanning based APC in a compact range,” in *8th European Conference on Antennas and Propagation (EuCAP)*, The Hague (Netherlands), 2014, pp. 3399–3403.
 - R. Cornelius, T. Salmerón-Ruiz, F. Saccardi, L. J. Foged, D. Heberling, and M. Sierra-Castañer, “A comparison of different methods for fast single-cut near-to-far-field transformation,” *IEEE Antennas and Propagation Magazine*, vol. 56, no. 2, pp. 252–261, Apr. 2014.
 - H. Schippers, R. Cornelius, G. Vos, and A. Hulzinga, “Smart antenna technology for airborne communication,” in *7th European Conference on Antennas and Propagation (EuCAP)*, Gothenburg (Sweden), 2013, pp. 2735–2739.
 - H. Shakhtour, R. Cornelius, and D. Heberling, “Scattering suppression in a combined compact range and spherical near-field measurement facility,” in *AMTA 35th Annual Meeting and Symposium*, Columbus (USA), 2013, pp. 366–371.
 - H. Shakhtour, R. Cornelius, and D. Heberling, “Three antenna gain determination method in compact antenna test ranges,” in *Loughborough Antennas and Propagation Conference (LAPC)*, Loughborough (UK), 2013, pp. 392–396.
 - R. Cornelius, H. Shakhtour, and D. Heberling, “Extrapolation of truncated spherical near-field measurements,” in *42th European Microwave Conference (EuMC)*, Amsterdam (Netherlands), 2012, pp. 301–304.
 - H. Shakhtour, R. Cornelius, and D. Heberling, “Effect of different truncation angles in spherical near-field measurements,” in *Loughborough Antennas and Propagation Conference (LAPC)*, Loughborough (UK), 2012, pp. 1–4.
 - H. Schippers, R. Cornelius, A. Hulzinga, and G. Vos, “Real-time adaptive beamforming for vibrating airborne antenna arrays,” in *5th European Conference on Antennas and Propagation (EuCAP)*, Rome (Italy), 2011, pp. 1032–1035.

Curriculum vitae

Personal details

Name	Rasmus Cornelius
Place of birth	Köln, Germany
Date of birth	May 12 th , 1986
Nationality	German

Education

2011	Diploma in electrical engineering and information technology at RWTH Aachen University. Specialization in high frequency technologies and signal processing. Subject of diploma thesis: “Effect of truncated scanning area in spherical near-field antenna measurement”.
------	--

Work experience

06/2018 – today	Senior Research Specialist Radio Network Propagation Models, Deutsche Telekom IT GmbH.
02/2012 – 05/2018	Research assistant at Institute of High Frequency Technology (IHF), RWTH Aachen University.
10/2010 – 03/2011	Internship at Netherlands Aerospace Centre (NLR) in Marknesse (NL), department “Avionics”. Project: “Real-time adaptive beam-forming for vibrating airborne antenna arrays” EuCAP 2011 publication.

Grants / Awards

2017	AMTA Best Student Paper Award – 3rd Place.
2017	Kleinheubacher Tagung – Young Scientist Award.
2016	IEEE AP-S Doctoral Research Grant.
2015	PIERS Best Student Paper Award.
2013	EU COST Short-Term Scientific Mission: “Antenna Measurement Techniques Reference”, UPM Madrid University, Spain.
2010 – 2011	NRW-Bildungsfonds Stipendiat.